THE UNIVERSITY OF CHICAGO

COHERENT DYNAMICS AND REACTIONS IN ATOMIC AND MOLECULAR BOSE-EINSTEIN CONDENSATES

A DISSERTATION SUBMITTED TO
THE FACULTY OF THE DIVISION OF THE PHYSICAL SCIENCES
IN CANDIDACY FOR THE DEGREE OF
DOCTOR OF PHILOSOPHY

DEPARTMENT OF PHYSICS

BY
ZHENDONG ZHANG

CHICAGO, ILLINOIS
JUNE 2022

To my loving family and friends

TABLE OF CONTENTS

LIST OF FIGURES

LIST OF TABLES

ACKNOWLEDGMENTS

First of all, I would like to thank my PhD advisor Prof. Cheng Chin for guiding me through the fascinating ultracold quantum world with all of his enthusiasm and patience. I joined the Cs lab with little experience working on ultracold atom experiments before. I was nevertheless fascinated by the cool science studied in Cs lab during its history and Cheng kindly offered me a position at Cs lab after several discussion I had with him about the things I want to study on the system. He tried to make use of every opportunity to impart to me his great knowledge of the experiment and his thoughts about science, during our regular group meetings, sometimes during lunch or dinner and sometimes on the way when we go playing badminton together. After these five years, I find myself benefit from those conversations unconciously and I start to really think like a physicist with the vivid pictures and intuitions in mind instead of working on complicated math without really understanding what's going on physically. I would also like to thank him for his belief in me as the group chef for preparing food in many of the parties at his place for celebrating the festivals and so on.

I would also like to acknowledge the fantastic team members in Cs lab who worked with me. Thanks to Dr. Lei Feng for welcoming me to the lab. It is his reminders and suggestions that prevented me from breaking the essential lab equipment so that I can keep the experiment running smoothly for almost five years. I learnt a lot of things and good habits from Lei about how to do the experiments and analyze the data properly. Thanks to Dr. Jiazhong Hu for his kind patience in training me during my first year. He makes me understand better about the system and his way of building simple models for understanding the experimental results has a great influence on me. I also constantly benefit from my lab partner Kai-Xuan (Kevin) Yao. He is really smart and almost always immediately see through the key points of the problems. His quick feedback and suggestions make me work more efficiently in the lab and understand science problems better. Many thanks to

Dr. Liangchao Chen who worked very hard in the lab, even during the most difficult and uncertain time of the pandemics. Thanks to Shu Nagata for spending those late nights in the lab with me. Shu is very resilient when facing with problems and can keep working on it without giving it up. I also appreciate the knowledge I learnt about the experiment from Dr. Logan Clark, whose great works and discoveries together with Lei have formed the foundation of the works presented in this thesis.

I also appreciate the help and support from the rest of the Chin lab members and the great times we had together. I appreciate all the help and support from Geyue (Frank) Cai, who has been my roommate for almost 4 years, especially during those difficult times of the pandemic. His little humor and the knowledge of "philosophy" make me happy, usually when I come back home after a whole day of running the experiment. I also enjoy those little chats in the lab with Krutik Patel. Krutik is a really enthusiastic person to talk to and the time when we are working on problem sets together for Prof. Jon Simon's class was a lot of fun! I also appreciate his careful proofread for every single paper from us in the Cs lab during the past five years. Thanks to Jonathan Trisnadi for all of his help. I also enjoy his sometimes little humor and his great painting skills a lot. Thanks to Jiamei for her help on the Cs experiment during my first year. Thanks to Lauren Weiss and Henry Ando for setting up the event of Chin lab group lunch. They have injected fresh blood into the whole group. Thanks to Dr. Mickey McDonald for his help during my novice year and the fun board game of outer space exploration he created and invited me to play. Thanks to Dr. Brian Desalvo for his help on trouble shooting our experiment.

It's a great privilege to be able to work our collaborator Prof. Kathy Levin, who always encourages me to express my own thoughts. Thanks to Dr. Han Fu for the nice simulations she did for us. Thanks to Dr. Zhiqiang Wang, from whom I learnt a lot about condensed matter theory. I also would like to thanks my other thesis committee members Prof. Jonathan Simon and Prof. Yau Wah for their support and great interests in the research I did.

Thanks to the previous undergrad group members Misha Usatyuk and Frankie Fung, whose jokes always make me laugh and it's nice to see them around. Thanks to my friend and roommate Jiewei Xiang for his company during the first year of my PhD. Thanks to Amy Schulz for her nice greetings with my name precisely pronounced when I first came to UChicago. Thanks to Putri Kusumo and Zosia Krusberg for providing me the guidelines of PhD graduation. Thanks to Maria Jimenez for all your helps. I'm also grateful for the support from the University of Chicago and the donors through the Grainger Graduate Fellowship, Plotnick Fellowship, Yodh Prize and Quantum Creators Prize. Also thanks to Cheng, Kevin, Frank, Jon, Lauren and Shu for their careful proofreading of this thesis.

Lastly I would like to thank my parents for all their unconditional love and all the support during the most difficult times in my life. Thanks to my girlfriend Shanshan for you love, patient listening and company.

ABSTRACT

Discovery and understanding of new quantum phases of matter are essential for the development of modern science and technology. For example, the discovery of conventional and high-T_c superconductors, quantum Hall and fractional quantum effects have great potential in applications for efficient storage and transfer of energy and information. On the other hand, a deep understanding of the underlying many-body quantum states and their associated properties can greatly improve our knowledge of nature and eventually guide us to develop devices with optimal performance.

Ultracold quantum gas, enabled by the techniques of laser cooling and trapping and evaporative cooling, serves as an ideal laboratory for the study of many-body physics. The system of interacting ultracold atoms has been proven successful for demonstrating novel and strongly correlated quantum phases of matter, such us Bose-Einstein condensate (BEC), Bardeen-Cooper-Schrieffer (BCS) and Berezinskii-Kosterlitz-Thouless (BKT) superfluid and Mott insulator. On the other hand, the unique control of atomic interaction and external potential in a widely tunable range also allows us to drive the system far from equilibrium and to study its quantum dynamics happening at length and time scales that are easily tractable, which can reveal new phases of matter that typically do not occur near equilibrium and allow us to explore novel emergent coherent and collective phenomenon.

This thesis describes experiments on the coherent dynamics and reactions of ultracold, bosonic Cs atoms and Cs_2 molecules. Our apparatus is robust and versatile for extensive control of quantum gases. In particular, atomic BECs with different shape and dimensionalities are produced as the starting point of most of our experiments; we have precise temporal control over inter-atomic interactions through external magnetic field in vicinity of Feshbach resonances and we can project dynamic external potentials by our digital micromirror device (DMD).

Taking advantage of our apparatus, we first apply strong driving to a quasi-two dimen-

sional (2D) BEC by periodically modulating the atomic interaction between repulsive and attractive and observed novel stimulated emission of atomic matter wave jets from condensate into radial directions, which we name as "Bose fireworks". Even though locally the number of atoms in the jets follows thermal distribution, we find the spatial and temporal coherence by interfering two sets of matter wave jets with different momentum and time reversal of the jet emission, respectively. This suggests global unitary evolution of a closed system. By applying dual-frequency interaction modulation schemes, we observed spontaneous formation of density wave patterns with D_2, D_4 and D_6 symmetries emerging from uniform disk-shaped condensates. The patterns are revealed by our unbiased real-space pattern recognition algorithm, which provides richer information than conventional correlation functions. Furthermore, we identified a resonant nonlinear wave mixing process underlying the formation of hexagonal density wave pattern from a novel $g^{3/2}$ correlator. The D_6 pattern grows through an interplay of the $g^{3/2}$ correlator and population of excited momentum modes, which is expected to grow faster than exponential. On the other hand, the matter wave emission also serves as a tool for extracting the initial BEC wave function. As two examples, we studied jet emission from a nonuniform BEC with a relative phase between its two halves and a rotating BEC with vortices inside. The relative phase between two halves of the BEC and both the magnitude and chirality of angular momentum of vortices in the rotating BEC are extracted from the substructure of near field matter wave emission patterns.

Besides the interaction control, Feshbach resonances also allow us to directly associate atoms in a condensate into molecules. We demonstrated the creation of Cs_2 molecular BEC by pairing atoms in an atomic condensate near a narrow g-wave Feshbach resonance, which is confirmed by our equation of state measurement for the molecular quantum gas. We extract the elastic molecular scattering length to be +220 Bohr from the equation of state for the first time. The two-dimensional and flat-bottomed trap geometry and low

temperature help to stabilize the molecules and remain thermal equilibrium. Our work thus demonstrates the long-sought transition between atomic and molecular condensates, the bosonic analogue of BCS-BEC crossover in a degenerate Fermi gas. Apart from the equilibrium properties, we also studied reaction dynamics in an atomic BEC by quench magnetic field close to the resonance point. Molecules are produced rapidly from atomic samples after the quench. As a function of the atomic sample temperature, the initial molecule formation rates sharply transition from the values determined by thermal collisions between atoms in normal gas phase to those in the degeneracy regime where the wave nature of atoms dominates. Following the initial proliferation, the molecules reach quasi-equilibrium with the atoms and the number of molecules shows coherent oscillatory evolution with the oscillation frequency determined by both the molecular binding energy and the atomic density. We further enhance the amplitude of the molecule number oscillation by periodically modulating the molecular binding energy. Our experiments thus demonstrate collective chemical reactions in a strongly interacting atomic BEC.

CHAPTER 1

INTRODUCTION

Since its first prediction by Einstein almost a century ago, condensates of various types of atoms such as alkali metal, alkaline earth metal and lanthanide atoms can now be produced daily in the lab, thanks to the development of laser cooling and traping and collisional cooling techniques. This new form of matter emerges out of quantum statistics of indistinguishable bosons and it is achieved when the temperature reaches below a critical value T_c, where the thermal de Broglie wavelength of each particle is larger than the average inter-particle spacing. For a BEC in a weakly interacting dilute gas, almost all the atoms share the same wave function on the mean field level and show macroscopic coherence. Various exotic collective phenomena can thus occur in BECs, such as interference between two BECs [6], four-wave mixing with matter waves [45], bosenova explosion [46] and soliton train formation [132] in BECs with attractive interaction. Quantum phase transitions are also observed such as the transition from a superfluid to a Mott-insulator realized with the addition of external periodic potential—the optical lattice—formed by interference of counter-propagating laser beams [60].

Ultracold atom experiments offer great opportunities for us to study both the properties of quantum matter at or near equilibrium and novel dynamics when the system is driven far from equilibrium, due to several of their unique advantages compared to, e.g. condensed matter experiments. Prepared in a ultrahigh vacuum chamber, the atoms are well isolated from the environment. External potential felt by atoms can be precisely controlled with wide tunability in its strength and geometry. With the application of period potential formed by interference of laser beams, the dispersion of atoms can be largely modified either statically or dynamically [33]. Ultracold atoms loaded into an optical lattice also enable the simulation of fundamentally important models in condensed matter physics such as Bose- and Fermi-Hubbard models [18], whose solution requires exponentially large computation resources

as the system size increases. Together with the tunability of atomic interaction using the Feshbach resonance [30], all the parameters in the model to be simulated can be precisely controlled microscopically. On the other hand, the typical length scale of few micrometers and time scale of sub to few milliseconds in quantum gas system are easy to be detected using conventional optical imaging and electronic control techniques. Therefore, ultracold quantum gases provide an ideal platform for the benchmark of theory models as well as discovery of new phases of matter and out-of-equilibrium phenomena.

Here we are interested in studying emergent many-body dynamics when BECs are driven far from equilibrium. Specifically, we demonstrated the long range spatial coherence and correlation as well as temporal coherence in the stimulated emission of matter wave jets—the "Bose fireworks"—when the interaction strength between atoms is periodically modulated in vicinity of a Feshbach resonance, which is first observed by previous members in our lab [35]. Together with the fact that the emission happens only when the modulation amplitude exceeds a threshold value that is determined by the escape rate of atoms from BEC [35], "Bose fireworks" emission stands as a matter wave analogue of lasing of light in a gain medium. We thus build different kinds of atom-optical elements for manipulating the matter waves, by projecting various potential profiles using a digital micromirror device.

On the other hand, we also looked into how the system under the external driving evolves into a particular pattern starting from a uniform BEC. We developed three modulation schemes at two commensurate modulation frequencies, which allow us to create density waves with D_2, D_4 and D_6 symmetries on demand formed by the interference of excited atoms with remaining BEC atoms before the excited atoms leave condensate to form jets. The density wave patterns are identified from repetitive experiments by a real space pattern recognition algorithm we developed. We further found a nonlinear resonant wave mixing process underlying the D_6 pattern formation, revealed by a novel three point correlator we evaluate. This nonlinear wave mixing actually leads to faster-than-exponential population

growth in the momentum modes forming the D_6 pattern.

In addition, we found that the fireworks emission pattern contains essential information about both the density and phase distributions of the initial condensate. In particular, we demonstrate the extraction of the phase information either from a BEC separated into two halves with a relative phase or from a vortex embedded BEC. The relative phase between the two half BECs and the vortex winding number are extracted from the substructure of the density-density correlation function of the emitted atomic jets. In general, arbitrary initial BEC wave functions can be extracted with the interaction modulation technique as long as a set of correlators are measured from near field interference and far field momentum distribution of the emitted matter wave jets.

Feshbach resonance not only allows us to tune the effective interaction between atoms, it also opens the door to ultracold molecules where pairs of atoms are associated in condensates. Cold and ultracold molecules are important tools for precision measurements, ultracold chemistry, quantum simulation and quantum information processing, due to their rich energy structure and interaction properties [20, 22, 119]. In particular, theories [123, 120, 48] have predicted that a quantum phase transition can occur between an atomic and a molecular BEC, which is very different from the BCS-BEC crossover where overlapping fermion pairs smoothly turn into bound molecules across the Feshbach resonance in a degenerate atomic Fermi gas. In our case, we pair condensed Cs atoms in a 2D flat-bottomed box trap potential to create ultracold Cs_2 molecules by adiabatically ramping through a narrow g-wave Feshbach resonance. Through equation of state measurements, we demonstrated that the molecules also condense in the ground state of the trap. The low temperatue and 2D trap geometry help to suppress inelastic collision loss of the molecules such that they can reach thermal equilibrium. One the other hand, we induce reaction dynamics by quenching the magnetic field close to the resonance point starting from ultracold atoms. We observed that the initial molecule formation rate follows different rules for initial atomic samples prepared

in normal gas and quantum degenerate regimes. In the degeneracy regime, after the faster initial growth, the molecular population shows coherent oscillation, at a frequency that is determined by both the molecular binding energy and atomic density. We also demonstrated the coherence in the reverse reaction—molecule dissociation—starting from pure ultracold molecular samples, using a Ramsey type of pulse sequence approching the resonance. Possible many-body effects such as Bose stimulation in the reaction processes remain to be explored in our future experiments.

1.1 Overview of the thesis

This thesis proceeds as follows: First, in Ch.2 we describe the current status of our experimental system (details can be found in Ref. [72, 146, 62, 33, 54]) and the essential techniques we use in the experiments presented in later chapters. Next, in Ch.3, we present the theory for atomic BECs with periodically modulated interaction as well as the phase transition and reaction dynamics in atomic and molecular Bose-Einstein condensates near a narrow Feshbach resonance. The two subsequent chapters includes the main results of the thesis on coherent many-body dynamics in a driven BEC: In Ch.4 we present our study of spontaneous pattern formation from a uniform BEC driven at two commensurate frequencies. Then, in Ch.5 we demonstrate Bose fireworks emission as a tool to image the density and phase distributions of the initial BEC wave functions. The next two chapters present the core results of the thesis on coherent reaction dynamics in atomic and molecular Bose-Einstein condensates: In Ch.6, we demonstrate the creation of a molecular BEC by pairing atoms in a condensate trapped by a 2D flat-bottomed box potential via ramping through a narrow g-wave Feshbach resonance. In Ch.7, we present our systematic study of the coherent reaction dynamics in ultracold atoms and molecules. Finally, we conclude in Ch.8 with preliminary experimental results on building various atom-optical elements by DMD projection and a theory proposal for creating quasi-crystal patterns from a uniform BEC driven at three different frequencies.

CHAPTER 2

VERSATILE AND ROBUST ULTRACOLD CESIUM APPARATUS

2.1 General setup

For most of our experiments, we start by preparing a Cs BEC in a crossed dipole trap. First, atomic flux from a Cs oven heated up to $\sim 70^o$C flows through an intermediate region and Zeeman slower tube where a counter-propagating near-resonant laser beam slows down the atoms before they are captured by a magneto-optical trap (MOT) in the ultrahigh vacuum science chamber, see Fig. 2.1. Then stages of compressed MOT, optical molasses and degenerate Raman sideband cooling (dRSC) further cool atoms down to ~ 1.5 μK with around 6 to 8 million atoms. After dRSC, atoms are levitated by a magnetic field gradient of 31 G/cm against gravity and are trapped by crossed x-, y- and z-axis dipole trap (XDT,YDT and ZDT) beams shown in Fig. 2.3. X(Y)DT that is propagating in x(y) direction mainly provides confinement in y(x) direction. ZDT propagates at 45^o relative to X and YDT in the same horizontal plane and strongly confines atoms in the vertical direction, with additional confinement in the horizontal plane perpendicular to its propagation direction, which makes the atomic cloud elliptical. Then evaporative cooling is performed with the levitation field gradient gradually decreased to zero and the intensity of ZDT reduced simultaneously, at a magnetic field of around 20.8 G where the scattering length is 210 a_0 for the thermalization of remaining atoms [74]. A pure BEC with $\sim$60,000 atoms is obtained after $\sim$6 s of evaporation. We can control the temperature and density of atoms by tuning the intensity of the ZDT at the end of evaporation, as is used in Chapter 7.

For future users of the system, it's worth mentioning an accident that happened to the vacuum parts of the system. In August 2020, after we replaced a broken thermoelectric cooler (TEC) in the cooling block at the cold nipple between Cs oven and the intermediate

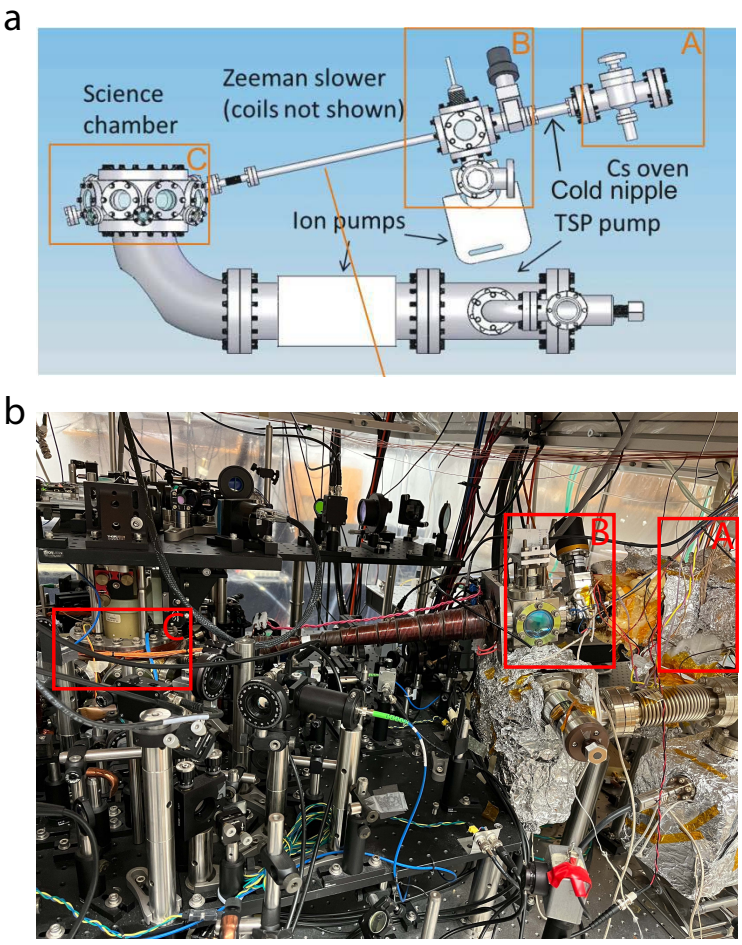

Figure 2.1: **Overview of the experimental system.** **a**, The vacuum design diagram including the Cs source and oven (A), the intermediate region (B) and the ultrahigh vacuum region (C). This figure is regenerated from Ref. [146]. **b**, A picture of the actual setup taken on 04/21/2022 by the author of this thesis.

region (see Fig. 2.1) by a new one, the lower aperture of the nipple tube seemed to be blocked, see Fig. 2.2 (see Ref. [72] for more about the cold nipple and small apertures on its two ends). We checked that the Zeeman slower beam cannot transmit through the higher side window in Cs oven region shown in Fig. 2.1. In this situation, after loading MOT for 2 s we could only get 16 million atoms whereas before the accident we can get 40 million. The atom number doesn't saturate after loading for 5 s, which means the atom flux is insufficient compared to before. We thus decided to heat up the two apertures to 110^oC using heating tape and heat the nipple tube up to 30^oC by turning off the TEC in the cooling block. After

one day, we found the MOT loading recovered to its previous performance and we got a BEC. But the number of atoms in BEC was only 38,000 based on our previous evaporation procedure, reduced by ∼40% compared to before and BEC 1/e lifetime drops to 6 s [36]. We found that the lower aperture is presumably still blocked because the Zeeman slower bean still cannot pass through the side window in the Cs oven region. Due to possibly high Cs vapour pressure in the science chamber where BEC is prepared, the collision between BEC atoms with background gas is more severe than before and we recover the atom number in the BEC by reducing the evaporation time to ∼4 s for less background gas collision time during the evaporation process. With the system running in this mode, we don't need to

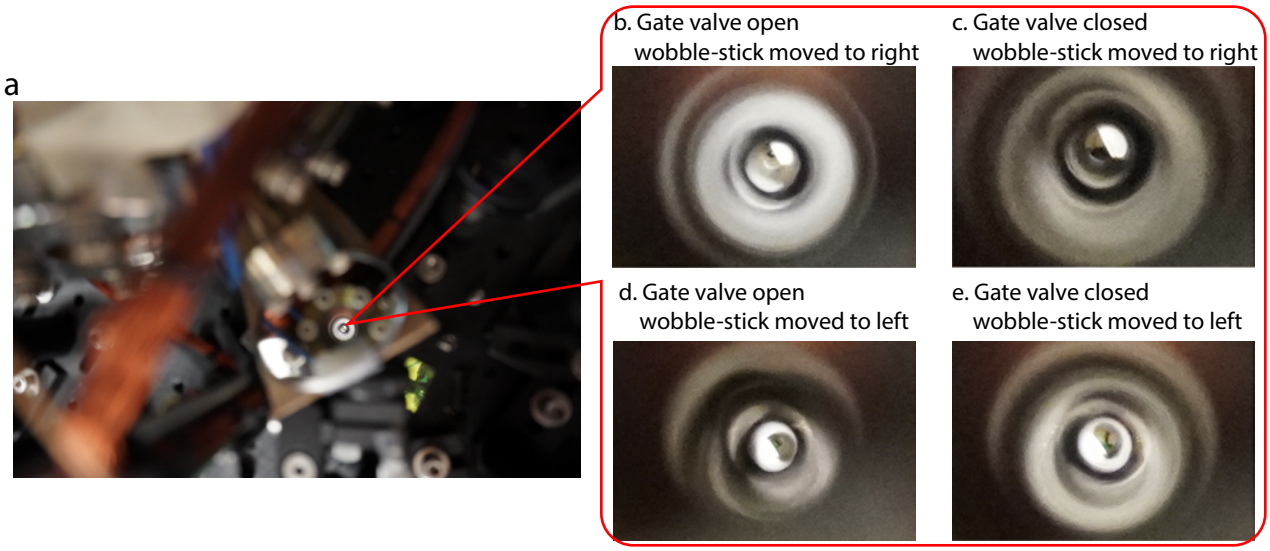

Figure 2.2: **Images of the lower aperture of the nipple tube. a**, Zoom out view of the lower aperture looking from one of the side windows on the science chamber. **b-e**, Zoom in view of the lower aperture with the wobble stick and gate valve in the intermediate region shown in Fig. 2.1 set to different states.

heat the Cs oven to 70^{o}C as we did previously but instead we keep it to be ∼20^{o}C, the same as the room temperature. Recently, we found that we have to increase MOT loading time to 3 s to maintain the performance of the BEC preparation, likely due to the reduction of Cs vapour pressure in the science chamber.

After a BEC is achieved in the crossed dipole trap, we can reshape the BEC adiabatically

by transferring it into a single site of a vertical lattice and arbitrary potential profile projected by DMD, see Fig. 2.3. Two 1064 nm laser beams split from a single source cross at a small angle of 16^o, and interfere to form the vertical lattice with lattice spacing 3.8 μm. By increasing the intensity of the ZDT to compress the atomic cloud vertically and adjusting the vertical cloud position using the magnetic field gradient, atoms can be loaded into a single site of the vertical lattice. Since the trap frequency of a single lattice site can go up to 2 kHz, which is much larger than the chemical potential and temperature of typical BECs, we can prepare a 2D quantum gas in which atomic wave function is frozen to the ground state of the vertical trap, as is used in Chapter 3-6. In addition, a BEC with horizontally uniform density profile can be achieved by loading it into flat-bottomed box potential projected by the DMD. We can also change the shape of the DMD potential to make a elongated BEC in the vertical lattice, as is used in Chapter 8.

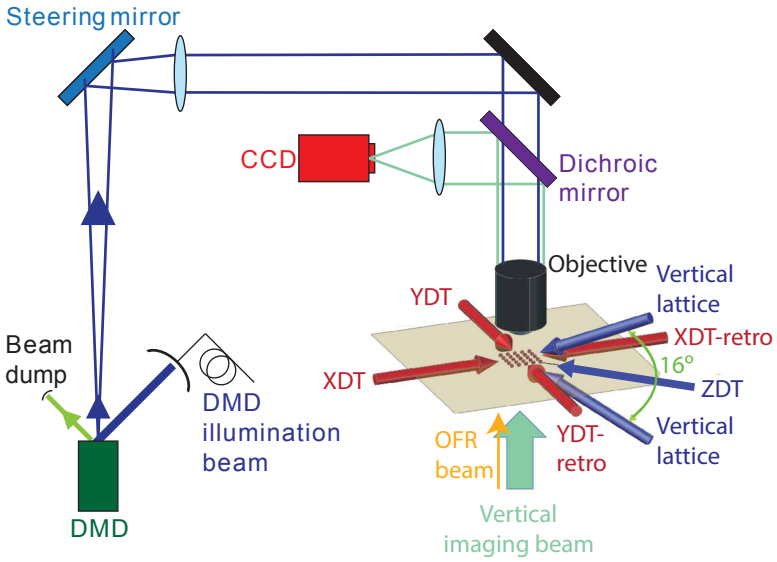

Figure 2.3: **Schematic diagram of the apparatus for manipulating and imaging ultracold Cs atoms.** The arrangement of crossed dipole trap beams, vertical lattice, DMD beam projection, optical Feshbach resonance (OFR) beam, imaging beam and associated optics, CCD camera are shown here. This figure is regenerated from Ref. [33].

Besides the control of external potential for atoms, we can also tune atomic interactions simply by changing external magnetic or optical fields thanks to Feshbach resonances [30].

We use a pair of Helmholtz coils running controllable currents to generate a uniform magnetic field in the region of atoms. With a bandwidth of 3.3 kHz, the coils allow us to modulate the magnetic field quickly to drive the system out of equilibrium and induce interesting dynamics. We can also use a near resonant optical field to generate an effective magnetic field using the vector light shift, which allows us to do modulation even faster with a bandwidth of $\sim$10 MHz and enables molecular spectroscopy across a wide range [36]. Feshbach resonance also opens the door to ultracold molecules by association of ultracold atoms near the resonance. We can either adiabatically ramp magnetic field across the resonance to create a molecular BEC from atomic BEC (see Chapter 6) or quench to the resonance to induce coherent reaction dynamics in an atomic or molecular BEC (see Chapter 6,7). All of the above techniques allow us to explore the fascinating ultracold world.

2.2 In situ and time-of-flight imaging of atoms and molecules

We use the standard absorption imaging method to image atoms by shining a light pulse with its frequency near resonant with the cycling transition from $|F = 4, m_F = 4\rangle$ to $|F' = 5, m_{F'} = 5\rangle$ in the Cs D_2 line. Since the atoms are usually in the hyperfine ground state $|F = 3, m_F = 3\rangle$ before imaging, we add another repumping beam to pump atomic population into $|F = 4\rangle$ before the imaging pulse. Depending on the density of atoms we want to image, we either use a light intensity about 5 times the saturation intensity I_{sat} of the imaging transition for high density samples or $\sim I_{\text{sat}}$ for low density samples.

The imaging naturally integrates out atomic density along the direction of the imaging beam and the resulting 2D atomic column density follows the modified Beer-Lambert law for our case where the imaging beam intensity is comparable to I_{sat}:

$$n(x, y)\sigma_0 = -\ln \frac{I_{\text{out}}(x, y)}{I_{\text{in}}(x, y)} + \frac{I_{\text{in}}(x, y) - I_{\text{out}}(x, y)}{I_{\text{sat}}}, \tag{2.1}$$

where σ_0 is the resonant scattering cross section proportional to laser wavelength squared and I_{out} (I_{in}) is the light intensity after (before) transmitting through the atomic sample. We usually take another image of the light pulse to get I_{in} after the first pulse that blows away all the atoms.

2.2.1 In situ imaging

To probe the atomic and molecular density distributions in trap, e.g. the density waves formed under modulation of atomic interaction in Chapter 4 and the equation of state measurement for molecules inside the flat-bottomed box potential in Chapter 6, we perform *in situ* imaging. Due to the finite resolution of our imaging system, the real density distribution

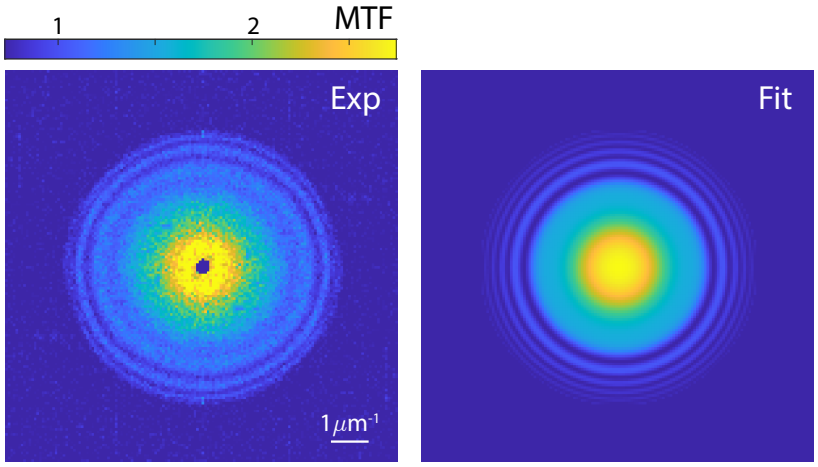

Figure 2.4: **Measurement of modulation transfer function for determination of response of the imaging system at different wave vectors.** Left panel is from Fourier transform of thermal gas density fluctuation and right panel is a fit to the experimental data based on the model in Ref. [76].

$n(\mathbf{r})$ is blurred by the point spread function $P(\mathbf{r})$, which results in the density distribution $n_{\text{exp}}(\mathbf{r})$ we measure in our experiment:

$$n_{\text{exp}}(\mathbf{r}) = \int d\mathbf{r} n(\mathbf{r}') P(\mathbf{r} - \mathbf{r}'). \tag{2.2}$$

In Fourier space, Eq. 2.2 has a simple form $n_{\rm exp}(\mathbf{k}) = n(\mathbf{k})P(\mathbf{k})$. It turns out the power spectrum of density fluctuation which can be extracted from the density distribution we measure is related to an important quantity–the structure factor$S(\mathbf{k})$– that characterize the collective and statistical behaviour of thermodynamic phases [76]:

$$\langle|\delta n_{\rm exp}(\mathbf{k})|^2\rangle = NS(\mathbf{k})M^2(\mathbf{k}), \tag{2.3}$$

where $\delta n_{\rm exp}(\mathbf{k}) = \int d\mathbf{r}[n_{\rm exp}(\mathbf{r}) - \bar{n}_{\rm exp}]e^{-i\mathbf{k}\cdot\mathbf{r}}$, N is total particle number and the modulation transfer function $M(\mathbf{k}) = |P(\mathbf{k})|$ is the magnitude of the Fourier transform of point spread function, which characterizes how much the imaging system response to the feature of an object at wave vecter $\mathbf{k}$.

For an ideal thermal gas at low phase-space density, the structure factor is almost constant up to the inverse of de Broglie wavelength, which is larger than the spatial sampling frequency in our case [76]. Therefore, we measure the density fluctuation power spectrum of a 2D thermal gas, from which we extract the modulation transfer function through Eq. 2.3, see Fig. 2.4. For the measurement of density waves in driven BEC in Chapter 4, we need to make sure the expected wave number of the density waves is within the sensitivity of our imaging system. When we calculate the strength of the density waves, we have to take into account the factor of $M(k)$.

2.2.2 Time-of-flight imaging

In the other case where we are interested in the momentum distribution of the sample in trap, we switch off the trap and let the particles fly for some time before doing the absorption imaging [18]. For example, the temperature of atoms after dRSC mentioned in Sec. 2.1 is measured after 60 ms time-of-flight, from which the velocity of atoms is extracted.

In Sec. 2.4, we also use the expansion of a pure BEC at different magnetic fields to measure

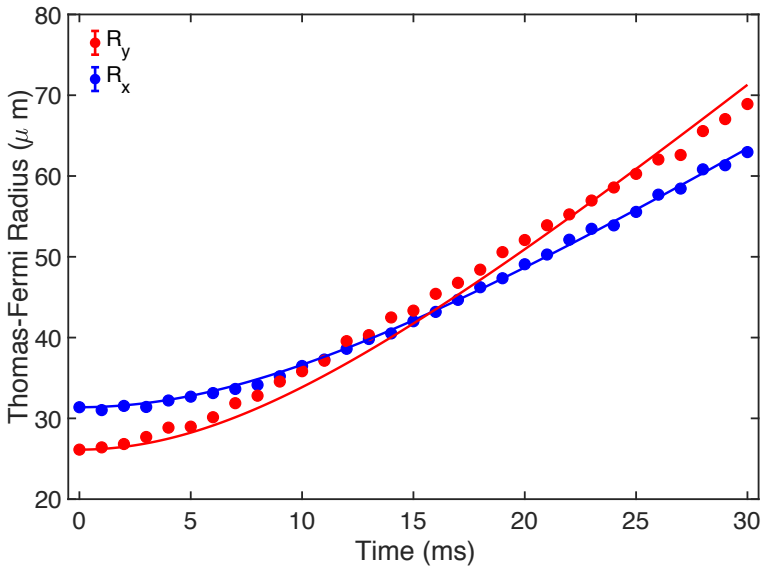

Figure 2.5: **Thomas-Fermi width of BEC during time-of-flight in horizontal plane confined in a single site of vertical lattice.** Solid lines are fits to the data based on Eq. 2.10.

the s-wave scattering length between atoms in the condensate. In this case the interaction energy of BEC is converted into kinetic energy during time-of-flight (see Fig. 2.5). To make use of our high resolution vertical imaging as characterized in Sec. 2.2.1, after turning off the horizontal confinement, we either keep the vertical lattice in the case of 2D BEC expansion as measured in Fig. 2.5 or switch on a levitation field gradient to keep the atoms in the focal plane of our objective.

In addition, short time-of-flight allows us to obtain near field interference patterns of matter waves with different momentums, e.g. for matter waves created from interaction modulation at different frequencies in Sec. 3.1.4 and matter wave emissions from two halves of a BEC with a relative phase and a rotating BEC in Chapter 5.

2.2.3 Focused time-of-flight imaging

Sometimes the particle density can become very low after time-of-flight, which leads to poor signal to noise ratio and makes the temperature measurement very hard, e.g. for low thermal

fraction density in an almost pure BEC in Chapter 7. In this situation, we focus particles with the same momentum to the same location after releasing them into an horizontal isotropic harmonic trap for a quarter trap period. To illustrate, let's consider a single particle moving in a 1D harmonic potential $V(x) = mw_x^2 x^2/2$. Its position at time t given the initial position x_0 and momentum p_0 is solved to be:

$$x(t) = \frac{p_0}{m\omega_x} \sin(\omega_x t) + x_0 \cos(\omega_x t). \tag{2.4}$$

Therefore after a quarter period $t_q = \pi/2\omega_x$, the particle reaches at $x(t_q) = p_0/m\omega_x$, which is proportional to the initial momentum p_0. This focused time-of-flight then maps particles having the same momentum to the same point in real space independent of the particles' initial positions, which helps to accumulate larger spatial density and thus higher signal to noise ratio.

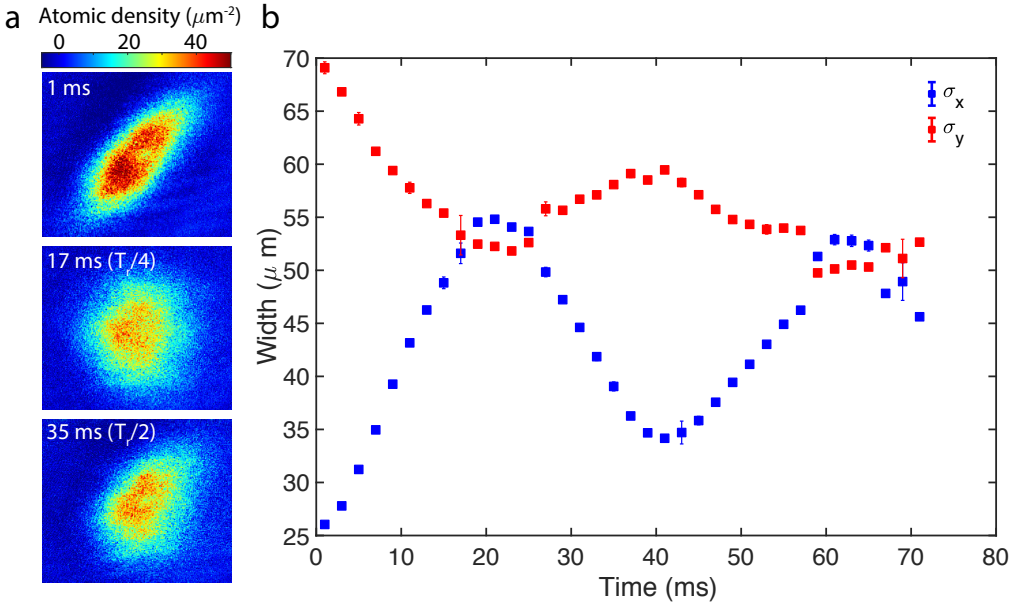

Figure 2.6: **Time-of-flight of a thermal gas in an isotropic horizontal harmonic trap. a**, 2D atomic densities in the horizontal plane where atoms are levited by a magnetic field gradient of 31 G/cm at different time after the release. **b**, Cloud width in long (red) and short axis (blue) directions at different time after being released into the isotropic harmonic trap.

In Fig. 2.6, we release an initially elliptical thermal gas into an isotropic harmonic trap having $\omega_x \approx \omega_y \approx 2\pi \times 15$ Hz. It can be seen that after a quarter period $t_q \approx 17$ ms, the cloud becomes elliptical, which signifies the momentum distribution in the initially elliptical thermal atomic sample. In Chapter 7, we use this method to measure the atomic and molecular densities in momentum space for extraction of their effective temperatures.

2.3 Preparation of BEC wave functions with dynamical potentials projected by DMD

After getting a BEC in the crossed dipole trap, we can reshape the BEC depending on our science goals by transferring it into different trap potentials projected by DMD. We typically dynamically project 64 patterns that smoothly transition from a big box trap including all the atoms to the final trap geometry we want within ∼700 ms. The underlying harmonic trap is gradually reduced at the same time and eventually turned off at the final trap geometry. During the transfer process, to make the center position of the trap remain roughly unchanged and thus induce less sloshing motion of the BEC, we use a quadrupole magnetic trap/anti-trap created by the pair of coils running currents in a superposition of Helmholtz and anti-Helmholtz configuration together with an offset magnetic field in the horizontal plane to align the trap center [76].

Figure 2.7 shows three examples of preparing different BEC density profiles. To make the matter waves directionally emit into a few momentum modes and demonstrate the various atom-optical elements in Sec. 8.2, we shape BEC into the one-dimentional geometry such that the stimulated matter wave emission mostly happens in the long-axis direction, see Fig. 2.7a. To demonstrate the BEC wave function reconstruction in Sec. 5.4.1, two half BECs with phase correlation are prepared and shown in Fig. 2.7b. The DMD can update the pattern it projects as fast as every 0.25 ms [33], which allows us to apply a light pulse of 0.4 ms on one half of the BEC to introduce an additional phase shift relative to the other half.

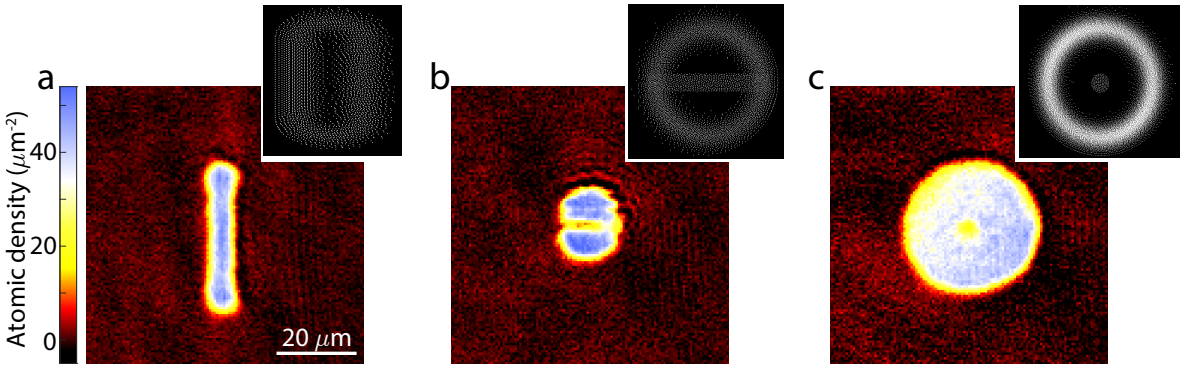

Figure 2.7: **Shaping BEC using potential profiles projected by DMD. a-c**, BEC 2D column densities in traps projected by DMD, with the patterns sent to DMD shown on the top right corners where each bright spot means a micro mirror that is turned on. The atomic densities in **a** and **b** are reduced by a factor of 2 for clarity when they are shown together with **c** on the same color scale.

The phase shift is controlled by the light pulse intensity. In addition, we can adiabatically ramp up a potential barrier, e.g. at the center of the trap (see Fig. 2.7c), to measure the density response of the sample as a function of local potential barrier height to extract the equation of state that characterizes its thermodynamic equilibrium properties.

2.4 Control of atomic interaction and creation of ultracold molecules with magnetic and optical Feshbach resonances

Feshbach resonances allow us to tune the effective interaction between atoms and to transfer population from free atoms to bound molecules, simply by changing the external magnetic field [30]. Thus it is essential to have a good knowledge and control of the magnetic field in our experiment.

To calibrate the magnetic field at the location of atoms, we perform microwave spectroscopy where the transition from $|F = 3, m_F = 3\rangle$ to $|F = 4, m_F = 4\rangle$ in the electronic ground state $6^2S_{1/2}$ is driven and we either hold for 30 ms to look at the inelastic loss between atoms in these two states or directly image the atoms transferred to $|F = 4, m_F = 4\rangle$ by absorption imaging [76]. The resonant microwave transition frequency is plugged into the

Breit-Rabi formula to calculate the magnetic field felt by the atoms [131].

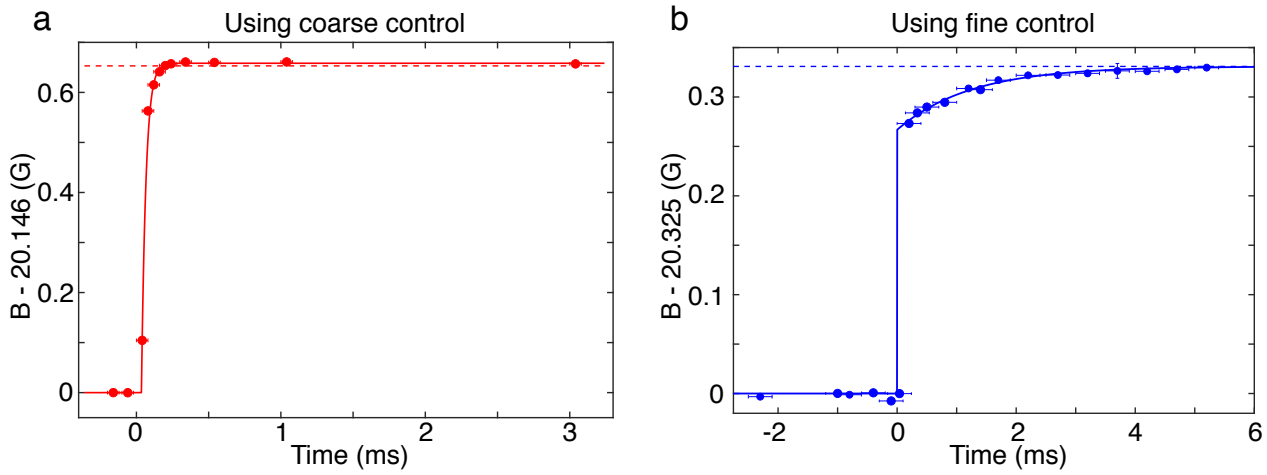

Figure 2.8: **Response of magnetic field at the location of atoms after quench using the coarse and fine controls. a**, The solid red line is a fit using $B(t) = \Delta B(1 - e^{-(t-t_d)/\tau_c})H(t - t_d)$, where $H(x)$ is the Heaviside step function, the delay time $t_d = 34(1)$ μs and the time constant $\tau_c = 30(3)$ μs. **b**, The blue solid line is a fit using $B(t) = \Delta B(1 - d \times e^{-t/\tau_f})H(t)$, where $d = 0.19(2)$ and $\tau_f = 1.24(16)$ ms. Dashed lines represent the set values of the final magnetic field for the quench.

We control the magnetic field with computer control voltages that change the current running through the coils. There are two channels that provide coarse and fine controls of the field, which have a stepsize of 0.33 G and 3 mG, respectively. To mitigate the limitation of magnetic field switching speed due to eddy currents in metallic parts of the science chamber and surroundings, a pre-emphasis circuit is installed to provide the current overshoots necessary to cancel the field contribution from eddy currents [146]. The coarse control has this pre-emphasis compensation and can switch the field with a time constant as fast as 30 μs (see Fig. 2.8a), which the fine control without the pre-emphasis switch the field with a much long time constant of 1.24 ms (see Fig. 2.8b).

The response function for a quench characterized in Fig. 2.8b as $R(t) = (1 - d \times e^{-t/\tau_f})H(t)$ allows us to build a pre-emphasis circuit in our future experiments for calculating the overshoot current needed to get the real magnetic field felt by atoms to match the waveform we want. To illustrate, let's first consider the actual magnetic field atoms feel

given an arbitrary input waveform $I(t)$ for the fine control. The input can be written as a superposition of the Heaviside step functions as

$$\begin{aligned} I(t) &= \sum_n I(t_n)[H(t-t_n) - H(t-t_{n+1})] \\ &= \sum_n [I(t_n) - I(t_{n-1})]H(t-t_n) \\ &= \sum_n I'(t_n)\Delta t \times H(t-t_n), \end{aligned} \tag{2.5}$$

where the time is discretized as $t_n = t_i + n\Delta t$. Since we know the response of the system to a quench of step function is $R(t)$, the output magnetic field is:

$$\begin{aligned} B(t) &= \sum_n I'(t_n)\Delta t \times R(t-t_n) \\ &= \int_0^t I'(t')R(t-t')dt', \end{aligned} \tag{2.6}$$

which is the convolution between the time derivative of the input waveform and the response function. Now we can invert Eq. 2.6 to solve for the waveform $I(t)$ we need to put in given the output waveform we want by doing Laplace transform:

$$I(t) = L^{-1}\{\frac{L\{B\}(p)}{pL\{R \times H\}(p)}\}(t), \tag{2.7}$$

where $L\{f\}(p) = \int_0^\infty f(t)e^{-pt}dt$ represents the Laplace transform.

In other cases where we need sinusoidal magnetic field oscillation near the zero crossing (see Chapter 3-5) or the resonance point (see Chapter 7) of a Feshbach resonance, the output magnetic field can in principle be calculated based on Eq. 2.6 to figure out its the possible phase delay. We can also confirm it using microwave spectroscopy to measure the actual oscillating magnetic field and compare it to the input waveform to extract the phase delay, see Fig. 2.9.

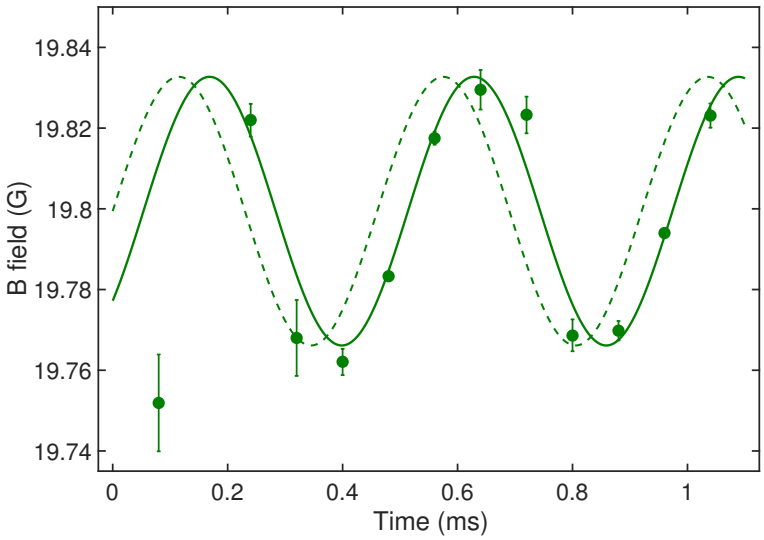

Figure 2.9: **Sinusoidally oscillating magnetic field at the location of atoms measured by microwave spectroscopy.** The solid line is a sinusoidal fit to data at 2.173 kHz, which has a phase delay of 0.73(18) rad compared to the dashed line representing current modulation in the coils.

With precise knowledge of magnetic field control in our system, we measure the s-wave scattering length that characterizes atomic interaction at different magnetic fields near a narrow g-wave Feshbach resonance around 19.8 G. Here the scattering length is inferred from the expansion of the quasi-2D BEC, where the mean field interaction energy is converted into kinetic energy during the expansion. We first prepare the BEC at an initial magnetic field B_i above or below the resonance where the scattering is a_i. The column density distribution in the Thomas-Fermi regime is:

$$n(x,y) = [\mu - \frac{1}{2}m\omega_x^2(0)x^2 - \frac{1}{2}m\omega_y^2(0)y^2]/g_{2D}, \tag{2.8}$$

where the coupling strength $g_{2D} = (\hbar^2/m)\sqrt{8\pi}a_i/l_z$, the harmonic oscillator length in vertical direction is $l_z = \sqrt{\hbar/m\omega_z}$ and the chemical potential $\mu = \sqrt{g_{2D}Nm\omega_x(0)\omega_y(0)/\pi}$ is determined by g_{2D}, the total atom number N and the initial trap frequencies $\omega_x(0)$ and $\omega_y(0)$ in horizontal plane.

Then we quench the magnetic field to different values B_f where the scattering length is

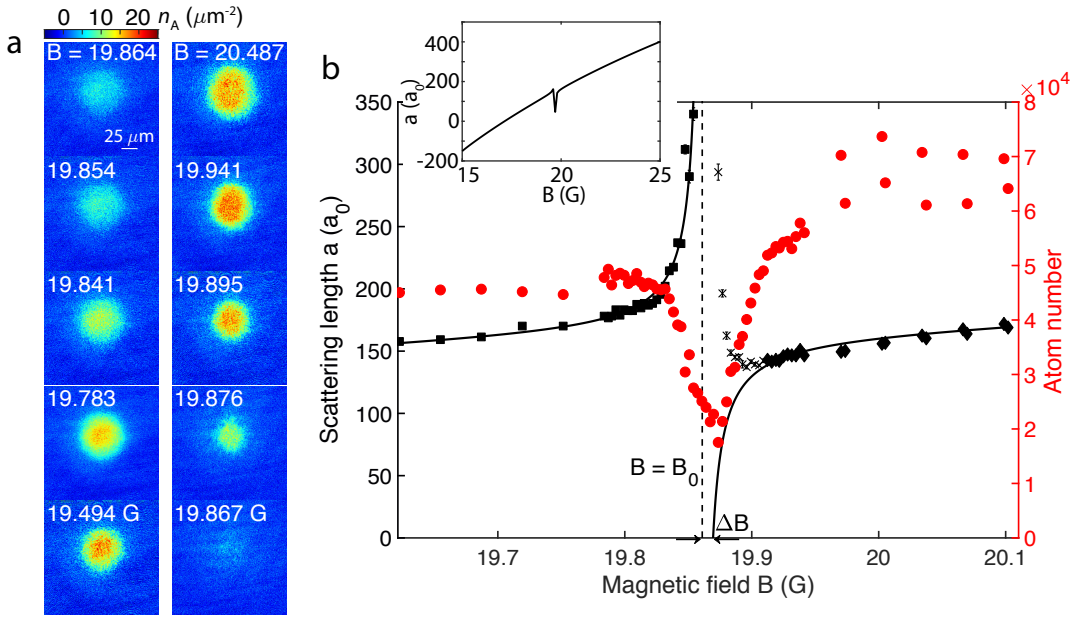

Figure 2.10: **Scattering length measurement near a narrow g-wave Feshbach resonance around 19.8 G by time-of-flight at different magnetic fields.** **a**, Atomic density distribution after 20 ms time-of-flight at magnetic field indicated at the top left corner of each image. The left (right) column corresponds to initial BEC prepared below (above) the Feshbach resonance. **b**, The scattering length (black) and total particle number (red) extracted from time-of-flight images as shown in **a**. The solid line is a fit to solid black data points based on Eq. 2.11. The trap frequencies used are $(\omega_x, \omega_y, \omega_z) = 2\pi \times (11, 13, 895)$ Hz. The inset shows scattering length over a wider range from 15 to 25 G from Ref. [16].

a_f and switch off the harmonic trap in the horizontal plane at the same time. According to Ref. [23], the dynamics of BEC after release follows a simple dilation with scaling parameters $\lambda_x(t)$ and $\lambda_y(t)$. The density distribution of the BEC at time t is thus:

$$n(x, y, t) = \frac{\mu - \frac{1}{2}m\omega_x^2(0)x^2/\lambda_x^2(t) - \frac{1}{2}m\omega_y^2(0)y^2/\lambda_y^2(t)}{g_{2D}\lambda_x(t)\lambda_y(t)}, \tag{2.9}$$

where the scaling parameters evolve as:

$$\begin{aligned} \ddot{\lambda}_x(t) &= \frac{a_f}{a_i}\frac{\omega_x^2(0)}{\lambda_x^2(t)\lambda_y(t)} \\ \ddot{\lambda}_y(t) &= \frac{a_f}{a_i}\frac{\omega_y^2(0)}{\lambda_y^2(t)\lambda_x(t)}. \end{aligned} \tag{2.10}$$

One example of the time evolution of the Thomas-Fermi radii $R_j = \sqrt{2\mu\lambda_j^2(t)/m\omega_j(0)^2}$ where $j = x, y$ at the initial magnetic field is shown in Fig. 2.5. Then we fix the time-of-flight to be 20 ms and scan the magnetic field where the BEC expands starting from $B_i = 20.481$ G or 19.498 G, to measure the Thomas-Fermi radii after the expansion. Eventually we extract a_f based on its one-to-one correspondence to the Thomas-Fermi radii in Eq. 2.10. The results are summarized in Fig. 2.10 and the scattering length as a function of magnetic field from the fit is given by:

$$a(B) = a_{\rm bg}[1 + \alpha(B - B_0)](1 - \frac{\Delta B}{B - B_0}), \tag{2.11}$$

where the resonance position $B_0 = 19.861(1)$ G, resonance width $\Delta B = 8.3(5)$ mG, $a_{\rm bg} = 163(1)a_0$ and $\alpha = 0.31(2)$/G. The background scattering length a_{bg} on resonance and slope α are consistent with the measurements in Ref. [16], which is also shown in the inset of Fig. 2.10b.

We can also perform spectroscopy of various molecular states below the scattering continuum by coupling free atoms to these bound states with a modulated magnetic field. This method is already used for determining the position of the narrow g-wave Feshbach resonance in Sec. 7.3.2 where the measured molecular state is only tens of kilohertz below the continuum. To probe deeper energy structure of Cs_2 molecules, here we modulate the intensity of a 858 nm laser that is close to D_2 line of Cs such that the effective magnetic field is modulated due to the vector light shift [36]. This optical Feshbach resonance (OFR) beam with σ^+ polarization is sent from bottom of the vacuum chamber to illuminate the atoms (see Fig. 2.3). Since the light intensity modulation using an acousto-optic modulator (AOM) has a bandwidth of 11 MHz, which is 3 orders of magnitude larger than the bandwidth of the coils, deep molecular states can be probed (see Fig. 2.11).

Here we observe an avoided crossing between two molecular states $|f = 6, m_f = 6; l =$

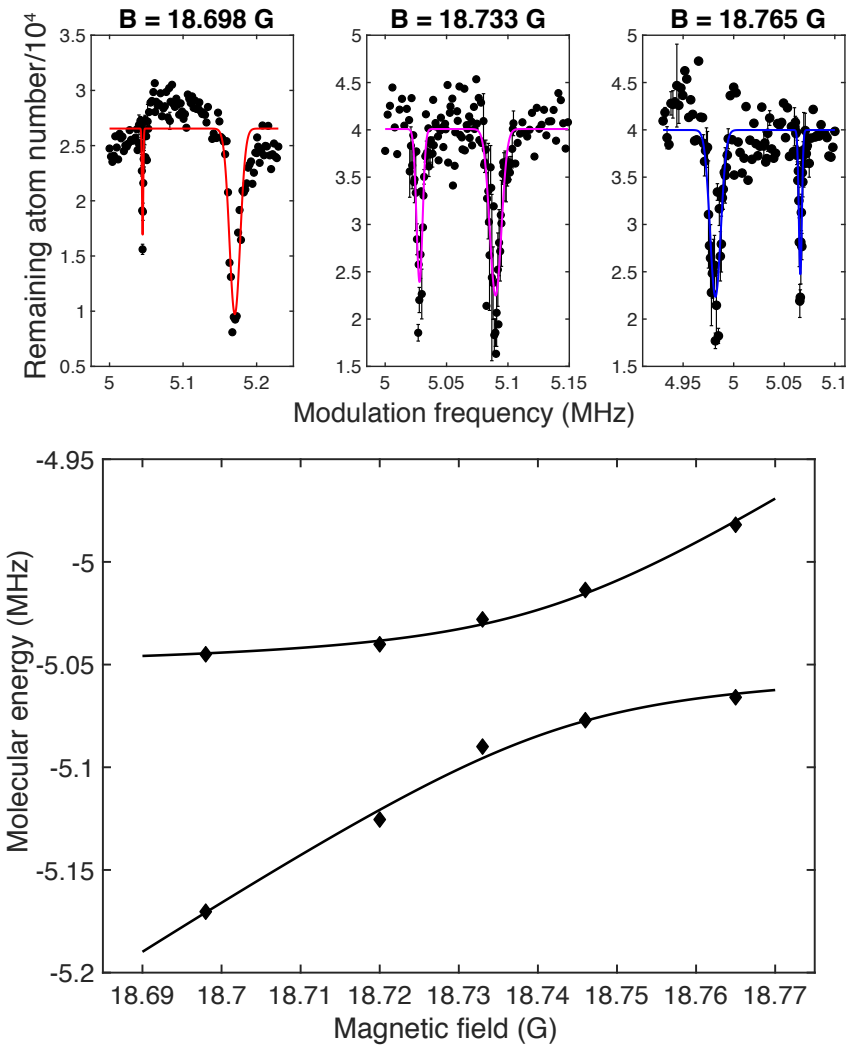

Figure 2.11: **Avoided crossing between two molecular states measured by fast modulation of light intensity.** (Upper) Number of remaining atoms after 30 ms light intensity modulation with effective modulation amplitude of tens of milligauss as a function of modulation frequency at different magnetic fields. Solid lines are fits based on sum of two Gaussian functions. (Lower) Resonant peak positions at different magnetic fields extracted as shown in the upper panel. Solid line is a fit based on Eq. 2.12.

$0, m_l = 0\rangle$ (6s) and $|f = 6, m_f = 6; l = 4, m_l = 0\rangle$ (6g(6)), with their energy consistent with

$$E_{1,2} = \frac{E_1 + E_2 \pm \sqrt{(E_1 - E_2)^2 + 4\Omega^2}}{2}, \tag{2.12}$$

where the coupling strength $\Omega = h \times 31$ kHz, see Fig. 2.11. Here the two molecular states

coupled to an atomic scattering state form a coupled three level system, which can be used to realize a matter wave analogue of the celebrated electromagnetically induced transparancy (EIT).

CHAPTER 3

DRIVEN ATOMIC BECS AND TRANSITION FROM ATOMIC TO MOLECULAR CONDENSATES

3.1 Atomic BECs with periodic interaction modulation

3.1.1 Evolution and observables of condensates with modulated interactions

We start with the second-quantization form of the Hamiltonian

$$H = \int d^3\mathbf{r}\Psi^\dagger(\mathbf{r},\tau)\frac{p^2}{2m}\Psi(\mathbf{r},\tau) + \frac{\tilde{g}(\tau)}{2}\int d^3\mathbf{r}\Psi^\dagger(\mathbf{r},\tau)\Psi^\dagger(\mathbf{r},\tau)\Psi(\mathbf{r},\tau)\Psi(\mathbf{r},\tau), \tag{3.1}$$

where $\tilde{g}(\tau) = 4\pi\hbar^2 a(\tau)/m$ is the coupling strength and is proportional to the scattering length $a(\tau)$. In our "Bose fireworks" experiment, the scattering length is modulated as $a(\tau) = a_{dc} + a_{ac}\sin\omega\tau$, where ω is the modulation frequency and $a_{dc} \ll a_{ac}$ in our experiments. By applying the Fourier transformation of the field operator

$$\Psi(\mathbf{r},\tau) = \frac{1}{\sqrt{V}}\sum_k e^{i\mathbf{k}\mathbf{r}}a_{\mathbf{k}}, \tag{3.2}$$

where V is the volume of the condensate, we obtain the Hamiltonian in momentum space as

$$H = \sum_{\mathbf{k}}\epsilon_{\mathbf{k}}a^\dagger_{\mathbf{k}}a_{\mathbf{k}} + \frac{\tilde{g}(\tau)}{2V}\sum_{\mathbf{k}_1,\mathbf{k}_2,\Delta\mathbf{k}} a^\dagger_{\mathbf{k}_1+\Delta\mathbf{k}}a^\dagger_{\mathbf{k}_2-\Delta\mathbf{k}}a_{\mathbf{k}_1}a_{\mathbf{k}_2}. \tag{3.3}$$

We eliminate the kinetic energy term $H_0 = \sum_{\mathbf{k}}\epsilon_k a^\dagger_{\mathbf{k}}a_{\mathbf{k}}$ by transferring the operators for atoms into a rotating frame with $a_{\mathbf{k}} \to a_{\mathbf{k}}e^{i\epsilon_{\mathbf{k}}\tau/\hbar}$ and ignore the fast varying terms. We further simplify the Hamiltonian under Bogoliubov approximation $a_0 \approx \sqrt{N_0}$ (ground state occupation $N_0 >> 1$), and apply energy-momentum conservation $\hbar\omega = \hbar^2 k_f^2/m$. The

resulting Hamiltonian reduces to

$$H = i\hbar g \sum_{|\mathbf{k}|=k_f} (a^\dagger_{\mathbf{k}} a^\dagger_{-\mathbf{k}} - a_{\mathbf{k}} a_{-\mathbf{k}}), \tag{3.4}$$

where $g = \pi\hbar N_0 a_{ac}/mV$ is the coupling constant.

The Heisenberg equations of motion of $a_{\mathbf{k}}$ and $a^\dagger_{-\mathbf{k}}$ are:

$$\begin{aligned} \dot{a}_{\mathbf{k}} &= g a^\dagger_{-\mathbf{k}} \\ \dot{a}^\dagger_{-\mathbf{k}} &= g a_{\mathbf{k}} \end{aligned} \tag{3.5}$$

from which we get the solution as

$$\begin{aligned} a_{\mathbf{k}}(\tau) &= \cosh(g\tau) a_{\mathbf{k}}(0) + \sinh(g\tau) a^\dagger_{-\mathbf{k}}(0) \\ a^\dagger_{-\mathbf{k}}(\tau) &= \cosh(g\tau) a^\dagger_{-\mathbf{k}}(0) + \sinh(g\tau) a_{\mathbf{k}}(0), \end{aligned} \tag{3.6}$$

which is of the same form as the transformation of quantum fields from Minkowski space to an accelerating frame and thus allows us to simulate the celebrated Unruh radiation using the time evolution of our system [70].

We typically start from a quasi-2D uniform BEC with negligible excitations $N_{\mathbf{k}} \approx 0$ for $|\mathbf{k}| > 0$. After the scattering length modulation begins, the mean population in one of the resonant modes increases as $\bar{n} = \langle a^\dagger_{-\mathbf{k}}(\tau) a_{-\mathbf{k}}(\tau) \rangle = \sinh^2(g\tau)$ starting from quantum fluctuations until the depletion of condensate population becomes significant.

Next let's consider the evolution of the wave function. In the perturbation regime, independent pairs of counter-propagating momentum modes k and $-k$ are populated from the modulation and we can rewrite the Hamiltonian as $H = \sum_{k>0} h_k$, where $h_k = i\hbar g(a^\dagger_k a^\dagger_{-k} - a_k a_{-k})$ determines evolution in a single pair of modes. In the following we only consider the evolution of one h_k. To simplify the notation without loss of the generality, we use h to

replace $h_{\vec{k}}$. The solution of the wave function is [141]

$$|\psi(\tau)\rangle = e^{-ih\tau/\hbar}\,|0,0\rangle = \frac{1}{\cosh(g\tau)}\sum_{n=0}^{\infty}\tanh^n(g\tau)\,|n,n\rangle\,, \tag{3.7}$$

where $|0,0\rangle$ is the vacuum state at $\tau = 0$, and the ket $|n,n\rangle$ indicates that there are both n particles in the modes with momenta k and $-k$, respectively. The reduced density matrix of one single mode such as k can be determined by tracing out the other mode $-k$, which yields

$$\hat{\rho}(t) = \mathrm{Tr}_{-k}|\psi(\tau)\rangle\,\langle\psi(\tau)| = \sum_{n=0}^{\infty} p_n\,|n\rangle_k\,\langle n|_k \tag{3.8}$$

where $p_n = \tanh^{2n}(g\tau)/\cosh^2(g\tau)$ is the probability of n particles in the mode. By comparing it with a thermal distribution of bosons in a quantum state

$$p_{\mathrm{th}}(n) = e^{-\frac{n\hbar\omega}{2k_{\mathrm{B}}T}}(1 - e^{-\frac{\hbar\omega}{2k_{\mathrm{B}}T}}), \tag{3.9}$$

we see that the reduced density matrix $\hat{\rho}(\tau)$ describes a thermal state with temperature given by

$$T = \frac{E}{2k_{\mathrm{B}}\ln\coth(g\tau)} \tag{3.10}$$

$$= \frac{E}{k_{\mathrm{B}}\ln(1+1/\bar{n})} \xrightarrow[\bar{n}\gg 1]{} \frac{E}{k_{\mathrm{B}}}\bar{n}, \tag{3.11}$$

where $E = \hbar\omega/2$ is the kinetic energy of the mode and the mean population

$$\bar{n} = \sum_{n=0}^{\infty} n p_n = \frac{1}{e^{E/k_{\mathrm{B}}T} - 1} \tag{3.12}$$

follows the Bose-Einstein distribution. We also evaluate the entropy of atoms in a mode. The von Neumann entropy $S = -k_{\mathrm{B}}\mathrm{Tr}\,(\hat{\rho}_k \ln\hat{\rho}_k)$ can be directly calculated as

$$S = 2k_{\mathrm{B}}[\ln\cosh(g\tau) + \sinh^2(g\tau)\ln\coth(g\tau)] \tag{3.13}$$

$$= k_{\mathrm{B}}[\ln(\bar{n}+1) + \bar{n}\ln\frac{\bar{n}+1}{\bar{n}}] \xrightarrow[\bar{n}\gg 1]{} k_{\mathrm{B}}\ln(e\bar{n}), \tag{3.14}$$

where $e = 2.718...$ is Euler's number.

3.1.2 Determination of mode width and effective temperature

In Ref. [35], the measurement of density-density correlation function $g^{(2)}(\theta)$ of Bose fireworks emission was reported. From the definition we have $g^{(2)}(0) = \langle n^2\rangle/\langle n\rangle^2$, which is equivalent to $\Delta n^2 = [g^{(2)}(0) - 1]\langle n\rangle^2$, where $\langle n\rangle$ and Δn^2 are the mean and variance of atom number in the mode.

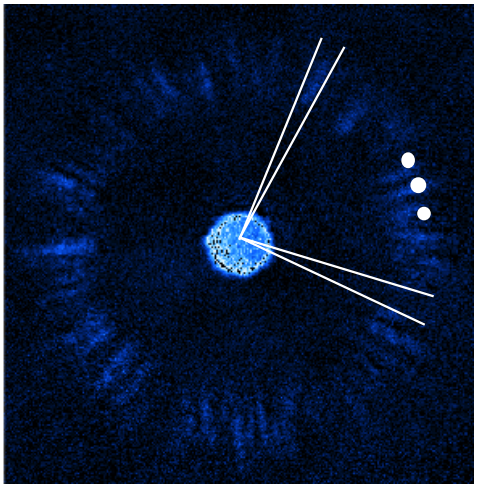

Figure 3.1: **An example of Bose fireworks emission pattern.** We cut the images into 180 slices and count excited atom number in each slice to build the histogram $P(n)$.

Experimentally we cut our emission patterns into 180 slices and count the atom number in each slice, see Fig. 3.1. Based on the histogram of atom number counting from the measurements, we build the probability distribution function $P(n)$ and calculate $\langle n\rangle = \int nP(n)dn$ and $\Delta n^2 = \langle n^2\rangle - \langle n\rangle^2 - \Delta n^2_{noise}$. Here Δn^2_{noise} is the variance contributed from

the detection noise which is statistically independent with the signal from excited atoms. From that, we find a linear dependence between the mean atom number squared and the variance in the experiment as (see Fig. 3.2),

$$\langle n \rangle^2 = \xi \Delta n^2. \tag{3.15}$$

Here $\xi = \Delta\theta_S/\Delta\theta_J = 1.49(7)$ is determined from the fit and is insensitive to the atom number calibration. This ratio also characterizes the ratio between the mode width $\Delta\theta_J$ and the width of the slice $\Delta\theta_S = 2^\circ$. Therefore, we obtain $\Delta\theta_J = 1.30^\circ$. Alternatively, we can do an independent calculation using the formula $\Delta\theta_J = 1.62/(Rk_f)$ in Ref. [35], which comes from the half width at half maximum of the peak at $\phi = 0$ in the $g^{(2)}$ correlation function and we obtain a consistent result of $\Delta\theta_J = 1.33^\circ$.

To test and verify that the emitted atom number in each mode follows a thermal distribution, we derive a more general formula for the probability distribution $p(n, \xi)$ in a slice with any width $\Delta\theta_S = \xi\Delta\theta_J$. Because the mean population per mode $\langle n_M \rangle$ is always larger than 1 in our measurements, we treat the distribution $p(n, \xi)$ as a continuous function where the summation $\sum_{n=0}^{\infty} p(n, \xi) = 1$ is replaced by an integral $\int_0^\infty dn p(n, \xi) = 1$.

Here we would like to list a few properties of the function $p(n, \xi)$. First, $p(n, \xi)$ must equal to 0 when n is a negative number. Second, if the angular slice only contains one momentum mode (*i.e.* $\xi = 1$), $p(n, 1)$ should be a thermal distribution, where $p(n, 1)$ equals $\beta e^{-\beta n}$ with $\beta = E/k_{\mathrm{B}}T$. Third, $p(n, \xi)$ have to satisfy the addition rule that combining two slices of ξ_1 and ξ_2 will create a new slice of $\xi_1 + \xi_2$. We can write the third requirement more explicitly as a mathematical equation

$$p(n, \xi_1 + \xi_2) = \int_{-\infty}^{\infty} p(n', \xi_1) p(n - n', \xi_2) dn'. \tag{3.16}$$

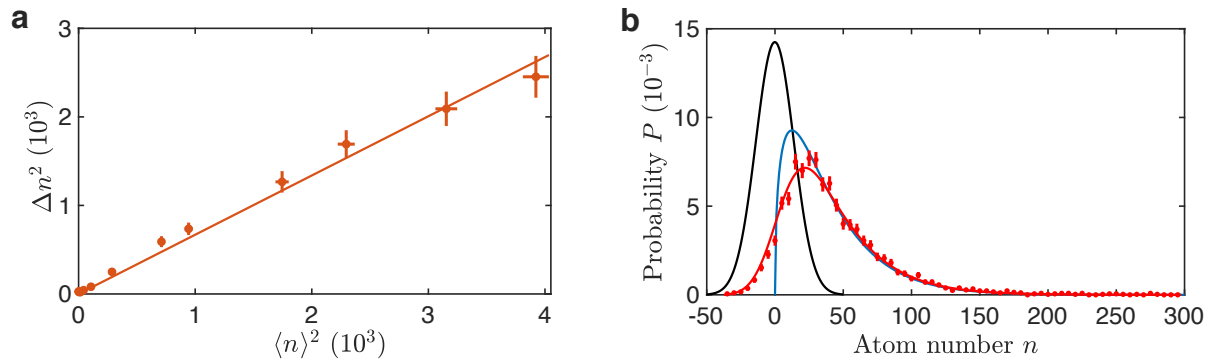

Figure 3.2: **Determination of the mode width and the fitting of the measured probability distribution P(n)**. **a** shows the linear dependence of mean square n^2 and variance Δn^2 of atom number distribution in the slice with an angular width $\Delta\theta_S = 2°$, from which we have subtracted the contribution from the detection noise. **b** shows the background atom number distribution $G(n, 1.5)$ (black line), ideal emitted atom number distribution $p(n, 1.5)$ (blue line) and the convolution between both of them $P(n, 1.5)$ (red line) which fits the measured probability distribution $P(n)$ (red circles) at the modulation time $\tau = 4.8$ ms.

From all the above conditions, we solve the probability distribution $p(n, \xi)$ analytically as

$$p(n,\xi) = \begin{cases} \beta^{\xi} n^{\xi-1} e^{-\beta n}/\Gamma(\xi) & n \geq 0 \\ 0 & n < 0, \end{cases} \tag{3.17}$$

where $\Gamma(\xi)$ is the gamma function.

In addition to signal from excited atoms, detection noise contributes to the measured probability distribution of the atom number as well. Experimentally we characterize this noise distribution $G(n, \xi)$ by inspecting the images without any radiation of atoms. Once we get $G(n, \xi)$, we convolve it with $p(n, \xi)$ to get a full distribution function

$$P(n,\xi) = \int_{-\infty}^{\infty} dn' p(n',\xi) G(n-n',\xi). \tag{3.18}$$

Then we use this function to fit our data extracting out the temperature T under the condition of $\xi = 1.5$ (see Fig. 3.2**b**).

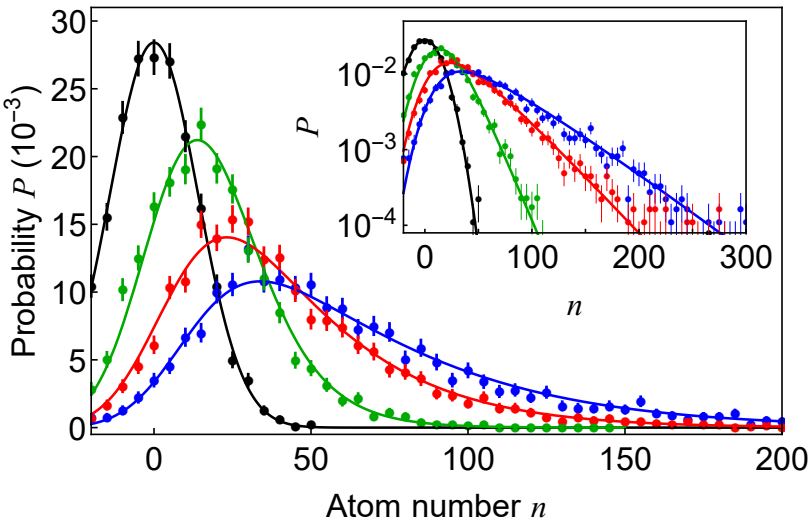

Figure 3.3: **Thermal distribution of number of atoms emitted into different directions.** The measured probability distribution $P(n)$ within a 2° slice of the emission pattern after modulation time $\tau =$ 0, 3.36, 4.8 and 6.24 ms correspond to black, green, red and blue circles. The solid lines are fits based on a thermal model. The inset shows the data in the log scale.

3.1.3 Characterization of entropy from population distribution

We define the entropy in one slice with the width of $\xi\Delta\theta_J$ as $S(\xi)$. First we use the probability distribution $p(n,\xi)$ derived in the previous section to evaluate $S(\xi)$, which gives

$$S(\xi)/k_{\mathrm{B}} = -\int_{-\infty}^{\infty} dn p(n,\xi)\ln p(n,\xi) = -\ln\beta + \xi + \ln\Gamma(\xi) - (\xi-1)\Gamma'(\xi)/\Gamma(\xi). \quad (3.19)$$

In our data analysis, we divide the emission pattern into 180 slices and determine the probability distribution $P(n)$. Thus, the entropy directly measured by the experiment is

$$S(1.5) = -k_{\mathrm{B}}\sum_n P(n)\ln P(n). \quad (3.20)$$

We show that the entropy in a single mode $S(1)$ is given by

$$S(1) = S(1.5) - S_0 = -k_{\mathrm{B}}\sum_n P(n)\ln P(n) - S_0 \quad (3.21)$$

based on Eq. (3.58) where $S_0 = k_{\mathrm{B}} \left[\xi - 1 + \ln \Gamma(\xi) - (\xi - 1)\Gamma'(\xi)/\Gamma(\xi)\right]|_{\xi=1.5} = 0.37 k_{\mathrm{B}}$.

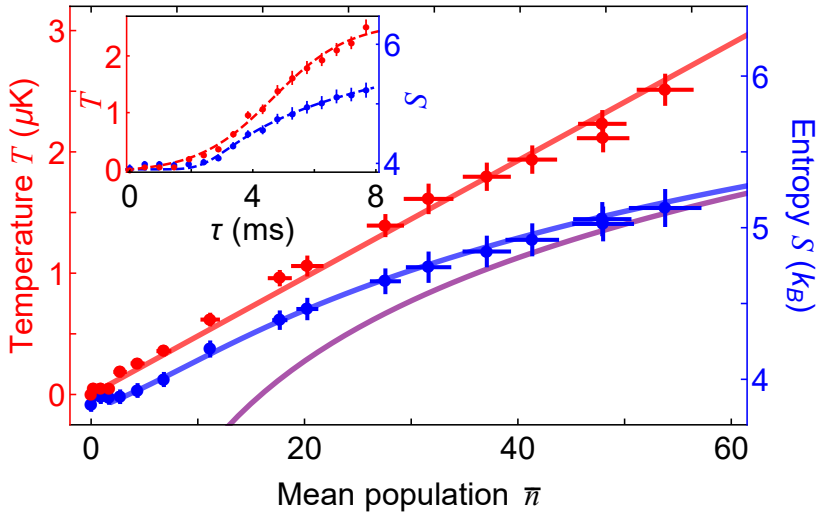

Figure 3.4: **Effective temperature T and entropy per mode S versus the mean population per mode.** The red solid line is a linear fit without offset. The blue solid line is the prediction that includes the detection noise while the purple line is the prediction excluding the noise. The inset shows time evolution of T and S. The dashed lines are guides to the eye. Here the condensate's radius is 13 μm. The scattering length is modulated at frequency $\omega/2\pi = 2.1$ kHz with a small offset of $a_{dc} = 3a_0$ and an amplitude of $a_{ac} = 50a_0$, where a_0 is the Bohr radius. All error bars correspond to one standard deviation of the mean values.

For the theoretical curve with noise plotted in Fig. 3.4**b** (blue solid line), we characterize the detection noise per mode $G(n, 1)$ and then evaluate the theoretical distribution by convolving $G(n, 1)$ with $p(n, 1)$ as

$$\tilde{P}(n, 1) = \int_{-\infty}^{\infty} dn' p(n', 1) G(n - n', 1). \tag{3.22}$$

And we calculate the entropy as

$$S = -k_{\mathrm{B}} \int dn \tilde{P}(n, 1) \ln \tilde{P}(n, 1), \tag{3.23}$$

which matches our experimental data very well. The purple line shows the calculation in the absence of detection noise.

3.1.4 Phase correlations of atomic radiation field

Here we calculate the phase correlations between interference fringes, which directly relate to that between emitted jets. We consider two sets of independent jets which are generated by two pulses of scattering length modulation with certain phase. In the interaction picture, the wave function can be written as $|\psi\rangle_I = |\psi^{(1)}\rangle_I \otimes |\psi^{(2)}\rangle_I$. Each $|\psi^{(j)}\rangle_I$ follows

$$|\psi^{(j)}\rangle_I = \frac{1}{\cosh(\gamma_j)} \sum_{n=0}^{\infty} \left[e^{i(\phi_{M_j} - \pi/2)} \tanh(\gamma_j) \right]^n |n,n\rangle_{k_j,-k_j} \tag{3.24}$$

under the Hamiltonian

$$H_I^{(i)} = g_j e^{i\phi_{M_j}} a_{k_j}^\dagger a_{-k_j}^\dagger + g_j e^{-i\phi_{M_j}} a_{k_j} a_{-k_j} \tag{3.25}$$

where ϕ_{M_j} is given by the phase of external driving field, $\gamma_j = g_j \tau_j$ and τ_i is the modulation duration of the pulse.

To take the dynamical phase into account, we convert the wave function back to Schrödinger's picture, and the wave function is written as

$$|\psi\rangle_S = |\psi^{(1)}\rangle_S \otimes |\psi^{(2)}\rangle_S, \tag{3.26}$$

where $|\psi^{(j)}\rangle_S$ is given by

$$\begin{aligned} |\psi^{(j)}\rangle_S &= e^{-iH_0^{(j)} t/\hbar} |\psi^{(j)}\rangle_I \\ &= \frac{1}{\cosh(\gamma_j)} \sum_{n=0}^{\infty} \left[e^{i(\phi_{M_j} - \omega_j t - \pi/2)} \tanh(\gamma_j) \right]^n |n,n\rangle_{k_j,-k_j}. \end{aligned} \tag{3.27}$$

Here $H_0^{(i)} = \hbar\omega_i (a_{\mathbf{k}_j}^\dagger a_{\mathbf{k}_j} + a_{-\mathbf{k}_j}^\dagger a_{-\mathbf{k}_j})/2$ is energy term which was previously eliminated in the interaction picture.

We perform a matter-wave interference experiment by applying two independent pulses

of modulation on the scattering length; the first pulse has a lower frequency compared to the second one (see Fig. 3.5a). The two frequencies are incommensurate to avoid influence from nonlinear wave mixing, see Chapter 4. The pulses are arranged such that the atoms created by the second pulse leave the condensate later, but with a greater velocity than the atoms from the first pulse. When the two emitted waves overlap, they interfere and produce fringes (see Fig. 3.5b). The phase of the fringes ϕ is given by the relative phase of the interfering matterwaves, and varies across different emission angle θ.

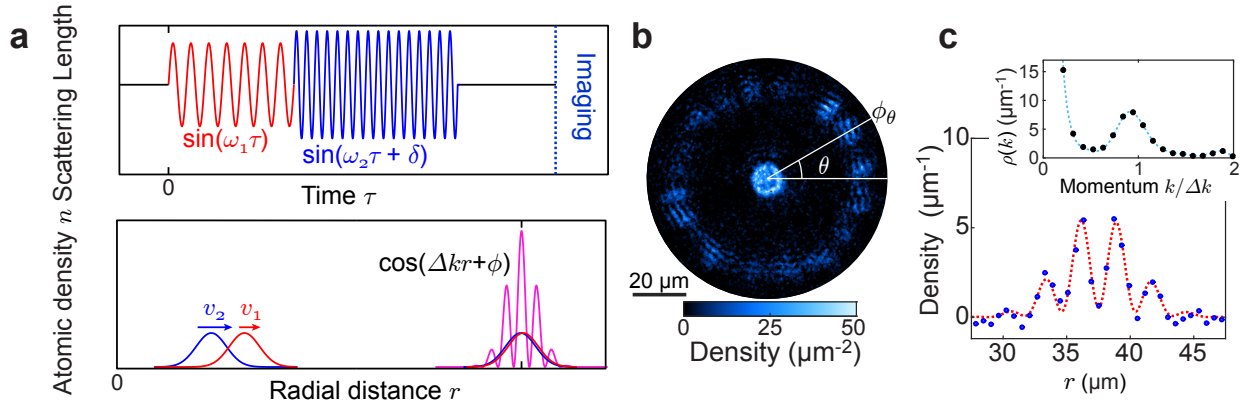

Figure 3.5: **Matter-wave jet interference from a double pulse scheme. a** illustrates the application of two pulses of scattering length modulation with frequencies $\omega_1/2\pi = 3$ and $\omega_2/2\pi = 5.63$ kHz, and modulation amplitudes $a_{ac} = 56$ and $72a_0$. The relative phase of the pulses is δ. The matter-wave jet created by the latter pulse propagates at a greater speed $v_2 > v_1$ and interferes with atoms from the first pulse when they overlap. Here the matter-wave speeds are $v_i = \sqrt{\hbar\omega_i/m}$ for the $i-$th pulse. The interference is characterized by the wavenumber difference $\Delta k = k_2 - k_1$, and the phase ϕ. **b** shows an example interference pattern of the two radiation fields. The phase of the interference fringes ϕ_θ is recorded as a function of the emission angle θ. **c** shows the radial cut of the interference pattern, from which we determine the phase of the fringes based on Fourier transformation. Dotted lines show guides to the eye.

The interference operators between the two sets of jets are $\hat{I}_f = a_{\mathbf{k}_1} a^\dagger_{\mathbf{k}_2}$ and $\hat{I}_b = a_{-\mathbf{k}_1} a^\dagger_{-\mathbf{k}_2}$ which correspond to the forward and backward directions. We introduce four more interference operators as $\hat{I}_{j+} = a_{\mathbf{k}_j} a_{-\mathbf{k}_j}$ and $\hat{I}_{j-} = a_{\mathbf{k}_j} a^\dagger_{-\mathbf{k}_j}$ with $j = 1$ or 2. The

mean value for the interference operator $\hat{I}_{j\pm}$ is evaluated as

$$\begin{aligned}
\langle \hat{I}_{j+} \rangle &= \langle \psi^{(j)}|_S \left(a_{\mathbf{k}_j} a_{-\mathbf{k}_j} \right) |\psi^{(j)}\rangle_S \\
&= \sqrt{\langle n_j \rangle (\langle n_j \rangle + 1)} e^{i(\phi_{M_j} - \omega_j t - \pi/2)} \qquad (3.28) \\
\langle \hat{I}_{j-} \rangle &= \langle \psi^{(j)}|_S \left(a_{\mathbf{k}_j} a^{\dagger}_{-\mathbf{k}_j} \right) |\psi^{(j)}\rangle_S \\
&= 0, \qquad (3.29)
\end{aligned}$$

where $\langle n_j \rangle$ is the mean atom number in each set of jets.

Phase correlation between interference fringes shown in Fig. 3.6 can be directly decomposed into the interference operators in each set of jets. The phase correlation $g_+(\pi) = |\langle e^{i\phi_\theta + i\phi_{\theta+\pi}} \rangle|$ is proportional to the correlation between $\hat{I}_f$ and $\hat{I}_b$, together with Eq. (3.28) we get

$$\begin{aligned}
\langle e^{i(\phi_\theta + \phi_{\theta+\pi})} \rangle \propto \langle \hat{I}_f \hat{I}_b \rangle &= \langle \psi^{(1)}|_S \otimes \langle \psi^{(2)}|_S \left(a_{\mathbf{k}_1} a^{\dagger}_{\mathbf{k}_2} a_{-\mathbf{k}_1} a^{\dagger}_{-\mathbf{k}_2} \right) |\psi^{(1)}\rangle_S \otimes |\psi^{(2)}\rangle_S \\
&= \langle \psi^{(1)}|_S \left(a_{\mathbf{k}_1} a_{-\mathbf{k}_1} \right) |\psi^{(1)}\rangle_S \langle \psi|^{(2)}_S \left(a^{\dagger}_{\mathbf{k}_2} a^{\dagger}_{-\mathbf{k}_2} \right) |\psi\rangle^{(2)}_S \\
&= \langle \hat{I}_{1+} \rangle \langle \hat{I}^{\dagger}_{2+} \rangle \\
&= \sqrt{\langle n_1 \rangle (\langle n_1 \rangle + 1)} \sqrt{\langle n_2 \rangle (\langle n_2 \rangle + 1)} e^{i\left[(\phi_{M_1} - \phi_{M_2}) - (\omega_1 - \omega_2) t \right]} \qquad (3.30)
\end{aligned}$$

Therefore, the sum of the phases of the forward and backward interference fringes only depends on the phase of the driving and the dynamical phase. Thus we have the phase constant $\phi_s = \phi_\theta + \phi_{\theta+\pi} = (\phi_{M_1} - \phi_{M_2}) - (\omega_1 - \omega_2)t$ and $g_+(\pi) = 1$.

Meanwhile, phase correlation $g_-(\pi) = |\langle e^{i\phi_\theta - i\phi_{\theta+\pi}} \rangle|$ is proportional to the mean value

of $\hat{I}_f\hat{I}_b^\dagger$, together with Eq. (3.29) we have

$$\begin{aligned}
\langle e^{i(\phi_\theta-\phi_{\theta+\pi})}\rangle \propto \langle \hat{I}_f\hat{I}_b^\dagger\rangle &= \langle\psi^{(1)}|_S\otimes\langle\psi^{(2)}|_S\left(a_{\mathbf{k}_1}a^\dagger_{\mathbf{k}_2}a^\dagger_{-\mathbf{k}_1}a_{-\mathbf{k}_2}\right)|\psi^{(1)}\rangle_S\otimes|\psi^{(2)}\rangle_S \\
&= \langle\psi^{(1)}|_S\left(a_{\mathbf{k}_1}a^\dagger_{-\mathbf{k}_1}\right)|\psi^{(1)}\rangle_S\langle\psi^{(2)}|_S\left(a^\dagger_{\mathbf{k}_2}a_{-\mathbf{k}_2}\right)|\psi^{(2)}\rangle_S \\
&= \langle\hat{I}_{1-}\rangle\langle\hat{I}^\dagger_{2-}\rangle \\
&= 0 \qquad (3.31)
\end{aligned}$$

therefore we have $g_{-}(\pi)=0$, indicating that phases in each pair of jets are totally random although their sum is fixed. The results from Eqs. (3.30, 3.31) are consistent with our measurement shown in Fig. 3.6c.

We also derive analytic formulas for the phase correlation functions $g_\pm(\varphi)=|\langle e^{i\phi_\theta\pm i\phi_{\theta+\varphi}}\rangle|$ between interference fringes at two arbitrary angular directions, in addition to that between the counter-propagating directions in Eqs. (3.30, 3.31), as follows,

$$\begin{aligned}
g_+(\varphi) &= \left|\frac{\langle a_{\mathbf{k}_1}a^\dagger_{\mathbf{k}_2}a_{\mathbf{k}'_1}a^\dagger_{\mathbf{k}'_2}\rangle}{\langle a^\dagger_{\mathbf{k}_1}a_{\mathbf{k}_1}\rangle a^\dagger_{\mathbf{k}_2}a_{\mathbf{k}_2}}\right| = \left|\frac{\langle a_{\mathbf{k}_1}a_{\mathbf{k}'_1}\rangle\langle a^\dagger_{\mathbf{k}_2}a^\dagger_{\mathbf{k}'_2}\rangle}{\langle a^\dagger_{\mathbf{k}_1}a_{\mathbf{k}_1}\rangle a^\dagger_{\mathbf{k}_2}a_{\mathbf{k}_2}}\right|, \\
g_-(\varphi) &= \left|\frac{\langle a_{\mathbf{k}_1}a^\dagger_{\mathbf{k}_2}a^\dagger_{\mathbf{k}'_1}a_{\mathbf{k}'_2}\rangle}{\langle a^\dagger_{\mathbf{k}_1}a_{\mathbf{k}_1}\rangle a^\dagger_{\mathbf{k}_2}a_{\mathbf{k}_2}}\right| = \left|\frac{\langle a_{\mathbf{k}_1}a^\dagger_{\mathbf{k}'_1}\rangle\langle a^\dagger_{\mathbf{k}_2}a_{\mathbf{k}'_2}\rangle}{\langle a^\dagger_{\mathbf{k}_1}a_{\mathbf{k}_1}\rangle a^\dagger_{\mathbf{k}_2}a_{\mathbf{k}_2}}\right|. \qquad (3.32)
\end{aligned}$$

Here $\mathbf{k}_1$ and $\mathbf{k}_2$ are the momenta of jets created from different modulation pulses which propagate along the same direction, while $\mathbf{k}'_1$ and $\mathbf{k}'_2$ represent another pair of such co-propagating jets along the direction with a relative angle of θ to that of $\mathbf{k}_1$ and $\mathbf{k}_2$. Following the same spirit as that in Ref. [35] and taking the finite size of the condensate into consideration, we obtained

$$a_{\mathbf{k}_j}a_{\mathbf{k}'_j} = e^{i(\phi_{M_j}-\omega_j\tau-\pi/2)}\frac{\tilde{\rho}(\mathbf{k}_j+\mathbf{k}'_j)}{2\pi}\cosh(\gamma_j)\sinh(\gamma_j), \qquad (3.33)$$

$$a^\dagger_{\mathbf{k}_j}a_{\mathbf{k}'_j} = \frac{\tilde{\rho}(\mathbf{k}_j-\mathbf{k}'_j)}{2\pi}\sinh^2(\gamma_j), \qquad (3.34)$$

where $\tilde{\rho}(\mathbf{k})$ is defined as the Fourier transformation of a uniform disk-shape density $\rho(\mathbf{r})$,

$$\rho(\mathbf{r}) = \frac{1}{2\pi}\int d^2\mathbf{k} e^{i\mathbf{k}\cdot\mathbf{r}}\tilde{\rho}(\mathbf{k}), \tag{3.35}$$

and $\rho(\mathbf{r})$ is the density distribution function of the condensate as

$$\rho(\mathbf{r}) = \begin{cases} 1 & |\mathbf{r}| \leq R \\ 0 & |\mathbf{r}| > R \end{cases} \tag{3.36}$$

with R the condensate radius. Therefore, the analytic formulas for $g_{\pm}(\varphi)$ when $\gamma_j \gg 1$ and $|\mathbf{k}_i|R \gg 1$ are

$$\begin{aligned} g_{+}(\varphi) &= \left|\frac{4\tilde{\rho}(\mathbf{k}_1+\mathbf{k}_1')\tilde{\rho}^*(\mathbf{k}_2+\mathbf{k}_2')}{\tilde{R}^4}\right| \\ &= \left|\frac{4J_1(|\mathbf{k}_1|R(\varphi-\pi))J_1(|\mathbf{k}_2|R(\varphi-\pi))}{|\mathbf{k}_1||\mathbf{k}_2|R^2(\varphi-\pi)^2}\right|, \end{aligned} \tag{3.37}$$

and

$$\begin{aligned} g_{-}(\varphi) &= \left|\frac{4\tilde{\rho}(\mathbf{k}_1-\mathbf{k}_1')\tilde{\rho}^*(\mathbf{k}_2-\mathbf{k}_2')}{\tilde{R}^4}\right| \\ &= \left|\frac{4J_1(|\mathbf{k}_1|R\varphi)J_1(|\mathbf{k}_2|R\varphi)}{|\mathbf{k}_1||\mathbf{k}_2|R^2\varphi^2}\right|, \end{aligned} \tag{3.38}$$

where $J_1(x)$ is the first order Bessel function of the first kind.

To experimentally extract the interference fringe phase ϕ_θ at a particular emission direction θ, we average over an angular span from $\theta - 0.12$ to $\theta + 0.12$ to obtain the radial density distribution $\rho(r,\theta)$ in order to achieve the best signal to noise ratio (see Fig. 3.5c). We then perform Fourier transformation on the radial density to get the complex density amplitude of the interference fringes in momentum space $\rho(k,\theta)$. The phase ϕ_θ at k_f is then evaluated from this complex amplitude. Although our jet width is small, that is 2° for

$\omega/2\pi = 3$ kHz and 1.5° for $\omega/2\pi = 5.63$ kHz, this average results in a significantly broadened phase correlation shown in Fig. 3.6b. To experimentally extract the phase constant ϕ_s, we fit the histogram of $\phi_\theta + \phi_{\theta+\pi}$ to get the peak position and find that $\phi_s = 0.79(3)$. We also calculate the expected phase shift based on our experimental sequence with a time of 18.5 ms from the start of the modulation to the start of imaging. The first sinusoidal modulation pulse lasts for 6 periods while the second lasts for 17 periods. Meanwhile we take into account the time delay of the modulation pulse of 0.041 ms due to system response. Therefore the phase constant estimated from our experimental sequence is 0.9(2) where the uncertainty arises from the duration of our 20 μs imaging pulse.

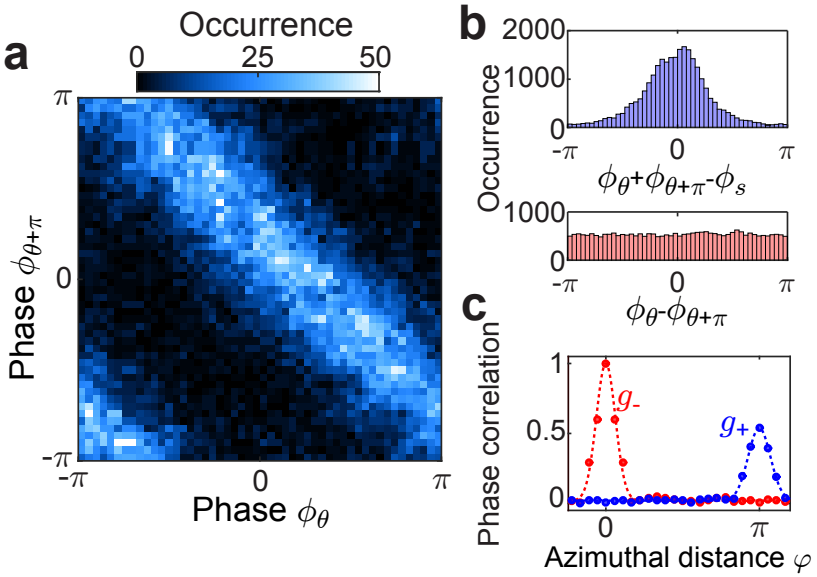

Figure 3.6: **Spatial phase correlations in matter-wave jet interference fringes.a** and **b** show the concurrence of the extracted phases in the opposite directions, ϕ_θ and $\phi_{\theta+\pi}$ for all emission angle θ from a collection of 200 images. A strong correlation of the two phases is described by $\phi_\theta + \phi_{\theta+\pi} = \phi_s$, where $\phi_s = 0.79(3)$ is obtained from fitting the data; $\phi_\theta - \phi_{\theta+\pi}$ appears to be random. **c** shows phase correlations g_+ (blue) and g_- (red) between fringes separated by an angular distance φ, see Eq. 3.32. Dots represent experimental data while dashed curves are guides to the eye.

3.1.5 Going beyond perturbation regime with time-dependent parametric approximation

Here we discuss the situation where BEC depletion is not negligible when significant population is excited into finite momentum modes due to the interaction modulation. So instead of using the Bogoliubov approximation where the field operator of condensate mode as a constant c-number, here we treat it as a dynamical variable.

1. Consider one pair of $\pm k$ modes and BEC

When we only consider one pair of opposite momentum modes and BEC, the Hamiltonian in the interaction picture is,

$$H_{int} = iA_0(a_0^\dagger a_0^\dagger a_k a_{-k} - a_0 a_0 a_k^\dagger a_{-k}^\dagger), \tag{3.39}$$

where we set $\hbar = 1$, A_0 is a real number without loss of generality. a and $a^\dagger$ are annihilation and creation operators for a certain mode.

The Heisenberg equation of motion for each mode is given by,

$$\begin{aligned} \dot{a}_0 &= 2A_0 a_0^\dagger a_k a_{-k} \\ \dot{a}_k &= -A_0 a_0^2 a_{-k}^\dagger \\ \dot{a}_{-k} &= -A_0 a_0^2 a_k^\dagger. \end{aligned} \tag{3.40}$$

Let's define the operators as $\hat{N}_0 = a_0^\dagger a_0$, $\hat{A} = a_0^\dagger a_0 + 2a_k^\dagger a_k$ and $\hat{B} = a_0^\dagger a_0 + 2a_{-k}^\dagger a_{-k}$. Using the commutators, $[a_0^\dagger a_0, H_{int}] = 2iA_0(a_0^\dagger a_0^\dagger a_k a_{-k} + a_0 a_0 a_k^\dagger a_{-k}^\dagger)$, $[a_k^\dagger a_k, H_{int}] = [a_{-k}^\dagger a_{-k}, H_{int}]$ $= -iA_0(a_0^\dagger a_0^\dagger a_k a_{-k} + a_0 a_0 a_k^\dagger a_{-k}^\dagger)$, we have,

$$[\hat{A}, H_{int}] = [\hat{B}, H_{int}] = 0, \tag{3.41}$$

which means $\hat{A}$ and $\hat{B}$ are conserved and $\langle\hat{A}\rangle = \langle\hat{B}\rangle = N$, if we start with a pure BEC of N particles.

We first evaluate the first derivative of $\hat{N_0}$,

$$\frac{d\hat{N_0}}{dt} = \dot{a}_0^\dagger a_0 + a_0^\dagger \dot{a}_0 = 2A_0(a_0^2 a_k^\dagger a_{-k}^\dagger + (a_0^\dagger)^2 a_k a_{-k}). \tag{3.42}$$

Since we still don't get a equation with only a_0,$a_0^\dagger$ and conserved quantity $\hat{A}$ and $\hat{B}$, let's go to the second derivative of $\hat{N_0}$,

$$\begin{aligned}\frac{d^2\hat{N_0}}{dt^2} = 4A_0^2\Big[&(2a_0^\dagger a_0 + 1)[(a_k^\dagger a_k + 1)(a_{-k}^\dagger a_{-k} + 1) + a_k^\dagger a_k a_{-k}^\dagger a_{-k}] - [(a_0^\dagger a_0)^2 + a_0^\dagger a_0 + 1] \\ &\times (a_{-k}^\dagger a_{-k} + a_k^\dagger a_k + 1)\Big],\end{aligned} \tag{3.43}$$

which can be written in terms of $\hat{A}$, $\hat{B}$ and $\hat{N_0}$ as,

$$\frac{d^2\hat{N_0}}{dt^2} = 8A_0^2\Big[(2\hat{N_0}+1)[(\hat{A}-\hat{N_0})(\hat{B}-\hat{N_0})+\hat{A}+\hat{B}-2\hat{N_0}+2]-(\hat{N_0}^2+\hat{N_0}+1)(\hat{B}+\hat{A}-2\hat{N_0}+2)\Big] \tag{3.44}$$

Now let's use the time-dependent parametric approximation $a_0 \approx a_0^\dagger \approx \sqrt{N_0(t)} \gg 1$ [13] and replace the conserved quantities $\hat{A}$ and $\hat{B}$ by the total particle number N, which enable us to get a second differential equation for the particle number $N_0(t)$ in BEC,

$$\frac{d^2N_0(t)}{dt^2} = 4A_0^2\Big[2N_0^3(t) - 3(N+\frac{1}{2})N_0^2(t) + (N^2+1)N_0(t) + \frac{1}{2}N^2\Big]. \tag{3.45}$$

Multiply the integration factor $2dN_0(t)/dt$ on both sides of (3.45) and integrate once, we can reduce it to a first order ODE with the intial condition $N_0(t=0) = N$ and $dN_0(t)/dt|_{t=0} = 0$,

$$\left(\frac{dN_0(t)}{dt}\right)^2 = 4A_0^2(N_0(t)-N)\Big[N_0^3(t) - (N+1)N_0^2(t) - (N-1)N_0(t) + N\Big]. \tag{3.46}$$

Then integrating (3.46) once again, we can get the following formal solution,

$$t = -\int_{N}^{N_0(t)} \frac{dN_0'(t)}{2A_0\sqrt{(N_0'(t)-N)[N_0'^3(t)-(N+1)N_0'^2(t)-(N-1)N_0'(t)+N]}}. \quad (3.47)$$

The elliptic integral in Eq. (3.47) can be represented by Jacobi elliptic functions.

Now let's solve (3.45) numerically and see how it works. Starting from a BEC of 14k atoms and set $A_0 = 0.04$ ms^{-1} , the solution is shown in Fig. 3.7.

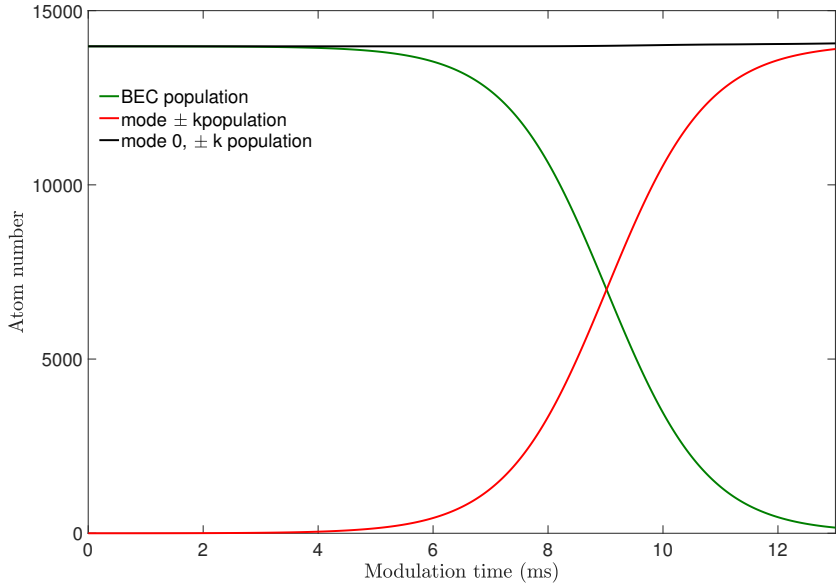

Figure 3.7: **Time evolution with BEC depletion and a single pair of opposite momentum modes.** The green curve shows BEC is depleted as time evolves and the red curve represents the population growth in $\pm k$ modes. The black curve is the total population in $0,\pm k$ modes, which is supposed to be conserved during the evolution. As population in BEC is comparable to that in $\pm k$ modes, this time-dependent parametric approximation is not valid anymore and the total atom number increased by around 0.5%.

After doing the time-dependent parametric approximation, the Hamiltonian becomes,

$$H'_{int} = iA_0N_0(t)(a_ka_{-k} - a_k^\dagger a_{-k}^\dagger). \quad (3.48)$$

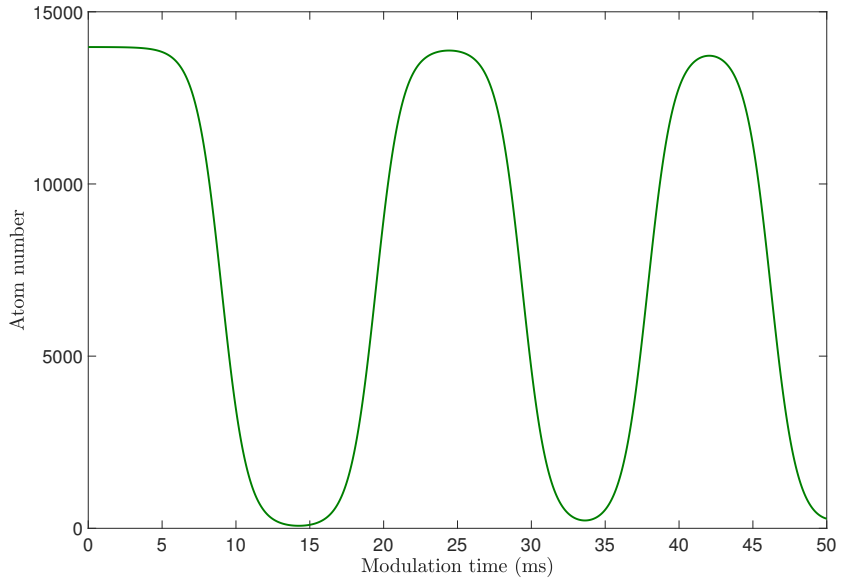

Figure 3.8: As time evolves, the BEC first becomes depleted and then recovers, because the population coherently oscillates between the 0 and $\pm k$ modes.

The solution of (3.48) is,

$$\begin{aligned} a_k(t) &= \cosh(\int_0^t g(t')dt')a_k(0) - \sinh(\int_0^t g(t')dt')a^\dagger_{-k}(0) \\ a^\dagger_{-k}(t) &= \cosh(\int_0^t g(t')dt')a^\dagger_{-k}(0) - \sinh(\int_0^t g(t')dt')a_k(0), \end{aligned} \tag{3.49}$$

where the time-dependent coupling constant $g(t) = A_0 N_0(t)$. The population in mode k is thus,

$$\bar{n}_k = \langle a^\dagger_k(t) a_k(t) \rangle = \sinh^2(\int_0^t g(t')dt') \tag{3.50}$$

The two-mode squeezing state at time t is given by,

$$|\psi(t)\rangle_I = e^{-i\int_0^t H'_{int}dt'} |0\rangle = \frac{1}{\cosh(\int_0^t g(t')dt')} \sum_{n=0}^{+\infty} \tanh^n(\int_0^t g(t')dt') \, |n,n\rangle \, . \tag{3.51}$$

Then the density matrix of mode k is obtained by tracing out mode -k,

$$\hat{\rho}_k = Tr_{-k} \left|\psi(t)\right\rangle_I \left\langle\psi(t)\right|_I = \sum_{n=0}^{\infty} p_n \left|n\right\rangle_k \left\langle n\right|_k \tag{3.52}$$

where the probability $p_n = \tanh^{2n}(\int_0^t g(t')dt')/\cosh^2(\int_0^t g(t')dt')$ and the effective Temperature is obtained,

$$\begin{aligned} T &= \frac{E_{k_f}}{2k_{\mathrm{B}} \ln\coth(\int_0^t g(t')dt')} \\ &= \frac{E_{k_f}}{k_{\mathrm{B}} \ln(1+1/\bar{n}_k)} \xrightarrow[\bar{n}\gg 1]{} \frac{E_{k_f}}{k_B}\bar{n}_k. \end{aligned} \tag{3.53}$$

where $E_{kf} = \hbar\omega/2$ is the kinetic energy of atoms in mode $\pm k$.

It can be seen that under the time-dependent parametric approximation, although the mean population in excited modes and effective temperature as a function of modulation time when BEC depletion is taken into account is different from that under Bogoliubov approximation, the scaling between the effective temperature T and mean population $\bar{n}_k$ in mode k is still linear.

2. Consider multi-pairs of modes $|k|$ and BEC

Since under our typical experimental conditions there are hundreds of momentum modes excited, we need to take multiple pairs of $\pm k$ modes into consideration.

However, the way of dealing with single pair of modes above cannot be directly extended to multiple pairs. Different pairs are not completely independent with each other anymore, which is different from the case under Bogoliubov approximation with a fixed population in BEC and thus a constant growth rate in excited mode population. Here since we're considering BEC depletion, if one pair of modes consume BEC atoms, the growth rate for other pairs of jets will become smaller and thus affecting their population.

Let's start with the Hamiltonian of multiple pairs of $\pm k$ modes,

$$H_{int} = iA_0 \sum_k^{N_m} a_0^\dagger a_0^\dagger a_k a_{-k} - a_0 a_0 a_k^\dagger a_{-k}^\dagger, \tag{3.54}$$

N_m is total number of pairs of $\pm k$ modes. Similarly, the Heisenberg equations of motion for each mode are given by,

$$\begin{aligned} \dot{a}_0 &= 2A_0 a_0^\dagger \sum_k^{N_m} a_k a_{-k} \\ \dot{a}_k &= -A_0 a_0 a_0 a_{-k}^\dagger \\ \dot{a}_{-k} &= -A_0 a_0 a_0 a_k^\dagger \end{aligned} \tag{3.55}$$

Also, the operators are defined as $\hat{N}_0 = a_0^\dagger a_0$, $\hat{A} = a_0^\dagger a_0 + 2\sum_k^{N_m} a_k^\dagger a_k$ and $\hat{B} = a_0^\dagger a_0 + 2\sum_k^{N_m} a_{-k}^\dagger a_{-k}$. Using the commutators $[a_0^\dagger a_0, H_{int}] = 2iA_0 \sum_k^{N_m} (a_0^\dagger)^2 a_k a_{-k} + a_0^2 a_k^\dagger a_{-k}^\dagger$, $[a_k^\dagger a_k, H_{int}] = [a_{-k}^\dagger a_{-k}, H_{int}] = -iA_0((a_0^\dagger)^2 a_k a_{-k} + a_0^2 a_k^\dagger a_{-k}^\dagger)$, we have

$$[\hat{A}, H_{int}] = [\hat{B}, H_{int}] = 0. \tag{3.56}$$

Then $\hat{A}$ and $\hat{B}$ are conserved quantities and $\langle A \rangle = \langle B \rangle = N$ if we start with a pure BEC of N particles.

The first order derivative of $\hat{N}_0$ is,

$$\frac{d\hat{N}_0}{dt} = \dot{a}_0^\dagger a_0 + a_0^\dagger \dot{a}_0 = 2A_0 \sum_k^{N_m} a_0 a_0 a_k^\dagger a_{-k}^\dagger + a_0^\dagger a_0^\dagger a_k a_{-k}, \tag{3.57}$$

which cannot be completely represented by a_0,$a_0^\dagger$ and $\hat{A}$,$\hat{B}$, so we go to the second derivative,

$$\frac{d^2\hat{N}_0}{dt^2} = 4A_0^2(a_0^\dagger a_0 + a_0 a_0^\dagger)\sum_{k'}^{N_m} a_{k'}a_{-k'}\sum_{k}^{N_m} a_k^\dagger a_{-k}^\dagger - 2A_0^2 a_0^2(a_0^\dagger)^2\sum_{k}^{N_m} a_{-k}a_{-k}^\dagger + a_k^\dagger a_k$$
$$+ 4A_0^2(a_0 a_0^\dagger + a_0^\dagger a_0)\sum_{k'}^{N_m} a_{k'}^\dagger a_{-k'}^\dagger \sum_{k}^{N_m} a_k a_{-k} - 2A_0^2(a_0^\dagger)^2 a_0^2\sum_{k}^{N_m} a_{-k}^\dagger a_{-k} + a_k a_k^\dagger. \quad (3.58)$$

Here terms like $\sum_{k'}^{N_m} a_{k'}a_{-k'}\sum_{k}^{N_m} a_k^\dagger a_{-k}^\dagger$ cannot be directly written in terms of the population of $\pm k$ modes $a_k^\dagger a_k$ and $a_{-k}^\dagger a_{-k}$ anymore because there are more than one pair of $\pm k$ modes here, and thus cannot be written using $\hat{N}_0$, $\hat{A}$ and $\hat{B}$ as before.

By observing that $\dot{a}_0\dot{a}_0^\dagger = 4A_0^2 a_0^\dagger a_0 \sum_{k'}^{N_m} a_{k'}a_{-k'}\sum_{k}^{N_m} a_k^\dagger a_{-k}^\dagger$ and $\dot{a}_0^\dagger\dot{a}_0 = 4A_0^2 a_0 a_0^\dagger \times \sum_{k'}^{N_m} a_{k'}^\dagger a_{-k'}^\dagger \sum_{k}^{N_m} a_k a_{-k}$, and also using the commutator $[\sum_{k'}^{N_m} a_{k'}a_{-k'}, \sum_{k}^{N_m} a_k^\dagger a_{-k}^\dagger] = \sum_{k}^{N_m} a_k a_k^\dagger + a_{-k}^\dagger a_{-k}$, Eq. (3.58) can be rewritten as,

$$\frac{d^2\hat{N}_0}{dt^2} = 2(\dot{a}_0\dot{a}_0^\dagger + \dot{a}_0^\dagger\dot{a}_0) + 4A_0^2\sum_{k}^{N_m} a_k a_k^\dagger + a_{-k}^\dagger a_{-k} - 2A_0^2[a_0^2(a_0^\dagger)^2$$
$$\times \sum_{k}^{N_m}(a_{-k}a_{-k}^\dagger + a_k^\dagger a_k) + (a_0^\dagger)^2 a_0^2\sum_{k}^{N_m}(a_{-k}^\dagger a_{-k} + a_k a_k^\dagger)]. \quad (3.59)$$

With $\sum_{k}^{N_m} a_k^\dagger a_k = \frac{1}{2}(\hat{A} - \hat{N}_0)$, $\sum_{k}^{N_m} a_{-k}^\dagger a_{-k} = \frac{1}{2}(\hat{B} - \hat{N}_0)$ and $(a_0^\dagger)^2 a_0^2 = (a_0^\dagger a_0)^2 - a_0^\dagger a_0 = \hat{N}_0^2 - \hat{N}_0$, $a_0^2(a_0^\dagger)^2 = (a_0^\dagger a_0)^2 + 3a_0^\dagger a_0 + 2 = \hat{N}_0^2 + 3\hat{N}_0 + 2$, $d^2\hat{N}_0/dt^2$ can be written only in terms of a_0, $a_0^\dagger$, $\hat{A}$ and $\hat{B}$,

$$\frac{d^2\hat{N}_0}{dt^2} = 2(\dot{a}_0\dot{a}_0^\dagger + \dot{a}_0^\dagger\dot{a}_0) - 4A_0^2\hat{N}_0(\hat{N}_0 + 1)[-\hat{N}_0 + N_m + \frac{1}{2}(\hat{A} + \hat{B})]. \quad (3.60)$$

Now we can do the time-dependent parametric approximation as in section I, i.e. $a_0 \approx a_0^\dagger \approx \sqrt{N_0(t)} \gg 1$ and $\hat{A} = \hat{B} = N$. Then $\dot{a}_0 \approx \dot{a}_0^\dagger \approx (1/(2\sqrt{N_0(t)}))dN_0(t)/dt)$, and the

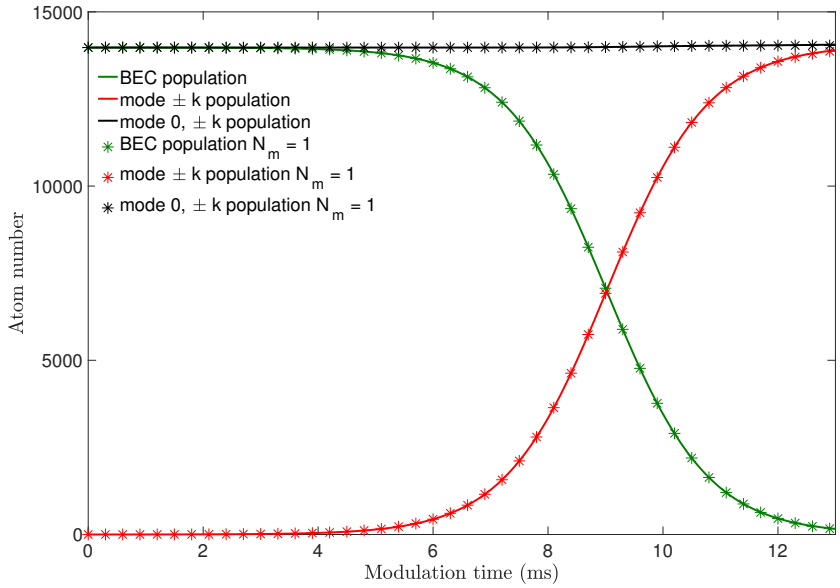

Figure 3.9: **Check the consistency between the multi-pair solution with $N_m = 1$ and single-pair solution.** The black, red and green points are calculated by setting $N_m = 1$, which matches the corresponding solid lines calculated by only considering a single pair of $\pm k$ modes.

following second order differential equation for $N_0(t)$ is obtained,

$$\frac{d^2N_0(t)}{dt^2} = \frac{1}{N_0(t)}\left(\frac{dN_0(t)}{dt}\right)^2 - 4A_0^2N_0(t)[N_0(t)+1][-N_0(t)+N_m+N]. \tag{3.61}$$

After solving the BEC population $N_0(t)$ as a function of modulation time, we plug it into the Hamiltonian in Eq. 3.54 and get a two-mode squeezing Hamiltonian with time-dependent squeezing parameter similar to that in Eq. 3.48,

$$H'_{int} = iA_0N_0(t)\sum_k^{N_m} a_k a_{-k} - a_k^\dagger a_{-k}^\dagger, \tag{3.62}$$

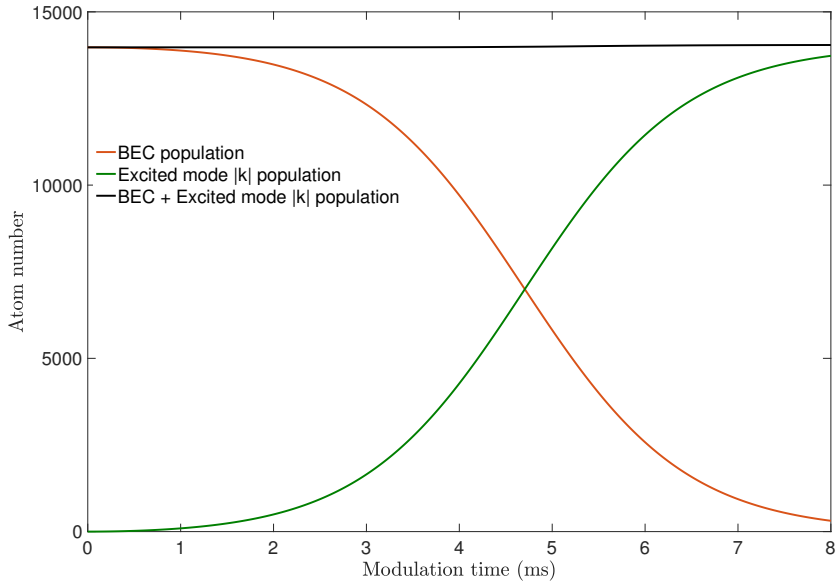

Figure 3.10: **Solution for 131 pairs of momentum modes and BEC.** The orange curve is the decrease of population in BEC versus modulation time by considering 131 pairs of $\pm k$ modes using total particle number $N = 13976$ and $A_0 = 0.0406$. These two parameters are the same as in Fig. 3.7. The BEC population drops close to 0 within 8 ms by considering 131 pairs of $\pm k$ modes compared to 12 ms in Fig. 3.7 considering single pair of $\pm k$ mode.

from which we get the solutions

$$\begin{aligned} a_k(t) &= \cosh(\int_0^t g(t')dt')a_k(0) - \sinh(\int_0^t g(t')dt')a^\dagger_{-k}(0) \\ a^\dagger_{-k}(t) &= \cosh(\int_0^t g(t')dt')a^\dagger_{-k}(0) - \sinh(\int_0^t g(t')dt')a_k(0), \end{aligned} \tag{3.63}$$

where the interaction strength $g(t) = A_0 N_0(t)$, which is similar to the results in Eq. (3.49) but the BEC population $N_0(t)$ is obtained in a different way with multiple pairs of $\pm k$ modes. Similarly, the mean atom number in mode k is given by,

$$\bar{n}_k = \langle a^\dagger_k(t) a_k(t) \rangle = \sinh^2(\int_0^t g(t')dt'). \tag{3.64}$$

On the other hand, the effective temperature is given by,

$$T = \frac{E_{k_f}}{2k_{\mathrm{B}} \ln \coth(\int_0^t g(t')dt')} = \frac{E_{k_f}}{k_{\mathrm{B}} \ln(1 + 1/\bar{n}_k)} \xrightarrow[\bar{n} \gg 1]{} \frac{E_{k_f}}{k_B} \bar{n}_k. \tag{3.65}$$

So the the effective temperature T still scales linearly with mean population $\bar{n}_k$, although both of them are different from being obtained from Bogoliubov appromixition because of the BEC depletion.

In order to check if Eq. (3.61) is correct or not, we can simply set the number of pairs of modes $N_m = 1$ and use the same value of N and A_0 to see if the solution of Eq. (3.61) can be reduced to Eq (3.45). Figure 3.9 proves these two results are consistent, which implies Eq. (3.61)'s correctness and enables us to fit the data in Fig. 3.4.

Here we consider $N_m = 131$ pairs of $\pm k$ modes and total particle number $N = 13976$, coupling constant $A_0 = 0.0406$. Figure 3.10 shows the solution to Eq. (3.61). The BEC population drops close to 0 quickly within 8 ms with hundreds of pairs of excited modes compared to BEC depletion within 12 ms in Fig. 3.7 where only single pair of $\pm k$ mode is considered. This makes sense because with the same initial BEC population and coupling constant A_0, multiple excited modes will enhance the decay rate of BEC.

In order to fit our experiment data of mean atom number in mode k versus modulation time, the total particle number and coupling constant are optimized to be $N = 13976 \pm 837$ and $A_0 = 0.0406 \pm 0.0036$. The calculation matches well with the data in Fig. 3.11. Then using the same N and A_0, the corresponding effective temperature is calculated which is shown in Fig. 3.12 together with corresponding data.

Put the data and fitting results together into Fig. 3.13 we get the relation of effective temperature with mean population in mode k, which is linear as discussed above from two-mode squeezed modes with time-dependent squeezing parameter in Eq. 3.65.

Thus, within the frame of four-wave mixing Hamiltonian in Eq. 3.54 using the time-dependent parametric approximation instead of the Bogoliubov approximation, the BEC

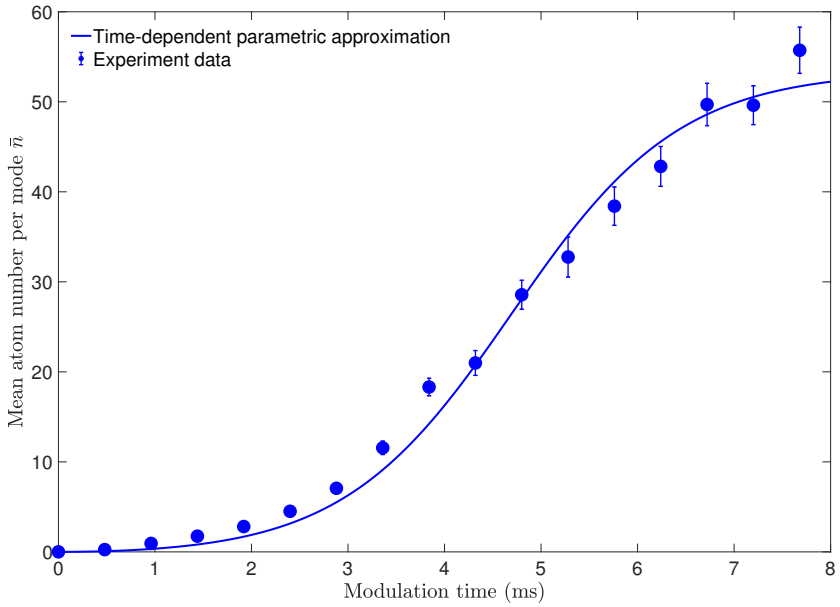

Figure 3.11: **Excited atom number in each mode versus modulation time.** Blue dots are the experimental data of mean population in mode k versus the modulation time. The solid blue line is the fitting to data using time-dependent parametric approximation. The two fitting parameters are $N = 14000(800)$ and $A_0 = 0.041(4)$.

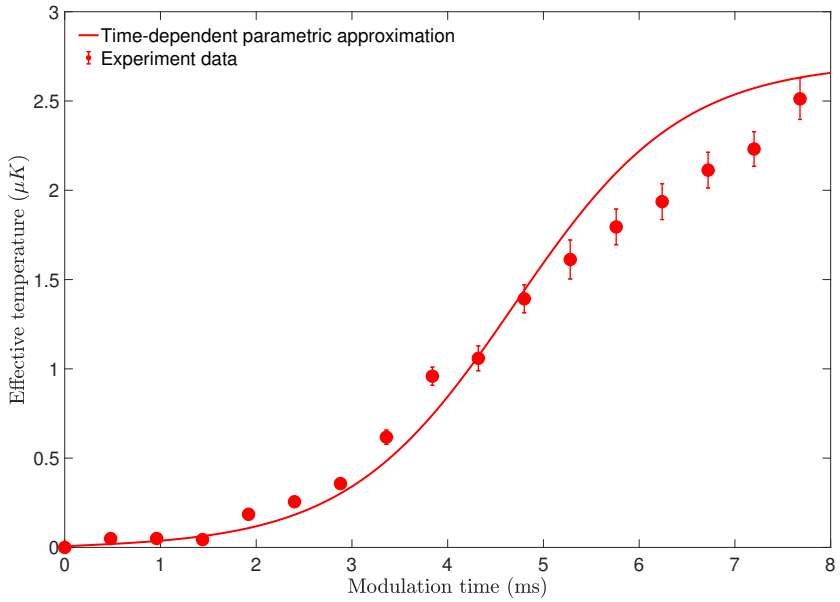

Figure 3.12: **Effective temperature veresus modulation time.** Red dots are the experimental data of effective temperature in mode k versus modulation time. The red line is a theory curve using the same parameters of N and A_0 as in Fig. 3.11.

depletion is calculated and the corresponding excited mode population matches well with the experiment. But the linear relation between the effective temperature T and mean population $\bar{n}_k$ in mode k is still valid when $\bar{n}_k \gg 1$. So the deviation of experimental data for $n > 40$ in Fig. 3.13 from the linear relation doesn't come from BEC depletion as one may intuitively conjecture, but possibly comes from secondary collision processes as demonstrated in Ref. [54] when the interaction modulation amplitude used is large.

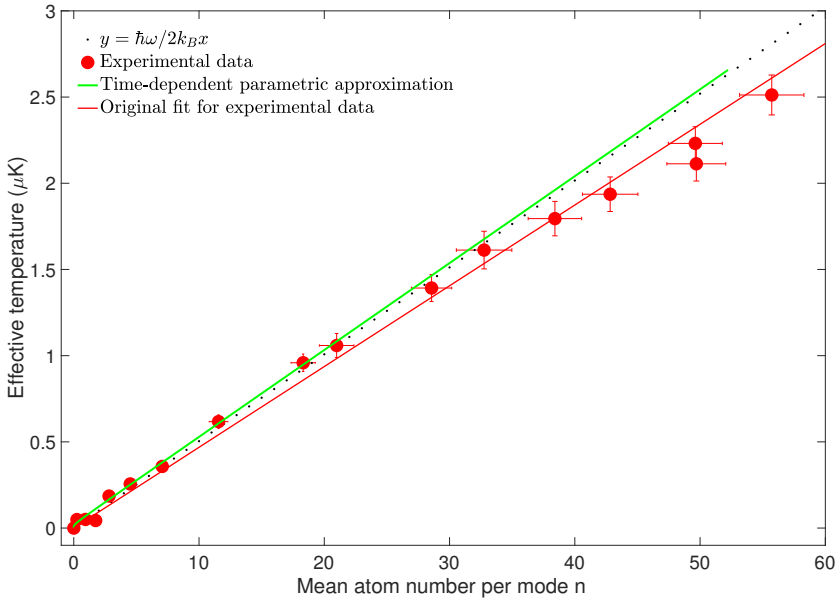

Figure 3.13: **Effective temperature versus mean excited atom number per mode.** The red dots and red solid line are the data of effective temperature versus mean atom number in mode k and its linear fitting,respectively, as shown in Fig. 3.4. The slope of the black dotted line corresponds to $\kappa = \hbar/2\pi k_B = 1.22pK \cdot s$, which matches the slope of the green line plotted using the calculated effective temperature and mean atom number in mode k in Fig. 3.11 and Fig. 3.12 obtained by using the time-dependent parametric approximation, which predicts the linear scaling.

3. Effect of secondary collision processes

When population in the $\pm k$ modes becomes large, two atoms in $+k$ (or$-k$) mode can also scatter with each other and get population transferred back to BEC and $+2k$ (or $-2k$) modes, conserving total momentum and energy by absorbing another energy quantum from

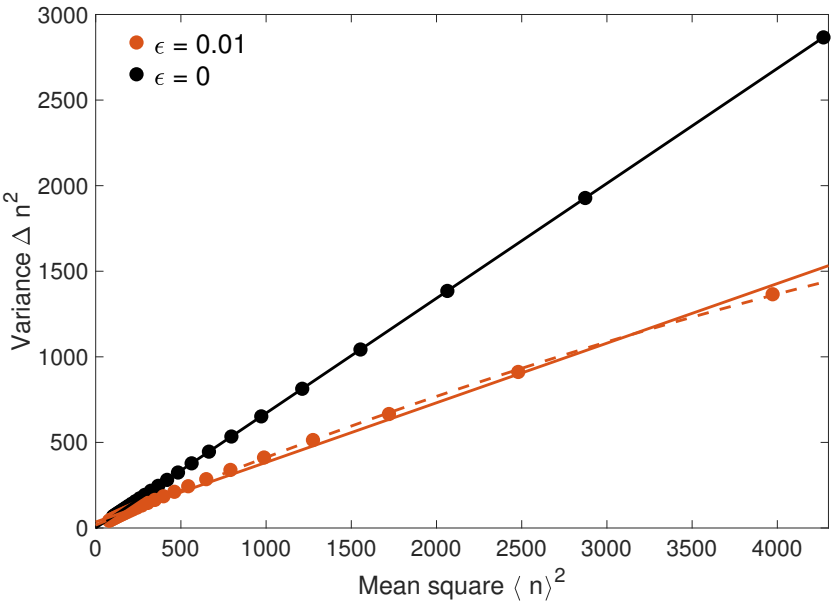

Figure 3.14: **Variance versus mean population squared in an excited mode with (orange) or without (black) considering secondary collision processes.** The circles are from numerical calculation based on Eq. 3.67 with $\epsilon = 0$ (black) and $\epsilon = 0.01$ (orange). ξ is fixed to be 1.49 and the inverse effective temperature β is varied to obtain the data points. Solid lines are linear fits and the dashed line is a quadratic fit to orange circles.

the modulation field (see Ref. [54] for more details). Thus the atom number n that satisfies the probability distribution $p(n, \xi)$ in Eq. 3.17 is the sum of remaining population in mode k and the population leaking out to other modes:

$$n = n_1 + \epsilon n_1^2, \tag{3.66}$$

where the second term ϵn_1^2 on right hand side of the above equation represents the population transferred from mode k to other modes and the reason it is quadratic is because the secondary collision involves two atoms in mode k. The parameter $\epsilon \sim 1/N \ll 1$, see Ref. [54]. Then we can obtain the probability distribution for n_1, which is what we really measure in the experiments, from the relation $p(n, \xi)dn = p(n_1, \xi)dn_1$:

$$p(n_1, \xi) = p(n, \xi)\frac{dn}{dn_1} = p(n_1 + \epsilon n_1^2, \xi)(1 + 2\epsilon n_1). \tag{3.67}$$

When $\epsilon = 0$ and thus pair production in mode $\pm k$ is the only process, the variance is proportional to the mean population squared in mode k, see Eq. 3.15 and black data points in Fig. 3.14 from numerical calculation based on Eq. 3.67. However, if secondary collision process happens, the variance of population in mode k is reduced and seems to depend on the mean population squared quadratically, see Fig. 3.14. This behaviour is consistent with deviation of the measurements in Fig. 3.2 from the linear fit and may also contribute to the slight deviation of the measurements of effective temperature versus mean population in Fig. 3.4 from being linear.

3.2 Analytical and numerical results for dynamics and phase transition in a coupled atom-molecule BEC system

In this section we solve the model for coherent conversion between atomic BEC and molecular BEC. Two cases with either a static magnetic field or a magnetic field ramp are considered. The full model with atom-atom, atom-molecule and molecule-molecule interaction is solved numerically. In particular, a phase transition from a pure molecular BEC to atomic BEC is obtained by adiabatically sweeping the magnetic field from below the Feshbach resonance. The reverse ramp from atomic BEC to molecular BEC is also studied, where we find the saturated molecule number as a function of the ramp speed more consistent with the recent analytic result in Ref. [98] than the Landau-Zener formula. Analytical results for the growth of molecule number or atom number at a fixed magnetic field in the perturbation regime are obtained, which show different growth behaviour in early time.

3.2.1 Hamiltonian of the system and the mean field equations

We start from the Hamiltonian for the coupled atom-molecule system[123]:

$$\hat{H} = \int d\vec{x}\hat{\psi}_m^\dagger(\vec{x},t)[-\frac{\hbar^2\nabla^2}{4m} + \delta(B)]\hat{\psi}_m(\vec{x},t) + \int d\vec{x}\hat{\psi}_a^\dagger(\vec{x},t)[-\frac{\hbar^2\nabla^2}{2m} + \frac{T_{bg}}{2}\hat{\psi}_a^\dagger(\vec{x},t)\hat{\psi}_a(\vec{x},t)]$$
$$\times \hat{\psi}_a(\vec{x},t) + \int d\vec{x}g[\hat{\psi}_m^\dagger(\vec{x},t)\hat{\psi}_a(\vec{x},t)\hat{\psi}_a(\vec{x},t) + \hat{\psi}_a^\dagger(\vec{x},t)\hat{\psi}_a^\dagger(\vec{x},t)\hat{\psi}_m(\vec{x},t)] + \int d\vec{x}\frac{T_{mm}}{2}$$
$$\times \hat{\psi}_m^\dagger(\vec{x},t)\hat{\psi}_m^\dagger(\vec{x},t)\hat{\psi}_m(\vec{x},t)\hat{\psi}_m(\vec{x},t) + \int d\vec{x}T_{am}\hat{\psi}_m^\dagger(\vec{x},t)\hat{\psi}_m(\vec{x},t)\hat{\psi}_a^\dagger(\vec{x},t)\hat{\psi}_a(\vec{x},t), \quad (3.68)$$

where $\hat{\psi}_m^\dagger(\vec{x},t)$ and $\hat{\psi}_a^\dagger(\vec{x},t)$ are creation operators for a bare molecule and an atom respectively, m is the atomic mass, the detuning $\delta(B) = \Delta\mu(B - B_0)$ and B_0 is the pole of the Feshbach resonance, $\Delta\mu$ is the difference between magnetic moments of two free atoms and one molecule. The coupling strength $g = \hbar\sqrt{2\pi a_{bg}\Delta B\Delta\mu/m}$ is determined by the background scattering length a_{bg} between atoms and the resonance width ΔB. The T matrices are $T_{bg} = 4\pi\hbar^2 a_{bg}/m$, $T_{mm} = 4\pi\hbar^2 a_{mm}/2m$ and $T_{am} = 3\pi\hbar^2 a_{am}/m$.

Let's assume both atoms and molecules are in the ground state of a harmonic trap in z direction as $\psi_a(z) = (\frac{m\omega_z}{\pi\hbar})^{1/4}e^{-z^2/2l_z^2}$ and $\psi_m(z) = (\frac{2m\omega_z}{\pi\hbar})^{1/4}e^{-z^2/l_z^2}$, where the harmonic oscillator length $l_z = \sqrt{\hbar/m\omega_z}$. Also, the wave functions are uniform in horizontal plane, which is equivalent to considering only the momentum mode at $k = 0$:

$$\hat{\psi}_a(\vec{x},t) = \frac{1}{\sqrt{A}}\hat{b}_a(t)\psi_a(z), \hat{\psi}_m(\vec{x},t) = \frac{1}{\sqrt{A}}\hat{b}_m(t)\psi_m(z), \quad (3.69)$$

where A is the area of the sample in horizontal plane, $\hat{b}_a(t)$ are $\hat{b}_m(t)$ are annihilation operators of an atom and a molecule, respectively. Substituting Eq. 3.69 into Eq. 3.68, we get:

$$\hat{H} = \epsilon_m\hat{b}_m^\dagger\hat{b}_m + \epsilon_a\hat{b}_a^\dagger\hat{b}_a + g'(\hat{b}_m^\dagger\hat{b}_a\hat{b}_a + \hat{b}_m\hat{b}_a^\dagger\hat{b}_a^\dagger) + T'_{bg}\hat{b}_a^\dagger\hat{b}_a^\dagger\hat{b}_a\hat{b}_a + T'_{mm}\hat{b}_m^\dagger\hat{b}_m^\dagger\hat{b}_m\hat{b}_m$$
$$+T'_{am}\hat{b}_m^\dagger\hat{b}_m\hat{b}_a^\dagger\hat{b}_a, \quad (3.70)$$

where $\epsilon_m = \hbar\omega_z/2+\delta(B)$, $\epsilon_a = \hbar\omega_z/2$, $g' = g/((2\pi)^{1/4}\sqrt{Al_z})$, $T'_{bg} = T_{bg}/(2\sqrt{2\pi}Al_z)$, $T'_{mm} = T_{mm}/(2\sqrt{\pi}Al_z)$ and $T'_{am} = \sqrt{2/3\pi}T_{am}/(Al_z)$. Plugging in the experimental parameters for Cs atoms in hyperfine ground state near the g-wave Feshbach resonance at 19.87 G $a_{bg} = 160a_0$, $\Delta B = 11$mG, $\Delta\mu = 0.57\mu_B$ and the trap parameters $R = 15\mu m$, $A = \pi R^2$, $\omega_z = 2\pi \times 400$ Hz and using the theoretical results $a_{mm} = 4a_{bg}$, $a_{am} = 32a_{bg}/3$ from Ref.[123], we get $g' = h \times 7$ Hz, $T'_{bg} = h \times 5.2$ mHz, $T'_{mm} = h \times 14.8$ mHz and $T'_{am} = h \times 97$ mHz, which we will use for the numerical calculations presented below.

The Heisenberg equations of motion for the annihilation operators based on the Hamiltonian in Eq.3.70 are:

$$\begin{aligned}\frac{d\hat{b}_a}{dt} &= -i(\epsilon_a\hat{b}_a + 2g'\hat{b}_m\hat{b}_a^\dagger + 2T'_{bg}\hat{b}_a^\dagger\hat{b}_a^2 + T'_{am}\hat{b}_m^\dagger\hat{b}_m\hat{b}_a)\\ \frac{d\hat{b}_m}{dt} &= -i(\epsilon_m\hat{b}_m + g'\hat{b}_a^2 + 2T'_{mm}\hat{b}_m^\dagger\hat{b}_m^2 + T'_{am}\hat{b}_m\hat{b}_a^\dagger\hat{b}_a),\end{aligned} \tag{3.71}$$

Then the first derivative of the occupation operator $\hat{N}_m = \hat{b}_m^\dagger\hat{b}_m$ can be obtained as:

$$\frac{d\hat{N}_m}{dt} = ig'[(\hat{b}_a^\dagger)^2\hat{b}_m - \hat{b}_m^\dagger\hat{b}_a^2] \tag{3.72}$$

The occupation operator for atoms is related to $\hat{N}_m$ by $\hat{N}_a + 2\hat{N}_m = \hat{N}$, where the total occupation operator $\hat{N}$ is a conserved quantity since $[\hat{N}, \hat{H}] = 0$.

In order to get a closed equation for $\hat{N}_m$, we take the second derivative [90]:

$$\frac{d^2\hat{N}_m}{dt^2} = 2g'^2(12\hat{N}_m^2 - 8\hat{N}\hat{N}_m + \hat{N}^2 - \hat{N}) - \frac{1}{2}(\{\hat{A}, \hat{B}\} + i[\hat{A}, \frac{d\hat{N}_m}{dt}]), \tag{3.73}$$

where the operators $\hat{A}$ and $\hat{B}$ are given by:

$$\hat{A} = 2\epsilon_a - \epsilon_m + 2T'_{bg}(2\hat{N} - 4\hat{N}_m + 1) - 2T'_{mm}(\hat{N}_m - 1) + T'_{am}(4\hat{N}_m - 2 - \hat{N}) \tag{3.74}$$

$$\hat{B} = \hat{H} - \epsilon_m\hat{N}_m - \epsilon_a(\hat{N} - 2\hat{N}_m) - T'_{bg}[4\hat{N}_m^2 - (4\hat{N} - 2)\hat{N}_m + \hat{N}^2 - \hat{N}] - T'_{mm}(\hat{N}_m^2 - \hat{N}_m) - T'_{am}(\hat{N}\hat{N}_m - 2\hat{N}_m^2) \tag{3.75}$$

Now we do the approximation by replacing the operators in Eq. 3.73-3.75 by real numbers:

$$\frac{d^2N_m}{dt^2} = 2g'^2(12N_m^2 - 8NN_m + N^2 - N) - AB \tag{3.76}$$

3.2.2 Stationary magnetic field near the resonance

Starting from atomic BEC

If the initial state is taken to be the fock state $|N_a = N, N_m = 0\rangle$ and the magnetic field is fixed at a particular value, the total energy is conserved to be $H = \epsilon_a N + T'_{bg}(N^2 - N)$. Then Eq. 3.76 is solved numerically with initial conditions $N_m|_{t=0} = dN_m/dt|_{t=0} = 0$ and total particle number $N = 60,000$, see Fig. 3.15.

In the perturbation regime where $N_m \ll N$:

$$\frac{d^2N_m}{dt^2} \approx 2g'^2N^2 - PN_m, \tag{3.77}$$

where $P = 16g'^2N + [2\epsilon_a - \epsilon_m + 2(2N + 1)T'_{bg} + 2T'_{mm} - (N + 2)T'_{am}][2\epsilon_a - \epsilon_m + 2(2N - 1)T'_{bg} + T'_{mm} - NT'_{am}]$. The solution of Eq. 3.77 is:

$$N_m = \frac{2g'^2N^2}{P}[1 - \cos(\sqrt{P}t)] \approx g'^2N^2t^2. \tag{3.78}$$

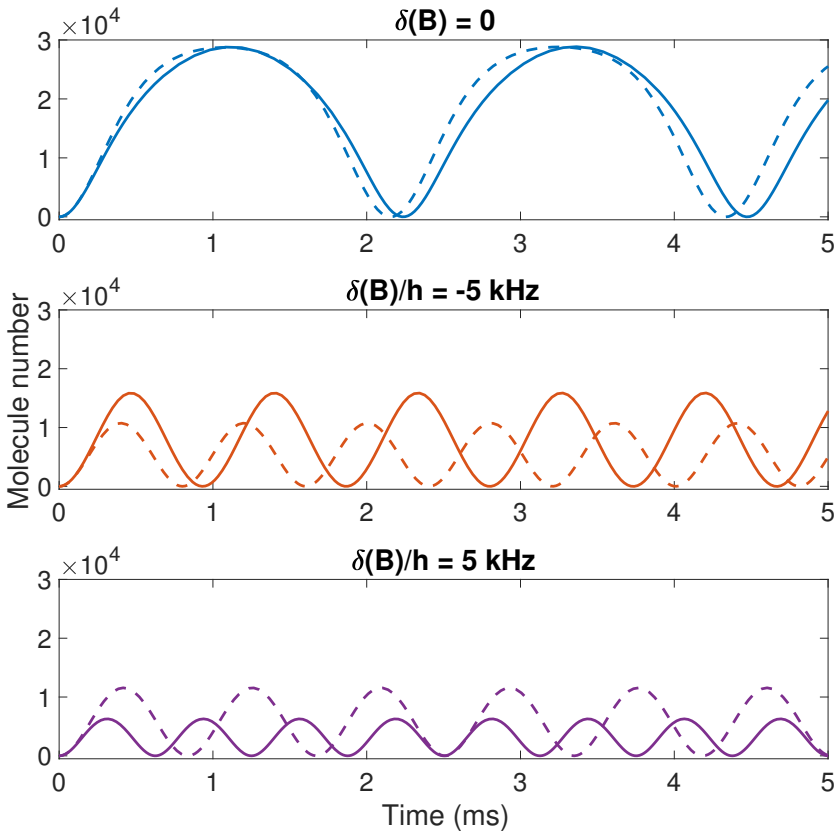

Figure 3.15: **Molecule production from atomic BEC at fixed magnetic fields with different detunings** $\delta(B)$**.** Positive (negative) detuning means the molecular state is above (below) the atomic scattering state, see text. The dashed lines are results when $T'_{bg} = T'_{mm} = T'_{am} = 0$.

So molecule number grows quadratically at early time independent of the detuning.

Starting from molecular BEC

If the initial state is $|0, N/2\rangle$ instead, $H = \epsilon_m N/2 + T'_{mm}(N^2/4 - N/2)$ and the initial conditions are $N_a|_{t=0} = 0$ and $dN_a/dt|_{t=0} = 0$ with the corresponding equation of motion for atomic population N_a:

$$\frac{d^2N_a}{dt^2} = 4g'^2(N + 2NN_a - 3N_a^2) + 2AB, \tag{3.79}$$

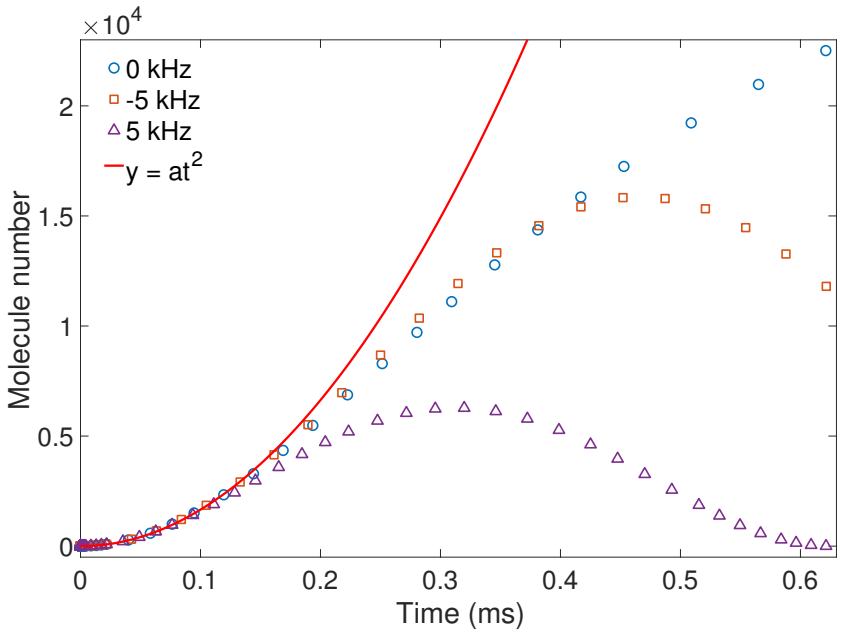

Figure 3.16: **Early time dynamics of the number of molecules produced from atomic BEC at different detunings.** The data points are from numerical calculation considering the interaction terms corresponding to the solid curves in Fig. 3.15. The solid red line is a quadratic fit in the low molecule number regime.

where $A = 2\epsilon_a - \epsilon_m + 2T'_{bg} + (N-2)(T'_{am} - T'_{mm}) + (4T'_{bg} + T'_{mm} - 2T'_{am})N_a$ and $B = H - \epsilon_m N/2 - (N^2 - 2N)T'_{mm}/4 + [\epsilon_m - 2\epsilon_a + 2T'_{bg} + (N-1)T'_{mm} - T'_{am}N]N_a/2 + (T'_{am} - T'_{mm}/2 - 2T'_{bg})N_a^2/2$.

Using the particle number conservation relation $N_a + 2N_m = N$ and working in the perturbation regime where $N_a \ll N$, we get

$$\frac{d^2N_a}{dt^2} \approx 4g'^2N + QN_a, \tag{3.80}$$

where $Q = 8g'^2N + 4T'^2_{bg} - [N(T'_{am} - T'_{mm}) + 2\epsilon_a - \epsilon_m]^2$. The solution of Eq. 3.80 is:

$$N_a = \frac{8g'^2N}{Q}\sinh^2\left(\frac{\sqrt{Q}t}{2}\right). \tag{3.81}$$

If the factor $Q > 0$, atom number will increase exponentially in the beginning (see Fig. 3.17

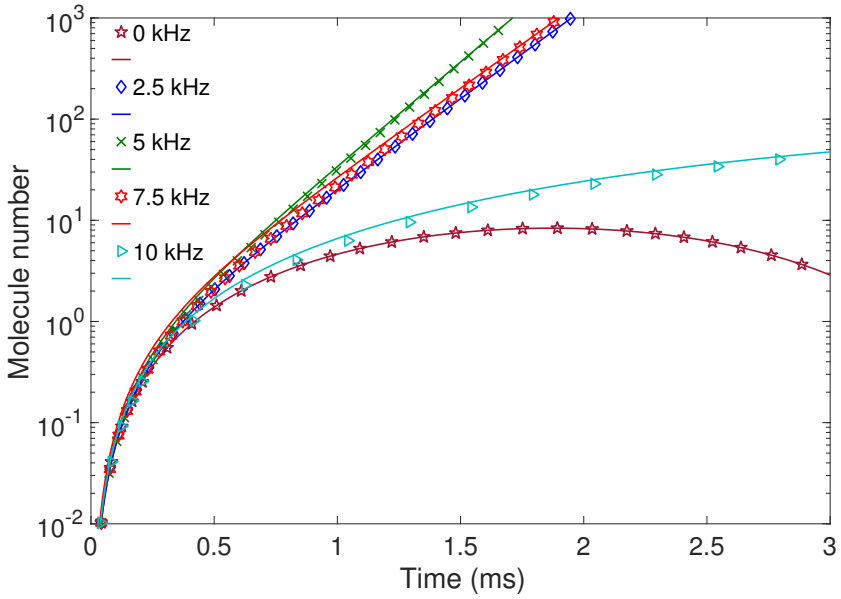

Figure 3.17: **Dissociation of molecular BEC at fixed magnetic fields with different detunings $\delta(B)$ at early time.** The data points are numerical results considering the interaction terms with nonzero T'_{bg}, T'_{mm} and T'_{am}. The solid lines are fits using Eq.3.81.

and Fig. 3.18), while if $Q < 0$, the atom number will oscillate sinusoidally with the oscillation frequency $\hbar\omega = \sqrt{|Q|} = \sqrt{(\hbar\omega_z/2 - \delta(B))^2 - 8g'^2N}$ if the interactions between atoms and molecules are neglected, see Fig. 3.19. The transition point between these two distinct behaviors is given by $Q = 0$, i.e. $B - B_0 = (-4g'\sqrt{2N} + \hbar\omega_z)/2\Delta\mu = -5.8$ mG, which is consistent with the transition point for an adiabatic ramp in Fig. 3.22.

We emphasize that if we do mean field approximation starting from Eq. 3.71 by replacing the operators $\hat{b}_a$ and $\hat{b}_m$ with c-numbers, there would be no dynamics happening for atoms starting from pure molecules and no atoms with $b_a = 0$. So our formalism here captures quantum fluctuation of the atomic field and reproduces the correct perturbative behaviour shown in Eq. 3.81, consistent with the perturbative fully quantum mechanical solution in Ref. [140].

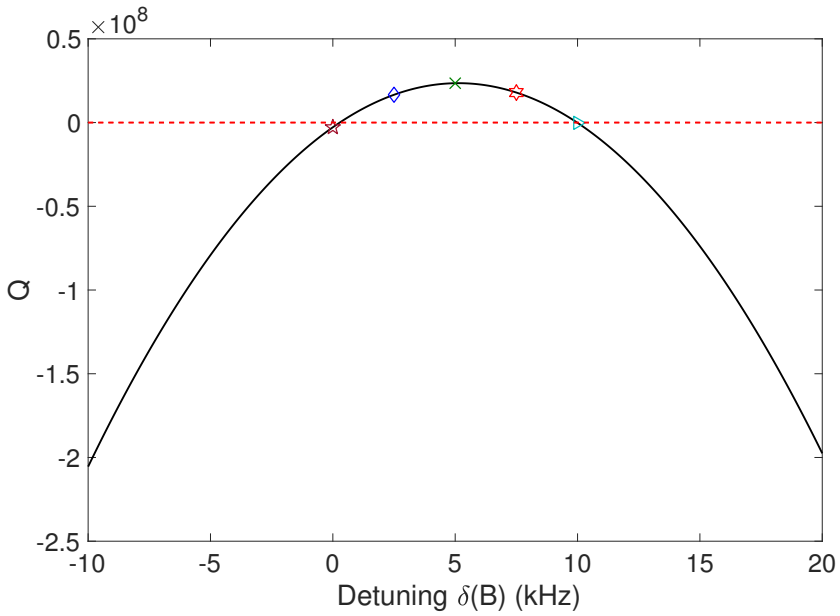

Figure 3.18: **The Q factor as a function of the detuning $\delta(B)$.** The region below the red dashed line corresponds to sinusoidal oscillation of the atom number while the region above corresponds to exponential increase.

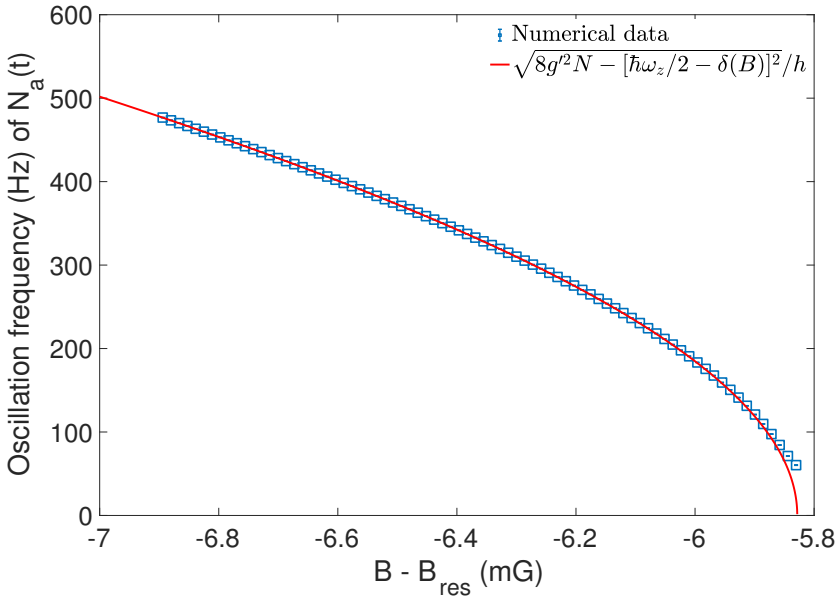

Figure 3.19: **The oscillation frequency of atom number at different magnetic field for negative Q factor starting from a pure molecular BEC.** Here we set $T'_{bg} = T'_{am} = T'_{mm} = 0$.

3.2.3 Magnetic field ramp across the resonance

Starting from atomic BEC

Molecule can also be created from an atomic BEC by ramping the magnetic field from B_i down across the resonance point at B_0 as $B(t) = B_i - \dot{B}t$. In this way, the detuning $\delta(B) = \Delta\mu(B_i - \dot{B}t - B_0)$ is time-dependent and the total energy H becomes time-dependent too, which obeys the equation of motion:

$$\frac{dH}{dt} = \frac{\partial H}{\partial t} = -\Delta\mu\dot{B}N_m. \tag{3.82}$$

Together with Eq. 3.76 and the initial conditions $N_m|_{t=0} = dN_m/dt|_{t=0} = 0$, $H|_{t=0} = \epsilon_a N + T'_{bg}(N^2 - N)$, the dynamics of molecule number is solved as shown in Fig. 3.20.

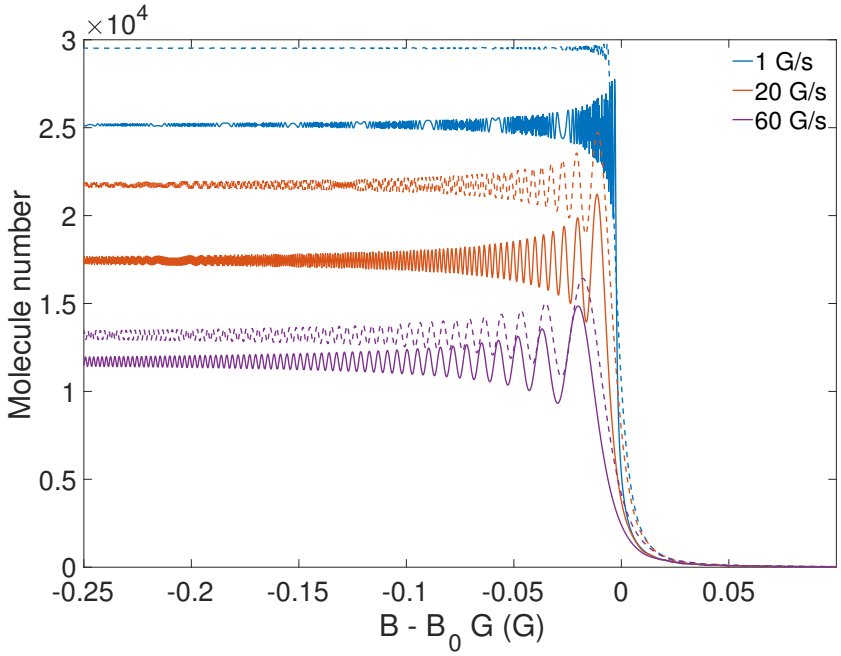

Figure 3.20: **Dynamics of molecule number starting from an atomic BEC through magnetic field ramps from high fields with different speeds.** The solid lines are solutions considering all the interaction terms and the dashed lines corresponds to setting $T'_{bg} = T'_{am} = T'_{mm} = 0$.

According to Ref. [86], the probability of pairing atoms in BEC into Feshbach molecules

is given by:

$$p = 1 - e^{-2\pi\delta_{LZ}^{BEC}}, \tag{3.83}$$

where the Landau-Zener parameter is given by:

$$\delta_{LZ}^{BEC} = \bar{n}\frac{4\pi\hbar}{m}|\frac{a_{bg}\Delta B}{\dot{B}}|. \tag{3.84}$$

The average atomic density in our case is $\bar{n} = \int n^2(\mathbf{r})d\mathbf{r}/\int n(\mathbf{r})d\mathbf{r} = N/(\sqrt{2\pi}l_z\pi R^2)$. Substituting the parameters we used for the above numerical calculations, we get $\bar{n} = 7.8 \times 10^{13}$ cm^{-3}. Setting the resonance width ΔB as a fitting parameter, we use the formula $p = 1 - \exp(-2\pi C_0 \Delta B/\dot{B})$ to fit the numerical data presented in Fig. 3.21, where the constant $C_0 = 3.9$ kHz. The fit gives an effective resonance width of 2 mG.

On the other hand, according to the recent analytical result from Ref. [98],

$$N_m = N + \frac{\ln(2 - x^N)}{\ln(x)}, \tag{3.85}$$

where $x = \exp(-g^2/\Delta\mu\dot{B})$. Eq. 3.85 fits the numetical data in Fig. 3.21 perfectly, with the coupling strength $g = h \times 33$ Hz.

Starting from molecular BEC

According to Ref. [123], a phase transition occurs when the magnetic field is ramped adiabatically from below the resonance starting from a pure molecular BEC. Here we use a small ramp rate in our numerical simulation starting from the initial state $|\psi_0\rangle = |0, N/2\rangle$ to find out the phase transition point.

Figure 3.22 shows the result of an adiabatic ramp from low field to high field values

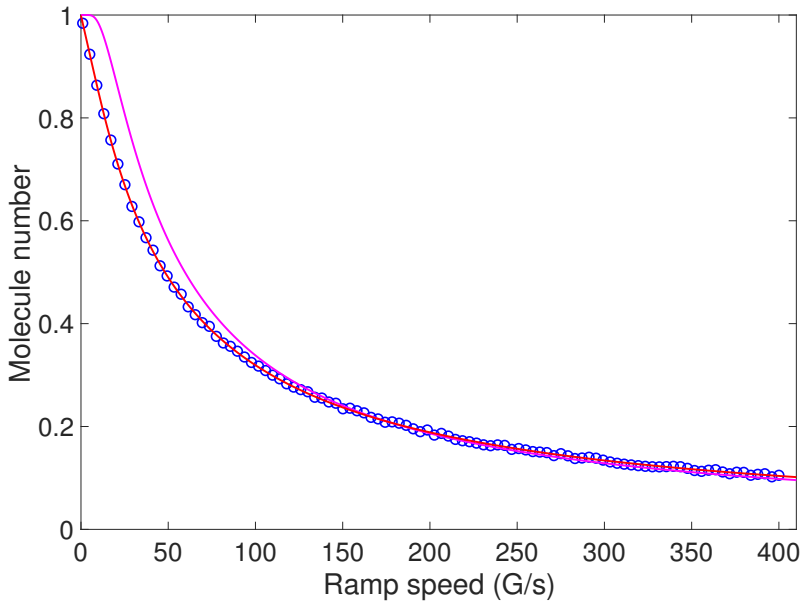

Figure 3.21: **Saturated molecule fraction at the end of the magnetic field ramp with different speeds.** The blue data points corresponds to the saturated value of the molecule number at low field e.g. see Fig. 3.20 and the magenta solid line is a fit to the part where $p \leq 0.3$ using the Landua-Zener formula. The red solid line is a fit using Eq. (10) in Ref. [98].

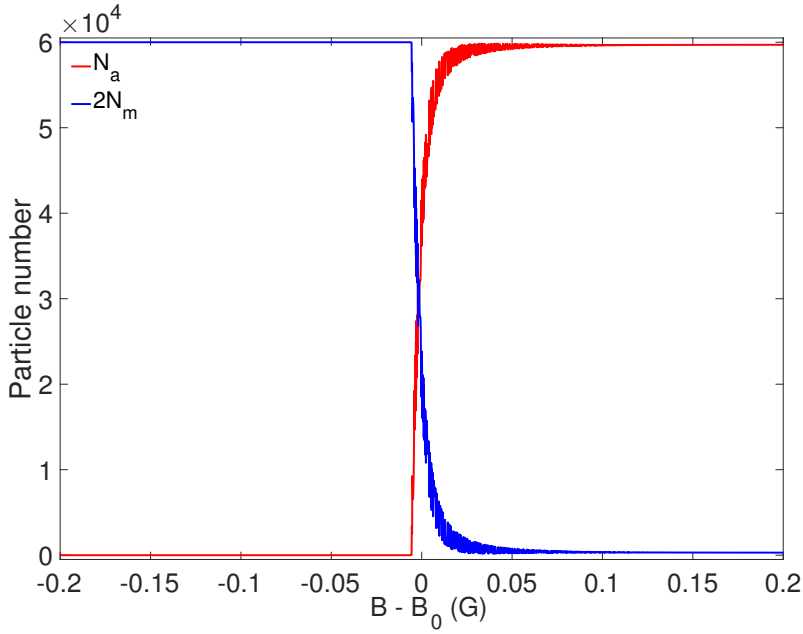

Figure 3.22: **Population of atoms and molecules for adiabatic ramp from low field to high field values starting from a pure molecular BEC.** The ramp speed is chosen to be 0.05 G/s. The result already converges for 0.1 G/s. Here we set $T'_{bg} = T'_{am} = T'_{mm} = 0$.

starting from a pure molecular BEC. The transition to atomic BEC happens at 6 mG below the resonance, consistent with the prediction of the transition point in Ref .[123].

3.2.4 Exact numerical solutions

Here we solve the following Hamiltonian exactly in the Fock basis $|M, N-2M\rangle$, where N is the total particle number and $M = 0, 1, 2, ..., N/2$ (when N is even) is the molecule number:

$$\hat{H} = \Delta \hat{b}_m^\dagger \hat{b}_m + g'(\hat{b}_m^\dagger \hat{b}_a \hat{b}_a + \hat{b}_m \hat{b}_a^\dagger \hat{b}_a^\dagger), \tag{3.86}$$

where $\Delta = \epsilon_m - \epsilon_a$ is the molecular energy relative to the free atom scattering threshold.

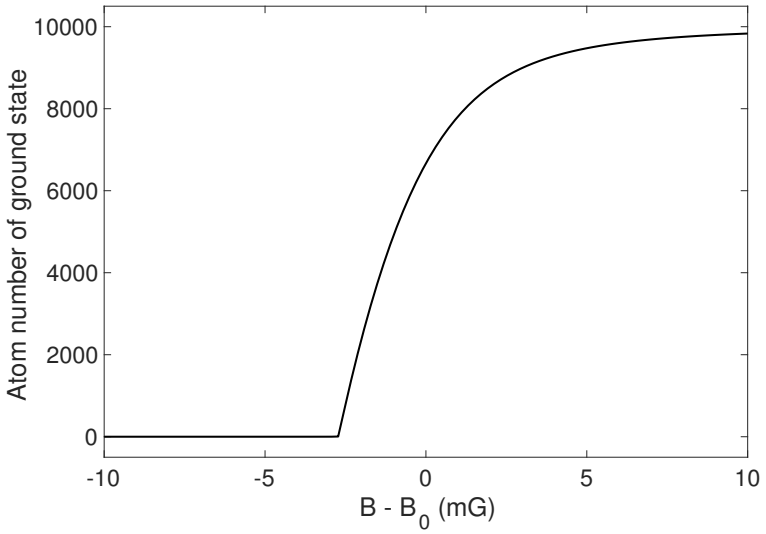

Figure 3.23: Mean atom number of the ground state at different magnetic field for total particle number N = 10,000.

To look at the ground state property, we diagonalize the Hamiltonian exactly for 10,000 particles and calculate the mean atom number associated with the ground state wavefunction (see Fig. 3.23). The result is consistent with that from the adiabatic ramp in the mean field approximation (see Fig. 3.22), where the mixture of atomic and molecular BECs suddenly appear at a magnetic field value below the resonance.

When the magnetic field is on resonance and the initial state is a pure atomic BEC,

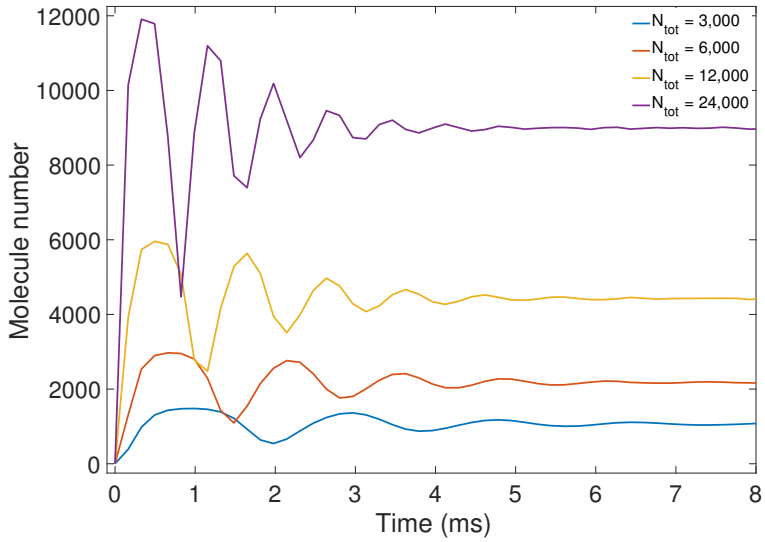

Figure 3.24: Evolution of mean molecule number on resonance $\Delta = 0$ starting from atomic BEC $|0, N\rangle$ with different total particle number.

coherent oscillation between atoms and molecules occurs as shown in Fig. 3.24. It can be seen that the oscillation damps out after several cycles and saturates to some constant value, unlike the mean field calculation results in Fig. 3.15. We perform Fourier transform to extract the main oscillation frequency as a function of total particle number, which follows the scaling $\sqrt{N}/\ln N$, see Fig. 3.25(left) [140]. The final saturated conversion efficiency $2M/N$ is close to 75% at large total particle number, see Fig. 3.25(right).

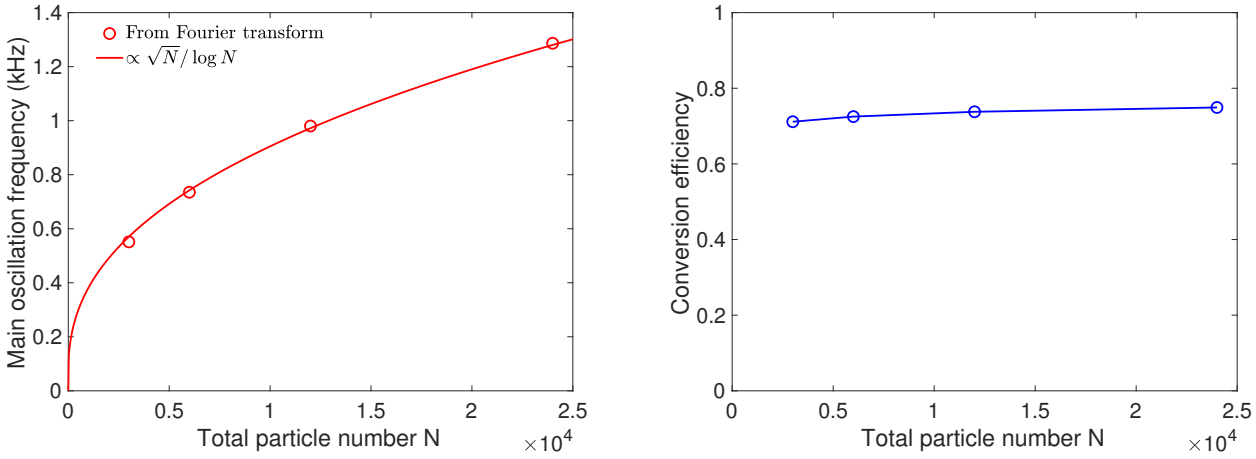

Figure 3.25: (left) Main oscillation frequencies (open circles) extracted from the Fourier transform of the numerical data in Fig. 3.24 compared to the scaling $\sqrt{N}/\ln N$ (solid line). (right) Saturated conversion efficiency $2M/N$ at late time in Fig. 3.24.

CHAPTER 4

PATTERN FORMATION IN A DRIVEN BOSE-EINSTEIN CONDENSATE

Pattern formation is ubiquitous in nature at all scales, from morphogenesis and cloud formation to galaxy filamentation. How patterns emerge in a homogeneous system is a fundamental question across interdisciplinary research including hydrodynamics [42], condensed matter physics [108], nonlinear optics [10], cosmology [94] and bio-chemistry [139, 82]. Paradigmatic examples such as Rayleigh-Bénard convection rolls and Faraday waves [19, 106] have been extensively studied and found numerous applications [50, 95, 8]. How such knowledge applies to quantum systems and whether the patterns in a quantum system can be controlled remain intriguing questions. Here we show that the density patterns with two- (D_2), four- (D_4) and six-fold (D_6) symmetries can emerge in Bose-Einstein condensates on demand when the atomic interactions are modulated at multiple frequencies. The D_6 pattern, in particular, arises from a resonant wave mixing process which establishes phase coherence of the excitations that respect the symmetry. Our experiments explore a novel class of non-equilibrium phenomena in quantum gases, as well as a new route to prepare quantum states with desired correlations.

4.1 Introduction

In classical systems, the onset of pattern formation can be understood from the dynamics and interaction of the excitations in the momentum space, described by the nonlinear amplitude equation [69, 133, 116, 124],

$$\frac{du_i}{dt} = \alpha_i u_i + \sum_{j,k} \beta_{ijk} u_j u_k + O(u^3), \tag{4.1}$$

where u_i is the amplitude of the i-th excitation mode. Starting from small amplitudes, the modes grow exponentially at the rate α_i. The quadratic term becomes important as the mode grows, and the tensor β_{ijk} describes the mixing of the modes and determines the resulting pattern. The explicit form of β_{ijk} is given by the underlying physics, e.g. Navier-Stokes equation for the hydrodynamic systems [91, 135].

In quantum systems, patterns, often characterized by correlation functions, frequently arise from long-range interactions or dynamics far from equilibrium. In polaritonic quantum fluids, hexagonal patterns emerge due to scattering between polaritons [9]. In cold atoms, Faraday waves induced by modulation of trap frequency [52, 61] or interactions [110, 115] occur in 1D Bose-Einstein condensates (BECs). BECs also develop spin [88] or density wave patterns [73] by quenches of atomic interaction. Droplets in a dipolar BEC form a hexagonal pattern due to Rosensweig instability [83]. Recently, supersolid order, for which a superfluid exhibits spatial correlations, emerges in condensates with spin-orbit coupling [93] or dipolar interactions [21, 134, 31].

We report formation of various 2D density wave patterns in a uniform BEC by modulating the atomic interactions at two frequencies in the vicinity of a Feshbach resonance (Fig. 4.1**a**). The interaction modulation is realized by applying an oscillating magnetic field to the sample [35, 56]. The magnetic field is in the $z-$direction perpendicular to the sample, while the pattern forms in the horizontal $x-y$ plane (Fig. 4.1**b**). By changing the ratio of the two modulation frequencies, density patterns with D_2, D_4 and D_6 symmetries are observed *in situ* and analyzed. The D_6 density wave pattern, in particular, results from a novel coherent process that resonantly couples six momentum modes.

To understand the pattern formation process in a driven condensate, we derive the associated quantum nonlinear amplitude equation as (see Sec. 4.2)

$$\frac{d\hat{a}_{\mathbf{k}}}{dt} = \gamma_1 \hat{a}^{\dagger}_{-\mathbf{k}} + \gamma_2 \sum_{\mathbf{k}_1} \hat{a}^{\dagger}_{\mathbf{k}_1-\mathbf{k}} \hat{a}_{\mathbf{k}_1} - \gamma_2^* \sum_{\mathbf{k}_2} \hat{a}_{\mathbf{k}_2} \hat{a}_{\mathbf{k}-\mathbf{k}_2}, \tag{4.2}$$

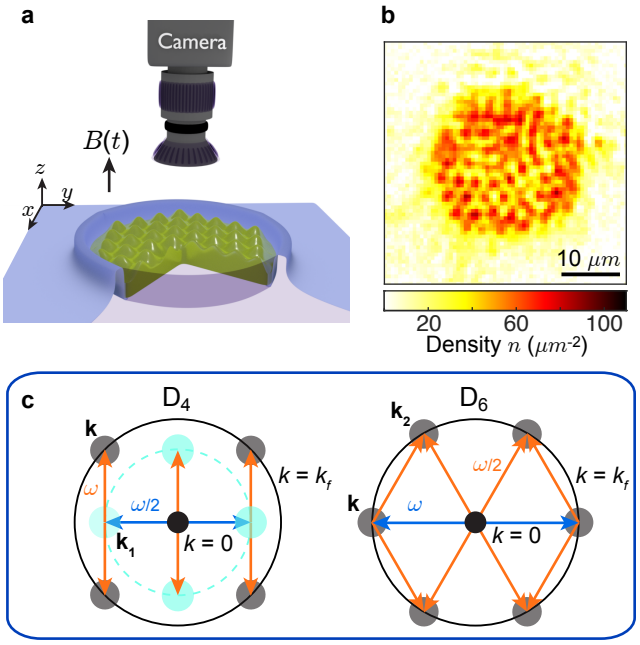

Figure 4.1: **Pattern formation in a BEC with interaction modulation at two frequencies. a**, A BEC (green) of ^{133}Cs atoms is trapped in a 2D circular potential well (blue). An oscillating magnetic field $B(t)$ in the z direction modulates the scattering length. The atomic density is recorded by a camera. **b**, An example image of the driven BEC displays density waves. **c**, Scattering processes that generate D_4 and D_6 density waves are illustrated in momentum space in two stages. In the seeding stage, BEC (black dot) at $k = 0$ produces atom pairs with opposite momentum (blue arrows). In the pattern forming stage, collisions between the atom pairs and the BEC generate four or six modes with $k = k_f$ (orange arrows) with equal angular spacing, which we study in this work. For the creation of D_4 and D_6 patterns, the modulation frequencies are $\omega/2$ followed by ω, and ω followed by $\omega/2$, respectively. Cyan circles indicate other modes populated during the scattering processes.

where $\hat{a}_{\mathbf{k}}$ and $\hat{a}^{\dagger}_{\mathbf{k}}$ are the bosonic annihilation and creation operators with momentum $\hbar\mathbf{k}$, respectively, $\hbar = h/2\pi$ is the reduced Planck constant, the summations include all resonant scattering processes, and the rate constants γ_1 and γ_2 are given by the modulation strengths. This equation is reminiscent of the classical amplitude equation Eq. 4.1.

The wave mixing processes leading to D_4 and D_6 patterns can be described in two stages (Fig. 4.1**c**). In the *seeding* stage, atom pairs with opposite momentum are generated from the condensate by a single-frequency modulation. Such a process, given by the first term in Eq. 4.2, seeds and amplifies the primary excitations that spontaneously break the rotational

symmetry of the system. In the *pattern forming* stage, the same or a different frequency component is introduced to the modulation, which stimulates scatterings into a particular pattern with the desired symmetry (see Sec. 4.2). This process is described by the nonlinear terms in Eq. 4.2. Finally, the excitation modes interfere with the BEC to form the density wave $n(r)$, which we observe. The density wave relates to the excitations $\hat{a}_{\mathbf{k}}$ as $\hat{n}(r) = n_0[\hat{1} + N_0^{-1/2}\sum_{\mathbf{k}}(\hat{a}_{\mathbf{k}} + \hat{a}^{\dagger}_{-\mathbf{k}})e^{i\mathbf{k}\cdot r}]$, where n_0 is the condensate density and $N_0 \gg 1$ is the atom number in the condensate. We emphasize that the spatial symmetry of the patterns is only controlled by the ratio of the modulation frequencies, and the sample is colllisionally thin. These contrast the former Faraday wave experiments [50, 95, 52, 61, 110, 115], where patterns rely on the strength of the modulation amplitudes, and relaxation in the hydrodynamic regime.

4.2 Quantum dynamics of pattern formation

We start from the general form of Hamiltonian of driven BECs,

$$\begin{aligned} H = &\int d^3\mathbf{r}\Psi^{\dagger}(\mathbf{r},t)\frac{p^2}{2m}\Psi(\mathbf{r},t) + \int d^3\mathbf{r}\Psi^{\dagger}(\mathbf{r},t)V(\mathbf{r})\Psi(\mathbf{r},t) \\ &+ \frac{g(t)}{2}\int d^3\mathbf{r}\Psi^{\dagger}(\mathbf{r},t)\Psi^{\dagger}(\mathbf{r},t)\Psi(\mathbf{r},t)\Psi(\mathbf{r},t), \end{aligned} \tag{4.3}$$

where the interaction strength is modulated as $g(t) = \frac{4\pi\hbar^2}{m}[a_{dc} + a_1(t)\sin\omega_1 t + a_2(t)\sin(\omega_2 t + \phi)]$. Here a_{dc} is a small offset scattering length to keep the condensate stable, $a_{1,2}$ are amplitudes of scattering length modulation and ϕ is the relative phase between the two frequency components ω_1 and ω_2.

The external potential $V(\mathbf{r})$ is neglected later because it only serves to determine the initial wavefunction of BECs and doesn't affect the dynamics. After doing the Fourier transform $\Psi(\mathbf{r}) = \frac{1}{\sqrt{V}}\sum_{\mathbf{k}}\hat{a}_{\mathbf{k}}e^{i\mathbf{k}\cdot\mathbf{r}}$, we obtain the Hamiltonian in momentum space as

$$H = \sum_{\mathbf{k}} \epsilon_{\mathbf{k}} \hat{a}^{\dagger}_{\mathbf{k}} a_{\mathbf{k}} + \frac{g(t)}{2V} \sum_{\mathbf{k}_1, \mathbf{k}_2, \Delta\mathbf{k}} \hat{a}^{\dagger}_{\mathbf{k}_1 + \Delta\mathbf{k}} \hat{a}^{\dagger}_{\mathbf{k}_2 - \Delta\mathbf{k}} \hat{a}_{\mathbf{k}_1} \hat{a}_{\mathbf{k}_2}, \tag{4.4}$$

where V is the volume of condensate and the dispersion is $\epsilon_{\mathbf{k}} = \hbar^2 k^2 / 2m$.

After transferring to the rotating frame with $\hat{a}_{\mathbf{k}} \to \hat{a}_{\mathbf{k}} e^{-i\epsilon_{\mathbf{k}} t/\hbar}$ and using the rotating wave approximation to eliminate the fast oscillating terms, the Hamiltonian becomes time-independent:

$$H_I = \frac{i}{4V} (\sum_{\mathbf{k}} g_1 \hat{a}^{\dagger}_{\mathbf{k}} \hat{a}^{\dagger}_{-\mathbf{k}} \hat{a}_0 \hat{a}_0 + \sum_{\mathbf{k}'} g_2 \hat{a}^{\dagger}_{\mathbf{k}'} \hat{a}^{\dagger}_{-\mathbf{k}'} \hat{a}_0 \hat{a}_0 + \sum_{\mathbf{k}_1, \mathbf{k}_2} g_2 e^{-i\phi} \hat{a}^{\dagger}_{\mathbf{k}_2} \hat{a}^{\dagger}_{\mathbf{k}_1 - \mathbf{k}_2} \hat{a}_{\mathbf{k}_1} \hat{a}_0) + h.c., \tag{4.5}$$

where $g_1 = 4\pi\hbar^2 a_1 / m$ and $g_2 = 4\pi\hbar^2 a_2 / m$ and the summations go over the processes that satisfy the following energy conservation conditions:

$$\begin{aligned} \epsilon_{\mathbf{k}} + \epsilon_{-\mathbf{k}} &= \hbar\omega_1, \\ \epsilon_{\mathbf{k}'} + \epsilon_{-\mathbf{k}'} &= \hbar\omega_2, \\ \epsilon_{\mathbf{k}_2} + \epsilon_{\mathbf{k}_1 - \mathbf{k}_2} &= \epsilon_{\mathbf{k}_1} + \hbar\omega_2. \end{aligned} \tag{4.6}$$

Here the left/right hand side is the total energy after/before the collision.

Then the equation of motion for $\hat{a}_{\mathbf{k}}$ is obtained to second order in the Bogoliubov approximation $\hat{a}_0 \approx \hat{a}^{\dagger}_0 \approx \sqrt{N_0}$ as

$$\frac{d\hat{a}_{\mathbf{k}}}{dt} = \gamma_1 \hat{a}^{\dagger}_{-\mathbf{k}} + \gamma_2 \sum_{\mathbf{k}_1} \hat{a}^{\dagger}_{\mathbf{k}_1-\mathbf{k}} \hat{a}_{\mathbf{k}_1} - \gamma_2^* \sum_{\mathbf{k}_2} \hat{a}_{\mathbf{k}_2} \hat{a}_{\mathbf{k}-\mathbf{k}_2}, \tag{4.7}$$

where the growth rates are given by $\gamma_1 = \frac{N_0 \pi \hbar a_1}{mV}$, $\gamma_2 = \frac{\sqrt{N_0}\pi\hbar a_2}{mV} e^{-i\phi}$. Here all the momenta are restricted to the horizontal plane and the magnitude of $\mathbf{k}$ is $|\mathbf{k}| = k_f = \sqrt{m\omega_1/\hbar}$. We have been using $\omega_1 = \omega = 2\pi \times 450$ Hz and $\omega_2 = \omega/2 = 2\pi \times 225$ Hz in our experiments.

The formation of density wave patterns originates from the momentum and energy conservation of underlying bosonic stimulated scattering processes (see Fig. 4.1**c**). For the D_4 pattern formation under Scheme III described in Sec. 4.4.2 , during the first modulation of frequency $\omega/2$, a pair of BEC atoms absorb a quantum of energy $\hbar\omega/2$ and scatter into a pair of atoms with opposite momenta $\pm\mathbf{k}_1$ at $|\mathbf{k}_1| = k_f/\sqrt{2}$ and energy $\epsilon_{\mathbf{k}_1} = \hbar\omega/4$. Then one atom with $\mathbf{k}_1$ collides with one BEC atom absorbing another quantum of $\hbar\omega/2$. One of them scatters into $\mathbf{k}$ with magnitude k_f and energy $\epsilon_{\mathbf{k}} = \hbar\omega/2$ at 45°(or -45°) relative to $\mathbf{k}_1$. The other one is scattered into $\mathbf{k}_1 - \mathbf{k}$ with magnitude $k_f/\sqrt{2}$ and energy $\epsilon_{\mathbf{k}_1-\mathbf{k}} = \hbar\omega/4$ at -90° (or 90°) relative to $\mathbf{k}_1$. This process is described by the second term on the right hand side (RHS) of Eq. 4.7. However, here the third term is zero because they don't satisfy both momentum and energy conservation by releasing an energy quantum of $\hbar\omega/2$ into the driving field. On the other hand, one atom with $-\mathbf{k}_1$ can collide with one BEC atom and one of the scattered atoms has momentum k_f at 45° or -45° relative to $-\mathbf{k}_1$. Thus, seeds of 4 momentum modes at k_f with 90° relative angular spacing are generated. Later, when another modulation of frequency ω is applied, those 4 modes get amplified with pairs of BEC atoms scattering into them. This corresponds to the first term on the RHS of Eq. 4.7. Finally the those 4 momentum modes with 90° angular spacing interfere with the BEC to form the D_4 density wave pattern. Note that the D_4 pattern emerges regardless of the presence of the modulation at $\omega/2$ in the pattern-forming stage, so only modulation at ω is applied there.

On the other hand, for D_6 pattern formation under Scheme II, a modulation of frequency ω is first applied to generate pairs of opposite momentum modes $\pm\mathbf{k}$ at k_f and energy $\epsilon_{\mathbf{k}} = \hbar\omega/2$. Then when the second frequency component $\omega/2$ is added, an atom with $\mathbf{k}$ collides with a BEC atom absorbing one energy quantum $\hbar\omega/2$ and scattering into atoms with $\mathbf{k}_2$ and $\mathbf{k} - \mathbf{k}_2$ with the same magnitude k_f and energy $\epsilon_{\mathbf{k}_2} = \epsilon_{\mathbf{k}-\mathbf{k}_2} = \hbar\omega/2$ at $\pm 60^\circ$ relative to $\mathbf{k}$. This corresponds to hermitian conjugate of the third term on the RHS of Eq. 4.7. Also, atoms with momentum $\mathbf{k}_2$ or $\mathbf{k} - \mathbf{k}_2$ can collide with one BEC atom into atoms with $\mathbf{k}$, corresponding to the second term on the RHS of Eq. 4.7. In the meantime, one atom with $-\mathbf{k}$ can collide with one BEC atom and scatter into $-\mathbf{k}_2$ or $-(\mathbf{k}-\mathbf{k}_2)$ at $\pm 60^\circ$ relative to $-\mathbf{k}$. Thus, 6 momentum modes with 60° relative angular spacing are generated and are amplified by the ω frequency component at the same time. Eventually they interfere with the condensate and form the D_6 density wave pattern.

To form a general n-fold symmetric pattern in momentum space, it is required to have three different modulation frequencies: two of them stimulate population into two momentum rings and another one creates coupling between these two momentum rings, see Sec. 8.1. Eventually N momentums will be distributed uniformly on each ring and form a N-fold symmetric pattern in real space by interfering with BEC. The D_4 and D_6 patterns are the only special cases we know that require less than 3 modulation frequencies. Moreover, the excitation modes associated with these patterns are expected to be squeezed and entangled due to the underlying pair production scattering processes. For example, counter-propagating momentum modes in the D_2 pattern are in a two-mode squeezed state $|\Psi(\tau)\rangle = \frac{1}{\cosh(g\tau)} \sum_{n=0}^{\infty} \tanh^n(g\tau)\, |n, n\rangle_{\pm\mathbf{k}}$ [36], where τ is interaction modulation time and g is the coupling constant proportional to modulation amplitude. The populations n in counter-propagating modes are always equal and thus maximally squeezed. Similarly, for D_6 patterns, the three pairs of modes with opposite momentum are also squeezed and with additional coupling between different pairs due to the second modulation frequency. We

expect them to be in a state with general form as

$$|\Psi(\tau)\rangle = \sum_{\alpha,\beta,\gamma,\delta=0}^{\infty} C_{\alpha,\beta,\gamma,\delta}(\tau)\,|\alpha,\beta,\gamma+\delta-\beta,\alpha+\beta-\gamma,\gamma,\delta\rangle_{\mathbf{k}_1,\mathbf{k}_2,\mathbf{k}_3,-\mathbf{k}_1,-\mathbf{k}_2,-\mathbf{k}_3}\,, \quad (4.8)$$

where $\alpha,\beta,\gamma,\delta = 0,1,2...$ with constraints $\gamma+\delta \geq \beta$ and $\alpha+\beta \geq \gamma$. $C_{\alpha,\beta,\gamma,\delta}(\tau)$ is a complex amplitude of the fock state at evolution time $t=\tau$. Due to the conservation of total momentum, the population difference $n_{\mathbf{k}_i} - n_{-\mathbf{k}_i}$ for a pair of opposite momentum modes $\pm\mathbf{k}_i$ is always equal to that of another pair $n_{-\mathbf{k}_j} - n_{\mathbf{k}_j}$. The squeezing and entanglement properties of this state is to be studied in our future experiments.

4.3 Experimental setup

We start with BECs of 60,000 cesium atoms loaded into a disk-shaped dipole trap with a radius of 14.5 μm in the horizontal direction. The horizontal confinement is provided by a blue-detuned laser at 780 nm. We shape the laser beam profile using a digital micromirror device and project it to the atom plane through a high-resolution objective. The resulting circular potential well has a barrier height of $h \times 140$ Hz. The uniformity of the potential well is reflected by the atomic density profile at the beginning of the modulation as shown in Fig. 4.2**b**, where the variation is approximately 10% of the mean density. Atoms are tightly confined in the vertical direction with a $1/e^2$ radius of 0.78 μm and a harmonic trap frequency of 259 Hz.

After preparing the sample, we modulate the magnetic field near a Feshbach resonance, which causes the s-wave scattering length a of the atoms to oscillate as $a(t) = a_{dc} + a_1(t)\sin\omega_1 t + a_2(t)\sin(\omega_2 t+\phi)$. We use an arbitrary waveform generator to control the current modulation in the coils, which leads to the magnetic field being modulated according to a designed waveform. A small positive offset scattering length $a_{dc} = 2a_0$ is

maintained throughout the experiment to keep the condensate stable. Since the chemical potential is much smaller than the vertical trapping frequency, the BEC is in the quasi-2D regime [113]. For generating the D_2 density wave pattern, we keep modulating the scattering length at frequency 450 Hz with amplitude 45 a_0 for 23.8 ms. For D_4 pattern, we first modulate at 225 Hz for 3 cycles with amplitude 45 a_0 and then switch to 450 Hz with the same amplitude for 24 ms. To generate D_6 pattern, the first 10 cycles of modulation is at 450 Hz with amplitude 30 a_0, which is then mixed with another frequency component at 225 Hz and amplitude 25 a_0 for 22.8 ms. The relative phase ϕ between these two frequency components is 0. The modulation frequencies we employ do not match the vertical trap frequency, and thus the atomic motion in the vertical direction is not excited. This distinguishes our experiment from the previous Faraday wave experiments on BECs [52, 115, 1]. In addition, it is only important that the two modulation frequencies have the proper ratio of 1:2 or 2:1 to ensure the phase matching condition. Specific value of any single frequency is unimportant.

We finally perform *in situ* absorption imaging to observe the resulting density waves in condensates using the high-resolution objective and a CCD camera. Our imaging system is sensitive to density fluctuations of spatial frequency ranging from 0 up to 3.44 μm^{-1} [76], which covers the density waves we observe at $k_f = 2.43\ \mu m^{-1}$.

In order to extract the population of excited modes from their interference with the condensate, we first Fourier transform the images including density waves. Then in the Fourier space we focus on the ring at $|k - k_f| \leq 0.1k_f$ and cut it using angular slices of 3° to count the average Fourier magnitude A_θ in the direction at angle θ. In general, the sensitivity of our imaging system varies for signals with different wavenumber. We measure the modulation transfer function $M(\mathbf{k})$ of thermal atoms and find that the proportional constant of measured strength of density fluctuations at k_f to its corresponding real strength is $M(k = k_f) = 0.45$ [76]. The relation between density wave amplitude A_θ and population $|a_\mathbf{k}|^2$ is $|A_\theta|^2 = 4N_0 \cos^2(\omega t/2)|a_\mathbf{k}|^2$, where the phase $\omega t/2 \approx 0.57$ rad at the time we perform the

imaging. Finally the population is evaluated as $|a_{\mathbf{k}}|^2 = |A_\theta|^2/[M^2(k=k_f)4N_0\cos^2(\omega t/2)]$. Also, we observe the density waves stroboscopically every 4.4 ms.

4.4 Results

4.4.1 Formation of density waves with D_6 symmetry

We first describe the experimental procedure for the formation of the density waves with D_6 symmetry. In the seeding stage, we apply a single-frequency modulation as $a(t) = a_{dc} + a_1 \sin\omega t$, where $\omega/2\pi = 450$ Hz, $a_1 = 30\ a_0$, $a_{dc} = 2\ a_0$ and a_0 is the Bohr radius. After $t = 22.2$ ms, in the pattern forming stage, we add a second frequency component to the modulation as $a(t) = a_{dc} + a_1 \sin\omega t + a_2 \sin\omega t/2$, where $a_2 = 25\ a_0$ (see Fig. 4.2**a**).

We analyze the symmetry of the density wave patterns based on Fourier analysis. In the seeding stage, only stripe patterns appear. In the pattern forming stage, hexagonal lattice patterns with D_6 symmetry emerge, signified by six distinct modes in the Fourier space. The modes are equally spaced by $\pi/3$ in their directions with the same wavenumber $k_f = \sqrt{m\omega/\hbar} = 2.43\ \mu m^{-1}$ [35] (see Fig. 4.2**b**), where m is the atomic mass.

The presence of the D_6 pattern can be further confirmed with a pattern recognition algorithm [54] (see Fig. 4.2**c**). To quantify the strength of the patterns, we evaluate the density correlation function $g^{(2)}(\theta) \equiv \langle |A_\varphi|^2 |A_{\varphi+\theta}|^2\rangle / \langle |A_\varphi|^2\rangle^2$, where $A_\theta = \int n(\mathbf{r}) e^{-i\mathbf{k}_\theta\cdot\mathbf{r}} d\mathbf{r}$ is the Fourier amplitude evaluated at $\mathbf{k}_\theta$ with magnitude $|\mathbf{k}_\theta| = k_f$ and angle θ. The angle brackets denote averaging over both the angle φ from 0 to 2π and the images. The evolution of $g^{(2)}$ confirms the growth of different patterns in the seeding and pattern forming stages (Fig. 4.2**d**).

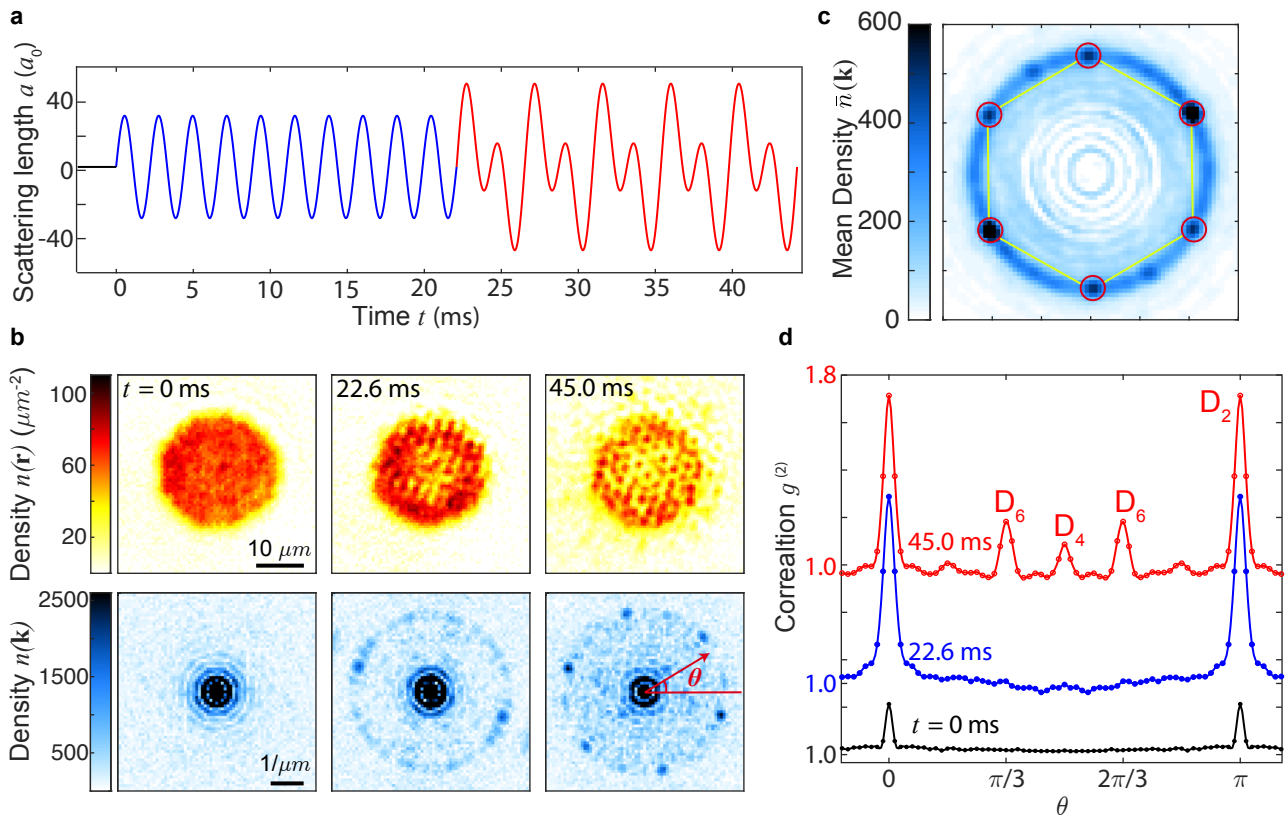

Figure 4.2: **Formation of density waves with D_6 symmetry. a**, The scattering length is modulated in two stages. The modulation frequency is 450 Hz in the first ten cycles, which is then superposed with a second modulation of 225 Hz (see text). **b**, Examples of *in situ* images at times $t = 0$, 22.6 and 45 ms (top row) and the corresponding Fourier transforms (bottom row). At 45 ms, the Fourier transform displays 6 peaks with $\pi/3$ angular spacing that break the rotation symmetry. The 6-peak patterns orient randomly in repeated experiments. **c**, Pattern recognition based on 185 Fourier transformed images yields six strong peaks (red circles) on the vertices of a hexagon (yellow). Two weaker ones come from patterns with D_4 symmetry. We remove the contribution from the BECs using principal component analysis. **d**, Correlations $g^{(2)}$ of the Fourier modes with angular spacing θ. The peaks at $\pi/3$, $\pi/2$ and π indicate the strength of the patterns with D_6, D_4 and D_2 symmetry respectively.

Principal component analysis (PCA)

In order to remove the background of Fourier space in Fig. 4.2**c**, we collect 100 images of pure BECs and apply PCA algorithm to construct the bases and subtract the projection onto these bases from the Fourier transform of BECs with density waves.

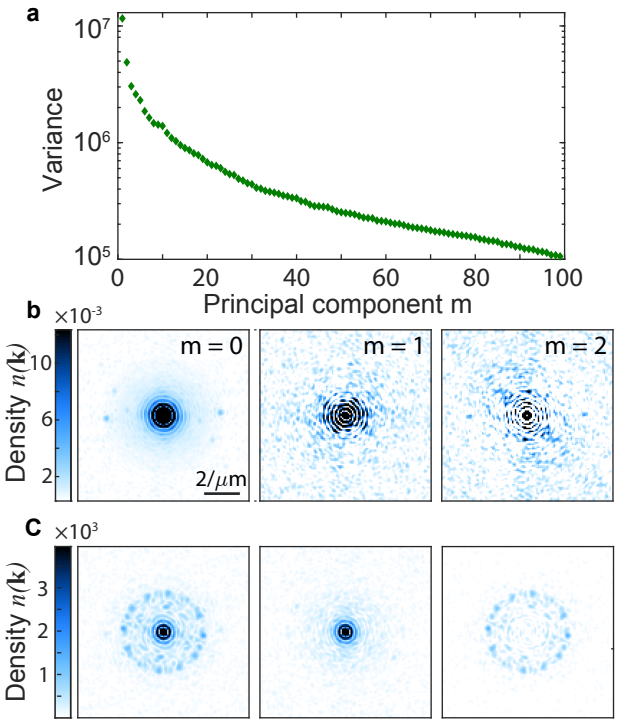

Figure 4.3: **Principal component analysis for removing the background in Fourier space.** **a**, The variance of the data matrix X's projection onto each principal components. The y axis is in log scale. **b**, The mean of the magnitude of Fourier transforms of pure BECs (left) and the first two bases from PCA (middle and right). **c**, One example of removing all the projection onto PCA bases (middle) from the Fourier space of BEC with density waves (left), only signals from the density waves survive (right).

We first get the Fourier amplitude's magnitude $n_i(\mathbf{k})$ of the i^{th} image of pure BEC atomic density $n_i(\mathbf{r})$. Each $p \times p$ square matrix $n_i(\mathbf{k})$ is rearranged into a $1 \times p^2$ row vector. Then all the row vectors are arranged to form a rectangular matrix M_{ij}, where j ranges from 1 to $p^2 = 121^2$. The mean value of each column is shifted to zero by subtracting the average of experimental realizations, resulting in the data matrix $X = M - \bar{M}$. Our goal is to diagonalize the covariance matrix $X^T X$ to find its eigenvectors w_j and eigenvalues λ_j, which corresponds to statistical independent bases (principal components) and variance of X's projection $X_{ij} w_j$ onto each basis, respectively. We use singular value decomposition (SVD) to perform this diagonalization.

The first 99 principal components are kept and the corresponding variances are shown in Fig. 4.3**a**. The average of $n_i(\mathbf{k})$ is counted as an additional basis w_0. In Fig. 4.3**b**, we plot the average of $n_i(\mathbf{k})$ and the two principal components that have the largest and second largest variances. Next, we use those constructed bases to remove the background in the Fourier space $n_d(\mathbf{k})$ of the atomic densities of BECs with density waves $n_d(\mathbf{r})$. As an example, in Fig. 4.3**c**, we project one $n_d(\mathbf{k})$ to all the principal components w_j to reconstruct the background. Finally the background is subtracted from the original Fourier space and only the signals from density waves are left.

4.4.2 Density wave patterns in real space

We tailor the modulation waveform to create different patterns. Here three modulation schemes that lead to patterns with D_2, D_4 and D_6 symmetries are reported. Scheme I: we apply the modulation at a single frequency ω. Scheme II: we modulate at frequency ω in the seeding stage and superpose a second frequency $\omega/2$ in the pattern forming stage (Fig. 4.2**a**). Scheme III: we modulate at frequency $\omega/2$ and then switch to frequency ω.

To reveal the density patterns in real space, we employ a 2D pattern recognition algorithm. Since the pattern in each image appears with random orientation and displacement,

the algorithm is developed to rotate and align the patterns (Fig. 4.4**a**).

We determine the orientation of each image as illustrated in Fig. 4.2**c**, and align all of them in the same direction. We then translate each of the images independently to maximize the spatial variance of their average. Finally we extract the underlying pattern by averaging all aligned images. To eliminate long wavelength variations that are uncorrelated with the pattern and to only focus on patterns formed at the wavelength corresponding to k_f, we filter the density fluctuations at $|\mathbf{k}| \leq 0.75k_f$ from the images to get the density waves $\tilde{n}(\mathbf{r})$.

The results of the 2D pattern recognition algorithm are shown in Fig. 4.4**b**. Single frequency modulation (Scheme I) produces D2 stripe patterns. Scheme II ($\omega \rightarrow \omega/2$) results in a hexagonal lattice pattern, consistent with Fig. 4.2. Scheme III ($\omega/2 \rightarrow \omega$) results in a square lattice pattern. We further determine the strengths of different symmetry components in each image P based on the fit: $P = c_2P_2 + c_4P_4 + c_6P_6$, where P_n are normalized patterns with D_n symmetry, and c_n are the fitting parameters. The results, shown in the bar diagrams of Fig. 4.4**b**, suggest that different schemes are effective in generating patterns with different symmetries.

Remarkably, all three patterns extend throughout the entire sample. The spatial extent of the patterns can be evaluated from their real space correlation functions $\tilde{g}^{(2)}(\mathbf{r}) \equiv \int \tilde{n}(\mathbf{r}_0)\tilde{n}(\mathbf{r}_0+\mathbf{r})d\mathbf{r}_0 / \int \tilde{n}^2(\mathbf{r}_0)d\mathbf{r}_0$. Correlations along principle directions, shown in Fig. 4.4**c**, extend across the entire sample of diameter 25 μm. We note that the finite correlations of 2D superfluid might limit the correlation length we report here. Comparing the patterns, we observe that the D_6 pattern is a factor of 5 more pronounced than D_4 even though these two schemes employ similar modulation strengths.

Real space pattern recognition algorithm

We consider each individual *in situ* absorption image as a combination of several common patterns with random orientations and displacements which contribute to the image with

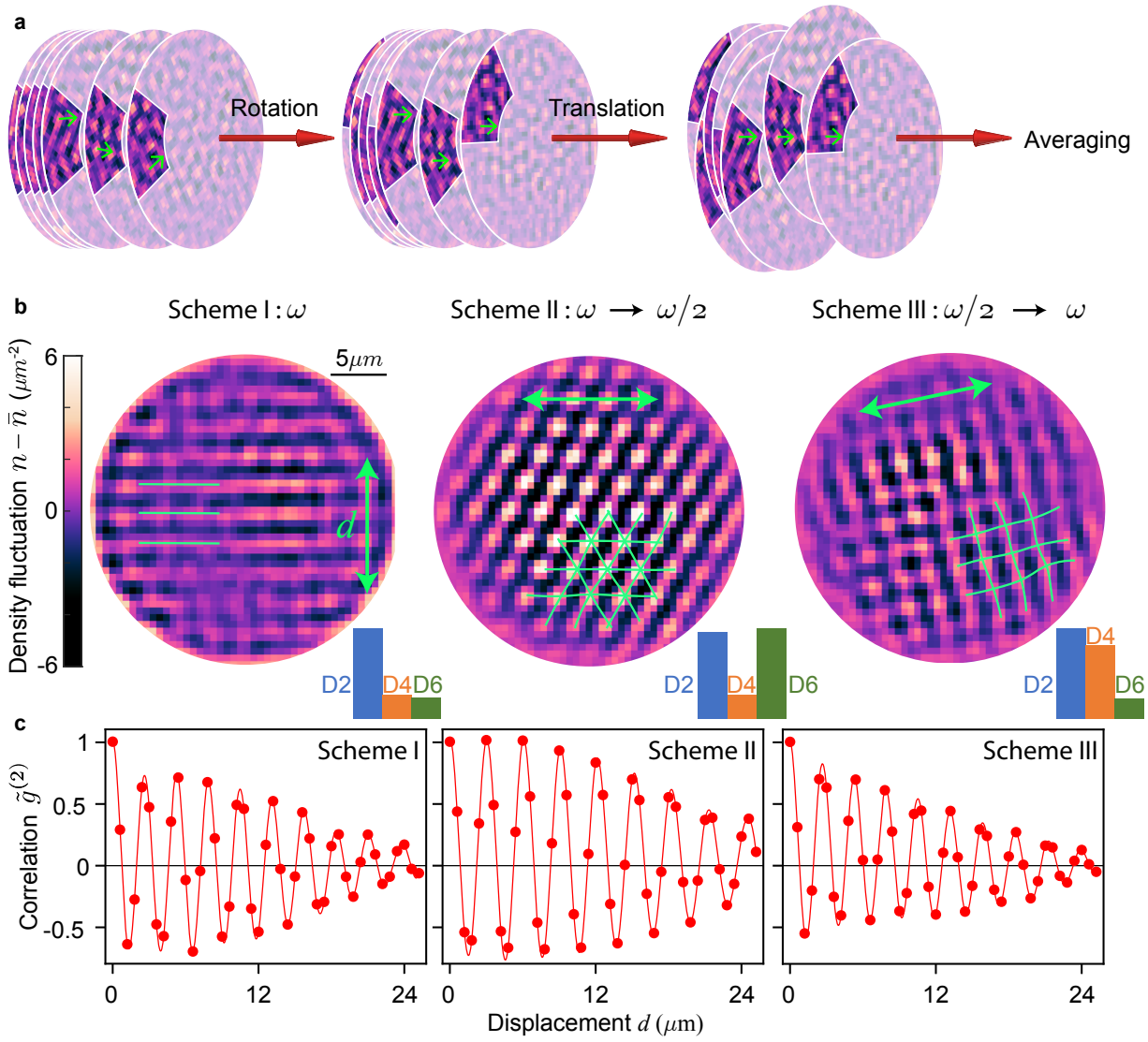

Figure 4.4: **Density wave patterns in real space.** **a**, In our pattern recognition algorithm, each of the *in situ* images is first rotated and then translated to overlap the density waves. The translation maximizes the variance of the averaged image. **b**, Resulting density waves from the algorithm for Scheme I (stripes): single modulation frequency ω, Scheme II (hexagonal lattice): ω followed by $\omega/2$, and Scheme III (square lattice): $\omega/2$ followed by ω. The green lines are guides to the eye to highlight the corresponding pattern. The green arrows show the direction along which the real space correlation is evaluated in panel **c**. The bar diagrams show the relative weights of D_2, D_4 and D_6 symmetry components from fitting the patterns. **c**, Real space correlation functions evaluated from the patterns. The oscillations have periods of 2.63(1), 3.05(1) and 2.65(1) μm for schemes I, II and III, respectively. The ratio of the periods is 1.156(2), consistent with theory value $2/\sqrt{3} \approx 1.155$. The solid lines are guides to the eye.

different weights. To reveal the common pattern, we align the strongest components from repeated experimental realizations and the weaker ones are averaged to zero. This alignment can be achieved from our real space pattern recognition algorithm.

Here we describe the details of the 2D pattern recognition algorithm (Fig. 4.4**a**). We first filter out the low frequency noise at $|\mathbf{k}| < 0.75k_f$ from the *in situ* absorption images to get a set of $N = 185$ filtered images of atomic density fluctuations, $\tilde{n}_i(x, y),\ i = 1, \cdots, N$ (see Fig. 4.7**a**). Let $\mathcal{T}_{\theta_i,\mathbf{r}_i}(\tilde{n}_i)$ denote the result of rotating $\tilde{n}_i$ by θ_i and then translating by $\mathbf{r}_i$, where we impose the constraint $|\mathbf{r}_i| < 2\pi/k_f$. The objective function L is the spatial variance of the average image $\bar{n}$ after rotating and translating individual images:

$$\bar{n}(\{\theta_i\}, \{\mathbf{r}_i\}) = \frac{1}{N} \sum_i \mathcal{T}_{\theta_i,\mathbf{r}_i}(\tilde{n}_i), \tag{4.9}$$

$$L(\{\theta_i\}, \{\mathbf{r}_i\}) = \frac{1}{S} \int \bar{n}^2 dxdy - \left(\frac{1}{S} \int \bar{n} dxdy \right)^2, \tag{4.10}$$

where S is the total area of the atomic density fluctuations. The optimal rotation angles and translation displacements $\{\theta_i\}, \{\mathbf{r}_i\}$ are found by maximizing L, and the pattern recognized is $\bar{n}$ with the optimal parameters.

Since the rotation angle θ_i and displacement $\mathbf{r}_i$ are independent degrees of freedom, we perform the optimization of the objective function L in two separate steps. We first find the orientation of each image from the angular distributions of density wave amplitudes F_θ obtained from fitting (see Fig. 4.7**b**). The rotation angles θ_i are changed for individual images in order to maximize the variance of the averaged angular distribution [54]. Then the angles are fixed to be the ones after the above optimization before we optimize the displacement of each image. Finally, we translate each image $\tilde{n}_i$ by $\mathbf{r}_i$ to maximize the spatial variance of resulting averaged density fluctuation $\bar{n}$. The recognized common patterns for different modulation schemes are shown in Fig. 4.4**b**.

Symmetry decomposition of density patterns

We consider each recognized pattern P shown in Fig. 4.4**b** as a superposition of normalized two-, four- and six-fold symmetry components $P_{2,4,6}$ with amplitudes $c_{2,4,6}$ and a small offset c_0. In order to find the contribution of each symmetry component, we fit the patterns using the following function:

$$P = c_2 P_2 + c_4 P_4 + c_6 P_6 + c_0, \tag{4.11}$$

where

$$P_2 = \mathcal{R}_{\theta_2} \cos(k_f x + \phi_2), \tag{4.12}$$

$$P_4 = \frac{1}{\sqrt{2}} \mathcal{R}_{\theta_4} \left[\cos(k_f x + \phi_{4,1}) + \cos(k_f y + \phi_{4,2}) \right], \tag{4.13}$$

$$\begin{aligned} P_6 = \frac{1}{\sqrt{3}} \mathcal{R}_{\theta_6} \Bigg[& \cos(k_f x + \phi_{6,1}) \\ & + \cos(-\frac{1}{2} k_f x + \frac{\sqrt{3}}{2} k_f y - \frac{1}{2} \phi_{6,1} + \frac{\sqrt{3}}{2} \phi_{6,2}) \\ & + \cos(-\frac{1}{2} k_f x - \frac{\sqrt{3}}{2} k_f y - \frac{1}{2} \phi_{6,1} - \frac{\sqrt{3}}{2} \phi_{6,2}) \Bigg]. \end{aligned} \tag{4.14}$$

Here $\mathcal{R}_\theta[\cdot]$ denotes rotation by angle θ. There are 12 fitting parameters in total: $\{c_2, c_4, c_6\}$ determine the strengths of the symmetry components, c_0 determines the overall offset, $\{\theta_2, \theta_4, \theta_6\}$ determine the orientations, and $\{\phi_2, \phi_{4,1}, \phi_{4,2}, \phi_{6,1}, \phi_{6,2}\}$ determine the displacements. The optimal fitting parameters are shown in Table S1. One example of the symmetry decomposition results for the D_6 density pattern under Scheme II is shown in Fig. 4.5.

Parameters	units	Scheme I	Scheme II	Scheme III
c_2	μm^{-2}	0.302(8)	-1.49(4)	-0.32(1)
c_4	μm^{-2}	-0.080(8)	-0.41(3)	-0.26(1)
c_6	μm^{-2}	0.070(6)	1.55(4)	0.072(8)
c_0	μm^{-2}	-0.009(3)	0.02(2)	0.005(4)
θ_2	rad	1.594(2)	-0.497(2)	0.274(2)
θ_4	rad	1.537(6)	-0.608(6)	0.206(2)
θ_6	rad	1.455(6)	-0.547(1)	0.008(7)
ϕ_2	rad	0.96(3)	5.96(3)	4.93(3)
$\phi_{4,1}$	rad	4.4(2)	6.2(1)	-1.72(5)
$\phi_{4,2}$	rad	5.6(1)	2.5(1)	3.84(4)
$\phi_{6,1}$	rad	1.2(1)	3.43(4)	2.6(2)
$\phi_{6,2}$	rad	2.7(1)	5.64(3)	3.8(2)

Table 4.1: Optimal fitting parameters for symmetry decomposition

.

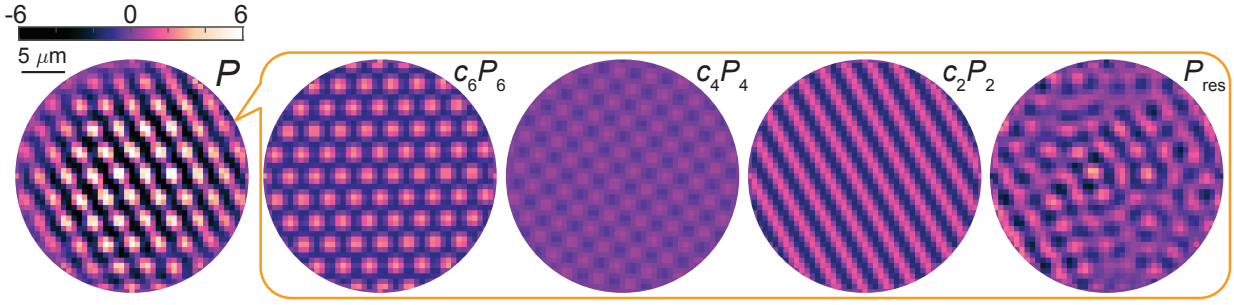

Figure 4.5: **Symmetry decomposition of the recognized D_6 density pattern under Scheme II.** The pattern $P = c_6P_6+c_4P_4+c_2P_2+P_{res}$ is projected onto the bases P_6, P_4 and P_2 with weights c_6, c_4 and c_2. The residual P_{res} is dominated by the spatial inhomogeneity of the sample.

4.4.3 Coherent properties of D_4 and D_6 density waves

The clear difference between the strength of the D_4 and D_6 patterns comes from the coherence of the underlying scattering processes. For D_4 patterns, phase coherence only exists between counter-propagating modes. The orthogonal modes are generated from independent scattering processes and are phase independent, illustrated in Fig. 4.6**a**. We evaluate the two-point phase correlation function of the density waves as $g^{(1)}(\theta) \equiv \langle A_\varphi A_{\varphi+\theta}\rangle / \langle |A_\varphi|^2\rangle$,

where $A_\theta = |A_\theta| e^{i\phi_\theta}$ is the Fourier amplitude of the mode with wavenumber k_f at angle θ and ϕ_θ is its phase. The result, see Fig. 4.6**b**, shows a single peak at $\theta = \pi$, simply due to the realness of density. The absence of other features, particularly at $\theta = \pi/2$, shows that the density waves in orthogonal directions are incoherent. Close inspection of the phases of orthogonal modes, see inset of Fig. 4.6**b**, confirms the absence of correlation.

The D_6 pattern, on the other hand, displays a novel phase coherence in triplets of modes angularly spaced by $2\pi/3$, see Fig. 4.6**c**. Here we evaluate the three-point phase correlation function as

$$g^{(3/2)}(\theta, \theta') \equiv \frac{\langle A_\varphi A_{\varphi+\theta} A_{\varphi+\theta'} \rangle}{\sqrt{\langle |A_\varphi|^2 \rangle \langle |A_{\varphi+\theta}|^2 \rangle \langle |A_{\varphi+\theta'}|^2 \rangle}}. \tag{4.15}$$

The correlation shows two peaks at $(\theta, \theta') = (2\pi/3, 4\pi/3)$ and $(4\pi/3, 2\pi/3)$ (see Fig. 4.6**d**), where θ and θ' are the relative angles between the three modes. This indicates phase coherence of any three modes angularly separated by $2\pi/3$. From repeated measurements, we find that the phases of the triplets are statistically constrained to $\phi_0 + \phi_{2\pi/3} + \phi_{4\pi/3} = 0$ modulo 2π with a small standard deviation of $\delta\phi = 1.1$, see Fig. 4.6**e** and **f**. The phase differences, e.g. $\phi_0 - \phi_{2\pi/3} - \phi_{4\pi/3}$, as well as other permutations, are uniformly distributed and thus uncorrelated.

The three-point phase correlation is an essential element to understanding the growth and the origin of D_6 patterns in our system. Based on Eq. 4.2, we show that the strength of the D_6 pattern satisfies the equation of motion (see Sec. 4.4.4)

$$\frac{dA_{rms}}{dt} = \gamma_1 A_{rms} + \gamma_2 g^{(3/2)} A_{rms}^2, \tag{4.16}$$

where A_{rms} is the root-mean-square of the six Fourier amplitudes that constitute the D_6 pattern and $g^{(3/2)} \equiv g^{(3/2)}(2\pi/3, 4\pi/3)$. A positive $g^{(3/2)}$ suggests that beyond small amplitudes, the nonlinear wave mixing term dominates and leads to a faster-than-exponential

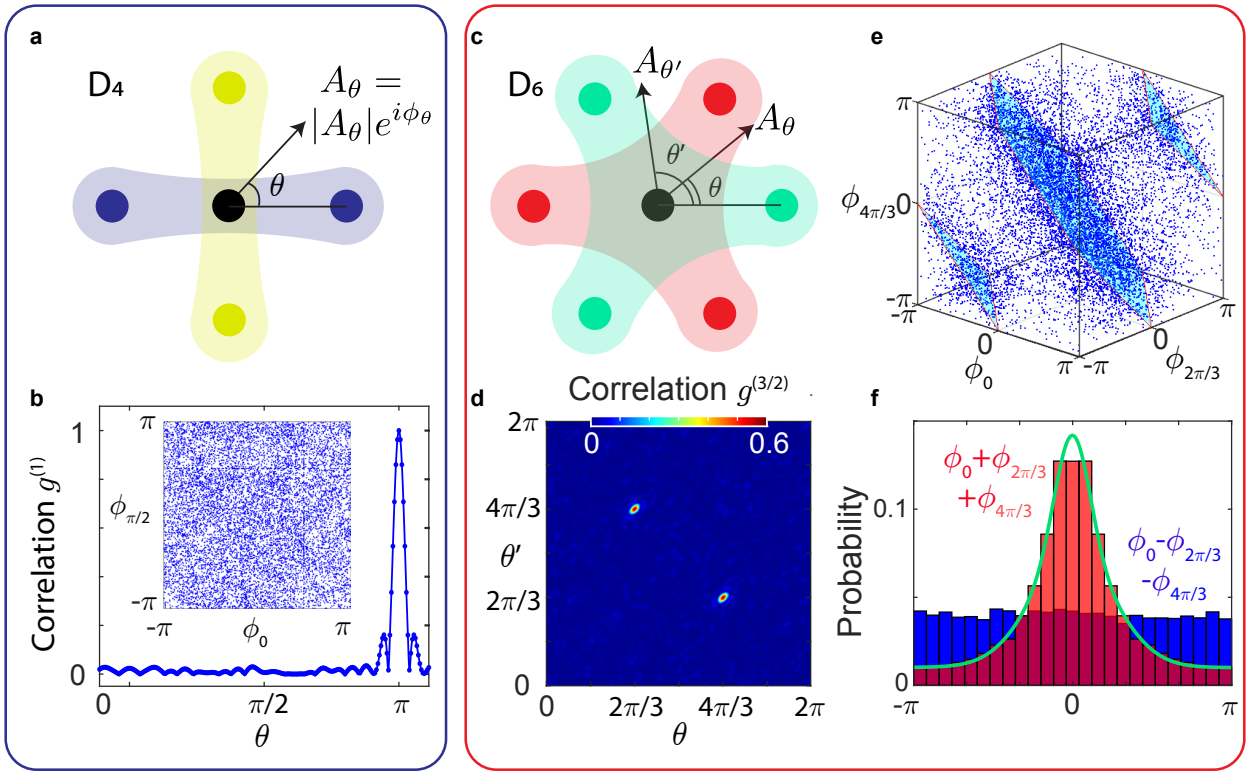

Figure 4.6: **Coherent properties of D_4 and D_6 density waves. a**, Pairs of modes with opposite momenta (blue and yellow) are phase correlated in the D_4 density wave pattern. **b**, Phase correlation function $g^{(1)}$ between Fourier components of the density wave is evaluated based on 123 images obtained with Scheme III. Strong correlations appear between modes moving in opposite directions $\theta = \pi$, but not perpendicular modes $\theta = \pi/2$. The inset is the histogram of the phase of perpendicular modes $\pi/2$, which shows no discernable correlation. **c**, Three-point phase coherence appears in triplet modes (green and red) of the D_6 density wave pattern. **d**, Phase correlation function $g^{(3/2)}$ of three Fourier amplitudes separated by angles θ and θ', evaluated based on 185 images with Scheme III, shows two peaks at $(\theta = 2\pi/3, \theta' = 4\pi/3)$ and $(4\pi/3, 2\pi/3)$, supporting phase correlations of the triplets. **e**, Phases of three modes separated by $2\pi/3$ and $4\pi/3$ show higher probability near the planes $\phi_0 + \phi_{2\pi/3} + \phi_{4\pi/3} = 0, \pm 2\pi$ (blue planes). **f**, The probability distribution (red) of the phase $\phi_0 + \phi_{2\pi/3} + \phi_{4\pi/3}$ weighted by the atom number of the triplet modes displays a peak at 0 (red bars). An Alternative combination of the phases, $\phi_0 - \phi_{2\pi/3} - \phi_{4\pi/3}$, is evenly distributed (blue bars). The green curve is from the numerical calculation.

(hyperbolic) growth of the D_6 density waves. The large measured value of $g^{(3/2)} = 0.58$ explains the strong D_6 pattern that we observe.

How does the three-point phase correlation emerge in a driven condensate? Starting from a condensate seeded by the single-frequency modulation, we see that $g^{(3/2)}$ increases quickly from zero after the two-frequency modulation starts (see Sec. 4.4.4). Theoretically the growth of the correlation is linked to the resonant nonlinear coupling of excitation modes that respect the symmetry and is described by $dg^{(3/2)}/dt = 3\gamma_2 A_{rms}$ for small amplitudes $A_{rms} << N_0^{1/2}$. Our measurement is in good agreement with the theory. Given the above, the three-point phase relation $\phi_0 + \phi_{2\pi/3} + \phi_{4\pi/3} = 0$ (see Fig. 4.6**f**) can be understood as the phase matching condition that maximizes the correlator $g^{(3/2)}$, which explains the dominance of the D_6 pattern in our experiment.

Our experiments thus provide insights into the origin of pattern formation from the coherent mixing of excitations in a homogeneous system. The pattern formation represents a new form of quantum dynamics in which spatial symmetries are determined by the temporal modulation. Moreover, the excitation modes associated with the patterns are phase correlated in a unique way and the modes are expected to be entangled. These patterns can thus serve as resource of multi-mode entanglement for applications in quantum control and quantum information processing.

Phases and amplitudes of density waves

In order to precisely determine the spatial phase of the density waves at different directions, we develop the following fitting procedure. Since the length scale of the density wave we care about is only around k_f, we first filter out the strong low frequency noise below $0.75k_f$ in the Fourier transform of *in situ* density profile $n(x, y)$ and inversely transform it back to obtain the filtered atomic density $\tilde{n}(x, y)$ as shown in Fig. 4.7**a**. $\tilde{n}(x, y)$ is the superposition of plane waves at different directions confined in a finite sized BEC, thus the precision of

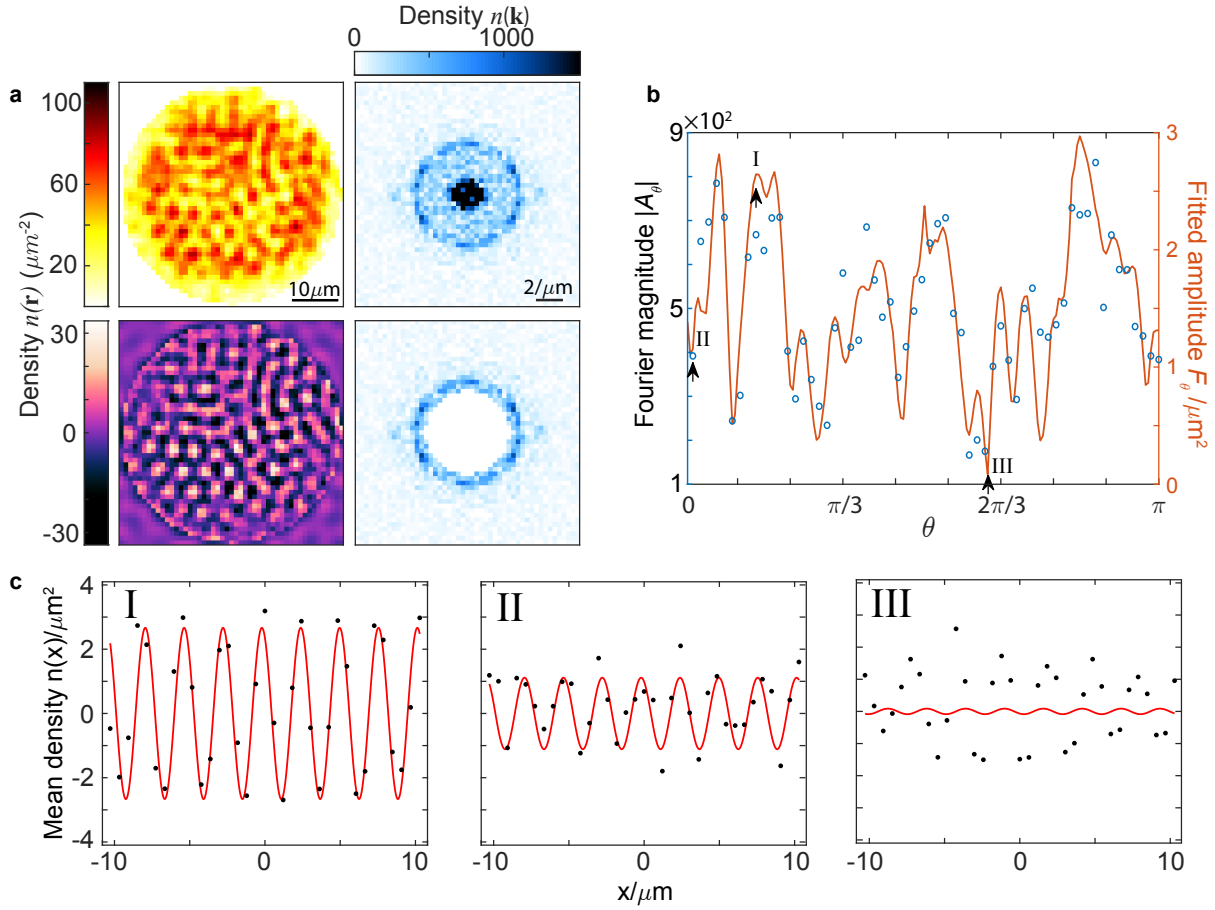

Figure 4.7: **Extraction of the phases and amplitudes of density waves at different directions.** **a**, The low frequency part at k $< 0.75k_f$ of the raw *in situ* atomic density and its Fourier transform (upper row) is filtered and the density fluctuations at k $\geq 0.75k_f$ and its Fourier transform are obtained (lower row). **b**, The angular distribution of the Fourier transform magnitude of original atomic density before the filtering (blue open circles) and the corresponding amplitude from fitting the 1D mean density fluctuation $n_\theta(x)$ of the filtered atomic density (orange solid line). The scale of the left and right y axis differ by a factor of 331, which is one half of the area where density waves exist in unit of μm^2. **c**, Three examples of fitting the 1D mean density fluctuation $n_\theta(x)$ at different directions with various Fourier magnitudes (indicated by arrows in **b**.)

extracting the phase from its Fourier transform is limited by the small number of density wave periods. In order to avoid this limitation, we first integrate the filtered atomic density along a certain direction θ normalized by the corresponding integrated circular BEC area to get the averaged 1D density oscillation $n_\theta(x) = \int dyn(x,y)/\sqrt{R^2 - x^2}$. Then the central

part $|x| \leq 10\ \mu m$ of $n_\theta(x)$ is fitted using fit function $f(x) = F_\theta \cos(k_f x + \phi_\theta)$, where F_θ and ϕ_θ are the amplitude and phase of the density wave at k_f and angle θ. Here the step size of angle θ is chosen to be 1° for better resolution compared to the Fourier transform. The amplitude F_θ and phase ϕ_θ are unaffected by density waves in other directions, which only contribute noise at spatial frequency smaller than k_f or are completely integrated out.

Figure 4.7**b** shows the angular distribution of density wave amplitudes from Fourier transform compared with that from fitting. It can be seen that the results obtained from these two methods are consistent with each other. At the angles indicated by the black arrows in Fig. 4.7**b**, three examples of the fitting results are shown in Fig. 4.7**c**. The density oscillation is fit very well when its Fourier amplitude is significant.

4.4.4 Hyperbolic growth and evolution of the phase relation of excited modes in resonant nonlinear wave mixing

Hyperbolic growth of D_6 pattern

As will be shown in Fig. 4.6, for D_6 pattern, only the Fourier modes separated by $2\pi/3$ are coupled together. Since each Fourier mode $A_\theta = \sqrt{N_0}(\hat{a}_{\rm k} e^{-i\omega t} + \hat{a}^\dagger_{-\rm k} e^{i\omega t})$ consists of two opposite momentum modes, six momentum modes separated by $\pi/3$ are coupled together. Let's first consider a simple model where there are only six modes $\hat{a}_i,\ i = 1, 2, \cdots, 6$, separated by $\pi/3$ with momentum $|\mathbf{k}_i| = k_f$. Under driving Scheme II, the equation of motion reads,

$$\frac{d\hat{a}_i}{dt} = \gamma_1 \hat{a}^\dagger_{i+3} + \gamma_2(\hat{a}^\dagger_{i+2}\hat{a}_{i+1} + \hat{a}^\dagger_{i-2}\hat{a}_{i-1}) - \gamma_2^* \hat{a}_{i+1}\hat{a}_{i-1}, \tag{4.17}$$

where the addition of indices is modulo 6, e.g. $4 + 3 = 1$.

Here we consider the case where the relative phase $\phi = 0$ between the two frequency components and thus γ_2 becomes real. After the first 10 cycles of single frequency modula-

tion, the population of each mode is amplified to be larger than the quantum fluctuation. Thus we approximate the operators $\hat{a}_i$ by complex numbers $\tilde{a}_i$. The equation of motion of amplitude for each mode becomes,

$$\frac{d\tilde{a}_i}{dt} = \gamma_1 \tilde{a}^*_{i+3} + \gamma_2(\tilde{a}^*_{i+2}\tilde{a}_{i+1} + \tilde{a}^*_{i-2}\tilde{a}_{i-1} - \tilde{a}_{i+1}\tilde{a}_{i-1}). \tag{4.18}$$

At the beginning of the two-frequency modulation, we set the population of each mode $n_i(0) = |\tilde{a}_i(0)|^2$ to satisfy a thermal distribution $p(n) = e^{-n/\bar{n}}/\bar{n}$ with the mean population $\bar{n}$ and $\tilde{a}_i(0) = \tilde{a}^*_{i+3}(0)$ with its phase randomly distributed from 0 to 2π [70]. Because the growth rates γ_1 and γ_2 are real, at any later time t, we always have

$$\tilde{a}_i = \tilde{a}^*_{i+3}. \tag{4.19}$$

Then the Fourier amplitude $A_{\theta_i} = \sqrt{N_0}(\tilde{a}_i e^{-i\omega t} + \tilde{a}^*_{i+3} e^{i\omega t}) = 2\sqrt{N_0}\tilde{a}_i \cos\omega t$ and Eq. 4.18 reduces to

$$\frac{d\tilde{a}_i}{dt} = \gamma_1 \tilde{a}_i + \gamma_2 \tilde{a}_{i+1}\tilde{a}_{i-1}. \tag{4.20}$$

Multiplying $\tilde{a}^*_i$ on both sides of Eq. 4.20 and summing their complex conjugates, we get

$$\frac{d|\tilde{a}_i|^2}{dt} = 2\gamma_1|\tilde{a}_i|^2 + 2\gamma_2 \Re[\tilde{a}^*_i \tilde{a}_{i+1}\tilde{a}_{i-1}], \tag{4.21}$$

where $\Re[\cdot]$ means taking the real part. Similarly,

$$\frac{d|\tilde{a}_{i-1}|^2}{dt} = 2\gamma_1|\tilde{a}_{i-1}|^2 + 2\gamma_2\Re[\tilde{a}^*_{i-1}\tilde{a}_i\tilde{a}_{i-2}], \tag{4.22}$$

$$\frac{d|\tilde{a}_{i+1}|^2}{dt} = 2\gamma_1|\tilde{a}_{i+1}|^2 + 2\gamma_2\Re[\tilde{a}^*_{i+1}\tilde{a}_{i+2}\tilde{a}_i]. \tag{4.23}$$

Using Eq. 4.19, it can be seen,

$$\begin{aligned}\Re[\tilde{a}^*_i\tilde{a}_{i+1}\tilde{a}_{i-1}] = \Re[\tilde{a}_{i+3}\tilde{a}_{i+1}\tilde{a}_{i-1}]\\ =\Re[\tilde{a}^*_{i-1}\tilde{a}_i\tilde{a}_{i-2}] = \Re[\tilde{a}^*_{i+1}\tilde{a}_{i+2}\tilde{a}_i].\end{aligned} \tag{4.24}$$

Thus by subtracting two of the equations out of Eqs. (4.21) to (4.23) and taking the average value on both sides of the equations, we have

$$\frac{dn_{i,i-1}}{dt} = 2\gamma_1 n_{i,i-1}, \tag{4.25}$$

where the population difference $n_{i,i-1} = \langle|\tilde{a}_i|^2\rangle - \langle|\tilde{a}_{i-1}|^2\rangle$. $n_{i,i+1}$ and $n_{i-1,i+1}$ also satisfy Eq. 4.25. Since at the beginning $|\tilde{a}_i|^2$, $|\tilde{a}_{i-1}|^2$ and $|\tilde{a}_{i+1}|^2$ satisfy the same distribution $p(n)$, they have equal average values $\langle|\tilde{a}_i(0)|^2\rangle = \langle|\tilde{a}_{i-1}(0)|^2\rangle = \langle|\tilde{a}_{i+1}(0)|^2\rangle$, which means the population differences $n_{i,i-1}(0) = n_{i,i+1}(0) = n_{i-1,i+1}(0) = 0$. Thus according to Eq. 4.25, at any later time t, the population differences $n_{i,i-1} = n_{i,i+1} = n_{i-1,i+1} = 0$, i.e.

$$\langle|\tilde{a}_i|^2\rangle = \langle|\tilde{a}_{i-1}|^2\rangle = \langle|\tilde{a}_{i+1}|^2\rangle. \tag{4.26}$$

As is defined in Eq. 4.15 of Sec. 4.4.3, the three point correlation function at $(\theta, \theta') =$

$(2\pi/3, 4\pi/3)$ is,

$$g^{(3/2)} \equiv g^{(3/2)}(\frac{2\pi}{3}, \frac{4\pi}{3}) = \frac{\langle A_\varphi A_{\varphi+2\pi/3} A_{\varphi+4\pi/3}\rangle}{\sqrt{\langle|A_\varphi|^2\rangle\langle|A_{\varphi+2\pi/3}|^2\rangle\langle|A_{\varphi+4\pi/3}|^2\rangle}} = \frac{\Re[\langle\tilde{a}_{i+3}\tilde{a}_{i+1}\tilde{a}_{i-1}\rangle]}{\sqrt{\langle|\tilde{a}_{i+3}|^2\rangle\langle|\tilde{a}_{i+1}|^2\rangle\langle|\tilde{a}_{i-1}|^2\rangle}}. \tag{4.27}$$

Since the average of the product $A_\varphi A_{\varphi+\theta} A_{\varphi+\theta'}$ is performed over all the angles with $0 \leq \varphi \leq 2\pi$, it always comes in pair with its complex conjugate, which guarantees that the three point phase correlation function is real. Also, the other possible definitions with one or more of the Fourier amplitudes in $A_\varphi A_{\varphi+\theta} A_{\varphi+\theta'}$ are equivalent to Eq. 4.15 with angular shifts in θ and θ', which doesn't show more information. Then we take the average value on both sides of Eq. 4.21 and plug in Eqs. (4.19), (4.26) and (4.27) to get

$$\frac{d\langle|\tilde{a}_i|^2\rangle}{dt} = 2\gamma_1\langle|\tilde{a}_i|^2\rangle + 2\gamma_2 g^{(3/2)}\langle|\tilde{a}_i|^2\rangle^{\frac{3}{2}}. \tag{4.28}$$

Let's define the root mean square (RMS) of $\tilde{a}_i$ as $A_{rms} = \sqrt{\langle|\tilde{a}_i|^2\rangle}$ and plug it into Eq. 4.28, we finally arrive at the equation of motion,

$$\frac{dA_{rms}}{dt} = \gamma_1 A_{rms} + \gamma_2 g^{(3/2)} A_{rms}^2. \tag{4.29}$$

Insert the initial value $A_{rms}(0)$, we obtain the solution of Eq. 4.29,

$$A_{rms}(t) = \frac{e^{\gamma_1 t}}{1/A_{rms}(0) - \gamma_2 \int_0^t g^{(3/2)}(t') e^{\gamma_1 t'} dt'}. \tag{4.30}$$

This solution exhibits hyperbolic growth that hits a finite time singularity at t_c which satisfies,

$$\int_0^{t_c} g^{(3/2)}(t')e^{\gamma_1 t'}dt' = \frac{1}{\gamma_2 A_{rms}(0)}. \tag{4.31}$$

As long as $g^{(3/2)}(t)$ decays slower than $e^{-\gamma_1 t}$, a finite time singularity exists.

However, in our experiment, if we look at the mean population n_m of the modes at all directions and images, it doesn't show clear deviation from simple exponential growth. Thus we choose the observable as the mean population $n_s = (n_{\pi/3} + n_{-\pi/3})/2$ at $\pm\pi/3$ relative to the strongest mode in each image. Because the nonlinear coupling between these three adjacent modes, n_s grows faster than n_m and can deviate from exponential growth. If only modulation of single frequency ω_1 is applied, $n_s = n_m$, because they are independent and share the same statistics.

Let's say we always choose $\tilde{a}_i$ as the strongest mode among all sets of coupled six modes, which have larger fluctuation to begin with. The other two modes $\tilde{a}_{i-1}$ and $\tilde{a}_{i+1}$ at $\pm\pi/3$ relative to it begin with the same mean population as all the other modes with $\langle|\tilde{a}_{i+1}|^2\rangle = \langle|\tilde{a}_{i-1}|^2\rangle$. We model the effect of the strongest sets of modes as an enhancement of γ_2 by a factor of α. Thus the solution of n_s is,

$$n_s^{1/2} = \frac{e^{\gamma_1 t}}{1/A_{rms}(0) - \alpha\gamma_2 \int_0^t g^{(3/2)}(t')e^{\gamma_1 t'}dt'}. \tag{4.32}$$

Because the nonlinear term is relatively weak for mean population n_m of all modes, it grows approximately exponentially as

$$n_m = A_{rms}^2(t) \approx A_{rms}^2(0)e^{2\gamma_1 t}. \tag{4.33}$$

Then n_s as a function of the mean population n_m of all modes is

$$n_s = \frac{n_m}{\left(1 - \frac{1}{2}\alpha\epsilon \int_{n_m(0)}^{n_m(t)} g^{(3/2)}(n'_m)/\sqrt{n'_m} dn'_m\right)^2}, \tag{4.34}$$

where $\epsilon = \gamma_2/\gamma_1$ is the ratio of the two rate constants.

In order to know how n_s grows as a function of n_m, we need to determine the evolution of the three point correlation $g^{(3/2)}$ as a function of n_m. Combining Eqs. (4.20), (4.21), (4.26) and (4.27), we have

$$\frac{dg^{(3/2)}}{dt} = 3\gamma_2 A_{rms}[g^{(2)} - (g^{(3/2)})^2], \tag{4.35}$$

where $g^{(2)}$ is the two point correlation function at $\theta = \pi/3$, i.e., $g^{(2)} = \langle |A_\varphi|^2 |A_{\varphi+\pi/3}|^2 \rangle$ $/\langle |A_\varphi|^2 \rangle^2 = (\langle |\tilde{a}_{i+1}|^2 |\tilde{a}_i|^2 \rangle + \langle |\tilde{a}_i|^2 |\tilde{a}_{i-1}|^2 \rangle + \langle |\tilde{a}_{i+1}|^2 |\tilde{a}_{i-1}|^2 \rangle)/3\langle |\tilde{a}_i|^2 \rangle^2$. In the perturbation regime where the population of modes in directions separated by $\pi/3$ are almost uncorrelated, i.e. $g^{(2)} \approx 1$, the three point phase correlation is given by

$$g^{(3/2)} = 1 - \frac{2}{1 + \exp[6\epsilon(\sqrt{n_m} - A_{rms}(0))]}. \tag{4.36}$$

Inserting the above result into Eq. 4.34, we arrive at

$$n_s = n_m[1 - \alpha\epsilon(A_{rms}(0) - \sqrt{n_m}) + \frac{\alpha}{3}\ln(1 - g^{(3/2)})]^{-2}. \tag{4.37}$$

Since our model only considered 6 excited modes, here the mean population n_m of a single

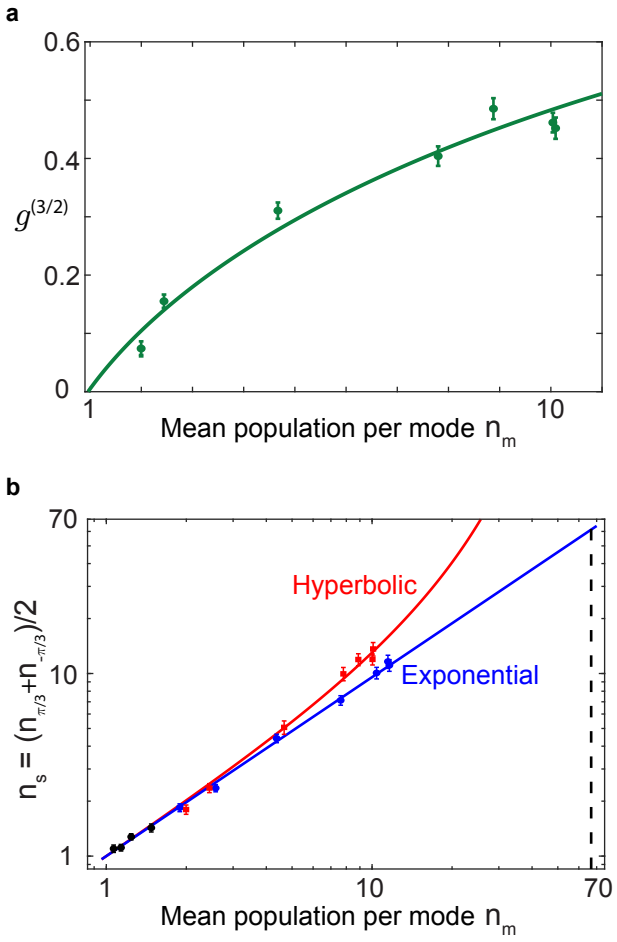

Figure 4.8: **The evolution of three point correlation $g^{(3/2)}$ and the mean population at $\pm\pi/3$ relative to the strongest modes during the D_6 pattern formation process.** **a**, The growth of three point correlation $g^{(3/2)}$ as a function of mean population n_m of modes at all directions in all images. Solid line is the theory curve from fitting using Eq. 4.36. **b**, The growth of mean population n_s of modes at $\pm\pi/3$ relative to the strongest modes versus the mean population per mode n_m under scattering length modulation Scheme II (red squares) compared with that under Scheme I (blue circles). Both the x and y axis are in log scale. The red and blue solid lines are theory curves from fitting. The vertical dashed line is the theory prediction of when the population n_s diverges during D_6 pattern formation.

mode is 1/6 of the total mean population. In our experiment, the total number of excited modes at $|\mathbf{k}| = k_f$ is $N_{mod} = 1.62/Rk_f \approx 136$ [35]. In order to generalize Eq. 4.36 and Eq. 4.37 for multiple sets of 6 modes with $\pi/3$ angular spacing, we need to do the replacements: $n_m \to \frac{N_{mod}}{6} n_m$, $A_{rms}(0) \to \sqrt{\frac{N_{mod}}{6}} A_{rms}(0)$ and $n_s \to \frac{N_{mod}}{6} n_s$. This is equivalent

to replace ϵ by $\sqrt{\frac{N_{mod}}{6}}\epsilon = \sqrt{\frac{N_{mod}}{6}}\frac{\gamma_2}{\gamma_1}$.

Using Eq. 4.36 to fit the data with ϵ and $A_{rms}(0)$ as fitting parameters as shown in Fig. 4.8**a**, we get $\epsilon = 0.08$ and $A_{rms}(0) = 0.98$. Thus $\gamma_2/\gamma_1 = 0.01$, which is close to the experimental value 0.003. The discrepancy is attributed to the exclusion of other collision processes that are also involved in the experiment, such as the pair generation from BEC at $|\mathbf{k}| = k_f/\sqrt{2}$ and secondary collision processes that lead to D_4 pattern. Then we use the value of ϵ and $A_{rms}(0)$ from fitting the three point correlation function $g^{(3/2)}$ and set α as another fitting parameter to fit n_s versus n_m as shown by the red solid line in Fig. 4.8**b**, which gives $\alpha = 2.78$. On the other hand, for single frequency modulation under Scheme I, we use the fit function $y = ax$ and the best fit is obtained with $a = 0.98$ as shown by the blue solid line in Fig. 4.8**b**, which is consistent with our expectation for the case without nonlinear wave mixing.

Evolution of the phase relation of modes forming D_6 density wave pattern

In order to study how the phase relation of modes that form hexagonal lattices evolve from completely uncorrelated to concentrated around the plane $\phi_0+\phi_{2\pi/3}+\phi_{4\pi/3} = 0$, we perform numerical calculation based on Eq. 4.18. Here we consider BEC with depletion, which couple to multiple sets of 6 modes with $\pi/3$ angular spacing at the same time. The corresponding equations of motion are:

$$\frac{d\tilde{a}_i}{dt} = [\gamma_1' N_0(t) - \gamma_e]\tilde{a}_{i+3}^\dagger + \gamma_2'\sqrt{N_0(t)}(\tilde{a}_{i+2}^\dagger\tilde{a}_{i+1} + \tilde{a}_{i-2}^\dagger\tilde{a}_{i-1} - \tilde{a}_{i+1}\tilde{a}_{i-1}) \tag{4.38}$$

$$N_0(t) = N_0 - \sum_{i=1}^{N_{mod}} |\tilde{a}_i|^2, \tag{4.39}$$

where the growth rates $\gamma_1' = \gamma_1/N_0$ and $\gamma_2' = \gamma_2/\sqrt{N_0}$. The decay rate due to modes flying out of the condensate is $\gamma_e \sim v/R$, where the velocity of the modes $v = \hbar k_f/m$ and R is the

radius of the condensate.

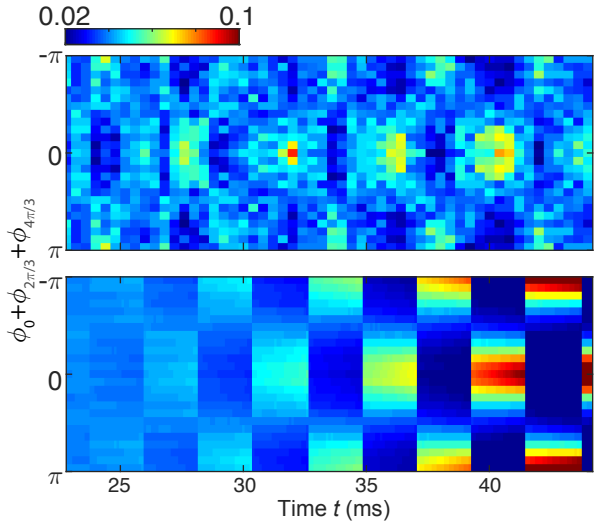

Figure 4.9: **Evolution of the phase distribution of $\phi_0 + \phi_{2\pi/3} + \phi_{4\pi/3}$ during D_6 density wave pattern formation process.** The upper panel is from the experiment under Scheme II where we perform *in situ* imaging of the condensate at different times. The peak position of the phase distribution oscillates between 0 and π and gets more concentrated as time evolves. The lower panel is from the numerical calculation with the modulation amplitudes $a_1 = 22.5\ a_0$ and $a_2 = 63.5\ a_0$ for frequency components of 450 Hz and 225 Hz, respectively. The escaping rate of momentum modes is 39 Hz. Other parameters are the same as the experiment.

The simulation starts from the beginning of the second pattern forming stage. At the end of the first seeding stage, the population n in each mode $\tilde{a}_i$ is thermally distributed according to the probability distribution $p(n) = e^{-n/\bar{n}}/\bar{n}$ with the mean population $\bar{n} = 2$. The phase of each mode $\tilde{a}_i$ is uniformly distributed from 0 to 2π and the modes in opposite directions are correlated as $\tilde{a}_i = \tilde{a}^*_{i+3}$. The simulation is repeated for 5000 times and each time the initial conditions of the phase and amplitude are independently sampled from their distributions. We finally take the phase of $\tilde{a}_i e^{-i\omega t} + \tilde{a}^*_{i+3} e^{i\omega t}$ as the phase of Fourier modes in the lab frame. The amplitude of scattering length modulation a_1 and a_2 and the escape rate γ_e are chosen as fitting parameters while all the other parameters are the same as our experiment for Scheme II. The green line in Fig. 4.6**f** is the result after 22.4 ms evolution time, using the initial condition of mean population at 22.6 ms in our experiment. The

corresponding amplitudes of modulation are $a_1 = 24\ a_0$, $a_2 = 68.5\ a_0$ and $\gamma_e = 39$ Hz. The evolution of the phase distribution of $\phi_0 + \phi_{2\pi/3} + \phi_{4\pi/3}$ within individual Floquet periods is also calculated as shown in the lower panel of Fig. 4.9, which is consistent with the experimental result in the upper panel. The peak position ϕ_{peak} of the phase distribution oscillates between 0 and π, due to the standing wave nature of the density waves. This also means the real space pattern changes back and forth between hexagonal lattice ($\phi_{peak} = 0$) and honeycomb lattice ($\phi_{peak} = \pi$). However, in the rotating frame, the phase distribution is always centered at 0, thus the three point correlation $g^{(3/2)}$ is always positve. This ensures the hyperbolic growth since the second term in Eq. 4.29 is positive.

4.5 Discussion

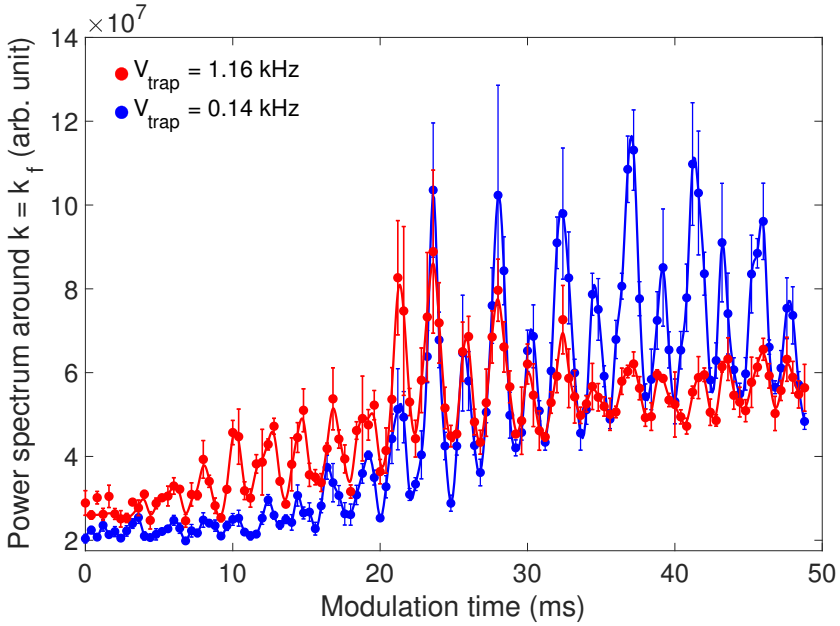

Figure 4.10: **Evolution of density wave amplitude characterized by the sum of power spectrum around $k = k_f$ with shallow (blue) and deep (red) box traps using scheme II as shown in Fig. 4.2a.** The box trap depth is 0.14 kHz for blue data and 1.16 kHz for red data.

We attempted to stabilize the density waves by raising the box trap depth, such that the

excited atoms don't escape out of the BEC. It turns out with a deep trap where the kinetic energy of atoms is much smaller than the potential barrier of the trap, we observe that the density waves are much weaker at later time compared to the case with a shallow trap, see Fig. 4.10. In the beginning of the evolution before density waves reach the boundary of the trap, density wave amplitudes also grows similarly within the deep trap as in the shallow trap. Presumably the reflection of density waves at the boundary of the trap leads to the fast damping of their amplitudes. The underlying mechanism requires further investigation.

CHAPTER 5

TOMOGRAPHY OF BEC WAVE FUNCTIONS USING JET SUBSTRUCTURE IN BOSE FIREWORKS EMISSION

We show that jet emission from a Bose condensate with periodically driven interactions, a.k.a. "Bose fireworks", contains essential information on the condensate wavefunction, which is difficult to obtain using standard detection methods. We illustrate the underlying physics with two examples. When condensates acquire phase patterns from external potentials or from vortices, the jets display novel sub-structure, such as oscillations or spirals, in their correlations. Through a comparison of theory, numerical simulations and experiments, we show how one can quantitatively extract the phase and the helicity of a condensate from the emission pattern. Our work demonstrating the strong link between jet emission and the underlying quantum system, bears on the recent emphasis on jet sub-structure in particle physics [85, 39].

5.1 Introduction

Cold atom systems are emerging as an important platform for quantum simulations in condensed matter [25] and in high energy physics [11]. In this context the application of temporal periodic drive has led to novel phenomena [49, 40] including topological phases [59, 81] and dynamical gauge fields for simulation of high energy physics models [34, 126, 57]. With driven Bose-Einstein condensates (BECs), a new regime of quantum scattering has appeared [35, 33, 104] where periodic variations of the atomic interactions excite pairs of atoms propagating in opposite directions. With sufficiently strong modulations, thin jets of atoms are expelled from the condensate in all directions. This Bose stimulation (Bose fireworks) reveals complex correlations [54, 145, 26, 27], and allows simulation of Unruh radiation [70], and density wave formation [56, 148].

In this chapter we show how this jet emission pattern can enable extraction of the condensate wavefunction. Such studies of jet substructure are reminiscent of current scattering experiments in particle physics performed at both the Large Hadron [85] and the Relativistic Heavy Ion [39] Colliders. It should be pointed out in this regard, that vorticity (a topic of interest here) is an active sub-field in particle physics [3]. Quark-gluon plasmas exhibiting anomalously high vorticity have been reported based on the structure of the particle emission. To illustrate this capability with cold atoms, a set of emission patterns from numerical simulations are shown in Fig. 5.1, which exhibit distinct structures for condensates with different non-uniform phase configurations.

We present two cases of study in our experiment. In the first, we consider condensates split into two halves with different phases. The relative phase emerges in the correlations of counter-propagating jets, and can be understood based on the double-slit interference of matterwaves. In the second case, we study condensates with vortices. Here the emission pattern exhibits a novel spiral sub-structure as seen in Fig. 5.1b. We show that one can directly extract the phase winding number of the vortices from the spirals based on comparison between experimental data and numerical simulations.

Our study shows jet emission as a new tool to probe the phase distribution of a condensate. We take vortex detection as an example. Time of flight [2] or *in-situ* imaging [143] does not reveal the helicity (the phase winding) of the vortex while the interference experiments do reveal the helicity but require preparation of two samples [102, 79, 41]. Our method uses only a single condensate (like Ref. [127]) to reveal the BEC phase distribution from the emitted atoms, and can in principle be implemented with little disturbance of the condensate.

In our simulations, we describe the evolution of the condensates with the Gross-Pitaevskii (GP) equation, including terms that simulate quantum fluctuations [56]. For a uniform BEC, periodic modulation of the interaction strength with frequency ω leads to pair production of

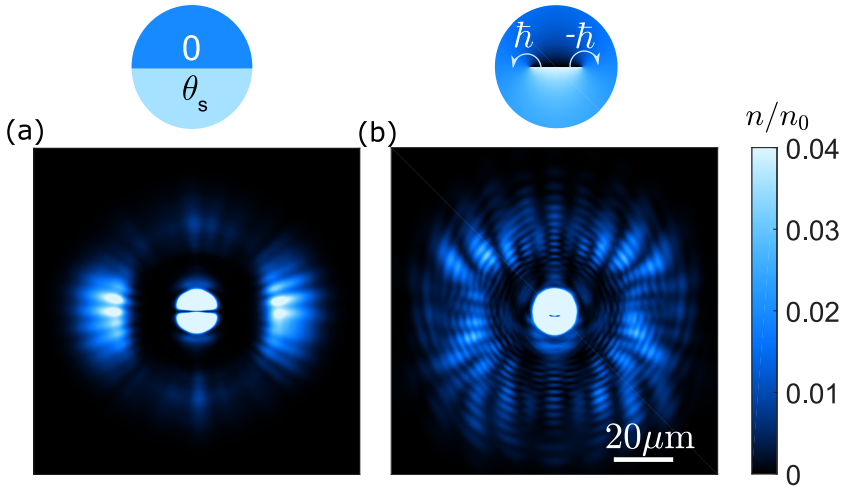

Figure 5.1: **Simulated emission patterns of BECs with interaction modulations. a** Jet emission from condensates with a soliton. The lower half is phase shifted relative to the upper half by $\theta_s = \pi$. **b** Jet emission from condensates with a vortex-antivortex pair, where the reduced Planck constant $\hbar$ corresponds to the angular momentum of the vortex. The atomic density n is normalized to the initial density of the condensate n_0.

matterwave jets with random but opposite momenta $(\hbar\mathbf{k_f}, -\hbar\mathbf{k_f})$, where $k_f = \sqrt{m\omega/\hbar}$ and m is the atomic mass. For non-uniform condensates, jets form in pairs of modes which are determined by the condensate wavefunction and driving frequency. When observed in the plane wave basis, the jets can show intricate correlations. The goal here is to demonstrate what we can learn about the condensate from the strength and correlations of the emitted jets.

5.2 Nonuniform BECs with period interaction modulation

Microscopically, the system under the periodic drive is excited from an initial state ψ_0 to $\psi(t) \equiv \psi_0 + \delta\psi$, where the wavefunction increment $\delta\psi$ can be seeded by quantum fluctuations and amplified by the drive. With short interaction times as in our experiment, the deviation can be treated perturbatively, and the evolution of the system is governed by the Hamiltonian

$$H \approx \sum_i E_i a_i^\dagger a_i + \frac{U(t)}{2} \sum_{i,i'} \left[F(i,i') a_i^\dagger a_{i'}^\dagger + h.c. \right], \tag{5.1}$$

where $U(t) = U_0 + U_1 \sin \omega t$ is the oscillating interaction strength, $\sum_i$ sums over the single particle modes φ_i that are initially unoccupied, the pair function $F(i, i')$ is described below, E_i is the kinetic energy of the $i-$th mode, and a_i and $a_i^\dagger$ are the annihilation and creation operators of the modes. Here we work in the regime where the modulation amplitude is much larger than the offset, and the driving energy is much greater than the energy of the initial state, i.e. $U_0 n_0 \ll U_1 n_0 \ll \hbar\omega$, where n_0 is the average density of the condensate [1].

The pair function $F(i, i')$ in Eq. (1) determines the strength as well as the correlations of the two modes i and i' in the emission. It is given by the overlap of the condensate wave function ψ_0 and the wave functions of the modes φ_i and $\varphi_{i'}$, namely,

$$F(i, i') = \int d\mathbf{r} \varphi_i^*(\mathbf{r}) \varphi_{i'}^*(\mathbf{r}) \psi_0^2(\mathbf{r}). \tag{5.2}$$

This equation shows that, in principle we can determine the square of the condensate wavefunction directly from the pair function F. As an example, if we choose a plane wave basis, $F(\mathbf{k}, \mathbf{k'})$ is the $\mathbf{k}+\mathbf{k'}$ Fourier component of ψ_0^2. When the condensate contains multiple excitations, those with larger amplitudes of $F(\mathbf{k}, \mathbf{k'})$ will lead to stronger emission of the matterwave jets with momenta $\mathbf{k}$ and $\mathbf{k'}$, providing they satisfy momentum conservation. The detailed mathematics needed to extract the pair function F and the experimental scheme to implement it is provided in Sec. 5.2.1. To validate these ideas and offer a physical picture, we study two examples of non-uniform BECs in our experiment. These cases involve BECs with two different phases and with vortices; both of which illustrate the links between the jet substructure and condensate wave functions.

1. In the high frequency limit, additional terms like $U(t) \int dxdy |\psi_0(x, y)|^2 \varphi_i^*(x, y) \varphi_{i'}(x, y)$ is negligible, see Ref. [33].

5.2.1 Extraction of the pair function F using complete correlation functions for general initial BEC wave functions

Here we first show that if one has full knowledge of all the two-operator correlation functions: $\langle a_i a_j \rangle$, $\langle a_i a_j^\dagger \rangle$, $\langle a_i^\dagger a_j \rangle$, $\langle a_i^\dagger a_j^\dagger \rangle$ at a given time t, one can recover the initial wavefunction. Then, we present a proposal for possible experimental measurement of these correlators.

In the interaction picture and dropping the far off-resonant terms, we obtain an effective Hamiltonian as

$$H = \frac{1}{2} \sum_{i,j} P_{ij} a_i a_j + h.c. \tag{5.3}$$

where $P_{ij} \approx U_1 F^*(i,j)/2i$. Assuming we have N bosonic modes $a_1,\ a_2, \ldots, a_N$, we define the vector $A = (a_1, a_1^\dagger, \ldots, a_N, a_N^\dagger)^T = (A_1, A_2, \ldots, A_{2N-1}, A_{2N})^T$. Then any matrix operating on A that has $2N \times 2N$ dimension can be reduced to a tensor product between a $N \times N$ matrix and a 2×2 matrix. From Eq. (5.3), we arrive at

$$i\hbar \frac{dA}{dt} = [A, H] = i(\text{Re } P \otimes \sigma_y - \text{Im } P \otimes \sigma_x)A = iKA \tag{5.4}$$

where Re P and Im P are respectively the real and imaginary parts of the matrix P and σ_i are Pauli matrices. Then, we have $A(t) = e^{Kt/\hbar} A(0)$. If we define the matrix γ as

$$\gamma_{ij} = \langle A_i A_j^\dagger + A_j^\dagger A_i \rangle, \tag{5.5}$$

we then find $\gamma(t) = e^{Kt/\hbar} \gamma(0) e^{Kt/\hbar} = e^{2Kt/\hbar}$ where $\gamma(0)$ can be easily derived to be the identity matrix as we start from vacuum. $\gamma(t)$ here is simply composed of all the two-operator correlation functions at t. Therefore, from the correlation functions, we can extract $\gamma(t)$ and

characterize P as

$$\begin{aligned} K =& \frac{\hbar}{2t} \ln \gamma(t) \\ \text{Re } P =& \frac{1}{2} \text{Tr}_\sigma \left[K \times (I \otimes \sigma_y) \right] \\ \text{Im } P =& -\frac{1}{2} \text{Tr}_\sigma \left[K \times (I \otimes \sigma_x) \right]. \end{aligned} \tag{5.6}$$

where I is the $N \times N$ identity matrix, $\text{Tr}_\sigma[\ldots]$ involves the trace over the 2×2 dimension. Since $F(i, i')$ can be obtained from the P matrix, and the original wavefunction ψ_0 can be derived from $F(i, i')$ according to Eq. (5.2) up to a sign uncertainty, we then can recover the wavefunction, ψ_0.

Our studies of jet emission from condensates associated with split BECs or vortices lay the foundation for a general experimental procedure which we outline below. As previously known [56], the emission can consist of interference of different modes overlapping at a spot $\mathbf{r}$:

$$n(\mathbf{r}) = \frac{1}{V_N} a_{\mathbf{r}}^\dagger a_{\mathbf{r}}, \quad a_{\mathbf{r}} = \sum_{\mathbf{k}} a_{\mathbf{k}} e^{i\mathbf{k}\cdot\mathbf{r}}, \tag{5.7}$$

where $n(\mathbf{r})$ is the local density that is experimentally measurable, V_N is the normalization constant. In the near field, the interference term in the density, $\propto {a_{\mathbf{k}}}^\dagger a_{\mathbf{k}'} \exp\left[i \left(\mathbf{k}' - \mathbf{k} \right) \cdot \mathbf{r} \right] + h.c.$, contains information on the relative phases between $a_{\mathbf{k}}$ and $a_{\mathbf{k}'}$. In the far field where jets do not overlap anymore, we can directly measure the occupation of each jet $a_{\mathbf{k}}^\dagger a_{\mathbf{k}}$ through $n(\mathbf{r})$. With all the information, we in principle can obtain the full knowledge of the two-operator correlators by averaging over many shots. In the limit where there is large occupation in each mode, we can regard the operator $a_{\mathbf{k}}$ as a classical complex number and obtain all the correlators mentioned above based on $a_{\mathbf{k}}^\dagger a_{\mathbf{k}'}$ and $a_{\mathbf{k}}^\dagger a_{\mathbf{k}}$. The structure and angular width of modes can be determined from the condensate size and the modulation frequency [35].

To implement this scheme experimentally, one should perform analysis for both the near- and far-field emission to determine the phase and density correlations of all pairs of modes i and j. There are two major challenges. First, the accuracy of the extracted correlators

would be primarily limited by statistics and signal to noise ratio. Sufficient repetitions are needed to suppress uncertainties due to relative phase fluctuations. Second, higher spatial resolution of the emission pattern is needed in order to extract correlations of more distant modes.

5.3 Experimental setup

We start with 3D BECs of 60,000 cesium atoms loaded into an elliptical crossed dipole trap. For the experiments where the initial state is a split BEC with two phases, 40,000 atoms are adiabatically transferred within 760 ms into a disk-shaped dipole trap with a diameter of 18 μm in the horizontal direction and a 6-μm wide central barrier along the diameter that splits the BEC into two halves. There is no central barrier applied for the other case where we start from a BEC with vortices, which arise non-deterministically from the finite cooling time in transition to condensation [32, 109, 17] with about 5% probability in our experiment. The potential barriers are provided by a blue-detuned laser at 788 nm. The laser beam profile is shaped by a digital micromirror device (DMD) and projected to the atom plane through a high-resolution objective (of 1 micron resolution). The resulting circular potential well and the central barrier have barrier height of $h \times 140$ Hz and $h \times 42$ Hz, respectively. Atoms are tightly confined in the vertical direction with a $1/e^2$ radius of 0.8 μm and a harmonic trap frequency of 259 Hz. The phase coherence of the two half BECs is maintained, which is revealed by the interference fringes formed during time-of-flight.

Then we use a DMD to project a 788 nm light pulse of duration $\tau = 0.4$ ms on one half of the BEC to induce a relative phase shift. The imprinted phase $\theta_s = -V_s\tau/\hbar$ is tuned by changing the light pulse intensity that determines the light shift V_s. The potential gradient in the imprinting process applies force to the imprinted half. Atoms emitted from the transition regime where the phase jumps gain an additional small velocity. This, to the leading order, has no influence on the magnitude of the jet momenta but bends their

direction. Therefore in the π-peak of the connected correlation $g^{(2)}_{\rm conn}(\phi)$ shown in Fig. 5.3c, the envelope is shifted while the interference fringes are not offset.

About 1 ms after the phase imprinting, we apply an oscillating magnetic field in the vicinity of a Feshbach resonance to the BECs, which modulates the atomic s-wave scattering length as $a(t) = a_{dc} + a_{ac}\sin(\omega t)$ with a small offset $a_{dc} = 9a_0$ and a large amplitude $a_{ac} = 47a_0$, at frequency $\omega/2\pi = 2.1$ kHz. After modulating the interaction for 34 ms, we perform *in situ* absorption imaging through the same high-resolution objective and a CCD camera to observe the structure of ejected atomic jets. For measuring the connected correlation $g^{(2)}_{\rm conn}(\phi)$, we wait for an additional 10 ms after the 34 ms interaction modulation before performing imaging. We do this because when the jets fly to the far field, the oscillation of the $\pi-$peak in the correlation function becomes more prominent.

In order to measure how much phase is imprinted onto one half of the BECs through the short light pulse, we let the two half BECs expand freely for 30 ms right after the phase imprinting. The two parts of the condensate acquire momentum $\pm k_t$ after being released and form interference fringes when they overlap in space. In this way, the phase shift of the fringes as shown in Fig. 5.2a for different light pulse intensity can reflect the value of θ_s. In Fig. 5.2b, the corresponding mean atomic density distributions along the x direction $n(x) = A(x)[\cos(k_t x + \theta_s) + C]$ are shown (the origin of coordinates is set according to the no-phase-imprinting case where $\theta_s = 0$.). We identify the positions of density peaks and valleys on the left of the highest peak and assign a phase of either even or odd multiple of π as shown in Fig. 5.2c. The data are fit linearly and the change of y-intercept corresponds to the change of imprinted phase. The black curve is when no light pulse is applied and serves as a reference at $\theta_s = 0$. By comparing the y-intercept to it, the orange and purple curves yield the values of θ_s that are near $-\pi/2$ and $-\pi$ as in Fig. 5.3d.

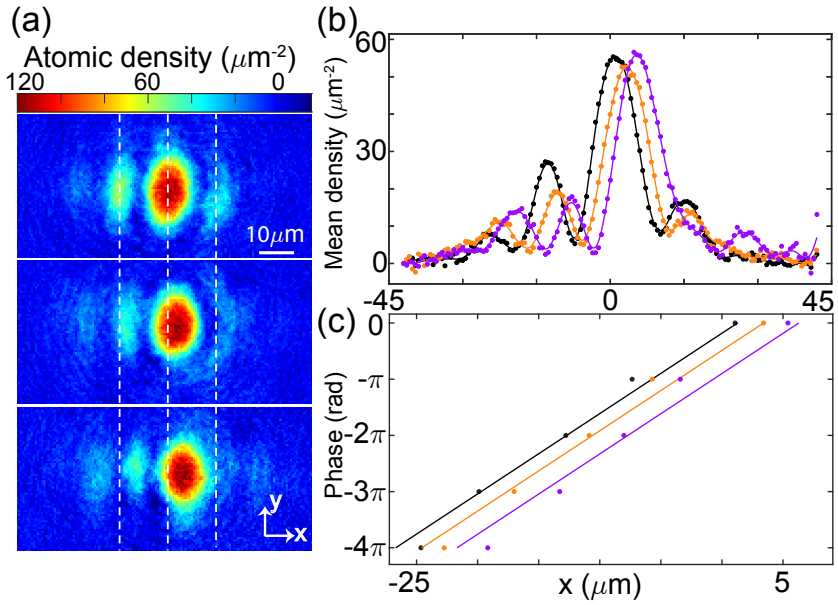

Figure 5.2: **Calibration of the imprinted relative phase between two halves of the BEC through TOF imaging.** **a**, Single-shot 30-ms TOF imaging of the interference fringes for imprinted phase θ_s around 0 (top), $-\pi/2$ (middle) and $-\pi$ (bottom). **b**, Mean atomic density along x direction corresponding to single shot images in **a** for imprinted phase θ_s around 0 (black), -$\pi/2$ (orange) and -π (purple). **c**, Peak and valley positions corresponding to the mean atomic density distributions in **b** with the same color scheme versus their phase. The phases are assigned according to whether they correspond to a peak (even multiples of π) or a valley (odd multiples of π).

5.4 Results

5.4.1 Jet substructure in emissions from Bose condensates split into two halves with and without a relative phase θ_s

A split BEC with two phases is our first, pedagogical example. A soliton-like structure arises where the phase jump occurs, and the condensate density is suppressed at the boundary. The advantage of considering a split BEC is that we are able to disentangle density and phase information which are strongly intertwined in the soliton case. We assume that at time $t = 0$ the phase of the lower half is θ_s and that of the upper half is zero, and the phase slip boundary is along the horizontal direction.

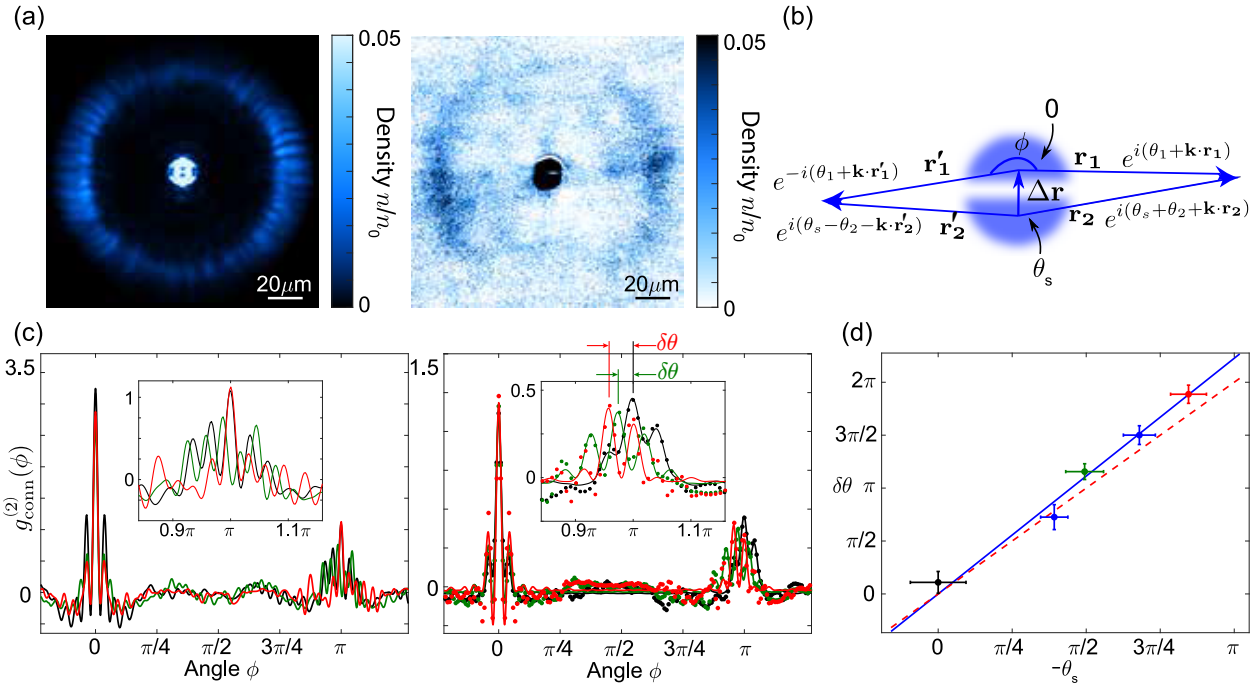

Figure 5.3: **Emissions from Bose condensates split into two halves with and without a relative phase θ_s.** **a**, Emission pattern for $\theta_s = 0$ from simulations (left) and experiments (right). The density is normalized by the initial average density n_0. **b**, Physical picture for the jet emission from two halves of the condensate. **c**, Connected correlations $g^{(2)}_{\rm conn}(\phi)$ for different relative angle ϕ (left: simulation, right: experiment) for $\theta_s = 0$ (black), $-\pi/2$ (green), and $-\pi$ (red). Solid lines are fits using the product of a sinc envelope and a sinusoidal function, borrowed from the double-slit interference model. The insets show jet-substructure of the π-peaks. The phase shift $\delta\theta$ of the oscillations are indicated by the arrows. **d**, Phase associated with π-peak shift $\delta\theta$ as a function of imprinted phase θ_s (plotted against $-\theta_s$). Dots with error bars are experimental data. The blue solid line is a linear fit without intercept and the red dashed line is the theory expectation $\delta\theta = -2\theta_s$, which is identical to results from GP simulation. Here, the data used in panel **c** are marked out with the same color codes. Error bars represent 1-σ standard deviation.

Emission patterns are obtained after the procedures described in Sec. 5.3, which are consistent with those from GP simulation based on identical parameters, see Fig. 5.3a. The emission pattern in Fig. 5.3a shows clear anisotropy: it's strong in the horizontal direction where the central potential barrier in oriented but is weak vertically. Since there is no phase imprinting in this case, the anisotropy is caused by density depletion in the region of central barrier of the trap. For excitations propagating in the vertical direction, there are fewer condensate atoms along their path, which gives rise to less stimulation in their populations. To see the relative phase, one needs to address the correlations.

We show below how this phase information can be quantitatively extracted. The phase difference between the two halves θ_s is revealed in the correlation between counter-propagating jets. We first calculate the connected correlation function $g^{(2)}_{conn}$, defined as

$$g^{(2)}_{conn}(\phi) = \frac{\langle \int_0^\pi d\phi_1 \Delta n_{\phi_1} \Delta n_{\phi_1+\phi} \rangle}{\pi \bar{n}^2}, \tag{5.8}$$

where $\Delta x = x - \langle x \rangle$ represents the fluctuation around the mean value, n_ϕ is the density of the emitted atoms at angle ϕ, $\langle \cdot \rangle$ denotes the average over all images and $\bar{n}$ is the average density over all directions and images. The correlation function displays a clear peak at $\phi \approx \pi$, called the π-peak, which indicates that jets form in pairs in counter-propagating directions.

Close examination shows that the π-peak contains fine oscillations (jet sub-structure) that depend on the condensate phase, see Fig. 5.3c. The phase of the oscillations is found to be proportional to the relative phase between the two halves θ_s. Comparing the phase $\delta\theta$ of the fine oscillations to the phase difference θ_s, we find a linear dependence with a slope -2.2(2) (see Fig. 5.3d), which is consistent with the theoretical prediction:

$$\delta\theta = -2\theta_s. \tag{5.9}$$

We provide an intuitive picture to understand this phase relation. In far field, emission from the upper BEC with probability amplitude $e^{i(\theta_1+\mathbf{k}\cdot\mathbf{r_1})}$ propagating to the right overlaps with the emission from the lower half with amplitude $e^{i(\theta_s+\theta_2+\mathbf{k}\cdot\mathbf{r_2})}$, where θ_1 and θ_2 are random phases determined by quantum fluctuations, $\mathbf{k}$ is the jet wavevector and $\mathbf{r_1}$ ($\mathbf{r_2}$) is the displacement vector toward the measurement point, see Fig. 5.3b. The two matterwaves interfere and produce a density wave of $\cos(\Delta\theta - \theta_s + \mathbf{k}\cdot\Delta\mathbf{r})$, where $\Delta\theta = \theta_1 - \theta_2$ and $\Delta\mathbf{r} = \mathbf{r_1} - \mathbf{r_2}$. Similarly, the left-propagating emissions of amplitudes $e^{i(-\theta_1-\mathbf{k}\cdot\mathbf{r_1'})}$ and $e^{i(\theta_s-\theta_2-\mathbf{k}\cdot\mathbf{r_2'})}$ overlap and result in a density wave $\cos(\Delta\theta + \theta_s + \mathbf{k}\cdot\Delta\mathbf{r})$, where we have made use of the fact that the phases of jets emitted from the same half of BEC sum to be twice the phase of that part of the BEC [70]. Comparing the two density waves, we see that the counter-propagating emissions are correlated with a relative phase shift of $\delta\theta = -2\theta_s$.

Details of extracting phase $\delta\theta$ from fitting correlation functions near $\phi = \pi$

To understand the interference pattern of split BECs, we refer to the double-slit interference model and make an approximate analogy between the split BEC and a conventional double slit problem. In this model the far field (Fraunhofer) diffraction intensity is proportional to

$$\mathrm{sinc}^2\left(\frac{\pi W \sin\alpha}{\lambda}\right)\cos^2\left(\frac{\pi D \sin\alpha}{\lambda} - \theta_r/2\right),$$

where α is the diffraction angle, λ is the light wavelength, D is the distance between the slit centers, W is the width of each slit, and θ_r is the relative phase between the light beams that pass the two slits.

We fit the oscillatory correlation function $g^{(2)}_{conn}(\phi)$ near $\phi = \pi$ with the following function to extract its phase $\delta\theta$, see Fig. 5.3c:

$$f(\phi) = A\,\mathrm{sinc}^2[b(\phi - \pi - c)]\left[\cos^2\left(\frac{k\phi - k\pi + \delta\theta}{2}\right) + d\right] + f_0,$$

where the sinc envelope captures the finite size of each half BEC, the cosine term describes the matterwave interference fringes, b describes the envelope oscillation frequency, c accounts for the small center of mass motion, k depends on the separation between the two half BECs, and the parameters d and f_0 describe the offset of the fringes and the envelope function, respectively. By fitting the π peaks using this functional form, we extract the phases $\delta\theta$ shown in Fig. 5.3d.

In our experiments we determine k by fitting the correlation function $g^{(2)}_{conn}(\phi)$ for condensates with no phase imprinting. The fitted value of k is then fixed for other situations with nonzero imprinted phase. Since our samples form 2 semi-circles instead of 2 slits, we do not expect the sinc function to precisely describe the measured envelope function near the π peaks. We have verified that the phase shifts $\delta\theta$ we extracted have negligible dependence on the form of the envelope function and offsets.

We finally want to note that the deviations in our experimental and simulation data are partly due to the strong fluctuations of the firework emission. Since the emission from split BECs is concentrated near the horizontal (x) direction, the number of modes that contribute to the data is much lower than those from uniform BECs. Fluctuations are thus relatively high. These effects are more important near the wing of the π-peak, but they do not systematically shift the center fringe.

5.4.2 Spiral emissions from vortex-embedded BECs

The second case study involves vortex-embedded BECs, where the resulting emission patterns display exotic spirals. In our system the initial condensate wave function is characterized by an integer winding number $l_0 = \pm 1, \pm 2, \ldots$ as

$$\psi_0(r, \phi) = \sqrt{n_0(r)} e^{i l_0 \phi} \tag{5.10}$$

in polar coordinates (r, ϕ). Since the healing length ξ (set by the chemical potential μ as $\hbar^2/2m\xi^2 = \mu$) is much smaller than the trap radius R, the condensate wavefunction is uniform outside the vortex core. Jet emission dynamics from a driven BEC with a vortex is simulated in Fig. 5.4a.

In our experiment, about 5% of condensates form with a vortex, arising from the finite cooling time in transition to condensation [32, 109, 17]. When the system reaches equilibrium, the vortex is expected to settle at the trap center. BECs with and without a vortex can be distinguished from the emission pattern, see Fig. 5.4b for emission from BECs with different vorticity.

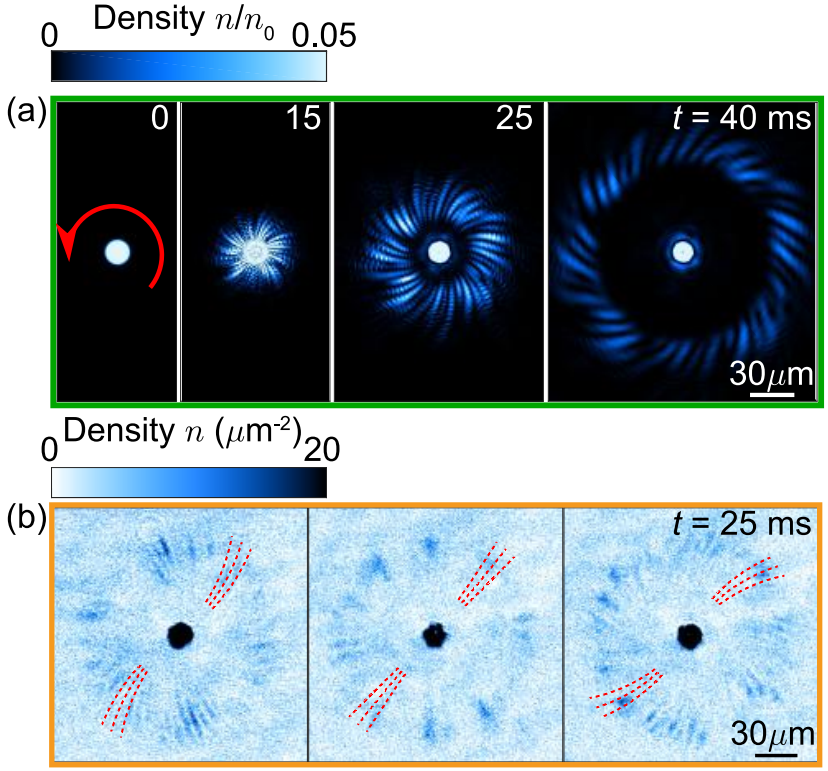

Figure 5.4: **Spiral emissions from vortex-embedded BECs. a**, Evolution of the fireworks emission for $\omega/2\pi = 2$ kHz and $l_0 = 1$ from GP simulation. The red arrow indicates the direction of the phase winding with $l_0 = 1$. **b**, Experimental images for $\omega/2\pi = 3$ kHz at $t = 25$ ms from BECs with different vortex winding numbers $l_0 = -1, 0, 1$ from left to right. The red dashed lines are guides to the eye, the curvature of which is calculated from the correlation function.

Our simulations and experiments show a consistent picture that the jet emission displays a spiral pattern in the presence of vorticity in the BEC. When the winding number is positive, the spirals are clockwise. The spiral emission pattern is the key observable that determines the winding number of the condensate.

This spiral pattern can be understood based on a semi-classical picture. Considering atoms inside the rotating condensate as independent emitters, an atom has a unique momentum $\mathbf{k}$ of magnitude l_0/r along the transverse direction. When two such atoms collide inelastically, they are excited to new momenta $\mathbf{k} \pm \mathbf{k_f}$, where $|\mathbf{k_f}| = k_f$. For an observation point outside the sample, jets emitted from different parts ("sources") of the condensate overlap and interfere, and the observed spirals are the resulting interference fringes.

To see the connection between the direction of the spiral and the angular momentum, we note that when the observer moves away from the condensate, the phase of the matterwave with relatively large momentum accumulates faster. Thus the fringe curves toward the jet with the higher momentum, namely, $\mathbf{k}+\mathbf{k_f}$, to maintain the same interference condition, see Fig. 5.5a. Theoretical analysis suggests $d\phi/dr = -\eta l_0/(k_f R^2)$ with η being a dimensionless constant. This equation describes the observed spirals.

To test these predictions, we evaluate the correlation function between two points with radial distance r and angular distance ϕ, namely,

$$g_t^{(2)} = \frac{\int d\phi' dr' \langle n(r', \phi') n(r' + r, \phi' + \phi) \rangle}{2\pi L_0 \tilde{n}^2}, \tag{5.11}$$

where the integration of r' covers the interval L_0 that jets manifest [2] and $\tilde{n}$ is the mean density in the interval.

The spiral pattern associated with the jet substructure can be understood as representing a linear relation between the radial and angular distances in the emission, see Fig. 5.5b,

2. Assuming jets appear within $r_{min} < r < r_{max}$, we integrate r' in the range such that both measurement points at r' and $r' + r$ are within this ring area.

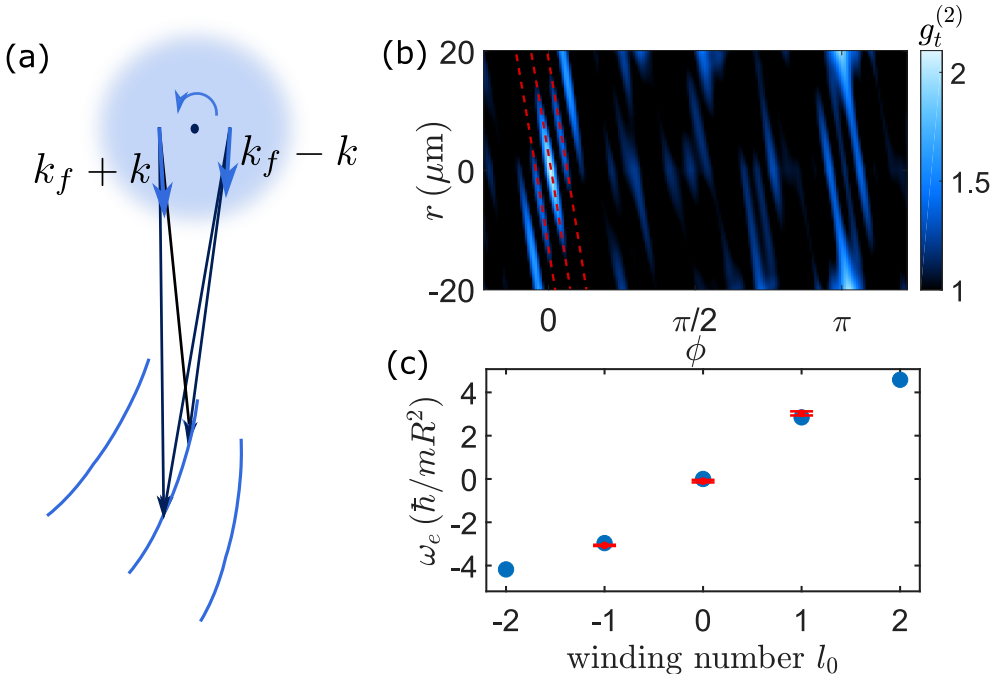

Figure 5.5: **Correlation analysis of spiral emission patterns. a**, A physical picture to explain the origin of the spiral patterns from a rotating BEC as interference fringes from matterwave emitters with different momenta, see text. **b**, Correlation functions $g_t^{(2)}$ in polar coordinates (r, ϕ) for $t = 40$ ms image in Fig. 5.4(a). Red dashed lines show linear fits to the correlations between r and ϕ. **c**, Effective angular velocity ω_e, expressed in units of $\hbar/mR^2$, for condensates with different winding number l_0. Blue circles are from simulations and red circles are from experiments. Error bars represent 1-σ standard deviation.

where the red dashed lines show linear fits to the correlations involving r and ϕ. This linear dependence suggests that the emission emerges with an effective angular velocity $\omega_e = -(\hbar k_f/m)d\phi/dr$, which can be compared with the winding number of the condensate according to

$$\omega_e = \eta \frac{l_0 \hbar}{mR^2}, \tag{5.12}$$

see Fig. 4c. From simulations, we determine $\eta = 2.90$ for $l_0 = \pm 1$ and $\eta = 2.19$ for $l_0 = \pm 2$. We speculate that the decrease of η for larger $|l_0|$ is a result of the instability of a vortex-containing-BEC with $l_0 = \pm 2$. A vortex with $l_0 = 2$ will quickly decay into two vortices with $l_0 = 1$, and the finite spatial separation between them reduces the effective angular velocity. For a classical, rigid uniform disk with the same radius R, we expect that the

angular velocity is $\omega_e = \eta_{cl} l_0 \hbar/(mR^2)$ with $\eta_{cl} = 2$.

The same analysis on the experimental data also yields a linear relationship between r and ϕ in the correlation function. Based on multiple repeated experiments, we find that ηl_0 takes on quantized values of $\eta l_0 = -3.07(3)$, $-0.10(6)$ and $3.0(1)$, which are in very good agreement with the simulation results for $l_0 = -1$, 0 and 1, see Fig. 5.5c. The agreement between experiments and simulations confirms our scheme to reveal the helicity of a BEC directly from the jet emission pattern.

Analysis for the experimental data of jet emission from vortex-embedded BECs

Here we provide detailed analysis of vortex features observed in the jet emission pattern. We can observe the vortex cores by time-of-flight which, however, does not reveal the helicity. The spontaneously created vortices can appear in arbitrary positions. However, for those close to the trap edge, they easily escape or are readily annihilated. In addition there is a small non-uniformity of the trap potential of about 0.3 nK, which makes the energy lower if the vortices locate at the center. Since we have a long cooling time of 760 ms in the circular trap and short equilibration time scale of 32 ms, before we start the experiments, we expect the vortices, if any, have already come to equilibrium at the center of the trap. That the vortex is located near the trap center in equilibration is already observed in literature, see for example, Ref. [144].

Now let's discuss how to extract the vortex winding number from emission patterns of vortex-embedded BECs in our experiments. To do so, we first calculate the auto-correlation of atomic density in emitted jets $g_t^{(2)}(\phi, r)$ as a function of azimuthal and radial displacements ϕ and r, as given by Eq. (5.11).

$$g_t^{(2)}(\phi, r) = \frac{\langle n(r_1, \phi_1) n(r_1 + r, \phi_1 + \phi) \rangle}{\langle n(r_1, \phi_1) \rangle \langle n(r_1 + r, \phi_1 + \phi) \rangle}, \tag{5.13}$$

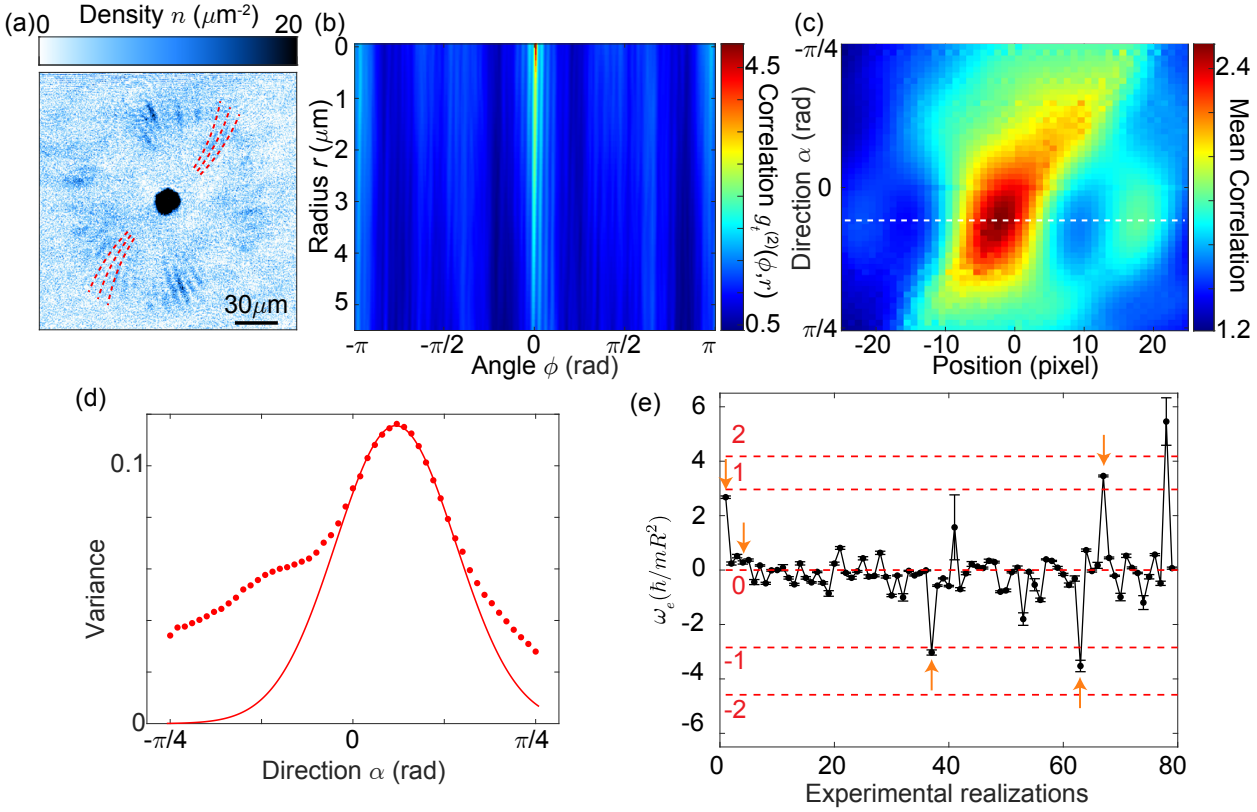

Figure 5.6: **Determination of vortex winding number from emission patterns of vortex-embedded BECs. a**, Example emission pattern from a vortex-embedded BEC. **b**, Auto-correlation of atomic density of emitted jets in **a** as a function of relative displacement r and ϕ in radial and azimuthal directions, respectively. **c**, Distribution of mean correlation averaged over different directions in **b** for the lower half with positive r. The values for the central 50 pixels are shown here. The white dashed line indicates the direction where the variance of mean correlation reaches maximum. **d**, The data points are variance of the mean correlation distribution averaged from different directions in **b**. The solid line is a Gaussian fit for the central 13 data points around the maximum, which determines the peak position precisely. The direction where the maximum variance occurs corresponds to the slope $d\phi/dr$ of the fringes around $\phi = 0$ in **b**, which then corresponds to the curvature of spirals in **a**. **d**, Angular velocity $\omega_e = d\phi/dr \times k_f R^2$ calculated from the slope $d\phi/dr$ following the procedure in **a-d** (corresponding to the 1^{st} experimental realization). The calculation is based on unsorted experimental realizations. The orange arrows indicate the data points identified as $l_0 = \pm 1$ with small error bars < 0.2. Other data points with error bars less than 0.2 are averaged and are identified as $l_0 = 0$. Data points with larger error bars are ignored. The results are shown as red circles in Fig. 5.5c. The error bars are 1-σ standard deviation.

where $\langle\cdot\rangle$ means averaging over all possible positions (r_1, ϕ_1) in the region of atomic jets. One example of the correlation function $g_t^{(2)}(r, \phi)$ is shown in Fig. 5.6b for the emission pattern from experiment in Fig. 5.6a. It can be seen that there are fringes near $\phi = 0$ in the auto-correlation with non-zero slope $d\phi/dr$, which is proportional to the vortex winding number. Next, we quantitatively extract the slope from the pattern of fringes in Fig. 5.6b using the pattern recognition algorithm which is described in the next paragraph, thus enabling us to extract the winding number.

To recognize the fringes, we can average the 2D correlation function $g_t^{(2)}(r, \phi)$ along different directions. The direction along which the mean correlation shows the oscillation structure most clearly, corresponds to the slope of those fringes. The mean correlation distribution in the central region of 50 pixels at different directions with angle α is shown in Fig. 5.6c, where $\alpha = 0$ is along the negative r axis in Fig. 5.6b and $\alpha = \pi/2$ is along the positive ϕ axis. We use the variance of the mean correlation distribution in certain directions to characterize its contrast, which is shown in Fig. 5.6d. There is a clear peak in the variance and we use a Gaussian function to fit the 13 data points around the maximum to find the peak position $\alpha_p = 0.184$ rad and use the uncertainty of the fit as error bars. Then the slope $d\phi/dr = \chi \tan(\alpha_p)$ is determined, where $\chi = 0.0216$ rad/μm is the ratio between the resolution in angular and radial direction in Fig. 5.6b. Finally, the angular velocity $\omega_e = d\phi/dr \times k_f R^2$ in units of $\hbar/mR^2$ is obtained.

We apply the same procedure as above for images from 79 repetitive experimental realizations and obtain their angular velocity ω_e as shown in Fig. 5.6e. The emission pattern in a corresponds to the first data point in e and the data points indicated by the orange arrows are the experimental data points shown in Fig. 5.5c. We determine the vortex winding number l_0 by comparing the measured angular velocity ω_e to the corresponding simulation results. In addition, we see that most of the measurements have zero winding number, since the vortices are non-deterministically generated.

Geometric analysis of the multiple-slit interference

Lastly, we present the geometric argument behind the intuitive multiple-slit interference picture.

As mentioned above, each point in the trap functions as an individual source emitting different modes, whose wavenumbers are $k_f + (mv/\hbar)\cos(\phi_r)$ dependent on the relative angle ϕ_r between final and initial velocities. For an observation point at distance $r \gg R$ from the trap center, there are jets emitted from different "sources" overlapping at this point, see Fig. 5.7. If the jet comes from a point at angular position ϕ (ϕ is measured with respect to the axis perpendicular to the line connecting the trap center and the measurement point), the jet wavenumber is then $k_f - (mv/\hbar)\cos\phi$ for each source. Therefore, when the measurement point shifts by a radial distance dr, the optical paths for the jets from different sources would all increase as $\sim dr$ but have different phase accumulations due to different k values. To keep the relative phases between different modes unchanged, the observation point needs to shift an angle of $d\phi$ so that the modes with larger k values would have shorter optical paths (see Fig. 5.7). In this way, the optical path changes by dx which can be easily derived from geometric analysis:

$$dx \approx r d\phi \sin\alpha,$$

where

$$\alpha \approx \beta, \quad r\sin\beta = R\cos\phi.$$

Therefore, the total phase accumulation for each mode is approximately

$$\left(k_f - \frac{mv}{\hbar}\cos\phi\right) dr + k_f R\cos\phi d\phi,$$

which is a constant for all modes only when

$$\frac{mv}{\hbar} dr = k_f R d\phi.$$

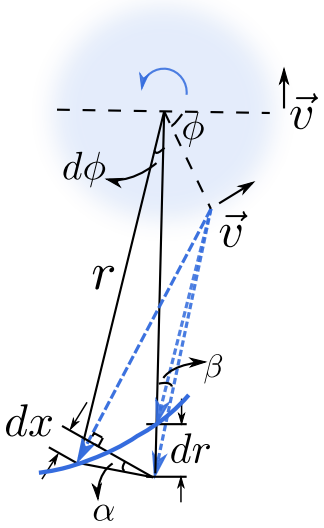

Figure 5.7: Schematic of spiral trajectories resulting from interference between emission from different parts of a vortex-embedded BEC.

Since the interference fringe is along fixed relative phases, we then obtain the trajectory as

$$\frac{dr}{d\phi} \approx \frac{k_f R^2}{l_0},$$

where $mv/\hbar \sim l_0/R$. This spiral winds in the opposite direction to that of the original vortex, as seen from Fig. 5.7.

In conclusion, we present a methodology for extracting the phase distribution of a BEC based on jet emission. From the jet substructure of a driven BEC, one can determine the density and phase correlations and in principle reconstruct the pair function F of the condensate. The two illustrative examples discussed here show how one can recover the wavefunction phase information from the far-field (split BECs) or near-field (vortex-imbedded BECs) emission. In the far field, density-density correlators of jets can be directly obtained. In the near field, interference between adjacent jets reveals the relative phases of the jets. Our experiments show excellent agreement with the theory and simulations. Remarkably, the jet sub-structure is an important observable in particle physics [85, 39] to understand the dense systems formed in high energy scattering experiments. Our analysis may offer a

convenient testbed to determine the properties of a many-body sample with its attendant jet emission pattern.

CHAPTER 6

TRANSITION FROM AN ATOMIC TO A MOLECULAR BOSE-EINSTEIN CONDENSATE

Preparation of molecular quantum gas promises novel applications including quantum control of chemical reactions, precision measurements, quantum simulation and quantum information processing [20, 22, 119]. Obtaining colder and denser molecular samples, however, is frequently hindered by fast inelastic collisions that heat and deplete the population [103, 78]. Here we report the formation of 2D Bose-Einstein condensates (BECs) of spinning molecules by inducing pairing interactions in an atomic condensate near a $g-$wave Feshbach resonance [86]. The trap geometry and the low temperature of the molecules help reducing inelastic loss to ensure thermal equilibrium. From the equation of state measurement, we determine the molecular scattering length to be +220(30) Bohr. We also investigate the unpairing dynamics in the strong coupling regime and find that near the resonance the dynamical time scale is consistent with the unitarity limit. Our work confirms the long-sought transition between atomic and molecular condensates, the bosonic analog of the BEC-BCS (Bardeen-Cooper-Schrieffer superfluid) crossover in a Fermi gas [123, 120, 48]. In addition, our experiment may shed light on condensed pairs with orbital angular momentum, where novel anisotropic superfluid with non-zero surface current is predicted for, e.g. ^{3}He-A [5, 67].

6.1 Introduction

Because of their rich energy structure, cold molecules hold promises to advance quantum engineering and quantum chemistry [20, 22, 119]; a wide variety of platforms are developed to trap and cool cold molecules [22]. The same rich energy structure, however, also causes complex reactive collisions that obstruct experimental attempts to cool molecules toward quantum degeneracy.

One successful strategy to prepare molecular quantum gas is to begin with an atomic quantum gas, and then pair the atoms into molecules [86]. A prominent example is the pairing of atoms in a two-component Fermi gas, which opens the door to exciting research on the BEC-BCS crossover [24, 58, 137]. Recently, degenerate Fermi gas of ground state KRb molecules is observed based on quantum mixtures of Rb and K atoms [43]. In these examples, molecules gain collisional stability from Fermi statistics and the preparation of molecules in the lowest rovibrational state, respectively.

For more generic molecules with many open inelastic channels, inelastic collision rates are difficult to predict and experiments frequently report rates near the unitarity limit, which means that all possible scatterings result in loss [103, 78]. The short lifetime hinders evaporative cooling toward quantum degeneracy.

Here we report the observation of BECs of Cs_2 molecules in a high vibrational and rotational state, see Fig. 6.1. The molecules are produced by pairing Bose-condensed cesium atoms in a 2D, flat-bottomed trap near a narrow $g-$wave Feshbach resonance [30]. The trap geometry allows molecules to form with very low temperature and low collision loss such that they emerge in the Berezinskii-Kosterlitz-Thouless (BKT) superfluid regime [89, 138, 75]. Our experiment opens exciting possibilities to investigate pairing and unpairing dynamics in a bosonic many-body system, described by the interaction Hamiltonian [123, 120, 48]

$$H_{\mathrm{int}} = g(\hat{a}_{\mathrm{m}}^{\dagger}\hat{a}\hat{a} + \hat{a}_{\mathrm{m}}\hat{a}^{\dagger}\hat{a}^{\dagger}),$$

where $\hat{a}_{\mathrm{m}}$ and $\hat{a}$ are the annihilation operators of a molecule and an atom, respectively, and g is the coupling constant. Pairing of bosons is expected on both sides of the Feshbach resonance and can lead to an Ising-like quantum phase transition [123, 120, 48]. Interestingly, in the molecular BEC phase, atoms and molecules are predicted to have BCS-like correlations [120].

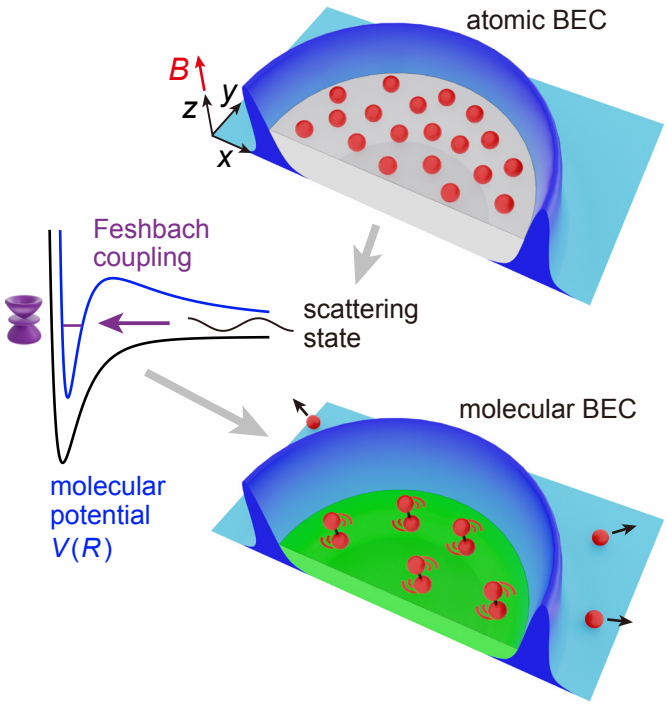

Figure 6.1: **Production of g−wave molecular condensate.** A uniform Cs BEC (gray) is initially confined in a 2D optical potential (blue). Cesium atoms (red circles) are paired into molecules through a narrow $g-$wave Feshbach resonance at magnetic field $B_0 = 19.87$ G. The molecules occupy a rotational state with orbital angular momentum $l = 4\hbar$ and its projection in the $z-$direction $l_z = 2\hbar$. The molecules form a molecular BEC (green) in the same optical trap, while the remaining atoms are expelled from the trap.

6.2 Experimental setup

The starting point of our experiment is a BEC of 6×10^4 cesium atoms prepared in a disk-shaped dipole trap with a radius of 18 μm in the $x-y$ horizontal plane[35]. The disk-shaped potential is provided by a digital micromirror device (DMD) which projects 788 nm blue-detuned laser light on the plane with 1 μm resolution. The sample is vertically confined with $1/e$ radius of 0.4 μm to a single site of an optical lattice with trap frequency $\omega_z = 2\pi \times 400$ Hz. A magnetic field gradient of 31 G/cm is applied to levitate the atoms. The atomic scattering length is 127 a_0 at $B = 19.2$ G and the global chemical potential is $\mu = h \times 365$ Hz, where $h = 2\pi\hbar$ is the Planck constant and a_0 is the Bohr radius. The initial state of the atoms is a BEC in the 2D-3D crossover regime at temperature $T = 11(2)$ nK, well below the BEC

critical temperature of 85 nK.

We create Cs_2 molecules by ramping the magnetic field across a closed-channel dominated Feshbach resonance at $B_0 = 19.87$ G starting from 20.03 G, based on a procedure similar to Ref. [65]. Since atoms and molecules have different magnetic moments, they tend to separate vertically in the presence of a magnetic field gradient. To better confine both atoms and molecules in the molecular formation phase, we increase the magnetic field gradient to 41.9 G/cm in 2 ms before ramping the magnetic field to 19.79 G in 2 ms which creates molecules. After the formation of molecules, the magnetic field gradient is increased to 50 G/cm in 0.5 ms, which levitates the molecules and overlevitates the atoms. The resonance has a small width $\Delta B = 11$ mG [100] and couples two scattering atoms into a weakly-bound molecule with a large orbital angular momentum $l = 4\hbar$ and projection along the magnetic field direction $l_z = 2\hbar$. The molecules are closed-channel dominated and chemically bound with the size given by the van der Waals length $R_{\mathrm{vdW}} = 5.3$ nm for Cs [30]. This resonance is chosen due to the superior collisional stability between the molecules. The molecules can be brought into other rotational states or superposition of rotational states by a time-dependent magnetic field [99].

The ramp is optimized to pair up to 15% of the atoms into molecules with the lowest achievable temperature. To remove residual atoms after the molecular formation phase, a resonant light pulse of 20 μs illuminates and pushes atoms away from the imaging area in 4 ms. Molecules are detected by reversely ramping the magnetic field which dissociates the molecules back to atoms, and the atoms are detected by *in situ* absorption imaging, see Fig. 6.4a. The final value of the magnetic field and the hold time are selected to give a reliable image that reflects the distribution of the molecules. In our experiments, we set the final magnetic field to be 20.19 G and do the detection in 0.1 ms after the reverse ramp. We estimate that the atoms expand by 1 μm during the dissociation process, which is comparable with the imaging resolution of our experimental system.

The produced molecules thus occupy the same trap volume as the atomic cloud. Slightly lower molecular density is observed at the trap center due to a weak magnetic field curvature of 21.5 G/cm^2 on the $x-y$ plane. The field curvature leads to a slightly deeper potential in the rim than the center by 1.1 nK for the molecules. The appearance of the ring structure in the molecular density profile, see Fig. 6.4a, suggests that the molecules are prepared at a temperature or chemical potential on the order of few nK. The ring structure forms soon after passing the Feshbach resonance during the magnetic field ramp, which suggests that the equilibrium of molecules is reached by their fast interactions with atoms near the resonance (see Sec. 6.3.1). This supports our following equation of state measurements of the molecular samples from their density profiles.

6.2.1 Characterization of external potential from atomic density profile

The strong magnetic field gradient for levitating the molecules leads to an additional magnetic anti-trapping potential on the horizontal plane. We also apply a central potential barrier projected from a DMD to measure the density response of the molecules. A precise knowledge of both the magnetic anti-trapping potential and the optical potential barrier are needed in order to extract the equation of state of the molecular gas presented in Sec. 6.3.1.

We load atomic BEC into the same trap as for molecules to calibrate the external potential. Since the magnetic moment and polarizability of the g-wave molecule are accurately known, the trapping potential for molecules can thus be obtained from the trapping potential for atoms.

The magnetic anti-trap frequency on the horizontal plane is given by

$$\omega_i^2 = \frac{\mu_m}{4mB_0}(B'^2 - 4\epsilon_i B_0^2), \tag{6.1}$$

where $i = x, y$, μ_m is magnetic moment, B_0 and B' are magnetic field and magnetic field

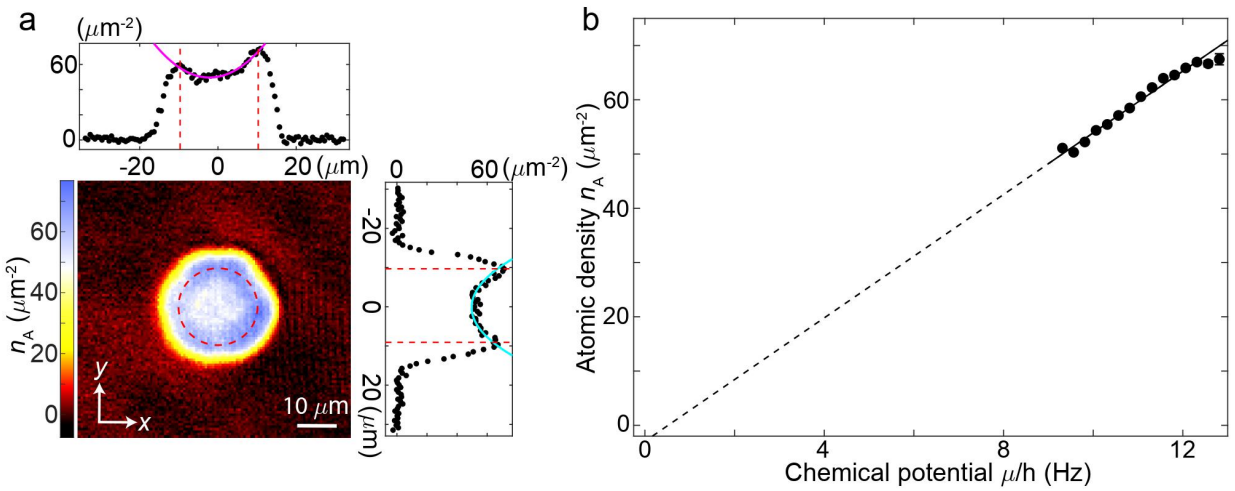

Figure 6.2: **Calibration of magnetic anti-trap potential from atomic density distribution.** **a**, Fit of the *in situ* atomic density profile for determination of the magnetic anti-trap frequencies ω_x and ω_y using Eq. 6.2. The top and right panels show line cuts of the 2D atomic density in x and y directions crossing at the center of the anti-trap. We choose the region within the red dashed circle for fit and extraction of the equation of state. **b**, Equation of state of atomic BEC shown in **a**. Each data point represents averaged density within a bin size $\delta\mu/h = 0.25$ Hz and error bars represent 1-σ standard deviation. The black solid line is a linear fit to the data while the black dashed line is an extrapolation of the fit toward origin.

gradient, respectively, at the location of particles and ϵ_i is determined from the coil geometry [72]. We determine the offset field value B_0 with an accuracy of 2 mG using microwave spectroscopy. We prepare atomic BEC at 17.2 G where the $s-$wave scattering length $a_S = 4\ a_0$. Because of the low chemical potential, the atomic density distribution is sensitive to the magnetic anti-trap and shows lower density at the center and higher density in the rim, see Fig. 6.2a. Since the vertical trap frequency $\omega_z/2\pi = 400$ Hz is much larger than the chemical potential $\mu_0/h \approx 10$ Hz, the BEC is in the quasi-2D regime and the column density under Thomas-Fermi approximation is given by

$$n(x,y) = \frac{m}{\hbar^2 g_{2D}}[\mu_0 - V_{\text{mag}}(x,y)], \tag{6.2}$$

where the 2D coupling strength $g_{2D} = \sqrt{8\pi}a_S/\sqrt{\hbar/m\omega_z}$, the magnetic anti-trap potential

$V_{\mathrm{mag}}(x,y)$ is parametrized by the trap frequencies ω_x and ω_y as $V_{\mathrm{mag}}(x,y) = m\omega_x^2(x - x_0)^2/2 + m\omega_y^2(y-y_0)^2/2$ and (x_0, y_0) is the center position of the anti-trap. To determine the trap frequencies and the global chemical potential, we fit the *in situ* atomic density distribution using Eq. 6.2, see Fig. 6.1a. From the fit we get $\omega_x/2\pi = 1.94(9)$ Hz, $\omega_y/2\pi = 2.24(9)$ Hz and $\mu_0 = h \times 9.19(7)$ Hz. In this way, we calibrate the geometric parameters to be $\epsilon_x = 0.54(3)$ cm^{-2} and $\epsilon_y = 0.45(3)$ cm^{-2}, which we use to calculate the anti-trap frequencies for molecules based on Eq. 6.1, which gives $\omega_x^{\mathrm{mol}}/2\pi = 3.35(4)$ Hz and $\omega_y^{\mathrm{mol}}/2\pi = 3.48(4)$ Hz. For consistency check, we plot out the atomic density n_{A} versus the local chemical potential $\mu = \mu_0 - V_{\mathrm{mag}}(x,y)$, which agrees with the equation of state of a pure 2D BEC $\mu = (\hbar^2 g_{2\mathrm{D}}/m)n(x,y)$ (see Fig. 6.2b).

We calibrate the optical potential barrier projected by DMD using atomic BEC prepared at 19.2 G, where the atomic scattering length is $a_{\mathrm{S}} = 127\ a_0$ and the vertical trap frequency is $\omega_z/2\pi = 409$ Hz. The intensity of the optical barrier is ramped up within 10 ms. After waiting for another 2 ms, absorption imaging is performed in the vertical direction to record the atomic column density, see Fig. 6.3a. Here the barrier height is controlled by the fraction of micromirrors f_{DMD} that are turned on. The fraction determines the intensity of the light projected onto the atom plane. In the region with higher light intensity, the atomic density is suppressed more, which in turn allows us to determine the light intensity. Because of the higher chemical potential of BEC in this case, the density depletion has a larger dynamical range that helps to calibrate larger range of barrier height. Since the chemical potential is comparable to the vertical trap frequency, the BEC is in 3D regime and the column density under Thomas-Fermi approximation is given by

$$n(x,y) = \alpha[\mu_0 - V_{\mathrm{opt}}(x,y)]^{3/2} \tag{6.3}$$

where $\alpha = 4\sqrt{2}/(3g\sqrt{m}\omega_z)$, the 3D coupling strength $g = 4\pi\hbar^2 a_{\mathrm{S}}/m$ and the local optical

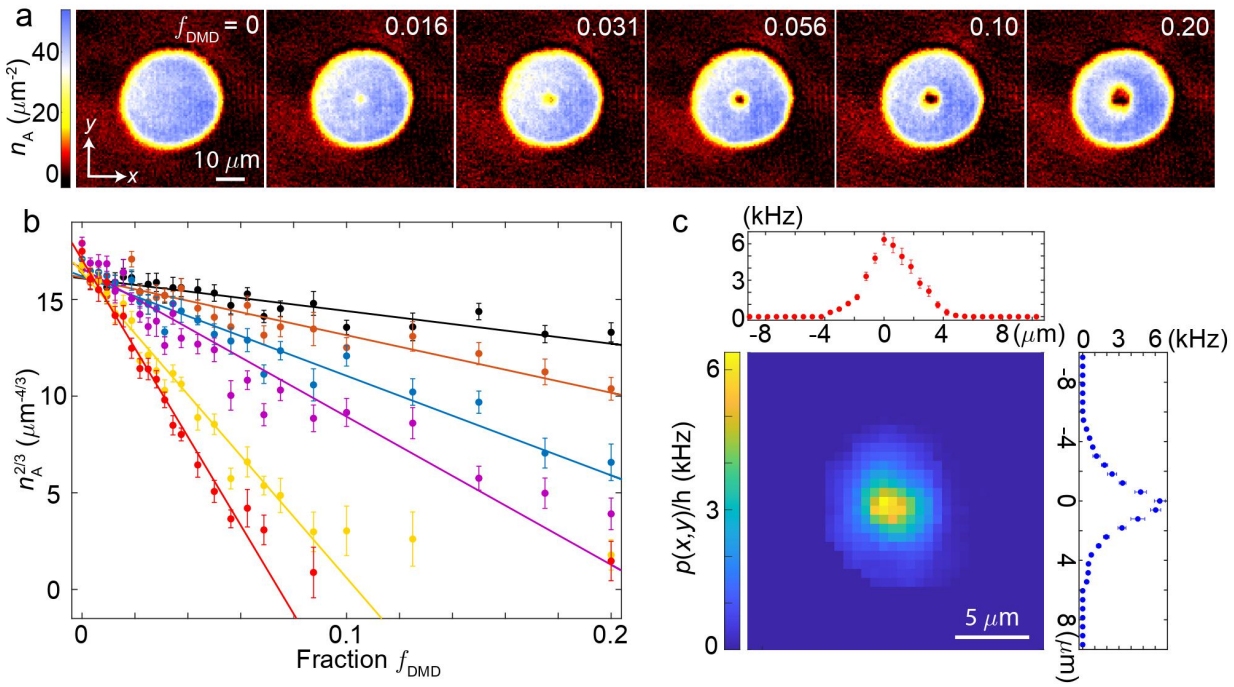

Figure 6.3: **Calibration of the optical potential barrier projected by DMD from the density response measurement of atomic BEC. a**, Images of *in situ* atomic column density with different central barrier height determined by different fraction of micromirrors f_{DMD} that are turned on in DMD. **b**, Example measurements of the proportionality $p(x, y)$ for 6 pixels at different locations. The solid lines are linear fits to the linear part of the data points, the slope of which gives $p(x, y)$. **c**, Spatial dependence of the proportionality $p(x, y)$. The upper and right panels are line cuts in x and y directions crossing the peak value.

potential $V_{\mathrm{opt}}(x, y)$ is proportional to the micromirror fraction as $V_{\mathrm{opt}}(x, y) = p(x, y) f_{\mathrm{DMD}}$. Thus for each pixel located at (x,y), we have $n^{2/3}(x, y) = \alpha^{2/3}[\mu_0 - p(x, y) f_{\mathrm{DMD}}]$, from which the proportionality $p(x, y)$ can be extracted from a series of measurements with different f_{DMD}, see Extended Data Fig. 2b. Repeating the same procedure for all the pixels within the region of optical barrier, we can map out the spatial dependence of the proportionality $p(x, y)$, see Fig. 6.3c. The polarizability of weakly bound molecules is approximately twice as large as that of a free atom, thus the corresponding proportionality for the molecules is $2p(x, y)$.

After calibrating both the magnetic potential $V_{\mathrm{mag}}(x, y)$ and the optical potential $V_{\mathrm{opt}}(x, y)$ for molecules, we can get the local molecular density as a function of the total external po-

tential $V(x,y) = V_{\mathrm{mag}}(x,y) + V_{\mathrm{opt}}(x,y)$ and follow the fitting procedure in Sec. 6.3.1 to extract the global chemical potential μ_0. Then we obtain the corresponding local chemical potential μ and average the density in a certain spatial area with a proper range of local chemical potential to get the equation of state for molecules from the density profile and optical barrier measurements in Fig. 6.4. In addition, with the knowledge of the optical potential profile, we get the equation of state for the BEC in 3D regime, see the inset of Fig. 6.4c.

6.3 Results

6.3.1 Equation of state of molecular gases.

To determine the molecular temperature, we find the conventional time-of-flight method impractical as the molecules expand very slowly within their lifetime. Instead we measure the density profile by slowly raising a potential barrier at the trap center over 10 ms and recording the density response, see Fig. 6.4b. With a high potential barrier, the molecules at the center becomes thermal with the density response $\partial n/\partial \mu = n/k_{\mathrm{B}}T$, where k_{B} is the Boltzmann constant. From fitting the data, we determine the molecular temperature to be 10(3) nK. The low temperature $k_{\mathrm{B}}T < \hbar\omega_z$ also suggests that the molecules form a 2D gas.

To probe the phase of the molecules at high densities, we measure the equation of state $n(\mu, T)$ from their *in situ* density distribution [68]. Precise knowledge of the magnetic anti-trap potential is obtained from identical measurements with atomic condensates shown in Sec. 6.2.1. The molecular density is found to linearly increase with the local chemical potential, consistent with the mean-field expectation $\mu = \hbar^2 g_{2\mathrm{D}} n_{\mathrm{M}}/2m$, where $g_{2\mathrm{D}} = 4\pi a_{\mathrm{M}}\sqrt{2m\omega_z/h}$ is the 2D coupling constant [114], n_{M} is the 2D molecular density and a_{M} is the molecular scattering length. Fitting the data with the theoretical prediction including finite temperature contribution [118], we obtain a temperature of 11(1) nK,

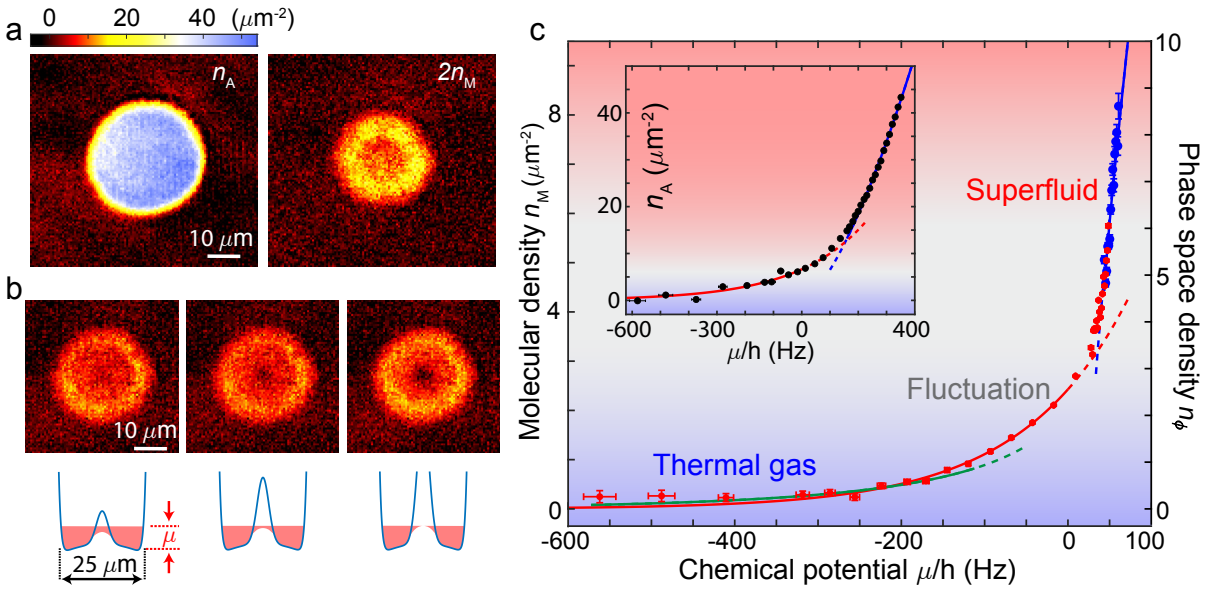

Figure 6.4: **Equation of state of molecular gases.** **a**, *In situ* images of atomic BEC (left) and molecular BEC (right) density profiles, both at $B = 19.2$ G, in the dipole trap. Atoms are paired into molecules near the $g-$wave Feshbach resonance, see text. **b**, Molecular density response to optical potential. A circular repulsive barrier with a radius of 4 μm is raised at the center of the trap with a barrier height of $h \times 83$ (left), $h \times 165$ (middle) and $h \times 330$ Hz (right). Molecular density response determines the equation of state for small and negative chemical potential. The total external potential is sketched below. **c**, Equation of state of atomic and molecular BEC. 2D phase space density $n_\phi = n_{\rm M}\lambda_{\rm dB}^2$ of molecules are derived from the optical barrier (red) and density profile (blue) measurements (see Methods), where $\lambda_{\rm dB}$ is the molecular de-Broglie wavelength. Background color shows the 2D gas in the thermal ($n_\phi \leq 2$, blue), fluctuation ($2 < n_\phi < n_c$, grey) and BKT superfluid ($n_\phi > n_c$, red) regimes, where the superfluid critical phase space density is $n_c = 6.5$ (exp.) and 7.5 (theo.), see text. Green and blue lines are fits in the thermal and superfluid regimes for a 2D Bose gas [118], respectively. The red line is a fit based on classical gas. Inset shows identical measurement on atomic condensates with fits in the thermal (red) and BEC (blue) regimes. Error bars represent 1-σ standard deviation.

consistent with the optical barrier measurement.

We combine both measurements to determine the equation of state $n(\mu, T)$ of the molecular gas. In Fig. 6.4c, we present the 2D density $n_{\rm M}$ as a function of the local chemical potential μ. Notably, the transition from exponential to linear dependence on μ is the hallmark of the thermal gas to superfluid phase transition. A global fit to the data shows excellent agreement with the theory in the thermal and superfluid limits (see Sec. 6.3.1). From

the fit, we determine the 2D coupling constant $g_{2D} = 0.19(3)$, molecular scattering length $a_M = +220(30)\ a_0$, the peak phase space density $n_\phi \approx 9$ and the global chemical potential $\mu_0 = h \times 61(7)$ Hz. Repeated experiments in the range of 18.2 G $< B <$ 19.5 G show that a_M is approximately constant. The peak phase space density exceeds the critical value for the BKT superfluid transition of $n_c = 6.5$ (exp.) [75] and 7.5 (theo.) [117] at $g_{2D} = 0.19$. Based on our trap geometry and the interaction strength, we expect that molecules condense in the superfluid regime [63], and estimate that 30% to 50% of the molecules are in the superfluid phase.

Density profiles of atomic and molecular BECs

Starting from a flat-top atomic density profile, we prepare a molecular condensate in the 2D box trap after the magnetic field is ramped across the Feshbach resonance. It is clear that the molecules do not inherit the density profile from the atoms, see Fig. 6.4a and Fig. 6.5. The molecular density profile sensitively depends on the curvature of the magnetic field and the optical barrier potential, which we introduce immediately after the ramp.

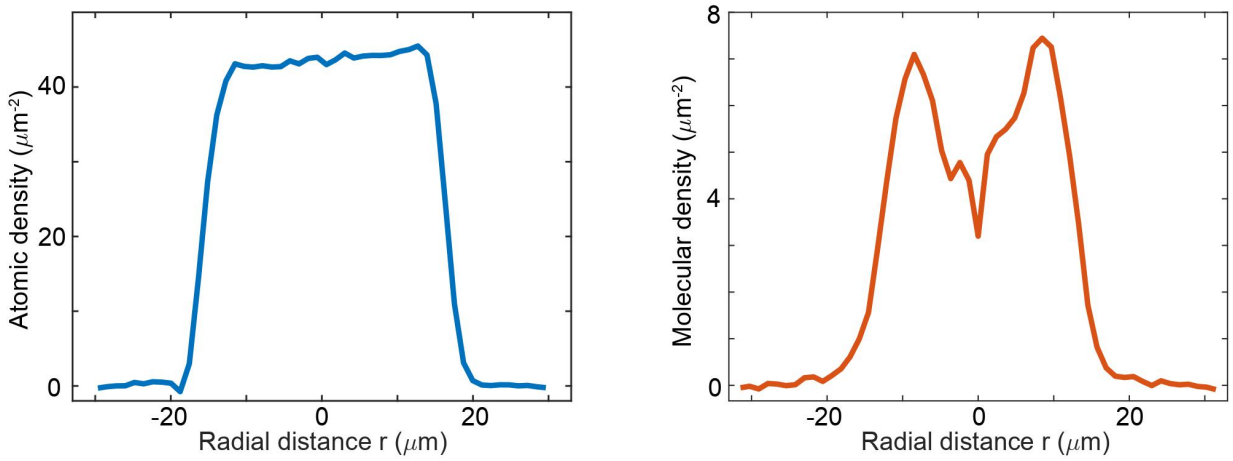

Figure 6.5: **Azimuthally averaged density profiles of the atomic (left) and molecular (right) clouds shown in Fig. 6.4a.** The atomic density profile is flat-top while the molecular density profile has a dip in the middle.

To understand the fast change of the molecular density profile, we note that there is a

drastic difference between the interaction energy scale near the Feshbach resonance where the molecules are created and far away from the resonance where we observe the molecular BEC. On resonance, the interaction energy scale is $h \times 8,000$ Hz, determined by the "Fermi energy" [66] in our system, and is also orders of magnitude higher than the molecular chemical potential of $h \times 61$ Hz measured far from the resonance. Thus, near the resonance the molecules can form and establish equilibrium with the other particles fast. In Fig. 6.6, it is clear that molecules are created from the atoms in 200 μs for various ramp speeds and develop the ring structure in their density profiles near the resonance.

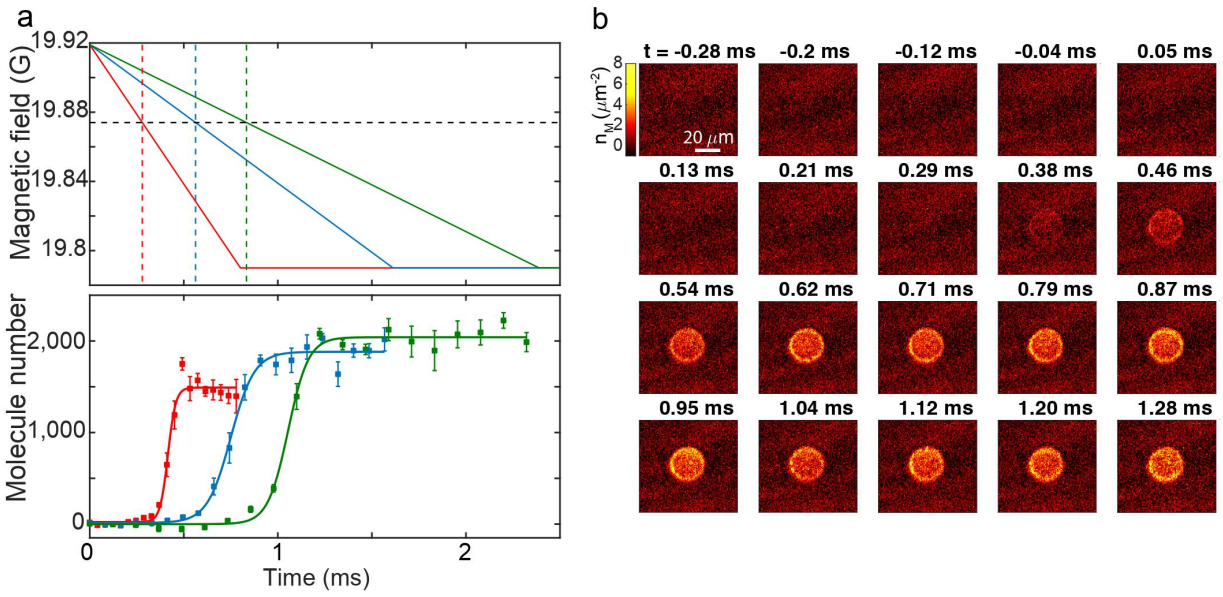

Figure 6.6: **Fast equilibration of molecules with atoms during the ramp across the Feshbach resonance.** **a**, Dynamics of the number of molecules during the magnetic field ramp across the Feshbach resonance at 19.87 G with different ramp speeds of 161 (red), 80 (blue) and 54 mG/ms (green). **b**, *In situ* images of molecular density profiles during the magnetic field ramp at 80 mG/ms.

Finally, after the formation of the molecules, the molecular density profile persists for 15 ms hold time or longer, see Fig. 6.7. In the presence of the optical barrier potential, the central molecular density is suppressed to $< 25\%$ of the peak density and the molecular lifetime is expected to be longer than 100 ms. In this case, we expect that the particle loss during the 10-ms ramp does not significantly influence the compressibility measurement.

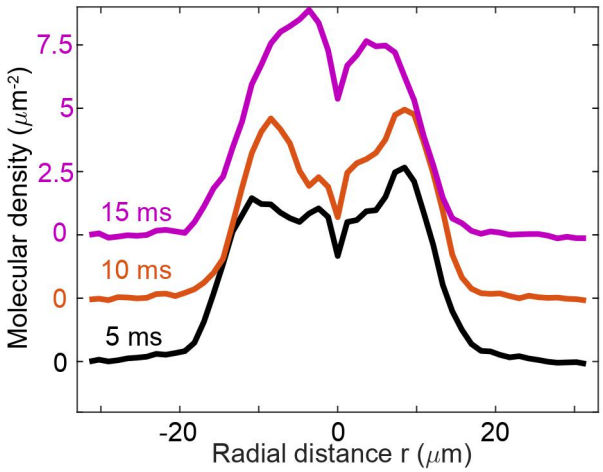

Figure 6.7: **Dynamics of molecular density profiles in the 2D box trap with magnetic anti-trap potential.** The azimuthally averaged molecular density profiles are shown as a function of the hold time after the formation of molecules. The dips in the middle result from the magnetic anti-trap potential and persist during the first 15 ms after the formation.

Fitting the equation of state for 2D and 3D Bose gases

For a nondegenerate 2D ideal Bose gas, the phase space density is given by $n_\phi = -\ln(1-\zeta)$, where $\zeta = \exp(\beta\mu)$ is the fugacity, $\beta = 1/k_{\mathrm{B}}T$ and $\mu = \mu_0 - V(x,y)$ is the local chemical potential. If the gas is interacting, a mean field potential $2(\hbar^2 g_{2\mathrm{D}}/2m)n(x,y)$ is added to the external potential based on the Hartree-Fock approximation [63]. Then the equation of state for interacting 2D Bose gas becomes:

$$n(x,y) = -\frac{1}{\lambda_{\mathrm{dB}}^2}\ln[1 - e^{\beta\mu - g_{2\mathrm{D}}n(x,y)\lambda_{\mathrm{dB}}^2/\pi}], \tag{6.4}$$

On the other hand, the density of 2D superfluid outside the fluctuation region is [117]:

$$n(x,y) = \frac{2\pi\beta}{g_{2\mathrm{D}}\lambda_{\mathrm{dB}}^2}\mu + \frac{1}{\lambda_{\mathrm{dB}}^2}\ln[2n(x,y)\lambda_{\mathrm{dB}}^2 g_{2\mathrm{D}}/\pi - 2\beta\mu], \tag{6.5}$$

We apply the above models for 2D Bose gas to describe the equation of state of the molecules, shown in Fig. 6.4c. We perform a global fit to the data points within the range $n_{\mathrm{M}} < 1\ \mu\mathrm{m}^{-2}$ and $n_{\mathrm{M}} > 4\ \mu\mathrm{m}^{-2}$ using Eqs. 6.4 and 6.5, respectively, with temperature T, global chemical potential μ_0 and 2D coupling constant $g_{2\mathrm{D}}$ as fitting parameters. Since the experimental condition drifted, the global chemical potential between the optical barrier and density profile measurements are different, and the chemical potential difference $\delta\mu$ is also set as an free parameter in the global fit. The fit gives $T = 11(1)$ nK, $g_{2\mathrm{D}} = 0.19(3)$ and the global chemical potential for the optical barrier and density profile measurements as $h \times 45(7)$ Hz and $h \times 61(7)$ Hz, respectively. We also performed independent fits to the data at low density $n_{\mathrm{M}} < 1\ \mu\mathrm{m}^{-2}$ and high density $n_{\mathrm{M}} > 4\ \mu\mathrm{m}^{-2}$. The resulting temperatures are 10(3) nK and 11(1) nK, in agreement with each other and with the global fit.

With the extracted 2D coupling constant $g_{2\mathrm{D}}$, the critical phase space density for BKT superfluid transition is evaluated as $\ln(\xi/g_{2\mathrm{D}}) \approx 7.5$, where the coefficient $\xi = 380(3)$ [117]. On the other hand, the BEC transition in our 2D box potential occurs at critical phase space density of $\ln(4\pi R^2/\lambda_{\mathrm{dB}}^2) \approx 7.5$ [63], which coincides with the BKT transition.

For BECs in 3D regime as shown in the inset of Fig. 6.4c, the low density part where the column density $n_{\mathrm{A}} < 10\ \mu\mathrm{m}^{-2}$ is fitted using the classical gas formula $n(x, y) = (2\pi l_z^2/\lambda_{\mathrm{dB}}^4)\exp(\beta\mu)$, where the harmonic oscillator length $l_z = \sqrt{\hbar/m\omega_z}$. The high density part is fitted based on Eq. 6.3.

6.3.2 Stability of a g−wave molecular condensate.

We further investigate the lifetime of the molecules. By holding the molecular BEC in the dipole trap with the initial mean density of $n_{3\mathrm{D}} \approx 1 \times 10^{13}\ \mathrm{cm}^{-3}$, the sample survives for more than 30 ms. Comparing samples with different densities and in different traps, we conclude that the decays are dominated by two-body collision loss, see Fig. 6.8a. The average loss coefficient of $L_2 = 4 \times 10^{-12}\ \mathrm{cm}^3/\mathrm{s}$ for molecules in the 2D trap with $\omega_z/2\pi = 400$ Hz

is significantly lower than previous measurements [55, 28], see Fig. 6.8b. It is also a factor of 500 below the unitarity limit $U_2 = (4h/2m)\langle k^{-1}\rangle = 2 \times 10^{-9}\mathrm{cm}^3/\mathrm{s}$, where $\langle k^{-1}\rangle$ is the thermal average of the reciprocal molecular scattering wavenumber k^{-1} [78], and a factor of 10 below the interaction scale $\mu_0/\hbar n_{3\mathrm{D}}$, see Fig. 6.8b.

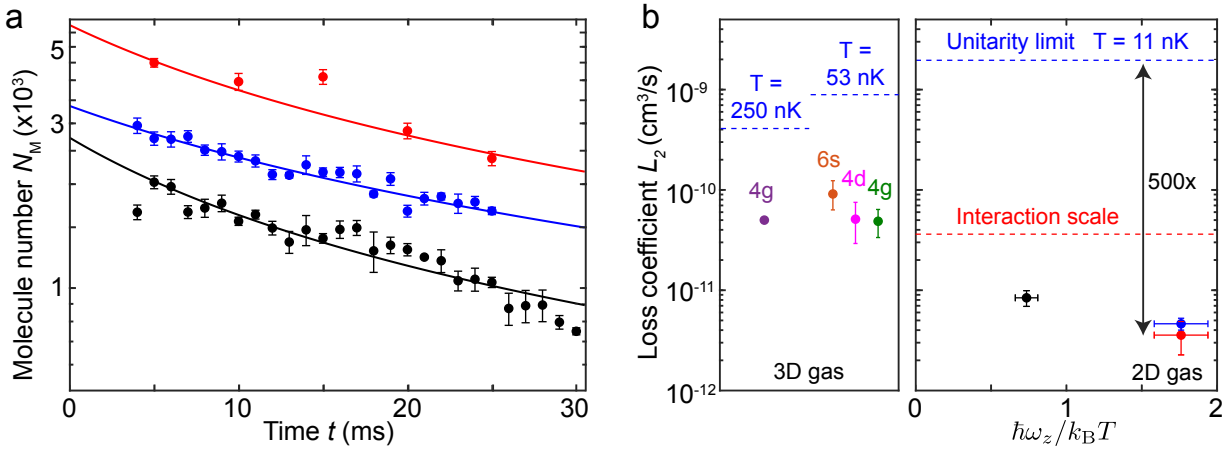

Figure 6.8: **Stability of g−wave molecular condensate. a**, Decay of total particle number for molecules with vertical trap frequency $\omega_z/2\pi = 400$ (red and blue) and 167 Hz (black) at 19.5 G. The solid lines are fits based on the two-body loss rate equation. **b**, The extracted loss coefficients L_2 in this work (right panel) are compared with former measurements on 3D thermal gases of Cs_2 molecules in the $6s$, $4d$ and $4g$ states (left panel) [55, 28]. The data points in right panel share the same color code as in panel **a**. The dashed lines indicate the unitarity limits of the two-body loss coefficients. The dotted line shows the interaction energy scale $\mu_0/\hbar n_{3\mathrm{D}}$ for the red data point at 10 ms in panel **a** with global chemical potential $\mu_0 = h \times 61$ Hz and mean 3D density $n_{3\mathrm{D}} = 1.1 \times 10^{13}$ cm^{-3}. Error bars represent 1-σ standard deviation.

The large suppression of inelastic collisions between the highly-excited $g-$wave molecules is remarkable. The comparison in Fig. 6.8b suggests that the collision loss is suppressed at low temperatures and possibly in the 2D regime [77, 105]. Since the unitarity limited loss scales as $T^{-1/2}$, smaller loss at lower temperature suggests that a larger suppression relative to the unitarity limit can be obtained by reaching down to even lower temperatures. At 10 nK, the loss coefficient we observe is already at the same level as the ground state fermionic molecules reported in Refs. [44, 129].

The observed lifetime of 30 ms is sufficient for many elastic scattering between molecules,

which occur at the time scale of $\hbar/\mu_0 = 2.7$ ms. While the lifetime is insufficient to redistribute molecules over the entire sample, thermal equilibrium in a (nearly) homogeneous system does not require global transport and can form by local interactions near the Feshbach resonance where fast collisions between atoms and molecules occur (see Sec. 6.3.1). It is remarkable that the measured temperatures at the trap center and in the rim are in good agreement with the atomic BEC at 11(2) nK. Our observation suggests that molecules produced at all locations in the trap are in thermal equilibrium with the atoms. Since the atoms are in thermal equilibrium, the molecules thus prepared are in thermal equilibrium with each other.

Extraction of the two-body inelastic loss coefficients

In order to study the lifetime of g-wave molecules, we hold the molecules in different traps and monitor the decay of total particle number as a function of the hold time. The two traps we used have horizontal radius $R_1 = 12.5$ μm, $R_2 = 9$ μm and vertical trap frequency $\omega_{z1}/2\pi = 400$ Hz, $\omega_{z2}/2\pi = 167$ Hz, respectively. The molecular density distribution in these traps are approximately uniform in the horizontal direction and Gaussian in the vertical direction, given by

$$n(\vec{r}) = \frac{N_{\mathrm{M}}}{\pi^{3/2} R_i^2 l_{zi}} e^{-z^2/l_{zi}^2} \theta(R_i - \rho), \tag{6.6}$$

where $i = 1,2$, $\rho = \sqrt{x^2 + y^2}$ and $\theta(x)$ is the Heaviside step function.

Even though the 1064 nm light intensity in the vertical direction of the two traps differ by a factor of $\omega_{z1}^2/\omega_{z2}^2 \approx 6$, the decay rate of molecular number are similar, see Fig. 6.8a. This suggests that the one-body loss process due to the off-resonant laser light is negligible. In fact, since the g-wave molecules are in a highly-excited rovibrational state, two-body loss

process dominates which is modelled by $\partial_t n(\vec{r},t) = -L_2 n^2(\vec{r},t)$. The molecular number decay corresponding to the density profile in Eq. 6.6 is thus given by

$$N_{\rm M}(t) = \frac{N_{\rm M}(0)}{1 + L_2' N_{\rm M}(0) t}, \tag{6.7}$$

where $L_2' = L_2/\sqrt{2}\pi^{3/2} R_i^2 l_{zi}$. We use Eq. 6.7 to fit the data of molecular number decay and extract the inelastic loss coefficient L_2 in Fig. 6.8b.

The unitarity limit of the two-body loss coefficient is $U_2(k) = 4h/2mk$, where k is the magnitude of the relative wavevector $\vec{k}$ between two colliding molecules, associated with the relative kinetic energy $E = \hbar^2 k^2/2m$ [30]. Due to the finite temperature in our experiment, the relative kinetic energy obeys Boltzmann distribution as $p(E) = A\exp(-E/k_{\rm B}T)$, where the coefficient $A = (1/4)(\hbar^2/\pi m k_{\rm B} T)^{3/2}$. The distribution of the wavenumber k is then given by

$$p(k) = 4\pi A k^2 e^{-\hbar^2 k^2/2mk_{\rm B}T}. \tag{6.8}$$

The unitarity limit that we evaluate in Fig. 6.8b is $U_2 = \int_0^\infty U_2(k) p(k) dk = (4h/2m)\langle k^{-1}\rangle$, where the thermal average of k^{-1} with respect to the distribution $p(k)$ is $\langle k^{-1}\rangle = \sqrt{\hbar^2/\pi m k_{\rm B} T}$. For comparison with the loss coefficients, we evaluate the interaction scale as $\mu_0/\hbar n_{\rm 3D}$, where the 3D mean density $n_{\rm 3D} = \int_{-\infty}^{+\infty} n^2(\vec{r}) d^3\vec{r} / \int_{-\infty}^{+\infty} n(\vec{r}) d^3\vec{r} = N_{\rm M}/\sqrt{2}\pi^{3/2} R_1^2 l_{z1}$.

6.3.3 Unpairing dynamics in a molecular condensate near the g−wave Feshbach resonance

The molecular superfluid opens a new door to investigate pairing and unpairing in a Bose condensate. A phase transition is expected when unpairing occurs in a molecular BEC

[123, 120]. Figure 6.9 presents our investigation into the unpairing dynamics. After forming the molecular condensate at $B = 19.4$ G, we ramp the magnetic field in 0.3 ms near and above the Feshbach resonance with a precision of 2 mG. We monitor the dissociation process by imaging the emerging atoms.

When the field is ramped high above the resonance, the molecules quickly and entirely dissociate. In particular, the dissociation rate follows Fermi's golden rule $\Gamma \propto E^{1/2}$, where $E = \Delta\mu(B - B_0)$ is the molecular energy above the continuum and $\Delta\mu = h \times 770$ kHz/G is the relative magnetic moment [28].

Near the Feshbach resonance the system enters the strong coupling regime and the measurement deviates from Fermi's golden rule. Here the measured dissociation energy $\hbar\gamma = \hbar \times 8$ ms^{-1} $= k_{\mathrm{B}} \times$ 61 nK, see Fig. 6.9b, is much greater than μ and T of the BEC and much smaller than the Feshbach resonance width $\Delta\mu\Delta B = k_{\mathrm{B}} \times 410$ nK. The energy is, however, comparable to the universal Fermi energy scale for the molecules $E_{\mathrm{F}} = (\hbar^2/4m)(6\pi^2 n_{3\mathrm{D}})^{2/3} = k_{\mathrm{B}} \times 63$ nK. This result suggests that the dissociation dynamics near the Feshbach resonance is unitarity-limited [66, 51]. Finally, we observe about 40% of the molecules converted back to atoms, and attribute the missing 60% to inelastic collisions between atoms and molecules in the strong coupling regime.

Empirical fits to dissociation rate and dissociated molecular fraction

After preparing a pure molecular BEC below the Feshbach resonance, if the magnetic field is then switched to a value high above the resonance, the molecules quickly dissociate into a continuum of free atoms. The dissociation rate follows Fermi's golden rule as $\Gamma = (2\pi/\hbar)|V_{\mathrm{MA}}|^2\rho(E) = 2m^{1/2}a_{\mathrm{bg}}\Delta\mu\Delta B E^{1/2}/\hbar^2$, where V_{MA} is the coupling matrix element between molecular and atomic states and is independent of the energy E above the continuum to leading order, the density of state $\rho(E) \propto E^{1/2}$ and a_{bg} is the background scattering length. In this high field limit, our measured dissociation rate is con-

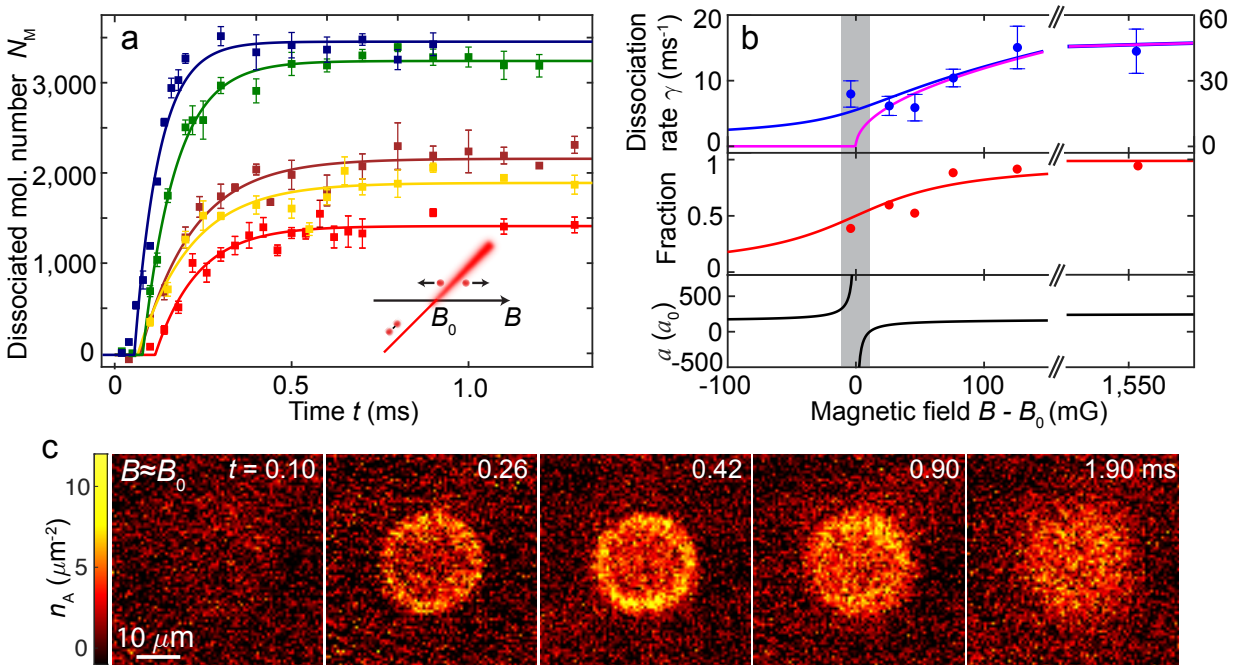

Figure 6.9: **Unpairing dynamics in a molecular condensate near the g−wave Feshbach resonance at $B_0 = 19.874$ G. a**, 5 ms after the formation of molecular BEC with mean 3D density $n_{3D} = 9.7 \times 10^{12}$ cm^{-3}, we ramp the magnetic field back to 19.87 (red), 19.90 (brown), 19.92 (yellow), 19.95 (green) and 20.0 G (blue) and image the atoms from the dissociated molecules. The inset illustrates the unpairing process. **b**, The unpairing rate (upper panel), unpaired fraction (middle panel) extracted from the solid line fits in panel **a** are compared with the atomic s-wave scattering length a (lower panel). The magenta and blue lines are empirical fits based on Fermi's golden rule with the bare and effective density of states, respectively. The red line is an empirical fit (see Methods). The grey shaded area represents the width of the $g-$wave Feshbach resonance. **c**, *In situ* images of unpaired molecules at $B = 19.870(2)$ G near the Feshbach resonance. Error bars represent 1-σ standard deviation.

sistent with Fermi's golden rule $\gamma = \alpha\Gamma$, where the coefficient $\alpha = 0.4(1)$. The fact that α is less than 1 may be because the resonance width ΔB from the measurement of Innsbruck group [100] we used in evaluating Γ is larger than actual resonance width. The dissociation rate in Fig. 6.9b is extracted by fitting the data in Fig. 6.9a using the formula $N_M(t) = N_M(t_0)\{1-\exp[-\gamma(t-t_0)]\}\theta(t-t_0)$, where t_0 is the time when the molecules start to dissociate.

On the other hand, when the magnetic field is ramped to near the resonance where

$\rho(E) \approx 0$, we still observe a finite dissociation rate of 8 ms^{-1}. This is because the molecular state can couple to a band of scattering states that are Lorentzian distributed [53]. We thus define an effective density of state ρ_{eff} to be a convolution between $\rho(E)$ and a Lorentzian distribution. Thus the effective dissociation rate becomes

$$\Gamma_{\mathrm{eff}} = \Gamma\sqrt{(\sqrt{1+\Omega^2/4E^2}+1)/2}, \tag{6.9}$$

where Ω is the full width of the Lorentzian distribution. We use Eq. 6.9 to fit the dissociation rate as a function of the magnetic field we measured, shown as the blue solid line in the upper panel of Fig. 6.9b.

The dissociated molecular fraction drops when the magnetic field is ramped back closer to the resonance, which we attribute to the inelastic collision loss between atoms and molecules near the resonance. The data of the fraction in Fig. 6.9b is fitted using a sigmoid function $f = N_s\{1/2 + (1/\pi)\arctan[\Delta\mu(B - B_0)/V_s]\}$, where N_s and V_s are set as free parameters.

To conclude, we realize BEC of highly-excited, rotating molecules near a narrow Feshbach resonance. The molecules are sufficiently stable at low temperatures to ensure local thermal equilibrium. Unpairing dynamics in molecular condensates is consistent with the universality hypothesis. Our system offers a new platform to study the long-sought atomic BEC−molecular BEC transition, and highlights the fundamental difference between Cooper pairing in a degenerate Fermi gas and bosonic pairing in a BEC.

6.3.4 Molecule formation with different ramp speed across the resonance

As the ramp speed across the Feshbach resonance for molecule formation varies, a dynamical phase transition from an atomic to a molecular BEC happens where the reaction efficiency is predicted to have a nonexponential denpendence on the ramp speed based on an analytical

solution found in a recent study in Ref. [98]. Here we tune the ramp speed by changing the time of the magnetic field ramp from 19.92 G to 19.79 G, starting from an atomic BEC as described in Sec. 6.2. The resulting total number of molecules created from the ramp as a function of the ramp speed is summarized in Fig. 6.10. Our data agrees very well with the analytical solution in Eq. 3.85, which suggests stimulated conversion from atoms in a condensate to molecules.

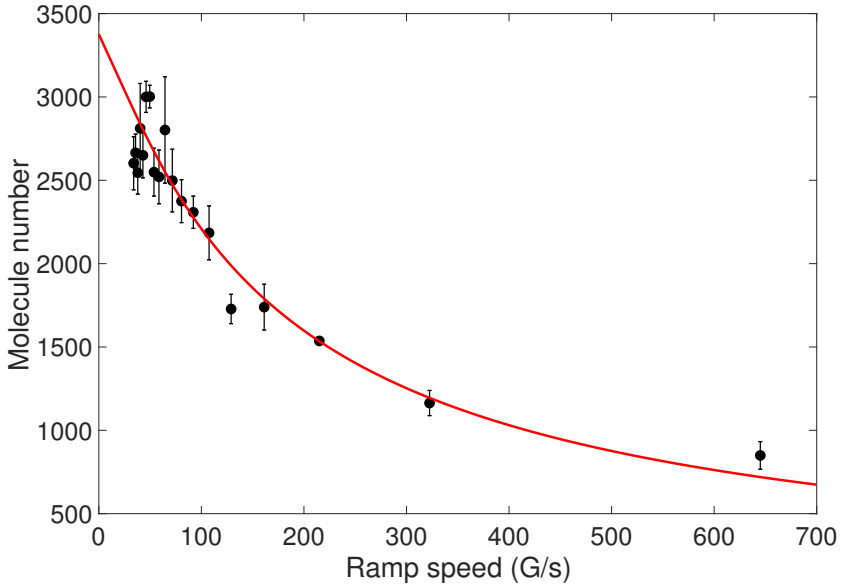

Figure 6.10: **Total number of molecules created after a ramp from 19.92 G to 19.79 G with different speed across the narrow Feshbach resonance.** Solid line is a fit to the data based on Eq. 3.85 with $N = 3.4(3) \times 10^3$ and $g/2\pi = h \times 30(4)$ Hz.

CHAPTER 7

COHERENT REACTION DYNAMICS IN QUANTUM DEGENERACY REGIME

Chemical reactions in the quantum degenerate regime can be drastically different from those in a normal thermal gas. Quantum statistics and collective behavior can dominate the reaction kinetics once the reactants are prepared close to their many-body ground state. Here we report coherent reaction dynamics in atomic Bose-Einstein condensates (BECs) near a g-wave Feshbach resonance. Molecules are produced rapidly from atomic samples after a quench close to the resonance. As a function of the atomic sample temperature, the initial molecule formation rates sharply transition from the values determined by thermal collisions between atoms in normal gas phase to those in the degeneracy regime where the wave nature of atoms dominates. Following the initial proliferation, the molecules reach quasi-equilibrium with the atoms and the number of molecules shows coherent oscillatory evolution with the oscillation frequency determined by both the molecular binding energy and the atomic density. We further enhance the amplitude of the molecule number oscillation by periodically modulating the molecular binding energy. Our observation demonstrates collective chemical reactions in a strongly interacting atomic BEC. We also prepare pure ultracold molecules from atomic BEC and demonstrate the molecule-atom coherence by a Ramsey-like pulse sequence near the Feshbach resonance.

7.1 Introduction

Chemical reactions, typically happening at hundreds of kelvin, are driven by thermal fluctuations that allow a small fraction of particles in the reactants to have high enough momentum to overcome a potential barrier before reaching the final products. The rate constant describing how fast the reaction proceeds follows the celebrated Arrhenius law and strongly

depends on temperature. Nevertheless, chemical reaction can still proceeds at a considerable rate in the zero temperature limit [12], where the wave nature of particles dominates. Thus, quantum statistics, coherence, quantum fluctuations and entanglement can play an important role in the reaction kinetics [122, 22].

Molecules can be prepared in the cold (1K to 1mK) and ultracold regimes (below 1mK) by various techniques [112, 142, 15, 80, 86]. In the cold regime where only a few scattering partial waves dominate, the molecular interaction potentials can be precisely mapped out from measurements of differential scattering cross sections [7] and chemistry can be controlled by external magnetic fields [87] or the geometry of confinement [44]. At ultralow temperature, reactants start to occupy a single external and internal quantum state and the reaction rate can be drastically modified by simply controlling the initial quantum state of reactants [111, 71]. With the addition of external static and oscillating fields, reactants can be tuned to be strongly repulsive at short range [130, 101, 4] and the elastic collision rate can be much larger than the loss rate, which allows efficient evaporative cooling of molecules to quantum degeneracy [125].

Deep in the quantum degeneracy regime where the system is close to its many-body ground state, collective effects can have fundamental influence on chemical reactions. A suppression of reaction rate in a degenerate Fermi gas of KRb molecules is obserseved due to an anti-bunching effect [43]. Recently, the creation of a molecular BEC from an atomic BEC is demonstrated by us, see Chapter 6. In a molecular Bose-Einstein condensate, novel Bose-enhanced chemistry is proposed to modify the branching ratio in photodissociation, which can lead to exponential buildup of the macroscopic population in the selected product states [107]. On the other hand, starting from an atomic BEC, molecules created from a coherent Raman transition can show collective oscillation in its population due to the bosonic stimulated emission of atoms or molecules into their condensed phases [64].

In zero temperature limit, the reaction dynamics originate from coupling between the

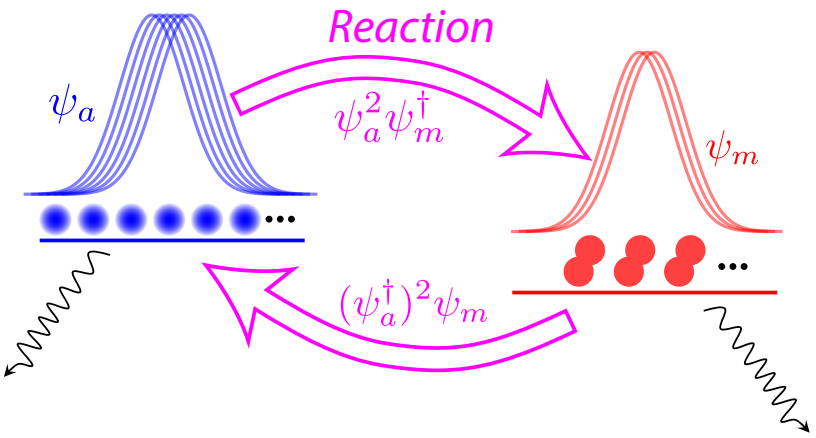

Figure 7.1: **Reactive coupling between atomic and molecular fields.** Cs atoms form a condensate in a 3D harmonic trap where each atom is described by a wave function ψ_a (blue). Near a Feshbach resonance where the atomic scattering state has an energy close to the molecular bound state, atoms are collectively paired into molecules described by wave function ψ_m (red) through the process $\psi_a^2\psi_m^\dagger$. Molecules can also coherently dissociate back to atoms through the reverse process $(\psi_a^\dagger)^2\psi_m$. Both atoms and molecules can decay to other channels through inelastic collisions between each other.

quantum fields of reactants and products. For a synthesis reaction, one of the simplest possible reactions in nature, the dynamics are induced by reactive coupling between atomic and molecular fields ψ_a and ψ_m, respectively (see Fig. 7.1). ψ_a and ψ_m evolve cooperatively according to the following equations of motion

$$\begin{aligned} i\dot{\psi}_m &= \delta(B)\psi_m + \Omega\psi_a^2 \\ i\dot{\psi}_a &= 2\Omega\psi_m\psi_a^\dagger, \end{aligned} \tag{7.1}$$

where Ω is the Feshbach coupling strength and $\delta(B)$ is the energy detuning between two free atoms and one molecule. Rich and interesting dynamics can be derived from Eq. 7.1, see Sec. 3.2 [140, 122]. Starting from a pure atomic BEC, coherent oscillation is predicted to happen between the atomic and molecular BEC population, which damps due to entanglement between them. The oscillation frequency depends strongly on atomic and molecular

densities, signifying collective behaviour of the reaction.

Here we report the observation of novel coherent synthesis reaction dynamics in condensates of Cs atoms near a narrow g-wave Feshbach resonance [30]. After quench close to the resonance, the number of Cs_2 molecules first grows monotonically from zero. By preparing the initial atomic sample at different temperature regimes, we can tune the initial molecule formation rate from the value determined by thermal collisions between atoms in normal phase to that in the quantum degenerate regime where the wave nature of particles dominates. The molecules then reach quasi-equilibrium with atoms after the first monotonic increase stage [97, 29] and develop coherent oscillations in their population [47]. The frequency f of the molecule number oscillation follows the generalized Rabi frequency $f = \sqrt{\delta(B)^2 + \Omega^2}$, with Ω depending on the atomic BEC density [140]. By adding a resonant AC modulation to the magnetic field, in the spirit of Shapiro resonances [121], we further amplify the oscillation of molecular population.

7.2 Experimental setup

Our experiment starts with an ultracold Bose gas of 1.6×10^4 to 4.7×10^5 cesium atoms near a Feshbach resoance. The atoms can be cooled to BEC in a 3D harmonic trap or 2D box potential [147]. We tune the temperature and total atom number by controlling the optical trap depth at the end of forced evaporation [74]. We induce the reaction between atoms by quenching the magnetic field to a value below or above a closed channel dominated g-wave Feshbach resonance at $B_0 = 19.849(1)$ G from our molecular binding energy measurements. This resonance has a narrow width $\Delta B = 8.3(3)$ mG from our scattering length measurements and couples two free atoms into a chemically bound spinning molecule with its size given by the van der Waals length $R_{\mathrm{vdW}} = 5.3$ nm [30], see Fig. 7.1. After some reaction time, we decouple the atoms and molecules by quickly tuning the magnetic field off resonance. Then we either image the remaining atoms at the same field or image the

produced molecules by first dissociating them above resonance at 20.48 G before imaging the atoms from dissociation [147].

7.3 Results

7.3.1 Molecule formation rate in classical and quantum degenerate regimes.

To demonstrate that chemical reaction follows a different rule in degeneracy regime from the thermal regime, we study the molecule production rate when the initial atomic sample is cooled below BEC transition temperature. In a thermal gas of ultracold atoms above the critical temperature, the production rate is determined by collisions between pairs of atoms, which is proportional to the atomic density n_a, collision cross section σ and relative velocity v. The branching ratio b_{n} for creating the molecules is usually imperfect and thus less than 1. Therefore, the rate equation that determines the molecular density n_m is given by $\dot{n}_m(\vec{r},t) = \beta_{\mathrm{n}} n_a^2(\vec{r},t)$, where the rate coefficient

$$\beta_{\mathrm{n}} = b_{\mathrm{n}} \sigma v. \tag{7.2}$$

We measure the molecular formation rate in a thermal atomic gas at 19.852(1) G in the unitary regime where the s-wave scattering length diverges [97] and the cross section $\sigma \propto 1/v^2$ [30]. In this regime, the rate coefficient averaged over thermal distribution is $\langle \beta_{\mathrm{n}} \rangle \propto b_{\mathrm{n}}/\sqrt{T}$. Right after magnetic field reaches the target value, the molecule number grows linearly (see Fig. 7.2a) and from the slope $\dot{N}_m$ we extract the rate coefficient as $\beta = \dot{N}_m / N_a \bar{n}_a$ (see Fig. 7.2b), where N_a and $\bar{n}_a$ are initial total atom number and average 3D atomic density, respectively. We find the rate coefficient we measure in the thermal regime is consistent with the $1/\sqrt{T}$ scaling, from which we extract the probability $b_{\mathrm{n}} = 6.5\%$ for each collision between two atoms to create a molecule. The fact that this branching ratio

is much less than 1 suggests that atoms decay into other channels which we cannot detect.

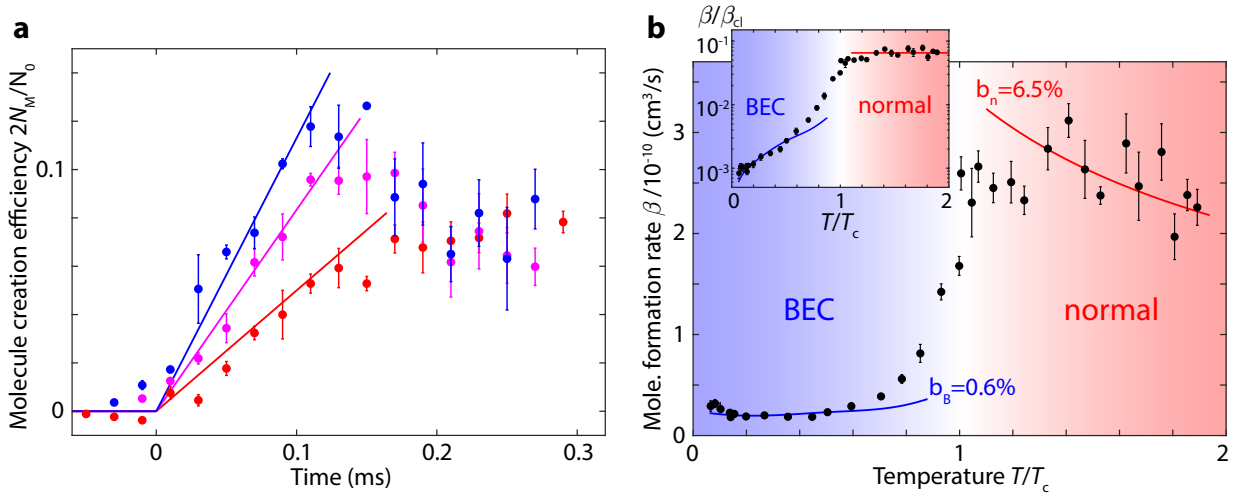

Figure 7.2: **Molecule formation rate in classical and quantum degeneracy regimes.** **a**, Time evolution of molecule creation efficiency after quench to 19.852(1) G for initial atomic temperature at $T/T_c = 1.8$ (red), 0.5 (magenta), 0.14 (blue). The solid lines are piecewise linear fits for extracting molecule formation rate $\dot{N}_{\rm M}$. **b**, The molecule formation rate coefficient β is extracted from measurements similar to those shown in **a**. The red line is a fit to the data at $T/T_c > 1.3$ using $\beta_{\rm cl} \propto 1/\sqrt{T}$, with the branching ratio $b_{\rm n} = 6.5\%$ for creating molecules from collisions between atoms in the normal gas. The blue line fits the data at $T/T_c < 0.7$, representing rate coefficient $\propto 1/\sqrt{E_n}$ in zero temperature limit with branching ratio $b_{\rm B} = 0.6\%$, where E_n is the Fermi energy determined by inter particle spacing in atomic BEC; see text. The inset shows the rate coefficient normalized by $\beta_{\rm cl}$ in log-linear scale. Data values in **a** represent the average and error bars represent one standard deviation of the mean, estimated from the statistical errors of 4-8 measurements. The error bars in **b** represents 95% confidence interval from fitting time traces of molecule number.

On the other hand, in the quantum degeneracy regime where all the atoms condense, thermal effect is absent and quantum fluctuation plays an important role. In the unitary regime, the energy scale of temperature $k_{\rm B}T$ is replaced by the Fermi energy $E_n = \hbar^2(6\pi^2\bar{n}_a)^{2/3}/2m$ that is determined by the only length scale — interparticle spacing $(1/\bar{n}_a)^{1/3}$ — remaining in the system (apart from the finite sample size), where $k_{\rm B}$ is the Boltzmann constant, $\hbar$ is the reduced Planck constant and m is atomic mass. Thus the corresponding rate coefficient in atomic BEC is

$$\beta_{\mathrm{B}} = b_{\mathrm{B}} \frac{32\hbar^2\sqrt{\pi}}{m^{3/2}\sqrt{E_n}} \tag{7.3}$$

in which b_{B} the effective probability of associating two atoms in BEC into a molecule.

Indeed, as we cool down atomic samples to below the critical temperature where condensate starts to form, we find the rate coefficient sharply transitions from β_{T} into the value that is consistent with β_{B} (see Fig. 7.2), with the branching ratio $b_{\mathrm{B}} = 0.6\%$, much lower than b_{n} in the thermal regime. This sharp transition is well captured by our two-component model in which the rate coefficient is a weighted sum of β_{T} and β_{B} with the weights determined by atomic density distributions of BEC and thermal fractions, respectively.

Derivation of molecular formation rate coefficients

Let's first consider collisions in a classical atomic gas, where the probability for each collision between two atoms to create a molecule is b_n. Within time Δt, the average number of atoms colliding with an atom moving with relative velocity v and collision cross section σ is (see Fig. 7.3)

$$\bar{q} = n(\mathbf{r}, t)\sigma v \Delta t, \tag{7.4}$$

where $n(\mathbf{r}, t)$ is the local atomic density. However, the number of collision events has some fluctuation around the average value $\bar{q}$ and here we assume it is a random variable q that follows the Poisson distribution $P(q) = e^{-\bar{q}}\bar{q}^q/q!$, where $q = 0, 1, 2, ...$ Then the probability for the atom to survive all the collisions within Δt is $P_N = \sum_{q=0}^{\infty}(1 - b_n)^q P(q) = \exp\left[-b_n n(\mathbf{r}, t)\sigma v \Delta t\right]$, which means the probability for the atom to be associated into a

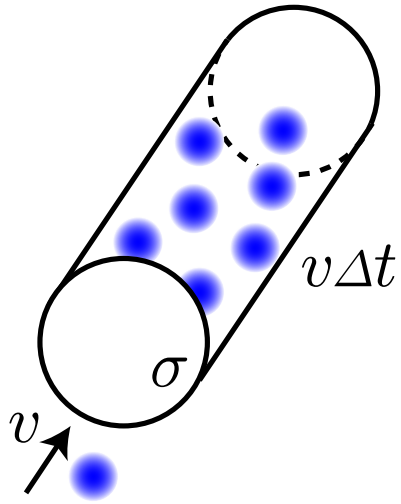

Figure 7.3: **Diagram for illustration of collisions in a classical atomic gas.** The collision happens within time Δt for an atom moving with relative velocity v and collision cross section σ.

molecule is:

$$P_A = 1 - P_N = 1 - e^{-b_n n(\mathbf{r},t)\sigma v \Delta t} \approx b_n n(\mathbf{r},t)\sigma v \Delta t. \tag{7.5}$$

Therefore, the change of local molecular density $m(\mathbf{r},t)$ is $\Delta m(\mathbf{r},t) = n(\mathbf{r},t)p_A = b_n n^2(\mathbf{r},t)\sigma v \Delta t$, i.e.,

$$\dot{m}(\mathbf{r},t) = \beta_n n^2(\mathbf{r},t), \tag{7.6}$$

in which the molecular formation rate coefficient is

$$\beta_n = b_n \sigma v. \tag{7.7}$$

In our experiment at finite temperature, the relative kinetic energy $E_k = \hbar^2 k^2/m$ is Boltzmann distributed with probability density $p(E_k) = \frac{2}{\sqrt{\pi}}(k_{\mathrm{B}}T)^{-3/2} e^{-E_k/k_{\mathrm{B}}T}\sqrt{E_k}$, from

which we obtain the probability density for relative momentum k as

$$p(k) = p(E_k)\frac{dE_k}{dk} = \frac{4\hbar^3 k^2}{\sqrt{\pi}(mk_{\mathrm{B}}T)^{3/2}} e^{-\hbar^2 k^2/mk_{\mathrm{B}}T}. \tag{7.8}$$

On Feshbach resonance, the unitarity-limited cross section is $\sigma = 8\pi/k^2$ [30]. We eventually get the thermally averaged rate coefficient as

$$\beta_n = b_n \langle \sigma v \rangle_T = b_n \int_0^\infty \frac{8\pi}{k^2}\frac{\hbar k}{m/2} p(k)dk = b_n \frac{32\hbar^2\sqrt{\pi}}{m^{3/2}\sqrt{k_{\mathrm{B}}T}}. \tag{7.9}$$

In the limit where thermal energy vanishes, after quench to the unitary regime on Feshbach resonance, universality suggests we should replace the thermal energy by the Fermi energy E_n that is determined by the only length scale—interparticle spacing—that remains in the system [97],

$$\beta_{\mathrm{B}} = b_{\mathrm{B}} \frac{32\hbar^2\sqrt{\pi}}{m^{3/2}\sqrt{E_n}}, \tag{7.10}$$

where b_{B} is the branching ratio in zero temperature limit.

In our experiment, we measure the initial formation rate of total molecule number (see Fig. 7.2a), which is an integration of local molecular density over space. Integrating over $\mathbf{r}$ on both sides of Eq. 7.6, we get $\dot{M}|_{t=0} = \beta N_0 \bar{n}_0$ with the initial average atomic density $\bar{n}_0 = \int n^2(\mathbf{r},t)d^3\mathbf{r} / \int n(\mathbf{r},t)d^3\mathbf{r}$ and total atom number N_0. The rate coefficient is thus obtained from

$$\beta = \frac{\dot{M}|_{t=0}}{N_0 \bar{n}_0}. \tag{7.11}$$

Molecule formation in an atomic mixture of thermal and BEC fractions

To capture the sharp transition of the rate coefficient around critical temperature T_c shown in Fig. 7.2b, here we develop the following two-component model including both the thermal and BEC fractions. There are three possible collision processes:

1. Collision between atoms in BEC:

$$\dot{m}_{\rm B}(\mathbf{r},t) = \beta_{\rm B} n_{\rm B}^2(\mathbf{r},t). \tag{7.12}$$

2. Collision between atoms in normal gas:

$$\dot{m}_{n}(\mathbf{r},t) = \beta_{n} n_{n}^2(\mathbf{r},t). \tag{7.13}$$

3. Collision between one atom in BEC and one atom in normal gas:

$$\dot{m}_{n\rm B}(\mathbf{r},t) = 2\beta_{n\rm B} n_{\rm B}(\mathbf{r},t) n_n(\mathbf{r},t) = 2\beta_{n} n_{\rm B}(\mathbf{r},t) n_n(\mathbf{r},t), \tag{7.14}$$

where we assume $\beta_{n\rm B} = \beta_n$.

Substituting Eq. 7.12-7.14 into Eq. 7.11, we get the molecular formation rate coefficient in the mixture to be

$$\begin{aligned}\beta &= \frac{\int d^3\mathbf{r} \beta_{\rm B} n_{\rm B}^2(\mathbf{r},t) + \beta_n [n_n^2(\mathbf{r},t) + 2 n_{\rm B}(\mathbf{r},t) n_n(\mathbf{r},t)]}{\int d^3\mathbf{r} [n_{\rm B}(\mathbf{r},t) + n_n(\mathbf{r},t)]^2} \\ &= w_{\rm B}\beta_{\rm B} + w_n \beta_n,\end{aligned} \tag{7.15}$$

where the weights of BEC and normal components are given by:

$$w_{\rm B} = \frac{\int n_{\rm B}^2(\mathbf{r},t) d^3\mathbf{r}}{\int [n_{\rm B}(\mathbf{r},t) + n_n(\mathbf{r},t)]^2 d^3\mathbf{r}},\ w_n = \frac{\int [n_n^2(\mathbf{r},t) + 2 n_{\rm B}(\mathbf{r},t) n_n(\mathbf{r},t)] d^3\mathbf{r}}{\int [n_{\rm B}(\mathbf{r},t) + n_n(\mathbf{r},t)]^2 d^3\mathbf{r}}. \tag{7.16}$$

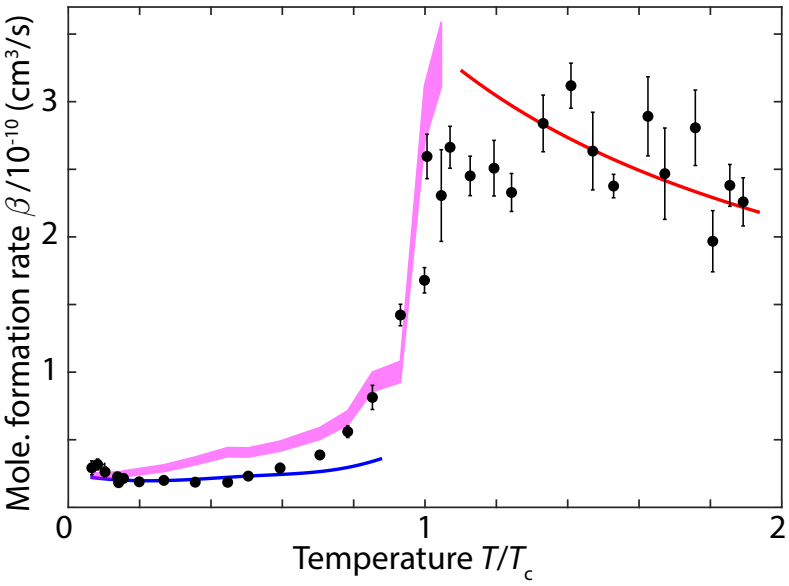

Figure 7.4: **Comparison between molecular formation rate coefficient calculated based on the two-component model and experimental data in Fig. 7.2b.** The magenta band is calculated based on Eq. 7.15 using the fit results shown by the red and blue lines and the weights w_{B} and w_n of BEC and normal fractions from measurements.

Note that the weights in Eq. 7.16 are different from BEC fraction squared and one minus BEC fraction squared due to the non-uniform density in the harmonic trap used for the rate coefficient measurements shown in Fig. 7.2. The two-component model captures the sharp transition of our measured rate coefficients around $T/T_c = 1$ very well, see Fig. 7.4.

Evaluation of the initial 3D average atomic density

To evaluate the initial 3D average atomic density, we model the atomic density distribution for the general case where both normal and BEC components exist as [84]

$$n(\mathbf{r}) = n_n g_{3/2}(\prod_{i=1}^{3} e^{-r_i^2/\sigma_i^2}) + n_{\mathrm{B}} \max(1 - \sum_{i=1}^{3} \frac{r_i^2}{R_i^2}, 0), \tag{7.17}$$

where $(r_1, r_2, r_3) = (x, y, z)$ are spatial coordinates and $g_{3/2}(x) = \sum_{k=1}^{\infty} x^k/k^{3/2}$ is the polylogarithm function. Our vertical absorption imaging integrate over z axis and obtains

the 2D column density as

$$n(x,y) = \int_{-\infty}^{\infty} n(\mathbf{r})dz = \sqrt{\pi} n_n \sigma_z g_2(\prod_{i=1}^{2} e^{-r_i^2/\sigma_i^2}) + \frac{4}{3} n_{\mathrm{B}} R_z (1 - \frac{x^2}{R_x^2} - \frac{y^2}{R_y^2})^{3/2}. \quad (7.18)$$

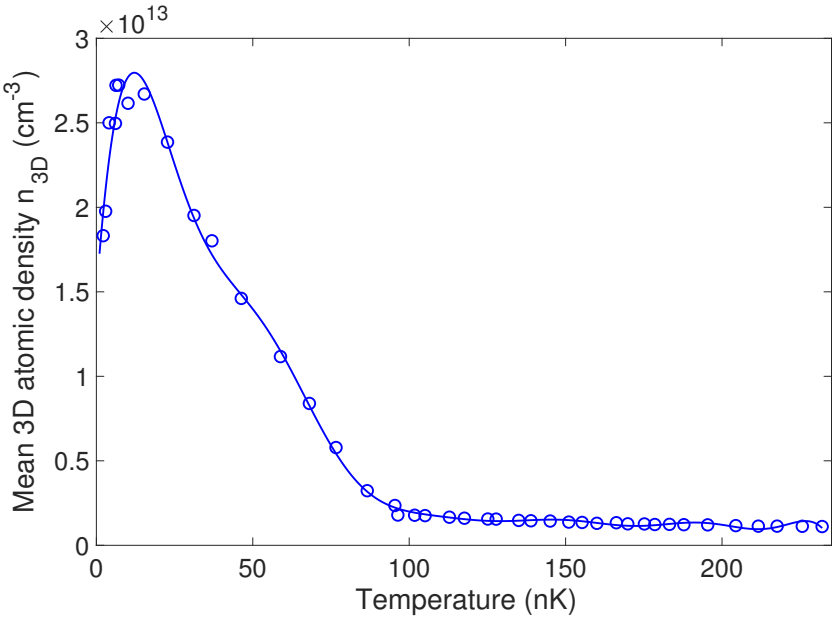

Figure 7.5: **Initial 3D average atomic density as a function of temperature, evaluated based on Eq. 7.20.** The solid line is an empirical fit to the data.

We use Eq. 7.18 to fit 2D column density distributions from our experiments and extract the widths σ_x, σ_y, R_x and R_y and total particle number N_n and N_{B} in normal and BEC fractions, respectively. We use the scaling to calculate cloud widths in z direction as $\sigma_z = (\omega_y/\omega_z)\sigma_y$ and $R_z = (\omega_y/\omega_z)R_y$ based our independent measurements of trap frequencies ω_y and ω_z. Then the 3D peak densities are given by

$$n_n = \frac{N_n}{g_3(1)\pi^{3/2}\bar{\sigma}^3}, \; n_{\mathrm{B}} = \frac{15N_{\mathrm{B}}}{8\pi\bar{R}^3}, \quad (7.19)$$

where $\bar{\sigma} = (\sigma_x\sigma_y\sigma_z)^{1/3}$ and $\bar{R} = (R_xR_yR_z)^{1/3}$. Eventually, with all the parameters deter-

mined in Eq. 7.17, we evaluate the 3D average density as

$$\bar{n} = \frac{\int n^2(\mathbf{r}) d^3\mathbf{r}}{\int n(\mathbf{r}) d^3\mathbf{r}}, \tag{7.20}$$

as shown in Fig. 7.5.

7.3.2 Dynamics of the molecular formation process after a quench close to the g-wave Feshbach resonance in atomic BECs.

The initial rapid production of molecules is accompanied by fast loss of atoms (see Fig. 7.6a). To reveal the underlying reaction mechanisms, we measure the atom loss rate γ_a over a wide range of 192 times the resonance width ΔB and observe a variation of γ_a over about 5 orders of magnitude (see Fig. 7.6c). For $\gamma < 10^{-2}$ ms^{-1}, the line shape agrees well with a symmetric Lorentzian profile. Since the molecule fraction in a coupled atomic and molecular two-level system also has a Lorentzian line shape as a function of the energy detuning $\delta(B)$, this suggests the loss is induced by coherent coupling between atoms and molecules and atoms are lost likely due to their inelastic collision with molecules [30].

Near and below the resonance (19.80 to 19.86 G), however, the loss rates are larger than the background values of the Lorentzian profile and are fitted well by a Gaussian function. We conjecture that the assymmetric enhancement of loss rate near the resonance comes from three-body recombination process where two hyperfine ground state atoms relax into a lower lying molecular state and release the binding energy into kinetic energy of the molecule and a third atom [30]. This is evidenced by the heating of atoms during their initial fast loss (see Fig. 7.6b). We also measured the corresponding molecule formation rate within a similar range near the resonance, and find the formation rate is also asymmetric about the center of the Lorentzian profile, see the inset of Fig. 7.6. This suggests that the molecules we detect near and below the resonance are partially coming from the enhanced atom loss process,

apart from the direct coupling from two atoms into a molecule.

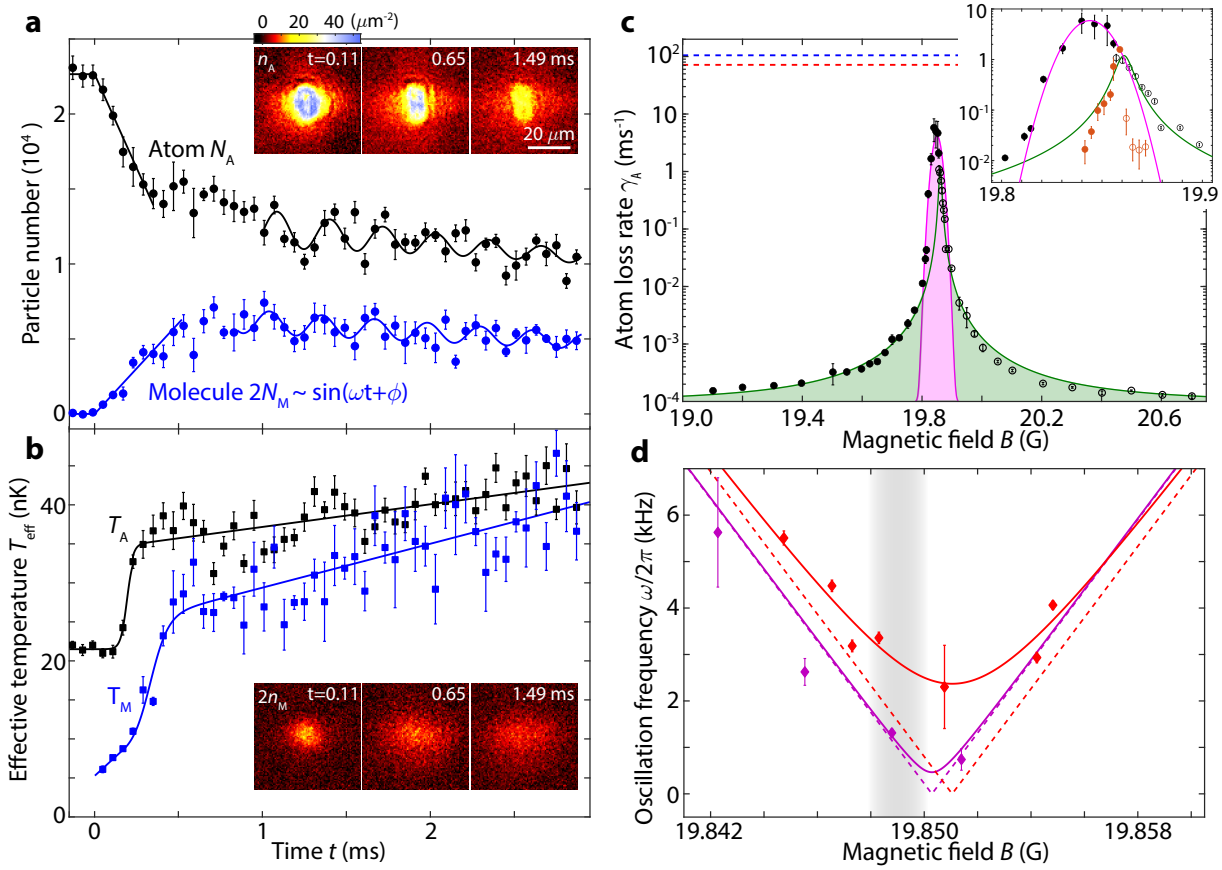

Figure 7.6: **Dynamics of molecular formation process after quench close to the g-wave Feshbach resonance in atomic BEC. a**, Evolution of atomic (N_{A}, black) and molecular population ($2N_{\mathrm{M}}$, blue) as a function of time staying at 19.847 G. Solid lines are fits to the data. **b**, Evolution of atomic (T_{A}, black) and molecular effective temperature (T_{M}, blue) as a function of time staying at 19.847 G. Solid lines are guides to the eye. Insets are example averaged images of atomic and molecular density distributions in momentum space. **c**, Loss rate of atomic population at different magnetic field near the Feshbach resonance. Solid and empty circles are data taken by approaching the target magnetic field from below and above the resonance, respectively. Green and magenta regions show Lorentzian and Gaussian fits. Blue and red dashed lines are unitarity limits for atom loss rate evaluated based on Eq. 7.9 and Eq. 7.10 with the branching ratios set as 1. Inset is a zoom in view for atom loss (black) and molecular formation (orange) rates around the resonance. **d**, Oscillation frequency of molecular population after quench to different magnetic fields close to the resonance (grey shaded region), starting from atomic BEC with mean densities 2.62×10^{13} (red) and 2.39×10^{13} cm^{-3} (purple), respectively. Solid lines are fits based on the generalized Rabi frequency formula $f = \sqrt{[\Delta\mu(B - B_m)]^2 + \Omega^2}$, where B_m is the minimum position and Ω is the Feshbach coupling strength. Dashed lines correspond to $f = |\delta\mu(B - B_m)|$.

The molecule formation and atom loss quickly saturate after the first hundreds of microseconds and atoms and molecules reach a quasi-equilibrium with similar temperature (see Fig. 7.6a,b). Interestingly, the atomic and molecular population are not saturated to constant values, but they show small amplitude oscillations instead. The frequencies of molecule number oscillation at different magnetic fields agree well with generalized Rabi frequency formula $f = \sqrt{\delta(B)^2 + \Omega^2}$, which suggests coherent coupling between atoms and molecules at later time of the reaction (see Fig. 7.6d). Away from the resonance, the relative phase winding between atomic and molecular states is mostly determined by the molecular binding energy $|\delta(B)|$ [47]. On the other hand, the oscillation frequency on resonance is predicted to be the Feshbach coupling strength Ω, which has a dependence on square root of the atomic density $\sqrt{\bar{n}_a}$ [140]. For two different atomic samples with average density of 2.39×10^{13} and 2.62×10^{13} cm^{-3}, we measured different Ω that are 0.6 and 2.6 kHz, respectively. It is remarkable that a small increase of atomic density by $\sim 10\%$ leads to enhancement of the oscillation frequency by $\sim$4 times and it requires further investigation into the discrepancy between our measurements and the theory prediction.

Determination of Feshbach resonance position from molecular binding energy measurements

To determine the position of the narrow g-wave Feshbach resonance in our system, we perform measurements of molecular binding energy at different offset magnetic fields using the magnetic field modulation spectroscopy [136, 92] and find the field value where the binding energy reaches zero.

We start with atomic BEC at 23 nK prepared at $\sim$19.5 G. Then we quench the field to an offset value $B_{\rm dc}$ near the resonance and simultaneously modulate the field sinusoidally with peak-to-zero amplitude $B_{\rm ac} = 5$ mG for 5 ms. We scan the modulation frequency and measure the number of remaining atoms or created molecules, see Fig. 7.7a. We have

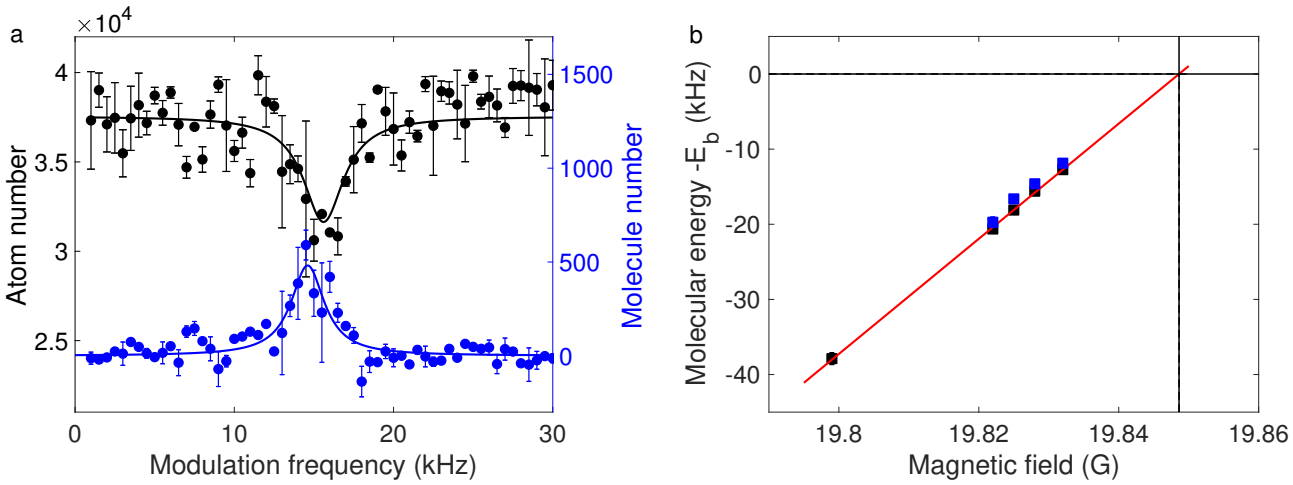

Figure 7.7: **Molecular binding energy measurement using magnetic field modulation spectroscopy for atomic BECs at different offset magnetic fields. a**, Atom loss (black) and molecule creation (blue) at different modulation frequencies for offset magnetic field $B_{\rm dc} = 19.828$ G and peak-to-zero modulation amplitude $B_{\rm ac} = 5$ mG applying for 5 ms. **b**, Molecular binding energy $E_{\rm b}$ extracted from peak positions of the spectra of atom (blck) and molecule (blue) number for similar measurements as shown in **a**. The red line is a linear fit to black data points and reaches 0 at $B_0 = 19.849(1)$ G.

confirmed that the resulting peak position of the spectrum is not sensitive to the modulation amplitude and modulation time. The spectra are fitted using the asymmetric line shape function [128]

$$N(f) = N_0 - \Delta N \frac{a(f - f_0 - b)^2}{(f - f_0)^2 + a(f - f_0 - b)^2}, \tag{7.21}$$

where N_0 is off resonant background value, ΔN is the signal on resonance. Parameters a and b control asymmetry of the line shape. The peak positions corresponding to molecular binding energies are extracted from the fit for different offset magnetic fields, see Fig. 7.7b. A linear fit to the data points from atoms in Fig. 7.7b gives resonance position to be $B_0 = 19.849(1)$ G where the binding energy goes to zero. The slope of the linear fit gives magnetic moment different between two free atoms and a molecule to be $\Delta\mu = 0.54(2)\mu_{\rm B}$, which is consistent with the measurements in Ref. [28].

Extraction of molecule number oscillation frequency

To extract the oscillation frequency of molecule number at late time of the evolution after quenching close to the resonance, we fit the data after 1 ms using the function (see Fig. 7.8a) [37]

$$y(t) = A - B(t - t_{\text{delay}}) + C\exp[-\gamma(t - t_{\text{delay}})]\sin[2\pi f(t - t_{\text{delay}}) + \phi], \tag{7.22}$$

where $t_{\text{delay}} = 0.15$ ms is the time for magnetic field to reach the target value. The first two terms describes overall decay of molecule number and the third term represents damped oscillation at frequency f.

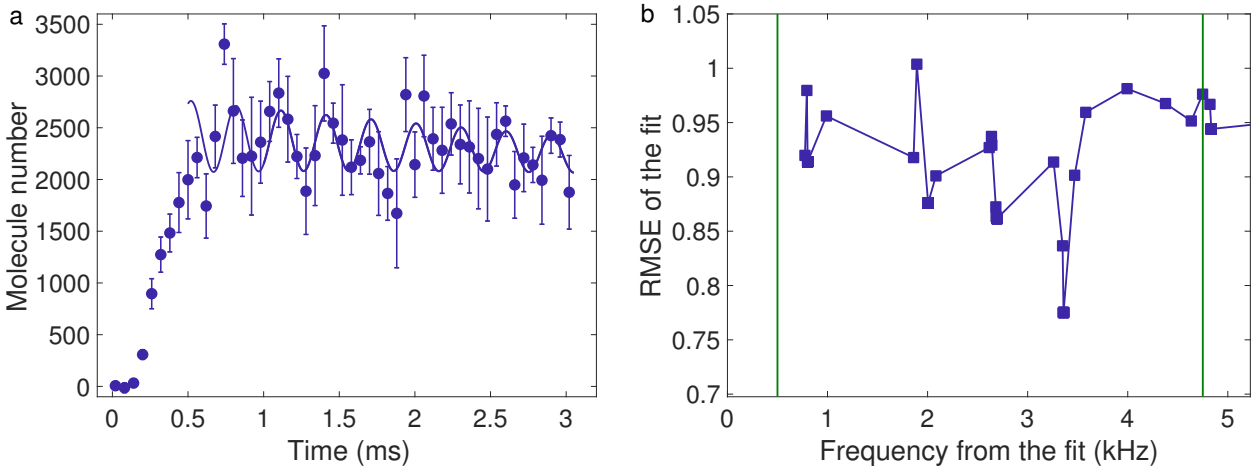

Figure 7.8: **Fitting time trace of molecule number for extraction of its oscillation frequency. a**, Fit of data (the same as that in Fig. 7.6a) at $t > 1$ ms using Eq. 7.22. **b**, The root mean squared error of fit results obtained from different initial guess of the frequency f in Eq. 7.22, see text.

Since the fit can easily fall into a local optimum, we tried different initial guess of the frequency f for the fit within the range of 0.75 kHz to 4.75 kHz with a stepsize of 0.05 kHz. The initial guess for rest of the parameters are fixed as: $B = \frac{N(t=1\text{ ms}) - N(t=3\text{ ms})}{3\text{ ms} - 1\text{ ms}}$, $A = N(t = 1\text{ ms}) + B \times (1\text{ ms} - t_{\text{delay}})$, $C = 500$, $\gamma = 0.25\text{ ms}^{-1}$, $\phi = 0$, which the fit result is not sensitive to. For each fit result, we evaluate the corresponding difference between fit

and data by calculating the root mean squared error (RMSE)

$$\text{RMSE} = \sqrt{[\frac{1}{\nu}\sum_{i=1}^{n} w_i(y_i - \hat{y}_i)^2]}, \tag{7.23}$$

where $y_i - \hat{y}_i$ is residual, w_i is the weight given by one over errorbar squared, ν is residual degrees of freedom given by the number of data points n minus the number of fitted coefficients m (m = 6 for this fit). Eventually, we pick the fit result that has minimum RMSE, see Fig. 7.8b.

7.3.3 Amplification of the molecule number oscillation through the magnetic field modulation.

To further steer the reaction process, we apply additional external driving to atomic samples near the Feshbach resonance. The coupled atomic and molecular BECs in our system is effectively a bosonic Josephson junction [96], in close analogy to Cooper-pair Josephson junction in superconducting devices [14]. Inspired by the Shapiro resonance effect where adding a small resonant ac component to an applied voltage enhances dc tunneling current in the superconducting Josephson junction, here we modulate the magnetic field at a frequency close to the free molecule number oscillation frequency at a static field, with the hope to facilitate the reaction. At 19.847 G, the molecule number oscillates around 4,000 at 1.4 kHz, with a contrast of $\sim$10% (see Fig. 7.9b). After the application of magnetic field modulation with a peak-to-zero amplitude of 4 mG around 19.847 G, we find the oscillation contrast increases by a factor of 3 to 4, see Fig. 7.9c and e. We also see clear damping of the molecule number oscillation with the driving field, likely due to additional heating introduced by the driving.

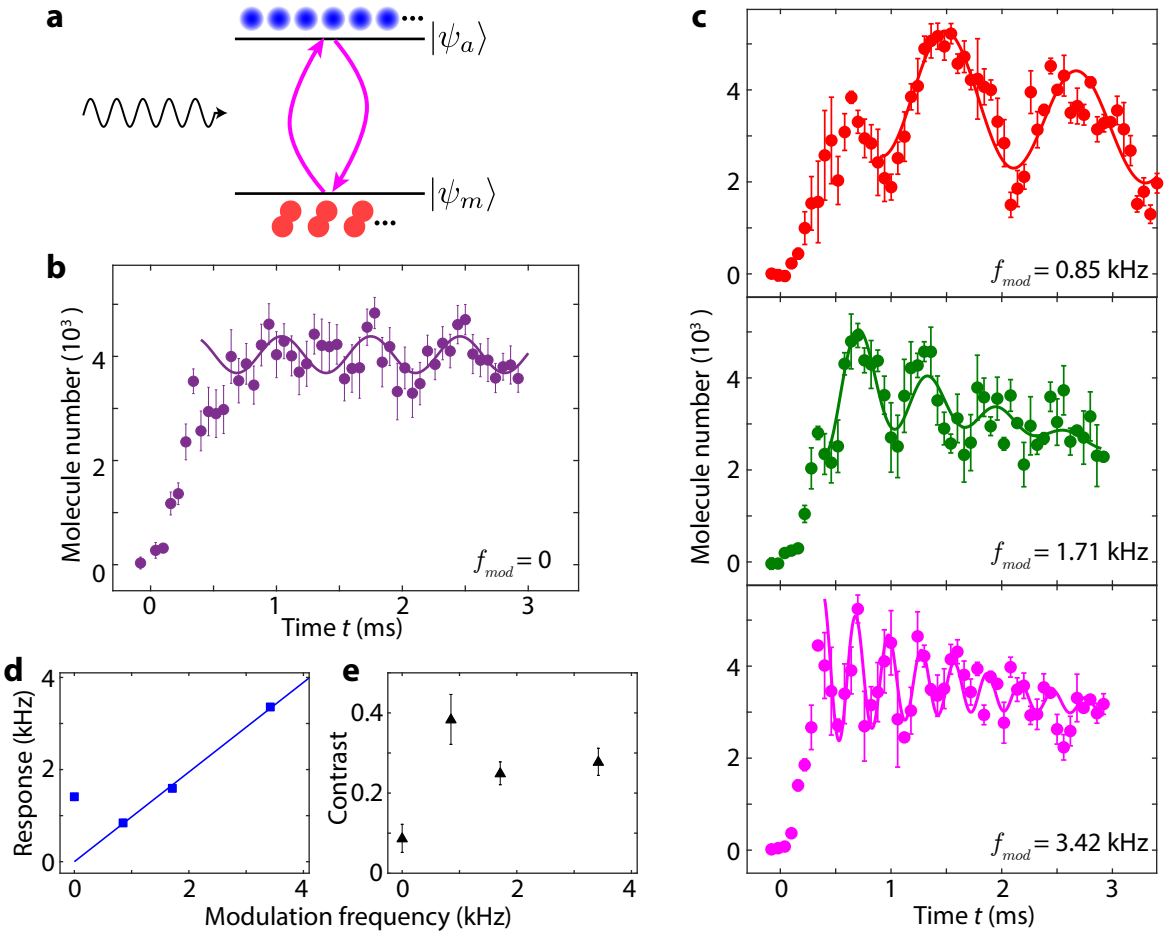

Figure 7.9: **Amplification of coherent oscillation of molecular population through magnetic field modulation. a**, Schematic diagram of molecular formation near Feshbach resonance with additional sinusoidal magnetic field modulation. **b**, Evolution of molecular population after quench to a static magnetic field at 19.847(1) G. **c**, Time traces of molecule number with magnetic field modulation at 0.85 (red), 1.71 (green) and 3.42 kHz (magenta) with peak-to-zero modulation amplitude $B_{\rm ac} \approx 4$ mG at an offset field $B_{\rm dc} = 19.847(1)$ G. **d** and **e**, Frequency and contrast of molecule number oscillation extracted from the fits in **b** and **c** (the solid lines) based on Eq. 7.22. Blue solid line is a linear fit without offset to data points with nonzero modulation frequencies, with a slope 0.97(3).

Subharmonic Shapiro-like resonance

As is predicted in Ref. [96], Shapiro resonances occur in ultracold molecule production from atoms when the molecular binding energy matches integer multiples of the magnetic field modulation frequency in vicinity of a Feshbach resonance. Previously in Sec. 7.3.2 we did the modulation spectroscopy for precisely measuring the molecular binding energy and thus

the resonance position in perturbation regime with small modulation amplitude, such that only a single resonance occurs that corresponds to the molecular binding energy, see Fig. 7.7. Here we double the modulation amplitude used in Sec. 7.3.2 and set the offset field to be $B_{\rm dc} = 19.833$ G where the binding energy is $E_{\rm b} = 12$ kHz, clear double peaks appear in both the atom and molecule number spectra at ~ 12 and 6 kHz, see Fig. 7.10. Further investigation are need to see if there is any many-body effect in these Shapiro-like resonances.

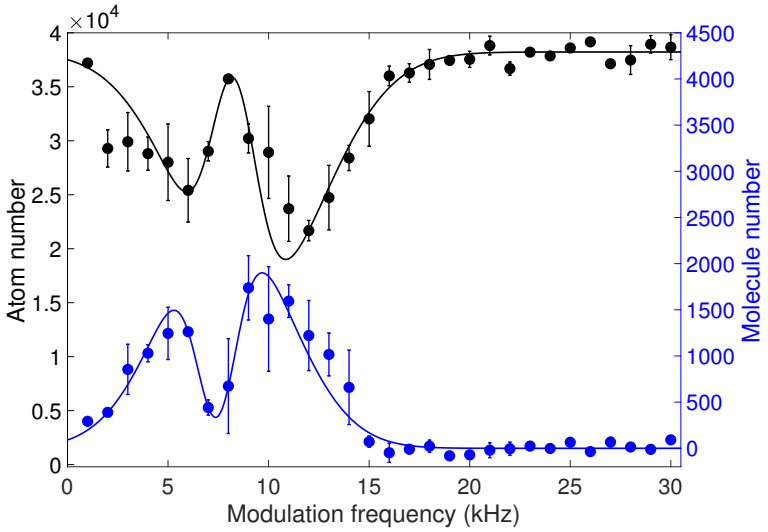

Figure 7.10: **Shapiro-like resonances in atomic BEC when the frequency of external magnetic field modulation is scanned with fixed modulation amplitude $B_{\rm ac} = 10$ mG at an offset field $B_{\rm dc} = 19.833$ G for 5 ms.** The solid lines are guides to the eye.

7.3.4 Coherence in the molecule dissociation revealed by a Ramsey-like pulse sequence

Here we prepare pure ultracold molecules as our starting point, instead of pure atoms as in previous sections, and bring the molecules to the resonance point and investigate molecule dissociation process. As is shown in Sec. 3.2.2, non-trivial dynamics can occur after quench close to the resonance starting from a molecular BEC, e.g. the population in atomic BEC can grow exponentially from quantum fluctuation. As a first attempt to investigate into molecule

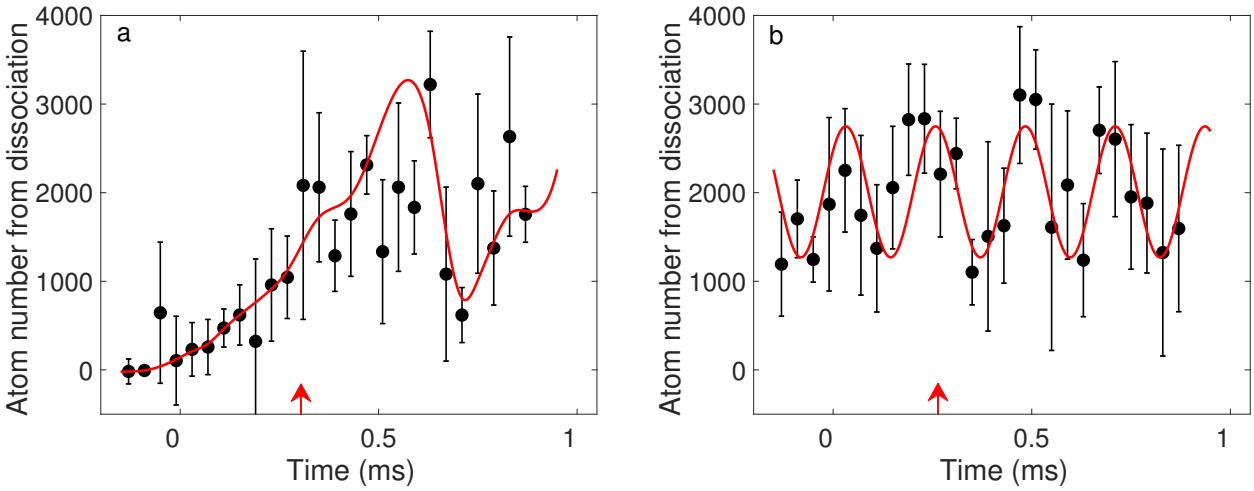

Figure 7.11: **Choosing length of the first and second pulses of magnetic field at Feshbach resonance. a**, Molecules are quenched to resonance and held for variable time before atoms from dissociation are imaged. The red arrow indicates the time when about half of the molecules are dissociated into atoms, which we choose as the duration $\tau_1 = 0.31$ ms of the first pulse. Red solid line is guide to the eye. **b**, After applying the first pulse with duration τ_1 and staying at $B_t = 19.838$ G for 0.2 ms, we scan the length of the second pulse and measure the resulting variation of atom number. We choose the time $\tau_2 = 0.23$ ms as duration of the second pulse when second maximum in the atom number occurs, as indicated by the red arrow. Red solid line is a sinusoidal fit.

dissociation process at Feshbach resonance, here we show that a coherent superposition of atomic and molecular states forms.

We first create ∼1700 molecules by associating atoms in a pure atomic BEC at $B_0 = 19.849(1)$ G for 0.4 ms and blowing away residual atoms using a resonant light pulse below the resonance. The molecular samples we prepare have a temperature of 26 nK from focused time-of-flight measurement (see Sec. 2.2). Then we bring the molecules close to resonance for dissociation. To demonstrate coherence in the dissociation process, we apply the Ramsey-like pulse sequence which is first used to show atom-molecule coherence in an atomic BEC in Ref. [47], see Fig. 7.12a. The duration of the two pulses approaching resonance point at B_0 is chosen such that each pulse dissociates half of the molecules, see Fig. 7.11. We scan the time t holding at B_t between the two pulses and measure the resulting number of atoms from dissociation. The atom number shows oscillation at a frequency close to the molecular

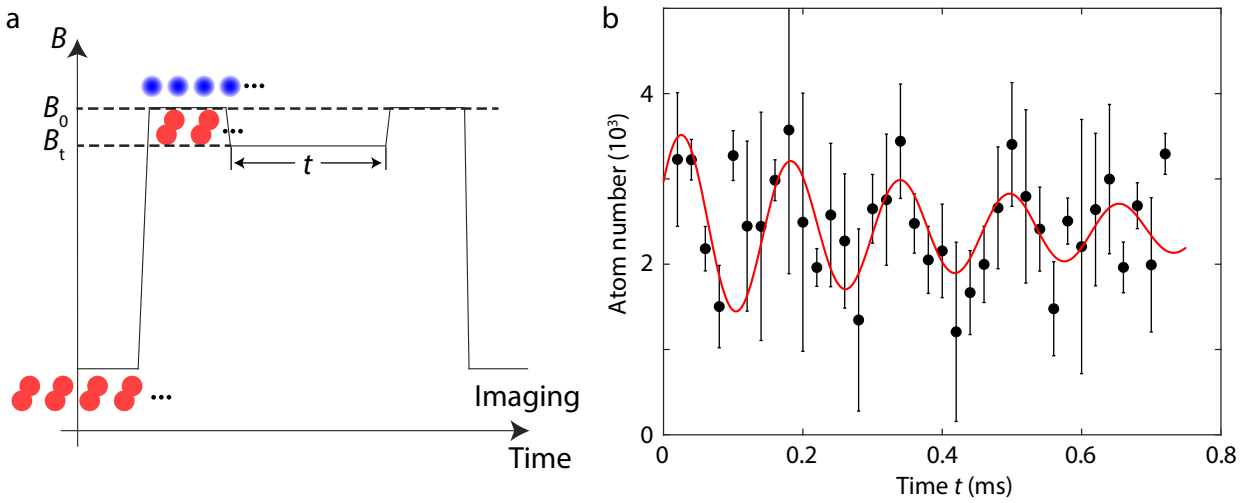

Figure 7.12: **Coherence in dissociation of ultracold molecules. a**, Schematic diagram of the Ramsey-like pulse sequence. Pure molecular sample is prepared at ∼19.5 G. Then two magnetic field pulses at resonance B_0 with their duration determined in Fig. 7.11 and a variable hold time t in between at B_t are applied before atoms from dissociation are imaged at 19.5 G. **b**, Number of atoms from dissociation as the time t holding at $B_t = 19.838$ G between the two pulses in **a** is scanned. Red solid line is a fit using a damped sinusoidal function, which gives oscillation frequency to be 6.4(7) kHz.

binding energy at B_t, see Fig. 7.12b.

We summarize our measurements of atom number oscillation frequencies at three different values of B_t in Fig. 7.13, which is consistent with our binding energy measurements in Sec. 7.3.2. This suggests that molecules turn into equal superposition of atomic and molecular states after the first pulse, and the two state components develop relative phase difference according to the molecular binding energy at B_t before the second pulse turn the phase accumulation into the variation of atom number.

To conclude, we have observed novel and rich dynamics of chemical reactions in a quantum degenerate Bose gas near a narrow g-wave Feshbach resonance. The molecule formation rate is drastically different in an atomic BEC from that in a normal thermal gas. By monitoring the population and temperature of both the reactants and products, we identified both two-body and three-body processes. After the initial monotonic production of molecules, their population shows coherent small amplitude oscillation, at a frequency consistent with

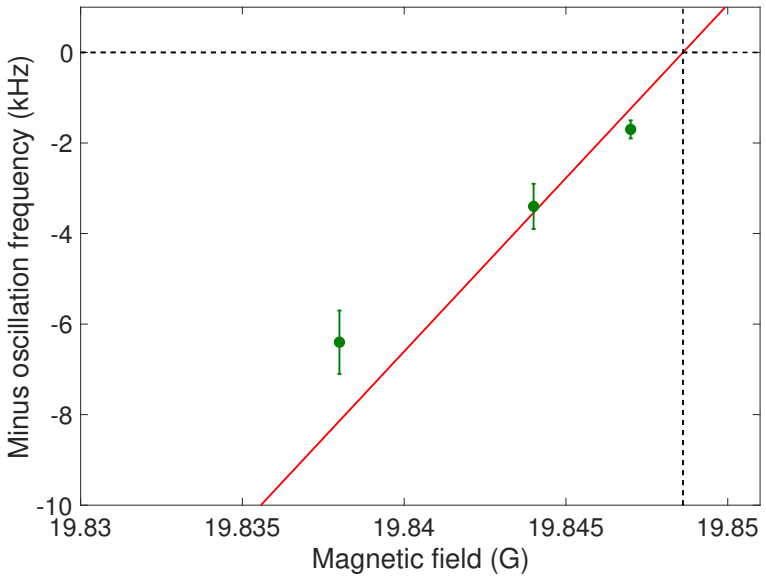

Figure 7.13: **Frequencies of atom number oscillation at different magnetic fields B_t between the two pulses.** Red solid line is from the binding energy measurements in Sec. 7.3.2.

the generalized Rabi frequency. We further steer the reaction dynamics by applying modulation of molecular binding energy, which greatly enhances the oscillation of molecular population. In addition, coherence is shown in the dissociation starting from pure ultracold molecular samples. Our experiments pave the way to further explore how quantum coherence, entanglement and many-body effect play a role in ultracold chemistry.

CHAPTER 8

OUTLOOK

8.1 N-fold symmetric pattern formation using three-frequency interaction modulation

As discussed in Sec. 4.2, in order to create patterns with higher symmetries beyond D_2, D_4 and D_6 patterns starting from a uniform BEC, three frequency components are required in the interaction modulation. Here we derive the conditions for the frequencies and phases of these three frequency components for n-fold symmetric pattern formation.

We start from the general form of the Hamiltonian of driven BECs:

$$H = \int d^3\mathbf{r}\Psi^\dagger(\mathbf{r},t)\frac{p^2}{2m}\Psi(\mathbf{r},t) + \int d^3\mathbf{r}\Psi^\dagger(\mathbf{r},t)V(\mathbf{r})\Psi(\mathbf{r},t) + \frac{g(t)}{2}\int d^3\mathbf{r}\Psi^\dagger(\mathbf{r},t)\Psi^\dagger(\mathbf{r},t)\Psi(\mathbf{r},t)\Psi(\mathbf{r},t), \tag{8.1}$$

where the interaction strength is modulated as $g(t) = 4\pi\hbar^2/m[a_{\rm dc} + \sum_{i=1}^{3} a_i \sin(\omega_i t + \beta_i)]$. Here, $a_{\rm dc}$ is a small offset scattering length to keep the condensate stable and will be neglected in the calculation. a_i is the amplitude of the modulation at frequency ω_i with phase β_i. m is the atomic mass and the momentum operator $\hat{p} = -i\hbar\nabla$. The external flat-bottomed potential $V(\mathbf{r})$ is neglected later because it only serves to determine the initial wavefunction of the BECs and does not affect the dynamics (the potential barrier is set to be lower than the modulation frequencies).

After doing the Fourier transform $\Psi(\mathbf{r},t) = \sum_{\mathbf{k}} \hat{b}_{\mathbf{k}} e^{i\mathbf{k}\cdot\mathbf{r}}$, we obtain the Hamiltonian in momentum space as:

$$H = \sum_{\mathbf{k}} \epsilon_{\mathbf{k}} \hat{b}^{\dagger}_{\mathbf{k}} \hat{b}_{\mathbf{k}} + \frac{g(t)}{2V} \sum_{\mathbf{k},\mathbf{k}',\Delta\mathbf{k}} \hat{b}^{\dagger}_{\mathbf{k}+\Delta\mathbf{k}} \hat{b}^{\dagger}_{\mathbf{k}'-\Delta\mathbf{k}} \hat{b}_{\mathbf{k}} \hat{b}_{\mathbf{k}'}, \tag{8.2}$$

where V is the volume of condensate and $\epsilon_{\mathbf{k}} = \hbar^2 k^2/2m$ is the free particle dispersion.

Then we go to the rotating frame with $\hat{b}_{\mathbf{k}} \to \hat{b}_{\mathbf{k}} e^{-i\epsilon_{\mathbf{k}} t/\hbar}$ and use the rotating wave approximation to eliminate the fast oscillating terms. The Hamiltonian becomes time-independent as:

$$H_I \approx \frac{i}{4V} (\sum_{\mathbf{k}_1} g_1 \hat{b}^{\dagger}_{\mathbf{k}_1} \hat{b}^{\dagger}_{-\mathbf{k}_1} \hat{b}_0 \hat{b}_0 + \sum_{\mathbf{k}_2} g_2 \hat{b}^{\dagger}_{\mathbf{k}_2} \hat{b}^{\dagger}_{-\mathbf{k}_2} \hat{b}_0 \hat{b}_0 + \sum_{\mathbf{k},\Delta\mathbf{k}} \hat{b}^{\dagger}_{\mathbf{k}+\Delta\mathbf{k}} \hat{b}^{\dagger}_{-\Delta\mathbf{k}} \hat{b}_{\mathbf{k}} \hat{b}_0) + h.c. \tag{8.3}$$

Here we keep it to the first order of the condensate operator $\hat{b}_0$ and $g_i = e^{-i\beta_i} 4\pi\hbar^2 a_i/m$. The first two terms represent pair production of opposite momentum modes on the rings at $|\mathbf{k}_1| = \sqrt{m\omega_1/\hbar}$ and $|\mathbf{k}_2| = \sqrt{m\omega_2/\hbar}$ determined by the corresponding modulation frequencies ω_1 and ω_2 [35]. We should first apply modulation only at those two frequencies such that the two momentum rings are macroscopically occupied. The third term is the coupling between momentum modes on those two rings provided by the third frequency component ω_3 and is dominated by the terms in the summation that involve the modes on the two rings and one BEC mode.

Now let's consider the following scattering process where ω_3 is involved (see Fig.8.1a),

$$0 + \mathbf{k}_1 \xrightarrow{\omega_3} \mathbf{k}_2 + \mathbf{k}'_1. \tag{8.4}$$

Due to momentum and energy conservation, we have:

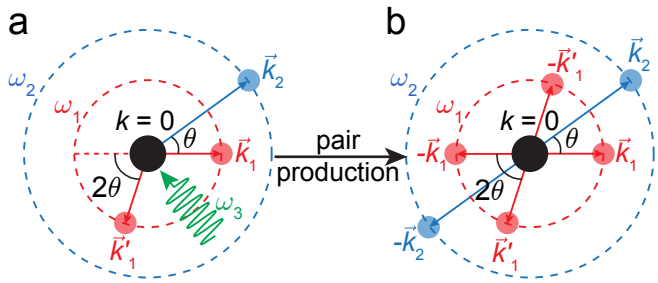

Figure 8.1: **Three-frequency modulation scheme for creating arbitrary angular correlation of pairs of modes with the same magnitude of momentum.** **a**, The two frequency components ω_1 and ω_2 generate two momentum rings at $k_1 = \sqrt{m\omega_1/\hbar}$ and $k_2 = \sqrt{m\omega_2/\hbar}$. The third frequency ω_3 helps to couple the modes on these two rings together at particular directions, determined by the values of the frequencies. **b**, Due to ω_1 and ω_2, the momentum modes in **a** are generated in pairs with the other one in the opposite direction. In this way, the correlation at relative angle 2θ is established on the inner momentum ring.

$$
\begin{aligned}
k_1 &= k_2 \cos\theta + k'_{1x} \\
0 &= k_2 \sin\theta + k'_{1y} \\
\frac{1}{2}\omega_1 + \omega_3 &= \frac{1}{2}\omega_2 + \frac{1}{2}\omega_1,
\end{aligned}
\tag{8.5}
$$

where $\mathbf{k}'_1 = (k'_{1x}, k'_{1y})$, $|\mathbf{k}'_1| = k_1 = \sqrt{m\omega_1/\hbar}$ and $k_2 = \sqrt{m\omega_2/\hbar}$. From Eq.8.5, we can derive the relation between the three modulation frequencies:

$$
\omega_2 = 4\cos^2\theta \times \omega_1 = 2\omega_3, \tag{8.6}
$$

in which $n \times 2\theta = 2\pi$, i.e., $\theta = \pi/n$ and $n \in \mathbb{N}$.

Supported further by the pair production processes by ω_1 and ω_2, the above three modes are accompanied by modes in the opposite directions, see Fig.8.1b. In this way, we obtain angular correlation at relative angle 2θ on the momentum ring 1, which in turn can lead to n-fold symmetric patterns in momentum space because of the rotational symmetry of the system.

With the general formula of Eq.8.6, now let's check if it can be reduced to the schemes for generating the patterns studied in Chapter 4 with lower symmetries. When $n = 3$, $\theta = \pi/3$. Thus we have $\omega_2 = \omega_1 = 2\omega_3$, which is consistent with the scheme for D_6 pattern formation. When $n = 4$, $\theta = \pi/4$. Then we have $\omega_2 = 2\omega_1 = 2\omega_3$ and this is consistent with the scheme for D_4 pattern formation.

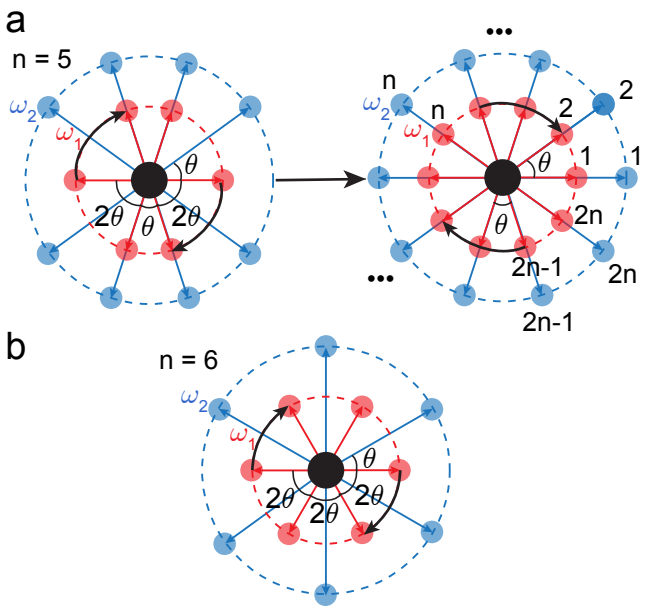

Figure 8.2: **Examples of the formation of n-fold symmetric patterns from the angular correlation at $2\theta = 2\pi/n$ established by the three-frequency modulation scheme in Fig. 8.1. a**, when n = 5 is an odd number, due to the inversion symmetry about the vertical direction, correlations at angle θ is created and the pattern is eventually 2n-fold symmetric. **b**, when n = 6 is an even number, the adjacent modes are coupled at angle 2θ and the pattern is n-fold symmetric.

Now let's move on to study the patterns with higher symmetries of $n > 4$. Since the case is different depending on whether n is an odd or even number, we should discuss it separately. For example, if $n = 5$, when the adjacent modes are coupled together according to Fig.8.1b at angle 2θ, we can find there would be modes coupled at angle θ as shown in Fig.8.2a. Eventually, the modes are evenly distributed with 2n-fold symmetry. This is understandable because whenever there is a pattern with odd symmetry, the pair production processes would make it reflectively symmetric and then it becomes even symmetry. When n

is even, for example $n = 6$ in Fig.8.2b, there is no such problem and the neighboring modes are separated by angle 2θ on the momentum ring 1.

It suffices to consider only the modes that are coupled to each other on the two momentum rings and label them by 1,2,3...,2n, see Fig.8.2a. The corresponding Hamiltonian is (here we're considering the case when n is odd, similar Hamiltonian can be written down when n is even):

$$H' = \frac{i}{4V}(\sum_{i=1}^{2n} g_1 \hat{b}^\dagger_{\mathbf{k}_1^i} \hat{b}^\dagger_{\mathbf{k}_1^{i-n}} \hat{b}_0 \hat{b}_0 + g_2 \hat{b}^\dagger_{\mathbf{k}_2^i} \hat{b}^\dagger_{\mathbf{k}_2^{i-n}} \hat{b}_0 \hat{b}_0 + \sum_{i=1}^{2n} g_3 \hat{b}^\dagger_{\mathbf{k}_2^{i+1}} \hat{b}^\dagger_{\mathbf{k}_1^{i-n+2}} \hat{b}_{\mathbf{k}_1^i} \hat{b}_0 + g_3 \hat{b}^\dagger_{\mathbf{k}_2^{i-1}} \hat{b}^\dagger_{\mathbf{k}_1^{i+n-2}} \hat{b}_{\mathbf{k}_1^i} \hat{b}_0) + h.c. \tag{8.7}$$

Here the addition of indices is modulo 2n, e.g. 1-5+2 = 8 for n = 5.

Since the phases of the modulation at different frequencies are important if we want to resonantly enhance the strength of the pattern, such as that in the D_6 pattern formation, we discuss in the following the condition that the phases satisfy for resonantly enhancing the n-fold symmetric pattern.

The phase matching conditions for the four-wave mixing processes corresponding to the four terms in Eq.8.7 are (the same relation between β_i's holds when n is even):

$$-\theta_i - \theta_{i-n} = \beta_1 \tag{8.8}$$

$$-\phi_i - \phi_{i-n} = \beta_2 \tag{8.9}$$

$$\theta_i - \theta_{i-n+2} - \phi_{i+1} = \beta_3 \tag{8.10}$$

$$\theta_i - \theta_{i+n-2} - \phi_{i-1} = \beta_3 \tag{8.11}$$

where we've treated the creation and annihilation operators as c-numbers $\hat{b}_{\mathbf{k}_1^i} \to |b_{\mathbf{k}_1^i}| e^{i\theta_i}$, $\hat{b}_{\mathbf{k}_2^i} \to |b_{\mathbf{k}_2^i}| e^{i\phi_i}$ and $\hat{b}_0 \to |b_0|$.

After inserting Eq.8.8-8.9 into Eq.8.10 and then substitute i by $i+n$, we obtain

$$\theta_i - \theta_{i-n+2} - \phi_{i+1} = \beta_2 - \beta_3. \tag{8.12}$$

Comparing Eq.8.10 and Eq.8.12, we get the relation between the phases β_2 and β_3:

$$\beta_3 = \beta_2/2. \tag{8.13}$$

The phase β_1 at modulation frequency ω_1 seems irrelevant and can simply be set as 0.

On the other hand, the phases θ_i and ϕ_i of the modes on the two momentum rings, however, are not uniquely determined. At least I've tried to solve θ_i's and ϕ_i's for $n = 5$ and find out that there are many solutions. Thus, the pattern in real space where the momentum modes interfere with BEC is not unique, unless we impose some boundary conditions to the initial condensate wavefunction, such as punching a hole at the center of the circular BEC to select out the pattern that has low density at the center.

8.2 Atom-optical elements built from DMD projected dipole trap potential

As is confirmed in Ref. [35] where the phenomenon of "Bose fireworks" is first observed, the stimulated emission of atoms happens only when the interaction modulation amplitude exceeds a threshold value, determined by the escape rate of the excited atoms. This is very similar to lasing of light from a gain medium. As is known, laser light typically has very large spatial and temporal coherence length and in our case the spatial and temporal coherence of the emitted matter waves are confirmed by the spatial interference and time

reversal experiments presented in Sec. 3.1 and Ref. [70]. With this close analogy between "Bose fireworks" and laser, here we develop various kinds of atom-optical elements based on potential profiles projected by DMD, the functions of which are demonstrated with our coherent matter waves acting on them.

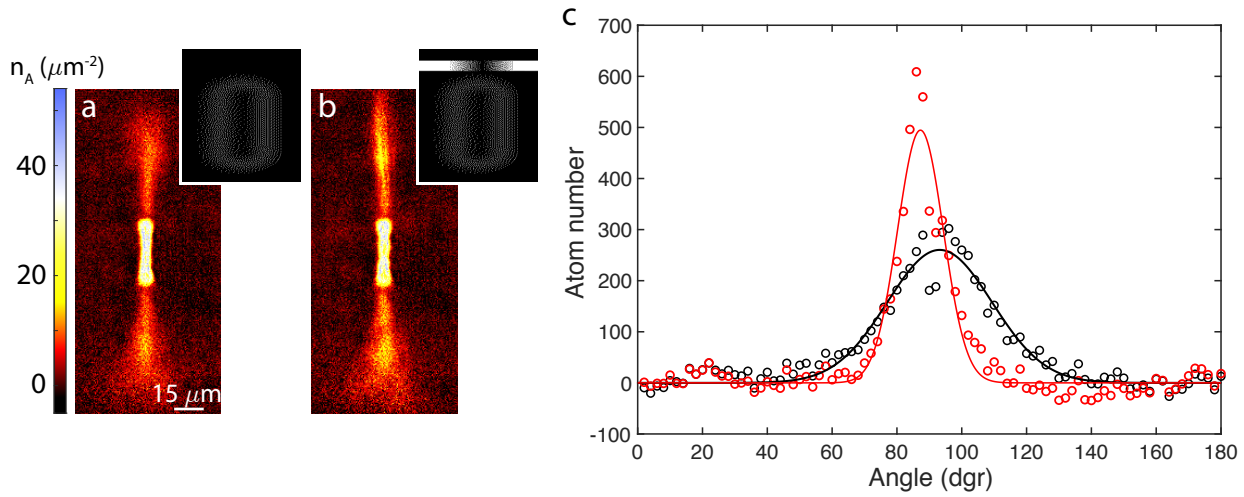

Figure 8.3: **Collimation of emitted matter wave from driven elongated BEC using harmonic potential projected by DMD. a** (**b**), Matter wave emission from a elongated BEC under interaction modulation without (with) harmonic potential projected by DMD on one side of the trap shown at the top right corner of the images. **c**, Angular distribution of atom number within 2^o slices centerred around the bottom of the upper emissions with (red) or without (black) the collimation. Solid lines are Gaussian fits with 1-σ width 16^o (black) and 7^o (red), respectively.

To make a good matter wave source where many atoms directionally emit into a single pair of modes, we shape the BEC into a elongated geometry before applying the interaction modulation, see Sec. 2.3. In Fig. 8.3a, we can see that the emission is mostly along the long axis of BEC, even though the atoms become diffusive as they propagate away from BEC. To collimate the matter wave, we use DMD to project a harmonic potential profile transverse to the matter wave propagation direction, see Fig. 8.3b. As is illustrated in Sec. 2.2.3, atoms with the same momentum are focused to the same location after a quarter period in a harmonic trap and their momentum are converted to be proportional to their initial position (see Eq. 2.4), which has small spread at the location of our projected harmonic potential.

Here we carefully adjust the trap frequency and width of the harmonic potential, such that the matter waves are collimated, see Fig. 8.3c.

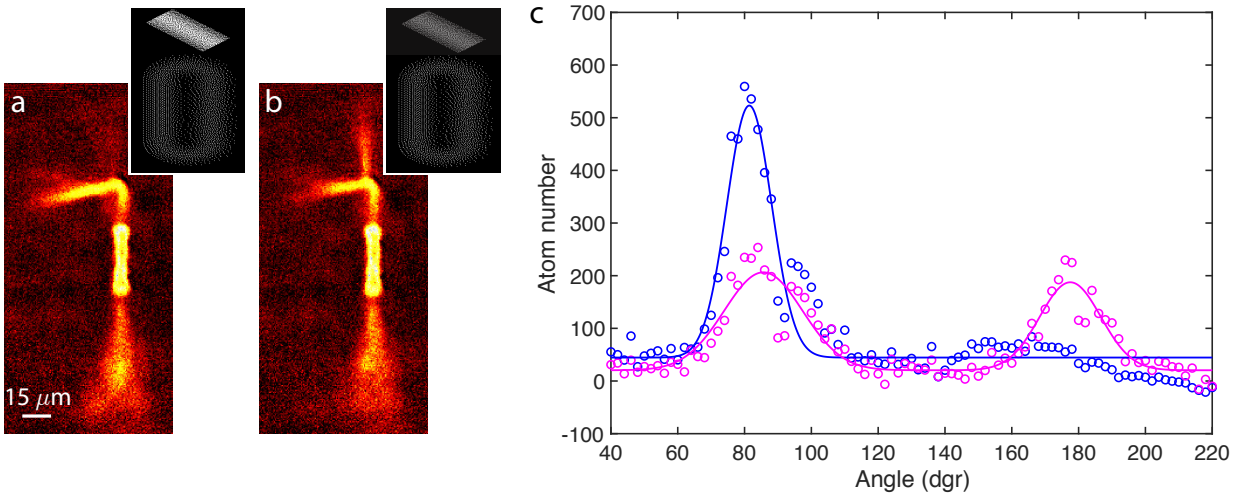

Figure 8.4: **Reflection and splitting of matter waves using a tilted square potential barrier projected by DMD. a** (**b**), Reflection (splitting) of matter wave emission by a higher (lower) square potential oriented 30^o relative to horizontal direction. **c**, Angular distribution of atom number within 2^o slices centered around the middle of the square potential with larger (blue) and lower (magenta) height.

Another two important elements in optics are mirror and beam splitter, which enable us to build interferometers, e.g. Mach Zehnder interferometer. To reflect and split matter waves, we project a square potential barrier with different height positioned with an angle relative to the matter wave propagation direction. When the potential barrier is very high compared to kinetic energy of the atoms, they are mostly reflected (see Fig. 8.4a), whereas when the barrier height is reduced to a proper value, the atom beam can be half transmitted and half reflected (see Fig. 8.4b). In principle, we can build a Mach Zehnder interferometer for the matter waves emitted from BEC using two "mirrors" and two "50%-50% beam splitters" we engineered here.

To explore quantum effects in matter waves scattering through a potential barrier, we project a square potential barrier with atom beam incident normally onto it. The situation here is similar to a quantum mechanical wave packet scattering off a 1D potential barrier

discussed in Ref. [38]. The transmission probability for a wave packet with momentum peaked around k incident onto a square potential barrier with height V_0 and width L is given by

$$T(k) = \begin{cases} \frac{1}{\cosh^2(\rho L)+[\frac{k^2-\rho^2}{2k\rho}\sinh^2(\rho L)]^2} & k < k_0 \\ \frac{1}{\cos^2(k' L)+[\frac{k^2+k'^2}{2kk'}\sin^2(k' L)]^2} & k \geq k_0 \end{cases}, \tag{8.14}$$

where $k_0 = \sqrt{2mV_0/\hbar}$, $\rho = \sqrt{k_0^2 - k^2}$ and $k' = \sqrt{k^2 - k_0^2}$.

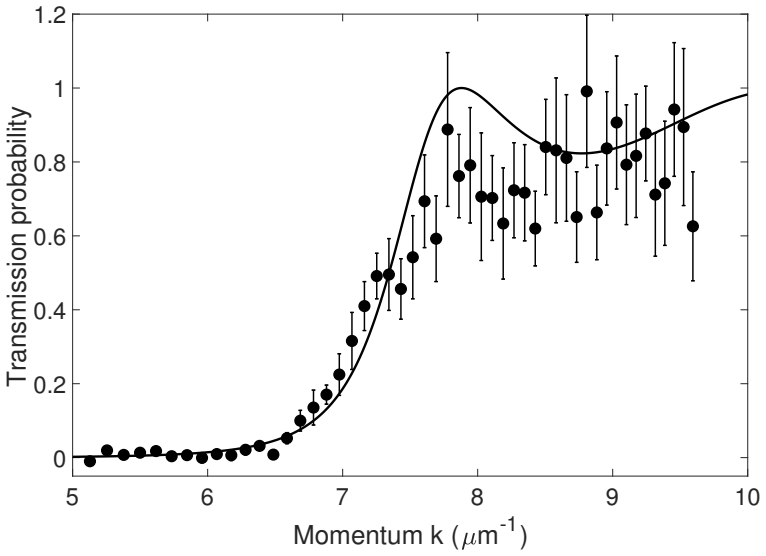

Figure 8.5: **Transmission probability through a square potential barrier as a function of the momentum of emitted matter waves.** Solid line is a fit to the data based on Eq. 8.14.

We first scan the momentum of matter waves by scanning the modulation frequency and monitor the fraction of atoms in matter wave that are transmitted through the barrier, see Fig. 8.5. From the fit based on Eq. 8.14, we get $k_0 = 6.8(1)\mu\text{m}^{-1}$ and $L = 0.80(5)\mu\text{m}$. The width of the squared potential barrier designed in the pattern we sent to DMD is supposed to be 2.4 μm on atom plane, the shape of which is presumably changed due to our finite imaging resolution (see Sec. 2.2.1). It turns out that the designed barrier width is a factor of 3 larger than the effective width extracted from the fit.

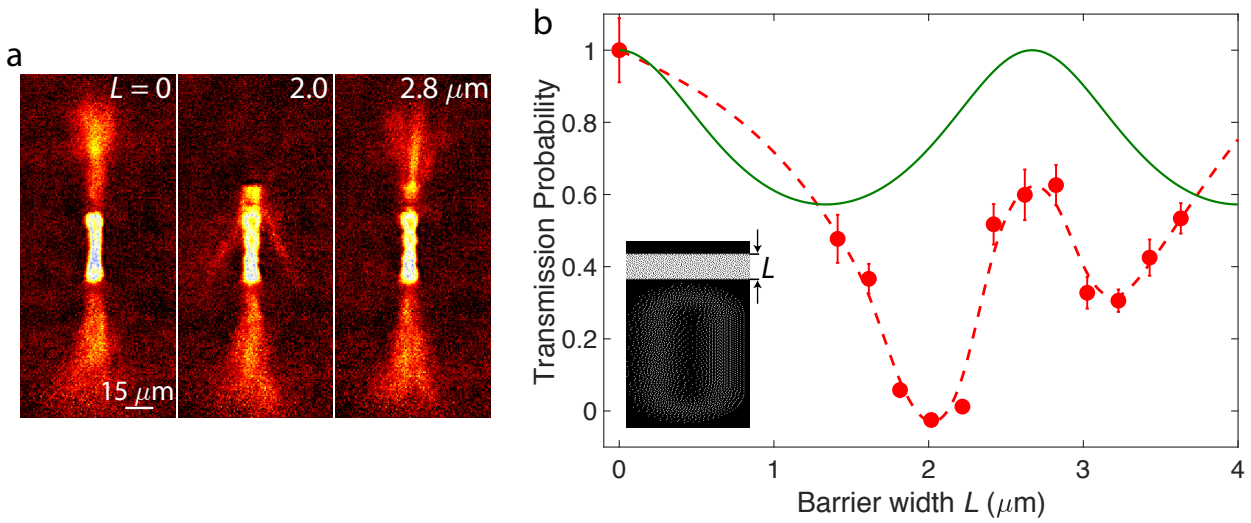

Figure 8.6: **Transmission of matter waves created at interaction modulation frequency of 4.5 kHz through a square potential barrier with variable width projected by DMD. a**, Transmission of matter waves emitting upwards through a square potential barrier with width $L = 0, 2, 2.8$ μm. **b**, Transmission probability as as function of width L of the potential barrier, as indicated by the pattern at bottom left corner which is sent to DMD for projection. Solid line is calculation based on Eq. 8.14 where $k_0 = 6.8$ μm^{-1} and the effective width used for calculation is converted into the designed barrier width in the horizontal axis. Dashed line is a guide to the eye.

Next we scan the width of the barrier while keeping its height to be similar to that in Fig. 8.5 and use an interaction modulation at 4.5 kHz that corresponds to $k = 7.7$ μm^{-1}. The transmission probability shows oscillatory behaviour as a function of the barrier width (see Fig. 8.6), in qualitative agreement with quantum reflection based on Eq. 8.14. Quantitatively, our data shows larger contrast at small barrier width and damping kicks in for wider barrier. It requires further investigation to figure out the discrepancy between our data and the simple model of a wave packet scattering off a 1D square potential barrier.

APPENDIX A

LIST OF PUBLICATIONS

(1) Kai-Xuan Yao, **Zhendong Zhang**, and Cheng Chin. Domain-wall dynamics in Bose–Einstein condensates with synthetic gauge fields. *Nature*, 602(7895):68–72, 2022.

(2) Han Fu, Andreas Glatz, F. Setiawan, Kai-Xuan Yao, **Zhendong Zhang**, Cheng Chin, and K. Levin. Dynamical preparation of an atomic condensate in a hofstadter band. *Phys. Rev. A*, 105:043301, 2022.

(3) **Zhendong Zhang**, Liangchao Chen, Kai-Xuan Yao, and Cheng Chin. Transition from an atomic to a molecular Bose–Einstein condensate. *Nature*, 592(7856):708–711, 2021.

(4) **Zhendong Zhang**, Kai-Xuan Yao, Lei Feng, Jiazhong Hu, and Cheng Chin. Pattern formation in a driven Bose–Einstein condensate. *Nature Physics*, 16(6):652–656, 2020.

(5) Han Fu, **Zhendong Zhang**, Kai-Xuan Yao, Lei Feng, Jooheon Yoo, Logan W. Clark, K. Levin, and Cheng Chin. Jet substructure in fireworks emission from nonuniform and rotating Bose-Einstein condensates. *Phys. Rev. Lett.*, 125:183003, 2020.

(6) Jiazhong Hu, Lei Feng, **Zhendong Zhang**, and Cheng Chin. Quantum simulation of Unruh radiation. *Nature Physics*, 15(8):785–789, 2019.

(7) **Zhendong Zhang**, Kai-Xuan Yao, Shu Nagata, Cheng Chin. Coherent reaction dynamics in quantum degenerate regime. *In preparation*, 2022.

REFERENCES

[1] Haruka Abe, Tetsuto Ueda, Michihiro Morikawa, Yu Saitoh, Ryuji Nomura, and Yuichi Okuda. Faraday instability of superfluid surface. *Phys. Rev. E*, 76:046305, Oct 2007.

[2] J. R. Abo-Shaeer, C. Raman, J. M. Vogels, and W. Ketterle. Observation of vortex lattices in bose-einstein condensates. *Science*, 292(5516):476–479, 2001.

[3] L. Adamczyk et al. Global λ hyperon polarization in nuclear collisions. *Nature*, 548:62, 2017.

[4] Loïc Anderegg, Sean Burchesky, Yicheng Bao, Scarlett S. Yu, Tijs Karman, Eunmi Chae, Kang-Kuen Ni, Wolfgang Ketterle, and John M. Doyle. Observation of microwave shielding of ultracold molecules. *Science*, 373(6556):779–782, 2021.

[5] P. W. Anderson and P. Morel. Generalized bardeen-cooper-schrieffer states and the proposed low-temperature phase of liquid he^3. *Phys. Rev.*, 123:1911–1934, Sep 1961.

[6] M. R. Andrews, C. G. Townsend, H.-J. Miesner, D. S. Durfee, D. M. Kurn, and W. Ketterle. Observation of interference between two bose condensates. *Science*, 275(5300):637–641, 1997.

[7] Vincenzo Aquilanti, Daniela Ascenzi, Massimiliano Bartolomei, David Cappelletti, Simonetta Cavalli, Miguel de Castro Vìtores, and Fernando Pirani. Molecular beam scattering of aligned oxygen molecules. the nature of the bond in the o2âo2 dimer. *Journal of the American Chemical Society*, 121(46):10794–10802, 1999.

[8] H. Arbell and J. Fineberg. Pattern formation in two-frequency forced parametric waves. *Phys. Rev. E*, 65:036224, Mar 2002.

[9] Vincenzo Ardizzone, Przemyslaw Lewandowski, Ming-Ho Luk, Yuen-Chi Tse, Nai-Hang Kwong, Andreas Lücke, Marco Abbarchi, Emmanuel Baudin, Elisabeth Galopin, Jacqueline Bloch, et al. Formation and control of turing patterns in a coherent quantum fluid. *Scientific Reports*, 3:3016, 2013.

[10] F.Tito Arecchi, Stefano Boccaletti, and PierLuigi Ramazza. Pattern formation and competition in nonlinear optics. *Physics Reports*, 318(1):1 – 83, 1999.

[11] Miguel Arratia. On the jets emitted by driven bose–einstein condensates. *Journal of Physics B: Atomic, Molecular and Optical Physics*, 52(5):055301, feb 2019.

[12] N. Balakrishnan and A. Dalgarno. Chemistry at ultracold temperatures. *Chemical Physics Letters*, 341(5):652–656, 2001.

[13] S. M. Barnett and P. L. Knight. Thermofield analysis of squeezing and statistical mixtures in quantum optics. *J. Opt. Soc. Am. B*, 2(3):467–479, Mar 1985.

[14] Antonio Barone and Gianfranco Paterno. *Physics and applications of the Josephson effect*, volume 1. Wiley Online Library, 1982.

[15] J. F. Barry, D. J. McCarron, E. B. Norrgard, M. H. Steinecker, and D. DeMille. Magneto-optical trapping of a diatomic molecule. *Nature*, 512(7514):286–289, 2014.

[16] Martin Berninger, Alessandro Zenesini, Bo Huang, Walter Harm, Hanns-Christoph Nägerl, Francesca Ferlaino, Rudolf Grimm, Paul S. Julienne, and Jeremy M. Hutson. Feshbach resonances, weakly bound molecular states, and coupled-channel potentials for cesium at high magnetic fields. *Phys. Rev. A*, 87:032517, Mar 2013.

[17] Jérôme Beugnon and Nir Navon. Exploring the kibble–zurek mechanism with homogeneous bose gases. *Journal of Physics B: Atomic, Molecular and Optical Physics*, 50(2):022002, jan 2017.

[18] I. Bloch, J. Dalibard, and W. Zwerger. Many-body physics with ultracold gases. *Rev. Mod. Phys.*, 80:885–964, July 2008.

[19] Eberhard Bodenschatz, Werner Pesch, and Guenter Ahlers. Recent developments in rayleigh-bénard convection. *Annual Review of Fluid Mechanics*, 32(1):709–778, 2000.

[20] John L. Bohn, Ana Maria Rey, and Jun Ye. Cold molecules: Progress in quantum engineering of chemistry and quantum matter. *Science*, 357(6355):1002–1010, 2017.

[21] Fabian Böttcher, Jan-Niklas Schmidt, Matthias Wenzel, Jens Hertkorn, Mingyang Guo, Tim Langen, and Tilman Pfau. Transient supersolid properties in an array of dipolar quantum droplets. *Phys. Rev. X*, 9:011051, Mar 2019.

[22] Lincoln D Carr, David DeMille, Roman V Krems, and Jun Ye. Cold and ultracold molecules: science, technology and applications. *New Journal of Physics*, 11(5):055049, may 2009.

[23] Y. Castin and R. Dum. Bose-einstein condensates in time dependent traps. *Phys. Rev. Lett.*, 77:5315–5319, Dec 1996.

[24] Q. Chen, J. Stajic, S. Tan, and K. Levin. Bcs–bec crossover: From high temperature superconductors to ultracold superfluids. *Phys. Rep.*, 412:1–88, February 2005.

[25] Qijin Chen, Jelena Stajic, Shina Tan, and K. Levin. Bcs-bec crossover: From high temperature superconductors to ultracold superfluids. *Physics Reports*, 412(1):1 – 88, 2005.

[26] Tao Chen and Bo Yan. Characterization of stimulated excitations in a driven bose-einstein condensate. *Phys. Rev. A*, 98:063615, Dec 2018.

[27] Liang-Ying Chih and Murray Holland. Driving quantum correlated atom-pairs from a bose-einstein condensate. *arXiv:2001.02315*, 2020.

[28] C. Chin, T. Kraemer, M. Mark, J. Herbig, P. Waldburger, H.-C. Nägerl, and R. Grimm. Observation of feshbach-like resonances in collisions between ultracold molecules. *Phys. Rev. Lett.*, 94:123201, Apr 2005.

[29] Cheng Chin and Rudolf Grimm. Thermal equilibrium and efficient evaporation of an ultracold atom-molecule mixture. *Phys. Rev. A*, 69:033612, Mar 2004.

[30] Cheng Chin, Rudolf Grimm, Paul Julienne, and Eite Tiesinga. Feshbach resonances in ultracold gases. *Rev. Mod. Phys.*, 82:1225–1286, Apr 2010.

[31] L. Chomaz, D. Petter, P. Ilzhöfer, G. Natale, A. Trautmann, C. Politi, G. Durastante, R. M. W. van Bijnen, A. Patscheider, M. Sohmen, M. J. Mark, and F. Ferlaino. Long-lived and transient supersolid behaviors in dipolar quantum gases. *Phys. Rev. X*, 9:021012, Apr 2019.

[32] Lauriane Chomaz et al. Emergence of coherence via transverse condensation in a uniform quasi-two-dimensional bose gas. *Nature Communications*, 6:6162, 2015.

[33] Logan Clark. *Quantum many-body dynamics with driven Bose condensates: Kibble-Zurek mechanism and Bose fireworks*. PhD thesis, University of Chicago, 2017.

[34] Logan W. Clark, Brandon M. Anderson, Lei Feng, Anita Gaj, K. Levin, and Cheng Chin. Observation of density-dependent gauge fields in a bose-einstein condensate based on micromotion control in a shaken two-dimensional lattice. *Phys. Rev. Lett.*, 121:030402, Jul 2018.

[35] Logan W. Clark, Anita Gaj, Lei Feng, and Cheng Chin. Collective emission of matter-wave jets from driven bose–einstein condensates. *Nature*, 551:356, 11 2017.

[36] Logan W. Clark, Li-Chung Ha, Chen-Yu Xu, and Cheng Chin. Quantum dynamics with spatiotemporal control of interactions in a stable bose-einstein condensate. *Phys. Rev. Lett.*, 115:155301, Oct 2015.

[37] N. R. Claussen, S. J. J. M. F. Kokkelmans, S. T. Thompson, E. A. Donley, E. Hodby, and C. E. Wieman. Very-high-precision bound-state spectroscopy near a ^{85}Rb feshbach resonance. *Phys. Rev. A*, 67:060701, Jun 2003.

[38] Claude Cohen-Tannoudji, Bernard Diu, and Frank Laloe. Quantum mechanics, volume 1. *Quantum Mechanics*, 1:898, 1986.

[39] Megan Connors, Christine Nattrass, Rosi Reed, and Sevil Salur. Jet measurements in heavy ion physics. *Rev. Mod. Phys.*, 90:025005, Jun 2018.

[40] N. R. Cooper, J. Dalibard, and I. B. Spielman. Topological bands for ultracold atoms. *Rev. Mod. Phys.*, 91:015005, Mar 2019.

[41] L. Corman, L. Chomaz, T. Bienaimé, R. Desbuquois, C. Weitenberg, S. Nascimbène, J. Dalibard, and J. Beugnon. Quench-induced supercurrents in an annular bose gas. *Phys. Rev. Lett.*, 113:135302, Sep 2014.

[42] M. C. Cross and P. C. Hohenberg. Pattern formation outside of equilibrium. *Rev. Mod. Phys.*, 65:851–1112, Jul 1993.

[43] Luigi De Marco, Giacomo Valtolina, Kyle Matsuda, William G. Tobias, Jacob P. Covey, and Jun Ye. A degenerate fermi gas of polar molecules. *Science*, 363(6429):853–856, 2019.

[44] M. H. G. de Miranda, A. Chotia, B. Neyenhuis, D. Wang, G. Quéméner, S. Ospelkaus, J. L. Bohn, J. Ye, and D. S. Jin. Controlling the quantum stereodynamics of ultracold bimolecular reactions. *Nature Physics*, 7(6):502–507, 2011.

[45] L. Deng, E. W. Hagley, J. Wen, M. Trippenbach, Y. Band, P. S. Julienne, J. E. Simsarian, K. Helmerson, S. L. Rolston, and W. D. Phillips. Four-wave mixing with matter waves. *Nature*, 398(6724):218–220, 1999.

[46] Elizabeth A. Donley, Neil R. Claussen, Simon L. Cornish, Jacob L. Roberts, Eric A. Cornell, and Carl E. Wieman. Dynamics of collapsing and exploding bose–einstein condensates. *Nature*, 412(6844):295–299, 2001.

[47] Elizabeth A. Donley, Neil R. Claussen, Sarah T. Thompson, and Carl E. Wieman. Atom–molecule coherence in a bose–einstein condensate. *Nature*, 417(6888):529–533, 2002.

[48] R.A. Duine and H.T.C. Stoof. Atom–molecule coherence in bose gases. *Physics Reports*, 396(3):115–195, 2004.

[49] André Eckardt. Colloquium: Atomic quantum gases in periodically driven optical lattices. *Rev. Mod. Phys.*, 89:011004, Mar 2017.

[50] W. S. Edwards and S. Fauve. Patterns and quasi-patterns in the faraday experiment. *Journal of Fluid Mechanics.*, 278:123–148, 1994.

[51] Christoph Eigen, Jake A. P. Glidden, Raphael Lopes, Eric A. Cornell, Robert P. Smith, and Zoran Hadzibabic. Universal prethermal dynamics of bose gases quenched to unitarity. *Nature*, 563(7730):221–224, 2018.

[52] P. Engels, C. Atherton, and M. A. Hoefer. Observation of faraday waves in a bose-einstein condensate. *Phys. Rev. Lett.*, 98:095301, Feb 2007.

[53] U. Fano. Effects of configuration interaction on intensities and phase shifts. *Phys. Rev.*, 124:1866–1878, Dec 1961.

[54] Lei Feng. *Coherent Nonequilibrium Many-Body Dynamics in Driven Bose Condensates.* PhD thesis, The University of Chicago, 2019.

[55] F Ferlaino, S Knoop, M Berninger, M Mark, H-C Nägerl, and R Grimm. Collisions of ultracold trapped cesium feshbach molecules. *Laser Physics*, 20(1):23–31, 2010.

[56] Han Fu, Lei Feng, Brandon M. Anderson, Logan W. Clark, Jiazhong Hu, Jeffery W. Andrade, Cheng Chin, and K. Levin. Density waves and jet emission asymmetry in bose fireworks. *Phys. Rev. Lett.*, 121:243001, Dec 2018.

[57] Frederik Görg et al. *Nature Physics*, 15:1161, 2019.

[58] S. Giorgini, L.P. Pitaevskii, and S. Stringari. Theory of ultracold atomic fermi gases. *Rev. Mod. Phys.*, 80:1215–1274, October 2008.

[59] N. Goldman, J. C. Budich, and P. Zoller. Topological quantum matter with ultracold gases in optical lattices. *Nature Physics*, 12:639, 2016.

[60] Markus Greiner, Olaf Mandel, Tilman Esslinger, Theodor W. Hänsch, and Immanuel Bloch. Quantum phase transition from a superfluid to a mott insulator in a gas of ultracold atoms. *Nature*, 415(6867):39–44, 2002.

[61] Alexander Groot. *Excitations in hydrodynamic ultra-cold Bose gases*. PhD thesis, Utrecht University, 2015.

[62] Lichung Ha. *Bose-Einstein condensates in a shaken optical lattice*. PhD thesis, The University of Chicago, 2016.

[63] Zoran Hadzibabic and Jean Dalibard. Two-dimensional bose fluids: An atomic physics perspective. *La Rivista del Nuovo Cimento*, 34(6):389–434, 2011.

[64] D. J. Heinzen, Roahn Wynar, P. D. Drummond, and K. V. Kheruntsyan. Superchemistry: Dynamics of coupled atomic and molecular bose-einstein condensates. *Phys. Rev. Lett.*, 84:5029–5033, May 2000.

[65] Jens Herbig, Tobias Kraemer, Michael Mark, Tino Weber, Cheng Chin, Hanns-Christoph Nägerl, and Rudolf Grimm. Preparation of a pure molecular quantum gas. *Science*, 301(5639):1510–1513, 2003.

[66] Tin-Lun Ho. Universal thermodynamics of degenerate quantum gases in the unitarity limit. *Phys. Rev. Lett.*, 92:090402, Mar 2004.

[67] Tin-Lun Ho. The bose-einstein condensate of g-wave molecules and its intrinsic angular momentum. 2021.

[68] Tin-Lun Ho and Qi Zhou. Obtaining the phase diagram and thermodynamic quantities of bulk systems from the densities of trapped gases. *Nature Physics*, 6(2):131–134, 2010.

[69] Rebecca Hoyle. *Pattern Formation: An Introduction to Methods*. Cambridge University Press, 2006.

[70] Jiazhong Hu, Lei Feng, Zhendong Zhang, and Cheng Chin. Quantum simulation of unruh radiation. *Nature Physics*, 15(8):785–789, 2019.

[71] Ming-Guang Hu, Yu Liu, Matthew A. Nichols, Lingbang Zhu, Goulven Quéméner, Olivier Dulieu, and Kang-Kuen Ni. Nuclear spin conservation enables state-to-state control of ultracold molecular reactions. *Nature Chemistry*, 13(5):435–440, 2021.

[72] Chen-Lung Hung. *In situ probing of two-dimensional quantum gases*. The University of Chicago, 2011.

[73] Chen-Lung Hung, Victor Gurarie, and Cheng Chin. From cosmology to cold atoms: Observation of sakharov oscillations in a quenched atomic superfluid. *Science*, 341(6151):1213–1215, 2013.

[74] Chen-Lung Hung, Xibo Zhang, Nathan Gemelke, and Cheng Chin. Accelerating evaporative cooling of atoms into bose-einstein condensation in optical traps. *Phys. Rev. A*, 78:011604, Jul 2008.

[75] Chen-Lung Hung, Xibo Zhang, Nathan Gemelke, and Cheng Chin. Observation of scale invariance and universality in two-dimensional bose gases. *Nature*, 470(7333):236–239, 2011.

[76] Chen-Lung Hung, Xibo Zhang, Li-Chung Ha, Shih-Kuang Tung, Nathan Gemelke, and Cheng Chin. Extracting density–density correlations fromin situimages of atomic quantum gases. *New Journal of Physics*, 13(7):075019, jul 2011.

[77] Zbigniew Idziaszek, Krzysztof Jachymski, and Paul S Julienne. Reactive collisions in confined geometries. *New Journal of Physics*, 17(3):035007, mar 2015.

[78] Zbigniew Idziaszek and Paul S. Julienne. Universal rate constants for reactive collisions of ultracold molecules. *Phys. Rev. Lett.*, 104:113202, 2010.

[79] S. Inouye, S. Gupta, T. Rosenband, A. P. Chikkatur, A. Görlitz, T. L. Gustavson, A. E. Leanhardt, D. E. Pritchard, and W. Ketterle. Observation of vortex phase singularities in bose-einstein condensates. *Phys. Rev. Lett.*, 87:080402, Aug 2001.

[80] Kevin M. Jones, Eite Tiesinga, Paul D. Lett, and Paul S. Julienne. Ultracold photoassociation spectroscopy: Long-range molecules and atomic scattering. *Rev. Mod. Phys.*, 78:483–535, May 2006.

[81] Gregor Jotzu et al. Experimental realization of the topological haldane model with ultracold fermions. *Nature*, 515:237, 2014.

[82] Philip K. Maini, Kevin J. Painter, and Helene Nguyen Phong Chau. Spatial pattern formation in chemical and biological systems. *J. Chem. Soc., Faraday Trans.*, 93:3601–3610, 1997.

[83] Holger Kadau, Matthias Dr. Schmitt, Michaela Wenzel, Clarissa Wink, Thomas Maier, Igor Ferrier-Barbut, and Tilman Pfau. Observing the rosensweig instability of a quantum ferrofluid. *Nature*, 530:194–197, 2016.

[84] Wolfgang Ketterle, Dallin S Durfee, and DM Stamper-Kurn. Making, probing and understanding bose-einstein condensates. *arXiv preprint cond-mat/9904034*, 1999.

[85] Roman Kogler et al. Jet substructure at the large hadron collider. *Rev. Mod. Phys.*, 91:045003, Dec 2019.

[86] Thorsten Köhler, Krzysztof Góral, and Paul S. Julienne. Production of cold molecules via magnetically tunable feshbach resonances. *Rev. Mod. Phys.*, 78:1311–1361, Dec 2006.

[87] R. V. Krems. Cold controlled chemistry. *Phys. Chem. Chem. Phys.*, 10:4079–4092, 2008.

[88] Jochen Kronjäger, Christoph Becker, Parvis Soltan-Panahi, Kai Bongs, and Klaus Sengstock. Spontaneous pattern formation in an antiferromagnetic quantum gas. *Phys. Rev. Lett.*, 105:090402, Aug 2010.

[89] Peter Krüger, Zoran Hadzibabic, and Jean Dalibard. Critical point of an interacting two-dimensional atomic bose gas. *Phys. Rev. Lett.*, 99:040402, Jul 2007.

[90] Sunil Kumar and C. L. Mehta. Theory of the interaction of a single-mode resonant radiation field with n two-level atoms. *Phys. Rev. A*, 21:1573–1588, May 1980.

[91] Lev Davidovich Landau and Evgeny M Lifshitz. *Course of Theoretical Physics Vol. 6 Fluid Mechanies*. Pergamon Press, 1959.

[92] A. D. Lange, K. Pilch, A. Prantner, F. Ferlaino, B. Engeser, H.-C. Nägerl, R. Grimm, and C. Chin. Determination of atomic scattering lengths from measurements of molecular binding energies near feshbach resonances. *Phys. Rev. A*, 79:013622, Jan 2009.

[93] Jun-Ru Li, Jeongwon Lee, Wujie Huang, Sean Burchesky, Boris Shteynas, Furkan Çağrı Top, Alan O Jamison, and Wolfgang Ketterle. A stripe phase with supersolid properties in spin–orbit-coupled bose–einstein condensates. *Nature*, 543(7643):91, 2017.

[94] Andrew R Liddle and David H Lyth. *Cosmological inflation and large-scale structure*. Cambridge University Press, 2000.

[95] Ron Lifshitz and Dean M. Petrich. Theoretical model for faraday waves with multiple-frequency forcing. *Phys. Rev. Lett.*, 79:1261–1264, Aug 1997.

[96] Bin Liu, Li-Bin Fu, and Jie Liu. Shapiro-like resonance in ultracold molecule production via an oscillating magnetic field. *Phys. Rev. A*, 81:013602, Jan 2010.

[97] P. Makotyn, C. E. Klauss, D. L. Goldberger, E. A. Cornell, and D. S. Jin. Universal dynamics of a degenerate unitary bose gas. *Nature Physics*, 10(2):116–119, 2014.

[98] Rajesh K Malla, Vladimir Y Chernyak, Chen Sun, and Nikolai A Sinitsyn. Coherent reaction between molecular and atomic bose-einstein condensates: integrable model. *arXiv preprint arXiv:2112.12302*, 2021.

[99] M. Mark, T. Kraemer, P. Waldburger, J. Herbig, C. Chin, H.-C. Nägerl, and R. Grimm. "stückelberg interferometry" with ultracold molecules. *Phys. Rev. Lett.*, 99:113201, Sep 2007.

[100] Manfred Mark, Florian Meinert, Katharina Lauber, and Hanns-Christoph Nägerl. Mott-insulator-aided detection of ultra-narrow feshbach resonances. *SciPost Phys*, 5:055, 2018.

[101] Kyle Matsuda, Luigi De Marco, Jun-Ru Li, William G. Tobias, Giacomo Valtolina, Goulven Quéméner, and Jun Ye. Resonant collisional shielding of reactive molecules using electric fields. *Science*, 370(6522):1324–1327, 2020.

[102] M. R. Matthews, B. P. Anderson, P. C. Haljan, D. S. Hall, C. E. Wieman, and E. A. Cornell. Vortices in a bose-einstein condensate. *Phys. Rev. Lett.*, 83:2498–2501, Sep 1999.

[103] Michael Mayle, Goulven Quéméner, Brandon P. Ruzic, and John L. Bohn. Scattering of ultracold molecules in the highly resonant regime. *Phys. Rev. A*, 87:012709, 2013.

[104] Tadej Mežnaršič, Rok Žitko, Tina Arh, Katja Gosar, Erik Zupanič, and Peter Jeglič. Emission of correlated jets from a driven matter-wave soliton in a quasi-one-dimensional geometry. *Phys. Rev. A*, 101:031601, Mar 2020.

[105] Andrea Micheli, Zbigniew Idziaszek, Guido Pupillo, Mikhail A. Baranov, Peter Zoller, and Paul S. Julienne. Universal rates for reactive ultracold polar molecules in reduced dimensions. *Phys. Rev. Lett.*, 105:073202, Aug 2010.

[106] John Miles. On faraday waves. *Journal of Fluid Mechanics*, 248:671–683, 1993.

[107] M. G. Moore and A. Vardi. Bose-enhanced chemistry: Amplification of selectivity in the dissociation of molecular bose-einstein condensates. *Phys. Rev. Lett.*, 88:160402, Apr 2002.

[108] OLE G. Mouritsen. Pattern formation in condensed matter. *International Journal of Modern Physics B*, 04(13):1925–1954, 1990.

[109] Nir Navon, Alexander L. Gaunt, Robert P. Smith, and Zoran Hadzibabic. Critical dynamics of spontaneous symmetry breaking in a homogeneous bose gas. *Science*, 347(6218):167–170, 2015.

[110] J. H. V. Nguyen, M. C. Tsatsos, D. Luo, A. U. J. Lode, G. D. Telles, V. S. Bagnato, and R. G. Hulet. Parametric excitation of a bose-einstein condensate: From faraday waves to granulation. *Phys. Rev. X*, 9:011052, Mar 2019.

[111] S. Ospelkaus, K.-K. Ni, D. Wang, M. H. G. de Miranda, B. Neyenhuis, G. Quéméner, P. S. Julienne, J. L. Bohn, D. S. Jin, and J. Ye. Quantum-state controlled chemical reactions of ultracold potassium-rubidium molecules. *Science*, 327(5967):853–857, 2010.

[112] Jesús Pérez-Ríos. *An Introduction to Cold and Ultracold Chemistry: Atoms, Molecules, Ions and Rydbergs*. Springer, 2020.

[113] D. S. Petrov, M. Holzmann, and G. V. Shlyapnikov. Bose-einstein condensation in quasi-2d trapped gases. *Phys. Rev. Lett.*, 84:2551–2555, Mar 2000.

[114] D. S. Petrov and G. V. Shlyapnikov. Interatomic collisions in a tightly confined bose gas. *Phys. Rev. A*, 64:012706, Jun 2001.

[115] S. E. Pollack, D. Dries, R. G. Hulet, K. M. F. Magalhães, E. A. L. Henn, E. R. F. Ramos, M. A. Caracanhas, and V. S. Bagnato. Collective excitation of a bose-einstein condensate by modulation of the atomic scattering length. *Phys. Rev. A*, 81:053627, May 2010.

[116] Yves Pomeau and Paul Manneville. Intermittent transition to turbulence in dissipative dynamical systems. *Communications in Mathematical Physics*, 74(2):189–197, Jun 1980.

[117] Nikolay Prokof'ev, Oliver Ruebenacker, and Boris Svistunov. Critical point of a weakly interacting two-dimensional bose gas. *Phys. Rev. Lett.*, 87:270402, Dec 2001.

[118] Nikolay Prokof'ev and Boris Svistunov. Two-dimensional weakly interacting bose gas in the fluctuation region. *Phys. Rev. A*, 66:043608, Oct 2002.

[119] Goulven Quéméner and Paul S. Julienne. Ultracold molecules under control! *Chemical Reviews*, 112(9):4949–5011, 09 2012.

[120] Leo Radzihovsky, Jae Park, and Peter B. Weichman. Superfluid transitions in bosonic atom-molecule mixtures near a feshbach resonance. *Phys. Rev. Lett.*, 92:160402, Apr 2004.

[121] S. Raghavan, A. Smerzi, S. Fantoni, and S. R. Shenoy. Coherent oscillations between two weakly coupled bose-einstein condensates: Josephson effects, π oscillations, and macroscopic quantum self-trapping. *Phys. Rev. A*, 59:620–633, Jan 1999.

[122] Florian Richter, Daniel Becker, Cédric Bény, Torben A Schulze, Silke Ospelkaus, and Tobias J Osborne. Ultracold chemistry and its reaction kinetics. *New Journal of Physics*, 17(5):055005, may 2015.

[123] M. W. J. Romans, R. A. Duine, Subir Sachdev, and H. T. C. Stoof. Quantum phase transition in an atomic bose gas with a feshbach resonance. *Phys. Rev. Lett.*, 93:020405, Jul 2004.

[124] Hidetsugu Sakaguchi and Helmut R Brand. Localized patterns for the quintic complex swift-hohenberg equation. *Physica D: Nonlinear Phenomena*, 117(1):95 – 105, 1998.

[125] Andreas Schindewolf, Roman Bause, Xing-Yan Chen, Marcel Duda, Tijs Karman, Immanuel Bloch, and Xin-Yu Luo. Evaporation of microwave-shielded polar molecules to quantum degeneracy, 2022.

[126] Christian Schweizer, Fabian Grusdt, Moritz Berngruber, Luca Barbiero, Eugene Demler, Nathan Goldman, Immanuel Bloch, and Monika Aidelsburger. Floquet approach to z_2 lattice gauge theories with ultracold atoms in optical lattices. *Nature Physics*, 15:1168, 2019.

[127] Sang Won Seo, Bumsuk Ko, Joon Hyun Kim, and Y. Shin. Observation of vortex-antivortex pairing in decaying 2d turbulence of a superfluid gas. *Scientific Reports*, 7(1):4587, 2017.

[128] D. Hudson Smith. Inducing resonant interactions in ultracold atoms with a modulated magnetic field. *Phys. Rev. Lett.*, 115:193002, Nov 2015.

[129] Hyungmok Son, Juliana J. Park, Wolfgang Ketterle, and Alan O. Jamison. Collisional cooling of ultracold molecules. *Nature*, 580(7802):197–200, 2020.

[130] Hyungmok Son, Juliana J. Park, Yu-Kun Lu, Alan O. Jamison, Tijs Karman, and Wolfgang Ketterle. Control of reactive collisions by quantum interference. *Science*, 375(6584):1006–1010, 2022.

[131] Daniel A Steck. Cesium d line data. 2003.

[132] Kevin E. Strecker, Guthrie B. Partridge, Andrew G. Truscott, and Randall G. Hulet. Formation and propagation of matter-wave soliton trains. *Nature*, 417(6885):150–153, 2002.

[133] J. Swift and P. C. Hohenberg. Hydrodynamic fluctuations at the convective instability. *Phys. Rev. A*, 15:319–328, Jan 1977.

[134] L. Tanzi, E. Lucioni, F. Famà, J. Catani, A. Fioretti, C. Gabbanini, R. N. Bisset, L. Santos, and G. Modugno. Observation of a dipolar quantum gas with metastable supersolid properties. *Phys. Rev. Lett.*, 122:130405, Apr 2019.

[135] Roger Temam and A Chorin. Navier stokes equations: Theory and numerical analysis, 1978.

[136] S. T. Thompson, E. Hodby, and C. E. Wieman. Ultracold molecule production via a resonant oscillating magnetic field. *Phys. Rev. Lett.*, 95:190404, Nov 2005.

[137] Eddy Timmermans, Kyoko Furuya, Peter W. Milonni, and Arthur K. Kerman. Prospect of creating a composite fermi/bose superfluid. *Physics Letters A*, 285(3):228 – 233, 2001.

[138] S. Tung, G. Lamporesi, D. Lobser, L. Xia, and E. A. Cornell. Observation of the presuperfluid regime in a two-dimensional bose gas. *Phys. Rev. Lett.*, 105:230408, 2010.

[139] Alan Mathison Turing. The chemical basis of morphogenesis. *Philosophical Transactions of the Royal Society of London. Series B, Biological Sciences*, 237(641):37–72, 1952.

[140] A. Vardi, V. A. Yurovsky, and J. R. Anglin. Quantum effects on the dynamics of a two-mode atom-molecule bose-einstein condensate. *Phys. Rev. A*, 64:063611, Nov 2001.

[141] Xiang-Bin Wang, Tohya Hiroshima, Akihisa Tomita, and Masahito Hayashi. Quantum information with gaussian states. *Physics Reports*, 448(1):1 – 111, 2007.

[142] Jonathan D. Weinstein, Robert deCarvalho, Thierry Guillet, Bretislav Friedrich, and John M. Doyle. Magnetic trapping of calcium monohydride molecules at millikelvin temperatures. *Nature*, 395(6698):148–150, 1998.

[143] Kali E. Wilson, Zachary L. Newman, Joseph D. Lowney, and Brian P. Anderson. In situ imaging of vortices in bose-einstein condensates. *Phys. Rev. A*, 91:023621, Feb 2015.

[144] Kali E. Wilson, Zachary L. Newman, Joseph D. Lowney, and Brian P. Anderson. In situ imaging of vortices in bose-einstein condensates. *Phys. Rev. A*, 91:023621, Feb 2015.

[145] Zhigang Wu and Hui Zhai. Dynamics and density correlations in matter-wave jet emission of a driven condensate. *Phys. Rev. A*, 99:063624, Jun 2019.

[146] Xibo Zhang. *Observation of quantum criticality with ultracold atoms in optical lattices*. PhD thesis, University of Chicago, 2012.

[147] Zhendong Zhang, Liangchao Chen, Kai-Xuan Yao, and Cheng Chin. Transition from an atomic to a molecular bose–einstein condensate. *Nature*, 592(7856):708–711, 2021.

[148] Zhendong Zhang, Kai-Xuan Yao, Lei Feng, Jiazhong Hu, and Cheng Chin. Pattern formation in a driven bose–einstein condensate. *Nature Physics*, 16(6):652–656, 2020.